PHD

An analysis of the locomotory behaviour and functional morphology of errant polychaetes

Hesselberg, Thomas

Award date:
2006

Awarding institution:
University of Bath

An analysis of the locomotory behaviour and functional morphology of errant polychaetes

Thomas Hesselberg

A thesis submitted for the degree of Doctor of Philosophy

University of Bath

Department of Mechanical Engineering

June 2006

ProQuest LLC
789 East Eisenhower Parkway
P.O. Box 1346
Ann Arbor, MI 48106-1346

Table of contents

Acknowledgements

The days when scientists were working isolated in their ivory towers are long gone and today research requires input from a number of people. This PhD study is certainly no exception and I have been lucky to receive help and guidance from many different sources.

Most thanks go to my supervisor Julian Vincent who always had many ideas and suggestions, although not all of them were given the attention they deserved. Special thanks go to the two post-doctoral scientists, Graham Whiteley and John Williams, involved with my project for their suggestions and advice as well as 'H' Jones for technical help. Thanks to all the participants of the BIOLOCH project especially to Michael Sfakiotakis, Giovanni La Spina and Dmitris Tsakiris for their help and advice.

I would like to thank all the members of the annelid email list and especially Torkild Bakken, Susan Chambers, Helmut Goerke, Jörg Hardege, Daniel Martin, Peter Olive and Lars Orrhage for sharing their knowledge of polychaete biology as well as their advice on catching and keeping worms. Jörg Hardege and Carsten Müller, furthermore, supplied me with different species of nereidids from their own laboratories.

I am grateful for the help I received from other departments at the University of Bath. Thanks to the Centre for Electron Optical Studies and especially to Ursula Potter for practical help on how to use the scanning electron microscope. Thanks to Grant Trewartha and Mark Brewin from Sport & Exercise Science for introducing me to the direct linear transformation method. Thanks to Biology & Biochemistry and especially Stuart Reynolds for his help to get me started and Jackie Rawlings for lending me various equipment.

I am very grateful to John Videler for allowing me to visit his group at the University of Groningen and to perform flow visualisation experiments there. Thanks to Eize Stamhuis and Peter Müller for showing me how to use the PIV equipment and software and for help with interpreting the data. Thanks to Jos de Wiljes for technical help and to the entire Department of Marine Biology for making me feel welcome.

Lastly I would like to thank all past and present colleagues at the Department of Mechanical Engineering for their many useful suggestions and comments. A special thank to William Megill for helping with LABVIEW and to Rorie Edmunds for his help

with the mathematical aspects of my work. Thanks to everybody that I shared office with throughout my time in Bath. Not only for their help with the engineering, graphical and language aspects of my study but also for making my time here very enjoyable. Rhodri Armour, Richard Bomphrey, Veronika Kapsali, Matthew Liston, Keith Paskins, Paul Riggs, Francisco Rojo, Bruce Saunders and Dave Stewart.

Declaration of work done in conjunction with others

Modern science is a highly collaborative field and this PhD project is no exception. Besides the invaluable suggestions from my supervisor a whole group of people has provided me with practical or theoretical help during some stages of this project. These people are either acknowledged after each published chapter and/or at the beginning of the thesis.

However, I am responsible for the work presented here and this thesis has been written by me. The only exception is chapter 4 which has been written in conjunction with Giovanni La Spina and John Williams. They were responsible for designing the robot and the test rig, whereas I was responsible for providing the biological data. The reason this chapter is included in this PhD thesis is that I designed the experiment and that it relates to the objectives of this thesis and the results of the other chapters.

The entire chapter was done in collaboration, but Giovanni La Spina was mainly responsible for the following sections; 4.3, 4.4.1, 4.4.2, 4.7. John Williams was mainly responsible for the following sections; 4.4.3, 4.5.1, 4.6 (jointly with me) and I was mainly responsible for the following sections; 4.1, 4.2, 4.5.2, 4.6 (jointly with John Williams).

I am responsible for all other chapters presented in this thesis.

Summary

The functional morphology and locomotion of marine polychaetes from the family Nereididae were investigated. A novel way of generating propulsion was discovered in the juvenile ragworm *Nereis diversicolor*. Thrust is generated by a continuous jet-like propulsion mechanism where the oscillating parapodia give rise to two distinct jets in the wake of the swimming worm. The main focus of the thesis, however, is on the functional role of the parapodial setae during locomotion. A seta consists of a blade and a shaft jointed together to allow passive movement of the blade relative to the shaft. A comparative study of five nereidid species on the morphology of parapodia and setae found no correlations between habitat and setal parameters thus suggesting that the setae are not adapted to a specific substrate. There was, furthermore, no difference in any of the parapodial or setal parameters measured between species that swim as juveniles and species that do not. This indicates that setae are not as important for swimming in juvenile ragworms as previously thought. Further support of that come from a seta-ablation study on *N. diversicolor* which found no difference in swimming performance between ablated and control worms. The study, however, found a difference in crawling performance with seta-ablated worms crawling slower and with faster body waves than controls. But no differences in the response to seta-ablation were found between worms crawling in mud and sand, thus, like the comparative morphology study, indicating that setae are not adapted to any specific substrate. It is also shown that attaching artificial setae in the form of stiff wires to a robot test bed can enhance the friction on slippery substrates and generate more thrust than a plate configuration above a certain particle size, thus proving the biomimetic potential of artificial seta-like structures.

Chapter 1

Introduction and background

1 Introduction and background

1.1 Objectives and outline of the thesis

This PhD thesis focuses on the study of morphology and locomotion in errant polychaetes. These marine worms are adapted to an active life-style with well-developed sense organs and laterally extending appendages (parapodia). The parapodia act as legs during crawling and as paddles during swimming and are, in cooperation with anterior propagating body waves, responsible for locomotion of the worm. This mechanism of locomotion allows the worms to move upon and through a wide range of marine environments, ranging from sand via mud to clay. It, furthermore, allows the worm to employ a range of different locomotion modes such as crawling, swimming and burrowing using essentially the same mechanism. It was, therefore, thought likely that this type of locomotion would be well suited for use in biomimetic autonomous robots required to move in complex and tortuous environments. This study is part of the European project BIOLOCH (BIOmimetic structures for LOComotion in the Human body) funded by the European Commission under the 5th Frame-work Programme (IST FET programme, IST-2001-34181), which aims to identify biologically inspired locomotion suitable for robots moving in the human gut. However, in order fully to utilise the biomimetic potential of a biological mechanism a thorough understanding of the biology behind it is crucial, so although time was devoted to explore technical applications of the findings presented in this thesis then the major focus has been on increasing our understanding of the locomotion of these worms.

The overall objective of my PhD project is:

• *To analyse different aspects of the morphology and locomotion of errant polychaetes, primarily using the common ragworm Nereis diversicolor as a model organism, and to identify mechanisms suitable for application in the design of biomimetic robots required to move in slippery and tortuous environments.*

This can be broken down into more specific objectives:

• To investigate the kinematic variables and gait types employed by the ragworm *Nereis diversicolor* as it moves on and through different substrates. To relay this information to the BIOLOCH consortium and subsequently derive an optimal design for a robotic worm required to move inside the slippery human gut.

• To analyse the flow around both the entire ragworm and around the individual parapodium in order to verify and update the current theories of swimming in these worms.

• To conduct a comparative study of the morphology and function of the parapodial setae in various species of errant polychaetes adapted to different habitats. Furthermore, to assess the relevance of seta-like structures on a robotic worm required to move inside the human gut.

In order to reach these objectives various experiments were conducted. These experiments are described in individual chapters in this thesis. However, before the results of the experiments are discussed, a general introduction is given to the worms and to the context in which this study is conducted. Below follows an outline of the thesis with a brief description of each chapter. Regarding the overall structure of the thesis I have decided to make each chapter a self contained entity with the references placed at the end of each chapter. This is mainly done because the experimental chapters are structured as scientific publications (two of them have already been published and two further ones are in review) and because I find that it eases the reader's ability to check up on references.

Chapter 1 starts by giving an outline of the thesis and the objectives of the study before it gives a brief introduction to the theory of aquatic locomotion, with focus on areas relevant to swimming and crawling in errant polychaetes. It then gives a short review of the history of biomimetics with some examples of past and current research topics. The main focus here is on the contribution of classical macro-organismal biology to biomimetics in general and robotics in particular and less on the contributions of

molecular and biochemical biology. Lastly I give a brief introduction to the BIOLOCH project and the ideas behind it.

A comprehensive review of the biology and locomotion of the ragworm is given in chapter 2. This includes all major biological fields from systematics via morphology and ecology to neurobiology and behaviour. However, despite the wide occurrence and high density of nereidid populations along the coast of most parts of the world relatively little is known about their neurobiology and what is known comes primarily from studies that are 50 or more years old. Other areas such as ecotoxicology and development are well researched but have barely been mentioned in this chapter as it focused on areas with relevance for the study of locomotion and morphology.

The first proper original research is described in chapter 3 and is a comparative study of the morphology of parapodia and setae in five species of errant polychaetes. Except for minor format differences this chapter is published in its entirety as a paper in the journal Animal Biology.

Chapter 4 describes the only practical biomimetic aspects of my work where a robotic test bed was designed to experimentally investigate the thrust produced by artificial seta-like hairs attached to a parapodium-shaped appendage in comparison with that produced by a plain appendage and by an appendage with plates attached. Except for minor format differences this chapter is published in its entirety as a paper in the Journal of Bionics Engineering.

In chapter 5 the first kinematic data is presented in a study that looks at worms moving on sand and mud with or without their setae removed. Crawling parameters were compared across the two substrates for both ablated and non-ablated worms. A comparison was, furthermore, made of the swimming parameters between non-ablated and ablated worms. Except for some minor format changes this chapter has been accepted for publication by the Journal of Experimental Marine Biology and Ecology.

The last experimental data is presented in chapter 6 and consists of a digital particle image velocimetry study of the flow around a swimming ragworm. The flow characteristics of the wake were compared with the kinematics of the whole worm and the kinematics of the oscillating parapodium. A shortened version of this chapter (with the lateral view experiments excluded and a more focused introduction and discussion) has been submitted to the Journal of Experimental Biology.

Chapter 7 draws the various experiments together and summarises the results reached. First the outcome of the BIOLOCH project is presented along with the specific

contributions of this PhD project. Then the outcome of the whole project is discussed and compared with the objectives stated in chapter 1.

In appendix A a theoretical discussion of various calibration methods is given before their reconstruction accuracy of set markers is compared under a realistic experimental set-up for a range of angles. This study is included to ensure that the most precise calibration method is used to convert image coordinates from recordings of worm locomotion into real world coordinates.

Appendix B gives a short description of the software programmes that I have written specifically for this PhD project. Its main purpose is to give the reader an idea of how the programmes are structured and to remind myself and other people well versed with LABVIEW and MATLAB how they are made. It is not meant to be a manual on how to use the programmes or a blueprint on how exactly they are written.

1.2 An Introduction to the hydrodynamics of aquatic locomotion

Swimming and flying are two types of locomotion that occur immersed in a fluid and they are thus subject to the same physical laws. However, the medium in which these activities takes place, differs. Water has (at 20 °C) a 55 times higher viscosity and a 850 times higher density than air resulting in much greater forces at equivalent speeds in the former (Vogel 2003). Thus, while lift is more easily achieved in water, the higher drag results in much higher resistance to locomotion in water explaining the generally higher speeds obtained by flying. Two kinds of viscosity exist. The first one is dynamic viscosity and it is usually referred to simply as viscosity. It is a measure of the internal stickiness or friction in the fluid and is represented by the symbol μ. The second one is kinematic viscosity. It is the ratio of dynamic viscosity to density and is represented by the symbol ν. Using this ratio instead of dynamic viscosity then air is 15 times more viscous than water at 20° C. The Reynolds number (or Re) gives a good indication of the conditions experienced by objects and animals immersed in fluids. This dimensionless number illustrates the relative importance of inertial forces and viscous forces operating on the object or animal. As the Reynolds number increases the relative magnitude of the viscous force decreases. The Reynolds number is defined as

$$\mathrm{Re} = \frac{\rho l U}{\mu} = \frac{l U}{\nu}.$$

Where ρ is density, l is the characteristic length (either a diameter or an actual length), U is relative speed of the fluid compared to the object, μ and ν are the dynamic and kinematic viscosity, respectively. The usefulness of the Reynolds number stems from the fact that at equal Reynolds numbers the patterns of flow are similar (Vogel 2003). For instance a ball with a diameter of 15 cm exposed to a wind moving at 10 m/s (ν (air at 20° C) = 15.0 x 10^{-6} m^2/s → Re = 100.000) has the same Reynolds number as a ball with a diameter of 1 m in a river flowing at 0.1 m/s (ν (water at 20° C) = 1.0 x 10^{-6} m^2/s → Re = 100.000). The variation of biologically relevant Reynolds numbers is considerable ranging from 10^{-6} for spermatozoa to 10^8 in large fast swimming whales (Wu 1977). For macroscopic animals, however, most locomotion occurs at intermediate and higher Reynolds numbers. Errant polychaete worms, for example, swim in a range of 1.000 < Re < 15.000 (based on kinematic data from chapter 6; Merz and Edwards 1998; Clark and Tritton 1970).

With the fundamental physical parameters introduced, it is time to turn the attention to swimming and the forces involved in that. Swimming results from a transfer of momentum from the animal to the water (Webb 1988). The main resistive force experienced by an animal swimming with constant speed is drag (Fig. 1.1). Drag is defined as the removal of momentum from a moving fluid by an immersed body and can be written as

$$D = \frac{1}{2}\rho U^2 C_D S.$$

Where S is a shape characteristic (like surface area/wetted area or frontal area/projecting area) and C_D is the drag coefficient, which is a function of the Reynolds number. All other parameters are defined above. Drag consists of two major components (Vogel 2003). The first one is the viscous drag or skin friction which is due to the stickiness of the fluid in the boundary layer around the body. The importance of this force is highest at low Reynolds numbers where the boundary layer is largest. The other type of drag is the pressure drag, which is caused by dynamic pressure being higher at the front, where the laminar streamlines are abruptly separated, than at the rear, where the streamlines take longer to return to their earlier state (Fig. 1.2a). The effect of pressure drag can be ameliorated by making the immersed body more streamlined.

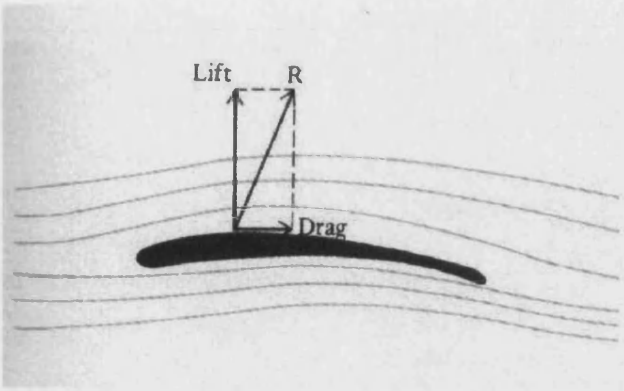

Fig. 1.1. A plate immersed in a laminar fluid flow with the resultant lift and drag force shown. R is the combined force of lift and drag. After Dorit *et al.* 1991.

Another significant fluid mechanical force is lift. This force is working perpendicularly to the direction of flow and in asymmetrical aerofoils it is generated when the fluid flows faster on one side than on the other side (Fig. 1.1). From Bernoulli's equation this results in a lower pressure on the side of the faster flow and there is therefore a force acting in that direction (Vogel 2003). Lift can also be generated with a symmetrical body if it is inclined at an angle, called the angle of attack, to the incoming flow. This causes the flow to be deflected downwards which creates a force and according to Newton's third law of motion a force is therefore generated in the opposite upward direction. Lift is described by the following equation

$$L = \frac{1}{2}\rho C_L U^2 S .$$

Where S is the body surface either taken as plane or top view area and C_L is the lift coefficient.

For an animal to swim it needs to generate a force, the thrust, to propel itself against the resistive forces. During steady swimming, i.e. when no maneuvering or accelerations are performed, this thrust must be equal and opposite the drag (Daniel and Webb 1987). So where does this thrust come from? It can be produced by undulation of the whole or part of the body, by flapping of appendages, by producing a jet stream or lastly in very small animals by beating of ciliary hairs or flagella (Vogel 2003). Propulsion by some kind of undulatory mechanism is by far the most widespread and is employed by fish, sea mammals and many soft-bodied invertebrates. Without going into details with any of the many existing theories of aquatic locomotion (see Wu 2001 and

Lighthill 1983 for a review), I will briefly mention the most general one; the resistive theory of aquatic locomotion. This theory was developed for elongated animals moving at intermediate to high Reynolds numbers by Taylor (1952) and refined and extended to low Reynolds numbers by Gray and Hancock (1955). The general idea is that the tangential and normal force components involved depends on the tangential and normal components of relative velocity. For movements at intermediate and high Reynolds number this force-velocity dependence is quadratic whereas it is linear at low Reynolds numbers (Wu 2001).

The fluid flow behind a stationary or moving object is either steady or unsteady. Steady flow occurs when the velocity of the fluid at a point remains constant with respect to time and when the streamlines do not cross (Fig. 1.2a,b). When these conditions are not met fluid is said to be unsteady (Fig. 1.2c,d). Most examples of fluid flow in biology are unsteady (Daniel 1984). The overall flow pattern is also described according to the presence and nature of streamlines. Streamlines describe the trajectory of individual particles throughout the flow field. When the particles follow clearly defined time independent streamlines from one end of the flow field to the other the flow is described as laminar (Fig. 1.2a). However, in many biologically relevant situations the flow is not laminar. If a cylinder is inserted into a flow then an increase in flow velocity produces small stationary vortices. A further increase results in numerous vortices being shed, before finally a sudden transition to turbulent flow occurs (Fig. 1.2). Turbulence is characterised by the individual water particles following irregular and chaotic paths (Vogel 2003).

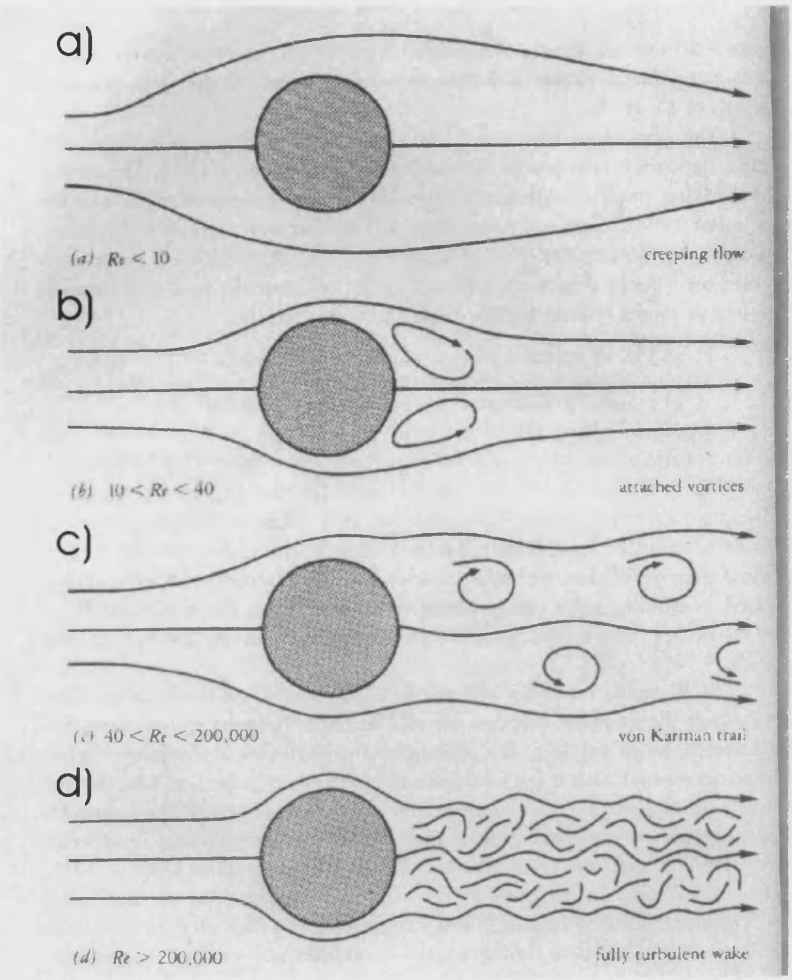

Fig. 1.2. Flow around a circular cylinder at various Reynolds numbers. a) Purely laminar flow at Re < 10. b) Laminar flow with attached vortices at 10 < Re < 40. c) Vortex shedding (a von Karman trail) at 40 < Re < 200.000. d) Turbulent flow at Re > 200.000. After Vogel 2003.

A dominant feature in the wake of almost all swimming animals, except for those swimming at very low Reynolds numbers, is the shedding of vortex rings, either as single rings or multiple rings chained to a latter like structure (Stamhuis *In press*; Videler *et al.* 1999). The reason for this stems from the periodic propulsion forces generated by almost all swimming animals, such as body or appendage oscillations and the periodic jet propulsion found in jelly fish and squids. This type of force generation results in separate parcels of water being accelerated away from the animal in the direction opposite of that in which the animal is moving (Stamhuis *In press*). Recent studies, with ejecting fluid from a pipe, show that shedding of vortex rings results in an optimal momentum transfer when the ratio of the length of the resultant jet ejected to the diameter of the pipe is around 3.5 to 4 (Linden and Turner 2004; 2001). This ratio

was also found to be inverse proportional to the Strouhal number (Linden and Turner 2004). The Strouhal number is a dimensionless number with the following definition

$$St = \frac{fl}{U}.$$

Where f is the flapping frequency of an appendage or the frequency of vortex shedding, l is a characteristic length and U is the forward speed of the animal. The relationship between the optimal vortices and Strouhal number probably explains recent studies showing that all flying or swimming animals cruise at Strouhal numbers in the range $0.2 < St < 0.4$ (Hedenström 2004; Taylor *et al.* 2003).

A further important contribution of unsteady flow is the emergence of another type of force called the acceleration reaction. It depends on the acceleration of an object relative to its fluid environment and can be viewed as a resistance to change in the velocity of that object (Daniel 1984). During acceleration not only the body itself, but also fluid around the body must be accelerated. In other words kinetic energy needs to be transferred to the surrounding fluid. The amount of surrounding fluid that needs to be accelerated is called the added-mass and the acceleration reaction is the force needed to accelerate both the body itself and the added mass (Daniel 1984). The acceleration reaction depends on the size, shape and acceleration of the body. As Daniel (1984) demonstrated, the acceleration reaction could theoretically be used to generate propulsion. Consider an animal with a symmetrical beating tail (Fig. 1.3). In steady state only drag forces are acting. When the tail is moving from the upper extreme position towards the midline, drag produces a tangential and normal force in the +x and +y direction, respectively. As the tail passes the midline and continues towards the lower extreme drag produces forces in the –x and +y direction. So after the first half beat of the tail only a resultant force in the +y direction is generated. This is, however, cancelled out with the other half of the tail beat, so no net locomotion of the body takes place. If we look at the unsteady state and ignore the drag forces then, as the tail accelerates towards the midline, the resistive acceleration reaction produces a force similar to the drag force from before in the +x and +y direction. However, as the tail passes the midline and moves towards the lower extreme it decelerates (or accelerate in the direction of the midline), so the acceleration reaction generates a force in the +x and –y direction. After the first half of the tail beat the forces in the y direction cancels out, but a net force is generated in the +x direction. The second half of the tail beat generates

more force in that direction, so the total net result is that the body moves in the +x direction.

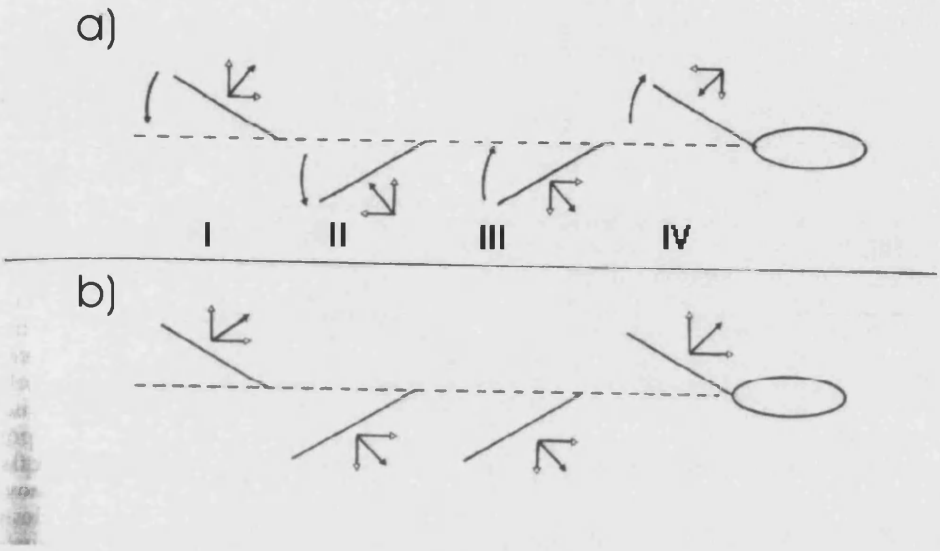

Fig. 1.3. A diagrammatic representation of the force vectors acting on a flapping tail. a) A steady analysis of the forces. b) An unsteady analysis of the force of acceleration reaction with the steady forces neglected. In both cases the tail moves from a lateral extreme position towards the midline (I), and from the midline to the opposite extreme lateral position (II). In (III) and (IV) the movement is reversed. After Daniel (1984).

The above description is a hypothetical example and in the real world many other factors are involved, but it shows that the acceleration reaction probably is important in many situations. Especially, when continuously accelerating and decelerating flapping appendages, such as found in errant polychaetes, are important for locomotion (Daniel 1995). Another example, where the acceleration reaction has proved to be important, is the swimming by periodic jet propulsion in jellyfish (McHenry and Jed 2003). In a similar study of swimming by periodic jet propulsion in the squid the acceleration reaction was found to be an important instantaneous force, but its relative contribution averaged over an entire jet cycle was found to be much smaller (Bartol *et al.* 2001). Although, it is difficult to make generalisations regarding the magnitude and total contribution of the acceleration reaction, the relative importance of it compared to drag and lift is indicated by the reduced frequency (Daniel and Webb 1987). It can be seen as a measure of the flow in the direction of body movement relative to the flow normal to body motion and is defined as

$$\sigma = \omega L / U .$$

Where ω is radian velocity (ω = 2πf, where f is the frequency of appendage oscillation) and L is a characteristic length (usually the length of the appendage). If $\sigma < 0.1$ then acceleration reaction can usually be ignored. If $0.1 < \sigma < 0.4$ then drag, lift and acceleration reaction all contribute to the force balance. At larger values acceleration reaction becomes the dominant force (Webb 1988).

For a swimming animal both resistive forces and thrust are present and they can be written in text as follows (Daniel and Webb 1987).

Resistance = Drag + Acceleration Reaction

Thrust = Drag + Lift + Acceleration Reaction

The relative importance of these forces is dependent on the Reynolds number (Fig. 1.4). At very low Reynolds numbers only the viscous drag is important, but as the Reynolds number increases, first pressure drag and then acceleration reaction becomes important. At even higher Reynolds numbers lift becomes significant and at extremely high Reynolds numbers it is the dominant force.

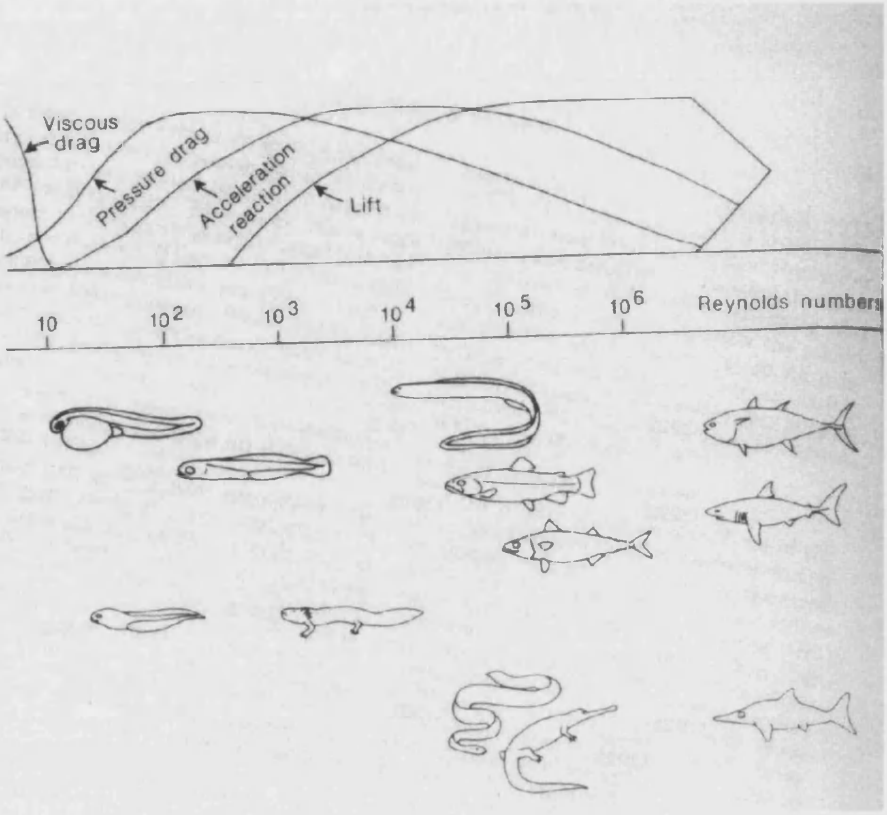

Fig. 1.4. The relative importance of force components as a function of Reynolds number. Below some representative vertebrates swimming at the particular Reynolds number. After Webb 1988.

Above we have focused on swimming, which is the most common type of locomotion by macro-organisms found in aquatic habitats. However, many benthic animals move by crawling over the substrate in a similar manner to their terrestrial counterparts. According to Newton's third law of motion the force exerted by the body as it touches the ground results in an opposite force, which is called the ground reaction force. During terrestrial walking and running the ground reaction force is the only force responsible for generating thrust and the friction between the ground and the body is the main resistive force, although aerodynamic drag can be of significance for small rapidly running animals (Full and Koehl 1993). However, in water the hydrodynamic forces are significant during walking (Martinez 1996). The ground reaction force is also much smaller, since its magnitude depends on the weight of the moving animals, which in water, due to the buoyancy, is much less than in air. Animals living in benthic coastal habitats are, furthermore, subjected to large destabilising forces arising from wave actions, tides and currents (Ayers 2004). Underwater walking animals have developed two strategies for increasing the ground reaction force. The first is to increase their

weight by carrying bulky and thick exoskeletons (which are also very useful for protection), such as found in crabs and lobsters (Ayers 2004; Martinez 1996). The second is to increase the friction with the substrate by morphological adaptations such as suckers on the feet of sea stars and setae on the body or parapodia of polychaete worms (Wootton 1999; Schroeder 1984; Sleigh and Barlow 1980). Despite the complex morphological adaptations and the interesting way in which underwater walkers or crawlers have overcome the problem of large hydrodynamic forces and a small ground reaction force, very few studies have focused on this issue and then mainly in crustaceans (Ayers 2004; Martinez 1996).

1.3 Biomimetics – From biology to engineering

1.3.1 Introduction

Since the earliest days of tool-making, man has tried to imitate the skills of nature. In pre-historic times this included using sticks for probes and wood for clubs, wearing fur to keep warm and the actual development of bone and stone tools to emulate the teeth and claws of animals (Vincent 2005). However, the ingenuity of man was not limited to blindly copying nature and soon human technology started to diverge from it. The most conspicuous example of this is, of course, the invention of the wheel, which has no counterparts in nature. However, contrary to popular belief a few animals actually use wheel-like locomotion in the form of rolling. The most common form is to roll down a slope to escape from predators. This can be seen in the desert spider *Carparachne aureoflava* which positions its legs around its body to make it round and thus roll down sand dunes to escape predatory wasps (Henschel 1990) and in the salamander *Hydromantes platycephalus*, which curls up into a ball and rolls down the volcanic slopes, on which it lives, when disturbed (Garcia-Paris and Deban 1995). Another example comes from the plant world. The Russian thistle (*Solsala tragus*) or tumble weed is an annual flowering plant inhabiting dry environments. It starts out as a normal bush but as it matures it grows more spherical and when it dies it breaks free of its root. The bush can then spread its seed over a large area thanks to wind powered rolling (Carnes *et al.* 2003). Active rolling is rare in nature, but the stomatopod *Nannosquilla decemspinosa* uses backward summersaults, where they roll as a true wheel for 40% of the time, to return to the water if they are cast ashore on sandy

beaches (Full *et al.* 1993). However, despite the above mentioned examples, except for the bacterial flagellar motor, no true axles and wheels are found in nature. Nature has, though, continued to inspire either by supplying concepts or in some cases even providing a full design. A case of the latter is the early unsuccessful attempts at building flying machines. In as early as 1488 Leonardo da Vinci designed a flying machine based on bats and 400 years later Otto Lilienthal built gliders based on an avian design. Although the first successful aeroplane, built by the Wright brothers in 1903, involved a radical new design, it was based on the pioneering work done by Lilienthal. It is, furthermore, likely as Vogel (1992) points out that humans would never have had the determination and conviction of eventual success, had insects, bats and birds not been around to show that flying is possible.

In the first half of the 20th century the idea that biological studies could provide inspiration for developing new technology was slowly spreading in the scientific community. In the late 50s the word bionics was used for technological designs and ideas learned from nature, but this word is now more associated with the replacement of body parts with artificial electronic devices, although it retains its original meaning in German speaking countries (Nachtigall 2001). The word 'biomimetic' made its first appearance in the title of a paper in 1969 and was included in Webster's dictionary in 1974. Biomimetics (or biomimicry as it is also sometimes called) can be used in many contexts that involve the transfer of skills or information from biology to applied science. A more strict definition of the biomimetic approach is given by Frans and Mallot (2000), and although their paper deals with biomimetics in robot navigation, I find it applicable also in a broader context. Their definition of a biomimetic approach is "..if the authors try to implement a mechanism described in the biological literature, and explicitly refer to the biological inspiration of their approach".

Since the early 90s biomimetics has turned into a discipline of its own, with numerous groups and centres spread around the world dedicated to look at natural processes for invention and innovation in a wide range of applied fields. The multidisciplinary aspect of biomimetics is pronounced, with many active groups comprising of computer scientists, physicists, chemists and philosophers working alongside biologists and engineers. The field of biomimetics, though, is still in its infancy and is continuously growing as can be seen from the increasing number of articles having a word with the root biomimetic in its title, abstract or keywords (Fig. 1.5).

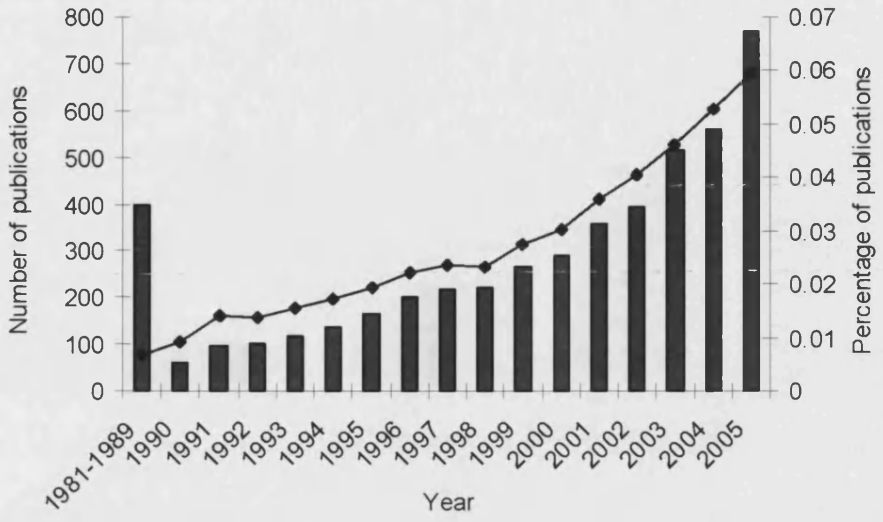

Fig. 1.5. Publications containing words with the root biomimetic in the title, abstract or keywords. The data is obtained from searching the ISI Web of Science database (SCI-EXPANDED, The Thompson Corporation, 2006) using the term biomimetic* in the topic field. The bars show the number of publications found in the database for each year and the line represents the percentage of publications out of the total number of publications in the database for each year.

The most famous example of the biomimetic approach is the invention of Velcro. In the late 1940s a Swiss engineer, George de Mestral, was taking his dog for a walk, when he noticed cockleburs sticking to both his clothes and the dog's fur. Upon returning home he examined the burs under a microscope and discovered that the surface of the burs consists of hundreds of small hooks. These hooks allow the cockleburs to attach to the tangle of hairs in animal fur and thus they facilitate the spreading of the seeds. By trial and error experiments George de Mestral could, in 1955, patent Velcro, based on the cockleburs. Velcro is a unique two-side fastener; one side with stiff hooks like the burs and the other side with soft loops like the fabric of clothes or animal furs.

A recent and promising example showing the potential of the biomimetic approach is the Lotus-Effect. This effect was discovered by the botanist Wilhelm Barthlott during a systematic scanning electron microscopy study of the leaf surface of some 10.000 plant species (Barthlott and Neinhuis 1997). Barthlott and one of his students observed that species with smooth leaf surfaces always had to be cleaned before examination, while those with a rougher and more irregular surface were almost

completely free of contamination (Barthlott and Neinhuis 1997). From further studies and experiments they discovered that epicuticular wax crystals cover the surface of rough leaves. Water droplets balance on the top of these crystals maintaining only limited surface contact to the leaf and can therefore roll off easily. The adhesion between dirt particles and crystals is similarly minimised, so the particle is attracted to the larger surface of the passing water droplet and with that removed from the leaf surface (Barthlott and Neinhuis 1997). They called this the Lotus-Effect, after the leaves of the sacred lotus or sacred water lily (*Nelumbo nucifera*), which give a particular impressive demonstration of this effect. The Lotus-Effect has significant potential for commercialisation and currently a house-paint is distributed under the name Lotusan. Further potentially lucrative applications include self-cleaning paint for cars, facades and roofs (Barthlott and Neinhuis 1998).

Most of the research conducted in biomimetics needs yet to prove that it can be commercially exploited. However, as is evident from figure 1.5, the field of biomimetics is very productive and comprises research in all scientific fields. It is beyond the scope of this chapter to mention all these investigations. Instead some of the most promising candidates in the field of composite materials will briefly be described before the benefits of applying biomimetics to the design of robots is described in some detail.

1.3.2 Composite materials

Composite materials consist of two or more constituent materials that remain separate and distinct on a macroscopic level while forming a single component. Two types of constituent materials exist: matrix and reinforcement. At least one portion of each type is required. The matrix material surrounds and supports the reinforcement materials by maintaining their relative positions. The reinforcements impart their special mechanical, electrical and physical properties to enhance the matrix properties. Most of the structural materials found in nature, such as bones, cuticle, shells and wood are composites (Vincent 2005; Thompson 1996). These structures have attracted considerable attention from material scientists as they are stronger and less brittle than man-made composites and they have the further advantage of being produced cheaply from an energy perspective without the need for high temperatures or pressures (Vincent 2002; 2000; Wang *et al.* 2000).

The most commonly used natural composite is unquestionably wood. Wood consists of microfibrils of cellulose embedded in a matrix of amorphous lignin, hemicelloluse, proteins and other components (Vincent 2005). The holes in the wood, caused by phloem and xylem used for transport of nutrients and water in the living tree, furthermore, increases its resistance to fracture (Vincent 2003). Wood has been intimately linked with human construction and tools since the earliest times due to its availability, low price, lightness, toughness and the ease with which it can be shaped and prepared (Ball 2001). Even today when steel and concrete have mostly replaced wood's structural role in building and construction, wood remains important in certain areas, such as material for musical instruments and for ornamental purposes (Vincent 2005). There are some negative aspects of wood as well, the main one being its limited durability in damp conditions and its susceptibility to pests. These problems can to some degree be solved by using hard wood such as mahogany and teak However, the increasing price and declining numbers of hardwood, due to tropical deforestation, provide a stronger and stronger incentive for developing artificial wood. Early attempts have given mixed results due to our limited understanding of the complex structure of the wood at a molecular level, but recent years have seen some promising progress (Vincent 2005; Ball 2001).

Another very interesting natural composite is nacre or mother-of-pearl found in the shells of abalones and other molluscs. The shell incorporates both organic compounds, in the form of a proteinaceous matrix secreted by the animal, and inorganic compounds, calcium carbonates predominantly in the form of aragonite concentrated from sea water (Jackson *et al.* 1988). The reinforcement material, aragonite, constitutes 95% of nacre by volume and the matrix only 5%. Such a high proportion of ceramic should make the material very brittle and yet the composite has a much higher work of fracture than aragonite alone (Jackson *et al.* 1988). The explanation for the high work of fracture is probably found in its unique structure. In contrast to wood and most other natural and man-made composites nacre is reinforced with platelets rather than fibres (Jackson *et al.* 1988). The aragonite platelets are stacked on top of each other in a brick wall structure (Fig. 1.6). First attempts of using the nacre design to change the brittleness of artificial composites such as talc tablets and silicon nitride ceramic powder in organic binding material have given promising results (Wang *et al.* 2000; Almqvist *et al.* 1999).

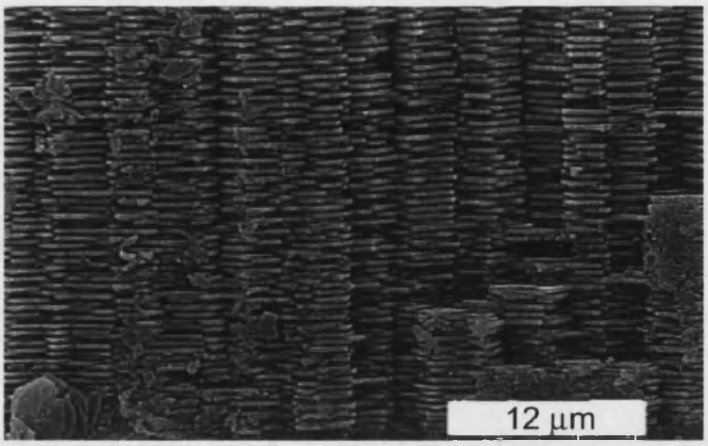

Fig. 1.6. SEM image of the microstructure of a gastropod shell of *Turbo undulates*. From Chaeteigner *et al.* 2000.

One of the most fascinating materials in nature is spider silk. Spider silk is a biopolymer and belongs to the fibroins. Each thread is a natural composite with protein crystals, consisting of β-pleated sheets, embedded into a matrix of loosely arranged α-chains (Vollrath 2000). It is this composite structure that gives spider silks its remarkable material properties including its high tensile strength and its strong viscoelastic effects (Elices *et al.* 2005; Köhler and Vollrath 1995). These properties compare favourably with man-made materials and spider silk outcompetes artificial materials especially for breaking strain and energy absorption (Table 1.1). For this reason spider silk has generated a lot of commercial interest in the past decades. However, despite huge research efforts, large problems still exist before any products are ready for the market. The main problem is that not only is the exact structure of the silk important for its physical properties, but these in turn also depend on the complex weaving pathway through the ducts and spinnerets of the spider, where the silk is changed from a liquid soup of proteins to solid threads (Vollrath 2000). The most promising artificial silk developed yet is BioSteel from the Canadian based Nexia Biotechnologies, Inc (Gould 2002). Their idea is to use transgenic goats to produce water soluble silk proteins. Although they have had some problems with identifying the right gene the technique looks promising. However, this method only deals with the material side of silk. Dr. David Knight and Prof. Fritz Vollrath have in their company Oxford Biomaterials Ltd concentrated on the spinning side and developed a fibre extrusion device mimicking the spinning system found inside the spider spinnerets. Major obstacles still lie ahead, not least the question of durability. In nature the spider

continuously produces new silk, because the silk's mechanical properties are affected by changes in temperature and moisture (Vollrath *et al.* 2001; Work 1981).

Table 1.1. The mechanical properties of spider silk from *Argiope trisfasciata*

Fiber type	*Density (g/cm^3)*	*Young's modulus (GPa)*	*Tensile Strength (GPa)*	*Breaking Strain (%)*	*Energy Absorption (MJ/m^3)*
Spider silk	1.3	1-10	1.2	30	100
Nylon	1.1	5	0.9	18	80
Kevlar	1.4	130	3.6	3	50
PBO	1.6	270	5.8	3	70
Steel	7.8	200	3.0	2	6

From Elices *et al.* 2005.

1.3.3 Biologically inspired robots

The first robots designed, using inspiration from animals, were also some of the first electromechanical robots developed. In 1949 the neurophysiologist Grey Walter built two small robots, which he called electromechanical tortoises. The robots did not resemble any biological organism as they were basically cans with wheels and a photoelectric cell that allowed the robots to detect and navigate toward a light source (Holland 2003). However, the control system of the robots was built to mimic a simple two-cell nervous system. By letting the robots interact with light, mirrors and each other Grey Walter was able to show that even such a simple control system could result in several distinct and complex behaviours (Holland 2003). The design of biologically inspired robots or biorobots is pursued by two groups of researchers. The first group, to which Grey Walter belonged, primarily build robots as a biological model to increase understanding of the underlying biological phenomena, whereas the second group uses inspiration from biology to build better and more useful robots (Alexander 2003; Koehl 2003; Webb 2001). However, the construction of biorobots, whatever the original aim, often both increases our knowledge of the underlying biology and leads to innovative ideas concerning robot design. In the following, though, focus will be on the second group where biologically inspired robots are designed in an effort to build more advanced robots.

An imitation of the various forms of animal locomotion is especially useful for robots required to move in more structural complex and tortuous environments, where the standard engineering solution of wheeled locomotion may not be applicable. Delcomyn and Nelson (2000) used the cockroach as a model organism for designing a hexapod robot with physical dimensions 12-17 times the size of the comparable

structures in the animal. To mimic the characteristics of the leg muscles in the cockroach, they used a pulsed pneumatic system for the robot's actuators. The hexapod blue print has been very popular with biorobotic engineers in recent years. The most agile and autonomous hexapod robot built to date is RHex. Although its legs rotate a full 360° during locomotion and thus do not resemble the motion found in insects its resultant locomotory patterns and ability to move in complex terrain are nevertheless very insect-like (Koditschek *et al.* 2004). The control of the robot is, furthermore, inspired from insects where coupled oscillators in the form of central pattern generators (CPGs) control the leg rhythm (Koditschek *et al.* 2004). These and other similar studies, although still simple in their robotic design, successfully show the potential of the biomimetic approach. One of the major constraints in the design of autonomous robots is keeping the power consumption down, but also here can solutions be found in nature. When a leg strikes the ground during running many animals temporarily store elastic strain energy, which is nearly all recovered during the propulsive second half of the stance phase (Dickinson *et al.* 2000). Attempts have been made to incorporate this into walking robots by developing a system of series elastic actuators (Robinson *et al.* 1999).

Another area that has received considerable attention, especially from the military, is the development of micro air vehicles (MAVs). The aim is to create small reconnaissance drones based on the principles of flight in insects. However, the technical difficulties to overcome in order to recreate these complex and not yet fully understood flight mechanisms are substantial and significant progress remains to be seen, despite the considerable funding that is available for this line of research (Ellington 1999). Mechanical models of insect flight, such as the flapper and the robofly, have, though, increased our understanding of the mechanisms involved as well as shed light on the technical obstacles remaining (Birch and Dickinson 2001; Lauder 2001; Ellington *et al.* 1996). The robofly project at the California Institute of Technology is an ongoing study modelling all aspects of insect flight, such as control, sensory input and integrations and muscular function as well as the aerodynamics, with the ultimate aim to develop a fully functional autonomous MAV (Lauder 2001).

Recently considerable research effort has been put into another class of robots, the segmented snake or worm robots which move by undulatory locomotion (Tsakiris *et al.* 2005; Ostrowski and Burdick 1998). Envisaged applications for this type of robots include inspection (Tsakiris *et al.* 2005), endoscopy (Menciassi and Dario 2003) and space exploration (Yim *et al.* 2003). Most of these projects, though, are only biomimetic

in the overall sense of applying a similar kind of undulatory locomotion to what is found in nature. However, one of the promising projects with slightly more biomimetic content is the AmphiBot project. AmphiBot I is an amphibious robot mimicking the S-shaped lateral undulatory locomotion found in most snakes (Crespi *et al.* 2005). It consists of 7 watertight segments enabling it to use the same CPG as a control mechanism both on land and in water. AmphiBot I uses passive wheels for providing directional friction and is not yet fully autonomous as it requires connection to a PC for the overall control (Crespi *et al.* 2005). Despite these shortcomings AmphiBot I is capable of generating some of the most life-like undulatory motion yet seen in robots.

So far the majority of biologically inspired robots built have been terrestrial robots. However, a few successful underwater biomimetic robots have been developed. The most famous is the RoboTuna, which is an eight linked pulley driven robot, inspired by the behaviour and morphology of the Bluefin Tuna (Triantafyllou and Triantafyllou 1995). Since then several other fish inspired robots have been developed, although problems remain especially with the behaviour and control part of these robots (Liu *et al.* 2004; Yu *et al.* 2004). In the Biomimetic Underwater Robot Program at Northeastern University – USA, a robot was developed by reverse engineering from the American lobster (Ayers 2004; Safak and Adams 2002). The autonomous robot uses shape memory alloys for emulating muscles, where electrical current generates the heat necessary for a phase transformation. The robot also mimics the sensory function of the lobster antennae by using artificial antennae with strain gauges added that bend or buckle when they make contact with obstacles (Ayers 2004). The robot is capable of moving in both unidirectional flow from tides and bidirectional flow from waves and can reach a maximum speed of 3 cm/s. Robotic engineers are not restricted to studying biomechanics when they want to be inspired by nature. The neurobiology of invertebrates is now so well understood that robot models can successfully replicate aspects of the behaviour of real animals (Webb 2002). Navigation strategies in insects have with some success been applied to robot navigation (see Franz and Mallot 2000 for a review). Lastly some of the more futuristic projects should be mentioned such as building artificial life forms capable of optimising their own design using evolutionary computation and reproducing by constructing new robots automatically using rapid prototyping technology (Lipson and Pollack 2000) or control and interaction of multiple-agent robots inspired by social insects (Bonabeau *et al.* 2000).

1.3.4 The biomimetic approach

Current research in biomimetics, as is hopefully clear from the above sections, covers a very wide range of topics and disciplines. Even more exotic examples of the biomimetic approach exist than described above. These include combining natural processes with creative thinking or the ambitious project of linking biology to TRIZ (the theory of inventive problem solving) with the aim of facilitating a systematic harvest of the knowledge of nature evolved through billions of years and incorporating this into our own technology (Vincent *et al.* 2005; Vincent and Mann 2002). Although, the biomimetic approach, with the exception of Velcro and possibly the Lotus-Effect, still lacks spectacular success stories then it is likely that it will play an increasing role in innovative technological developments in the coming decades. Biomimetics, furthermore, has the advantage, from a funding and awareness perspective, that it often sparks public and media interest. This is because the interesting and surprising stories from biology that leaves us with questions such as 'how in the world did it manage to do that?' are usually, for exactly the same reasons, interesting from a biomimetic perspective as well. One such example is the amazing ability of the gecko to climb on vertical glass walls. Biologists have shown that this ability comes from the thousands of microscopic keratinous hairs branching out to even finer structures which adhere to the substrate with the use of van der Waals forces (Autumn *et al.* 2000). Engineers have then attempted to mimic this ability with some success by making adhesive tape consisting of microfabricated polyimide hairs (Geim *et al.* 2003).

However, before we uncritically praise the biomimetic approach some caution is required. As the biologist Steven Vogel (1992) points outs, natural technology has evolved under several major constraints, which should not limit our technology. Nature, for instance, uses only a very limited number of materials, where our technology has a far greater variety available (Vincent 2000). Furthermore, designs in nature are usually not optimised for any single function, but instead have multiple functions. For example, the spider web's primary function is to detain prey long enough for the spider to catch it (Eberhard 1990). However, it also functions as a communication channel during courtship behaviour and in camouflage by blurring the outline of the spider. Therefore uncritical copying of biological structures will often not give useful results. Instead a careful analysis and assessment of the functions in nature is required before potential aspects can be identified and attempts made to imitate them. This will often be a

complex process and it is here that cooperation between biologists and engineers is of vital importance for a successful outcome.

1.4 The BIOLOCH project

The BIOLOCH (BIOmimetic structures for LOComotion in the Human body) project aims to understand motion and perception systems of lower animal forms and to design and fabricate bio-inspired mini- and micro-machines able to navigate in tortuous and difficult to access cavities in particular in the human body. The inspiration for the BIOLOCH project originates from the medical need to develop more powerful tools for micro-endoscopy and in particular for colonoscopy. Current colonoscopical practise is based on pushing a fairly stiff colonoscope up through the rectum of the patient. This is very difficult and requires highly skilled surgeons as well as resulting in considerable discomfort for the patient. It is estimated that application of a self-propelling colonoscope, using a biomimetic type of locomotion, would substantially reduce the pain level experienced by the patient, which could increase the patients' willingness to undergo the procedure. Ultimately this could save lives as diseases, such as cancer in the colon, would be discovered earlier and thereby increase the probability of a successful treatment.

The BIOLOCH project was funded by the IST (Information Society Technologies) – FET (Future and Emerging Technologies) programme under the Fifth Framework Programme (FP5) of the European Commission. BIOLOCH began in May 2002 and ran until October 2005. The project was carried out by a consortium of 6 European universities and institutions with the principal contractor being

- MiTech Lab, Scuola Superiore Sant'Anna (SSSA) in Italy.

Further participants were:

- Centre for Biomimetics and Natural Techonologies, Department of Mechanical Engineering, University of Bath (UoB) in the UK.
- Centro "E. Piaggio", Faculty of Engineering, University of Pisa (UoP) in Italy.
- FORTH – Foundation for Research and Technology Hellas (FORTH) in Greece
- Section for Minimally Invasive Surgery, University of Tübingen (UoT) in Germany.
- The Institute of Healthcare Industries, Steinbeis University Berlin (SUB) in Germany.

These different partners covered a broad range of expertise and the consortium was therefore well suited to the cross-disciplinary approach required in the BIOLOCH project. This approach included a review and analysis of biological locomotion systems in invertebrates, amphibians and reptiles with the aim of identifying a few potential systems suited for the design of a biomimetic locomotion unit. Computational and mathematical models were created in order to find optimal design parameters. Prototypes based on a few biological locomotion systems were then constructed and their performance tested in artificial structures that simulate the physical environment inside the human gut.

The project was divided into 9 work packages, where each partner was expected to contribute proportional to their expertise in the given field.

- WP0: Project Management. Overall supervision and coordination of the activities of the project. The main contributor was SSSA.
- WP1: Study of locomotion mechanisms of lower animal forms. Divided into three tasks, where the main one was a review of animals utilising a locomotion system with biomimetic potential, such as snakes, gut parasites and worms living in mud. The other tasks involved a study of adhesion mechanisms and research on objective biomechanical tissue parameters of the gastro-intestinal tissues. Main contributors were UoB, SSSA,SUB and UoT.
- WP2: Modelling and design of artificial structures that replicate biological mechanisms. Devoted to investigate the possibilities of actual implementation of the previously identified biological concepts of locomotion. Main contributors were SSSA, UoB and UoP.
- WP3: Enabling technologies and principles for fabricating biomimetic components. To review and experiment with biomimetic actuators and sensors based on smart materials. Main contributors were UoP and SSSA.
- WP4: Understanding and replicating biological perception of lower animal forms. To investigate the morphology and physiology of relevant sensory organs in animals and identify technologies that will allow a biomimetic implementation. Main contributors were UoB and UoP.

- WP5: Control strategy and control implementation. Design and implementation of motion control strategies for locomotion based on biological principles. Main contributors were FORTH and UoB.
- WP6: Fabrication of prototypes of biomimetic locomotion machines. Construction of prototypes based on the inchworm principle as well as on other biomimetic locomotive prototypes. Main contributors were SSSA, UoP and UoB.
- WP7: Experiments on biomimetic locomotion prototypes. To carry out experimental validation of the prototypes and to test their potential for medical exploitation. The main contributors were UoT and SUB.
- WP8: Dissemination and implementation. To identify the exploitable concepts and to establish contacts with companies. The main contributor was SSSA.

The success of the BIOLOCH project did not depend on the final prototype, indeed it was not expected that the project would result in a finished biomimetic colonoscope ready for the market. What, however, was expected was that the BIOLOCH project would generate new scientific knowledge in areas such as biomechanics of locomotion, control strategies, attachment mechanisms and the physical environment of the intestines. Furthermore, it was expected that the project would introduce new kinds of smart devices and actuators and finally that suitable designs for an autonomous biomimetic robot capable of moving in complex and slippery environments would be identified.

References

Alexander, R. M. 2003. Modelling approaches in biomechanics. *Philosophical transactions of the Royal Society of London. Series B.* **358**: 1429-1435.

Almqvist, N., Thomson, N. H., Smith, B. L., Stucky, G. D., Morse, D. E. and Hansma, P. K. 1999. Methods for fabricating and characterizing a new generation of biomimetic materials. *Materials Science and Engineering. C.* **7**: 37-43.

Autumn, K., Liang, Y. A., Hsieh, S. T., Zesch, W., Chan, W. P., Kenny, T. W., Fearing, R. and Full, R. J. 2000. Adhesive force of a single gecko foot-hair.

Nature **405**: 681-685.

Ayers, J. 2004. Underwater walking. *Arthropod Structure & Development* **33**: 347-360.

Ball, P. 2001. Life's lessons in design. *Nature* **409**: 413-416.

Barthlott, W. and Neinhuis, C. 1997. Purity of the sacred lotus, or escape from contamination in biological surfaces. *Planta* **202**: 1-8.

Barthlott, W. and Neinhuis, C. 1998. Lotusblumen und autolacke: Ultrastruktur pflanzlicher grenzflächen und biomimetische unverschmutzbare werkstoffe. In *Proceedings from the Bionik-Kongress, Munich* (Eds. Nachtigall, W. and Wisser, A.): 281-293.

Bartol, I. K., Patterson, M. R. and Mann, R. 2001. Swimming mechanics and behavior of the shallow-water brief squid *Lolliguncula brevis*. *Journal of Experimental Biology* **204**: 3655-3682.

Birch, J. M. and Dickinson, M. H. 2001. Spanwise of flow and the attachment of the leading-edge vortex on insect wings. *Nature* **412**: 729-733.

Bonabeau, E., Dorigo, M. and Theraulaz, G. 2000. Inspiration for optimization from social insect behaviour. *Nature* **406**: 39-42.

Carnes, J., Fernandez-Caldas, E., Marina, A., Alonso, C., Lahoz, C., Colas, C. and Lezaun, A. 2003. Immunochemical characterisation of Russian thistle (*Salsola kali*) pollen extracts. Purification of the allergen Sal k 1. *Allergy* **58**: 1152-1156.

Chateigner, D., Hedegaard, C. and Wenk, H. R. 2000. Mollusc shell microstructures and crystallographic textures. *Journal of Structural Geology* **22**: 1723-1735.

Clark, R. B. and Tritton, D. J. 1970. Swimming mechanisms in nereidiform polychaetes. *Journal of Zoology* **161**: 257-271.

Crespi, A., Badertscher, A., Guignard, A. and Ijspeert, A. J. 2005. *Amphibot I*: an amphibious snake-like robot. *Robotics and Autonomous Systems* **50**: 163-175.

Daniel, T. L. 1984. Unsteady aspects of aquatic locomotion. *American Zoologist* **24**: 121-134.

Daniel, T. L. 1995. Invertebrate swimming: integrating internal and external mechanics. *The Society for Experimental Biology*: 61-89.

Daniel, T. L. and Webb, P. W. 1987. Physical determinants of locomotion. In *Comparative Physiology: Life in Water and on Land* (Eds. P. Dejours, L. Bolis, C. R. Taylor and E. R. Weibel). Padovia, Liviana Press. **9:** 343-369.

Delcomyn, F. and Nelson, M. E. 2000. Architectures for a biomimetic hexapod robot. *Robotics and Autonomous Systems* **30**: 5-15.

Dickinson, M. H., Farley, C. T., Full, R. J., Koehl, M. A. R., Kram, R. and Lehman, S. 2000. How animals move: an integrative way. *Science* **288**.

Dorit, R. L., Walker, W. F. and Barnes, R. D. *Zoology*. Saunders College Publishing. Philadelphia 1991.

Eberhard, W. G. 1990. Function and phylogeny of spider webs. *Annual Review of Ecology and Systematics*. **21**: 341-372.

Elices, M., Perez-Rigueiro, J., Plaza, G. R. and Guinea, G. V. 2005. Finding inspiration in *Argiope trifasciata* spider silk fibers. *JOM* **57**: 60-66.

Ellington, C. P. 1999. The novel aerodynamics of insect flight: application to micro-air vehicles. *Journal of Experimental Biology* **202**: 3439-3448.

Ellington, C. P., Van den Berg, C., Willmott, A. P. and Thomas, A. L. R. 1996. Leading-edge vortices in insect flight. *Nature* **384**: 626-630.

Franz, M. O. and Mallot, H. A. 2000. Biomimetic robot navigation. *Robotics and Autonomous Systems* **30**: 133-153.

Full, R. J., Earls, K., Wong, M. and Caldwell, R. 1993. Locomotion like a wheel? *Nature* **365**: 495.

Full, R. J. and Koehl, M. A. R. 1993. Drag and lift on running insects. *Journal of Experimental Biology* **176**: 89-101.

Garcia-Paris, M. and Deban, S. M. 1995. A novel antipredator mechanism in salamanders: rolling escape in *Hydromantes platycephalus*. *Journal of Herpetology* **29**: 149-151.

Geim, A. K., Dubonos, S. V., Grigorieva, I. V., Novoselev, K. S., Zhukov, A. A. and Shapoval, S. Y. 2003. Microfabricated adhesive mimicking gecko foot-hair. *Nature materials* **2**: 461-463.

Gray, J. and Hancock, G. J. 1955. The propulsion of sea-urchin spermatozoa. *Journal of Experimental Biology* **32**: 802-814.

Gould, P. 2002. Exploiting spiders' silk. *Materials Today* December p. 42-47.

Hedenström, A. 2004. A general law for animal locomotion? *Trends in Ecology and Evolution* **19**: 217-219.

Henschel, J. R. 1990. Spiders wheel to escape. *South African Journal of Science* **86**: 151-152.

Holland, O. 2003. The first biologically inspired robots. *Robotica* **21**: 351-363.

Jackson, A. P., Vincent, J. F. V. and Turner, R. M. 1988. The mechanical design of nacre. *Proceedings of the Royal Society of London. Series B.* **234**: 415-440.

Koditschek, D. E., Full, R. J. and Buehler, M. 2004. Mechanical aspects of legged locomotion control. *Arthropod Structure & Development* **33**: 251-272.

Koehl, M. A. R. 2003. Physical modelling in biomechanics. *Philosophical transactions of the Royal Society of London. Series B.* **358**: 1589-1596.

Köhler, T. and Vollrath, F. 1995. Thread biomechanics in the two orb-weaving spiders *Araneus diadematus* (Araneae, Araneidae) and *Uloborus walckenaerius* (Araneae, Uloboridae). *The Journal of Experimental Zoology* **274**: 1-17.

Lauder, G. V. 2001. Flight of the robofly. *Nature* **412**: 688-689.

Lighthill, J. 1983. Aquatic animal locomotion: a survey of recent theoretical developments. In *Mathematical Biofluiddynamics* (Ed. J. Lighthill). Society for Industrial and Applied Mathematics, Philadelphia: 117-139.

Linden, P. F. and Turner, J. S. 2001. The formation of 'optimal' vortex rings, and the efficency of propulsion devices. *Journal of Fluid Mechanics* **427**: 61-72.

Linden, P. F. and Turner, J. S. 2004. 'Optimal' vortex rings and aquatic propulsion mechanisms. *Proceedings of the Royal Society of London. B.* **271**: 647-653.

Lipson, H. and Pollack, J. B. 2000. Automatic design and manufacture of robotic lifeforms. *Nature* **406**: 974-978.

Liu, J., Dukes, I., Knight, R. and Hu, H. 2004. Development of fish-like swimming behaviours for an autonomous robotic fish. *Control 2004*. University of Bath. Bath.

Martinez, M. M. 1996. Issues for aquatic pedestrian locomotion. *American Zoologist* **36**: 619-627.

McHenry, M. J. and Jed, J. 2003. The ontogenetic scaling of hydrodynamics and swimming performance in jellyfish (*Aurelia aurita*). *Journal of Experimental Biology* **206**: 4125-4137.

Menciassi, A. and Dario, P. 2003. Bio-inspired solutions for locomotion in the gastrointestinal tract: background and perspectives. *Philosophical transactions of the Royal Society of London. Series A.* **361**: 2287-2298.

Merz, R. A. and Edwards, D. R. 1998. Jointed setae - their role in locomotion and gait transitions in polychaete worms. *Journal of Experimental Marine Biology and Ecology* **228**: 273-290.

Nachtigall, W. 2001. Technische biologie und bionik. In *Bionik: Ökologische Technik nach dem Vorbild der Natur?* 2nd Ed. (Ed. Gleich, A. v.) B.G. Teubner. GmBH. Stuttgart: 11-22.

Ostrowski, J. and Burdick, J. 1998. The geometric mechanics of undulatory robotic locomotion. *International Journal of Robotic Research* **17**: 683-701.

Robinson, D. W., Pratt, J. E., Paluska, D. J. and Pratt, G. A. 1999. Series elastic actuator development for a biomimetic walking robot. *Proceedings of the 1999 IEEE/ASME Internation Conference on Advanced Intelligent Mechatronics*: 561-568.

Safak, K. K. and Adams, G. G. 2002. Dynamic modeling and hydrodynamic performance of biomimetic underwater robot locomotion. *Autonomous Robots* **13**: 223-240.

Schroeder, P. C. 1984. Chaetae. In *Biology of the Integument. Vol. I. Invertebrates* (Eds. Bereiter-Hahn, J., Matoltsy, A. G. and Richards, K. S.). Springer-Verlag. New York: 297-309.

Sleigh, M. A. and Barlow, D. I. 1980. Metachronal and control of locomotion in animals with many propulsive structures. In *Aspects of animal movement* (Ed. H. Y. Elder) Cambridge University Press. Cambridge: 49-70.

Stamhuis, E. J. Vortices rule the wake: structure and Reynolds' scaling of animal generate wake. In *Flow phenomena in Nature* (Ed. Liebe, R.). WIT Press. In press.

Taylor, G. 1952. Analysis of the swimming of long and narrow animals. *Proceedings of the Royal Society of London. A.* **214**: 158-183.

Taylor, G. K., Nudds, R. L. and Thomas, A. L. R. 2003. Flying and swimming animals cruise at a Strouhal number tuned for high power efficiency. *Nature* **425**: 707-711.

Thompson, B. S. 1996. Biomimetic materials: was Leonardo mistaken? - Part I. *SAMPE* **32**: 38-43.

Triantafyllou, M. S. and Triantafyllou, G. S. 1995. An efficient swimming machine. *Scientific American* **272**: 64-70.

Tsakiris, D. P., Sfakiotakis, M., Menciassi, A., La Spina, G. and Dario, P. 2005. Polychaete-like undulatory robotic locomotion. *International Conference on Robotics and Automation*, Barcelona.

Videler, J. J., Müller, U. K. and Stamhuis, E. J. 1999. Aquatic vertebrate locomotion:

wakes from body waves. *Journal of Experimental Biology* **202**: 3423-3430.

Vincent, J. F. V. 2000. Smart by name, smart by nature. *Smart Materials and Structures* **9**: 255-259.

Vincent, J. F. V. 2002. Survival of the cheapest. *Materials Today*. December: 28-41.

Vincent, J. F. V. 2003. Biomimetic modelling. *Philosophical transactions of the Royal Society of London. Series B.* **358**: 1597-1603.

Vincent, J. F. V. 2005. Selected natural materials in history. *Journal of Bionics Engineering* **2**: 161-176.

Vincent, J. F. V., Bogatyreva, O., Pahl, A.-K., Bogatyreva, N. and Boywer, A. 2005. Putting biology into TRIZ: a database of biological effects. *Creativity and Innovative Management* **14**: 66-71.

Vincent, J. F. V. and Mann, D. L. 2002. Systematic transfer from biology to engineering. *Philosophical transactions of the Royal Society of London. Series A.* **360**: 159-173.

Vogel, S. 1992. Copying nature: A biologist's cautionary comments. *Biomimetics* **1**: 63-79.

Vogel, S. 2003. *Comparative Biomechanics. Life's physical world.* Princeton University Press. Princeton.

Vollrath, F. 2000. Co-evolution of behaviour and material in the spider's web. In *Biomechanics in animal behaviour* (Eds. Domenici, P. and Blake, D. W.). BIOS Scientific Publishers Ltd. Oxford: 315-334.

Vollrath, F., Madsen, B. and Shao, Z. 2001. The effect of spinning conditions on the mechanics of a spider's dragline silk. *Proceedings of the Royal Society of London. B.* **268**: 2339-2346.

Wang, C.-a., Huang, Y., Zan, Q., Guo, H. and Cai, S. 2000. Biomimetic structure design - a possible approach to change in the brittleness of ceramics in nature. *Materials Science and Engineering. C.* **11**: 9-12.

Webb, B. 2001. Can robots make good models of biological behaviour? *Behavioral and Brain Sciences* **35**: 1033-1050.

Webb, B. 2002. Robots in invertebrate neuroscience. *Nature* **417**: 359-363.

Webb, P. W. 1988. Simple physical principles and vertebrate aquatic locomotion. *American Zoologist* **28**: 709-725.

Wootton, R. J. 1999. Invertebrate paraxial locomotory appendages: design, deformation and control. *Journal of Experimental Biology* **202**: 3333-3345.

Work, R. W. 1981. A comparative study of supercontraction of major ampullate silk fibers of orb-web-building spiders (Araneae). *Journal of Arachnology* **9**: 299-308.

Wu, T. Y. 1977. Introduction to the scaling of aquatic animal locomotion. In *Scale effects in animal locomotion* (Ed. Pedley, T. J.). Academic Press. London: 203-232.

Wu, T. Y. 2001. On theoretical modeling of aquatic and aerial animal locomotion. *Advances in Applied Mechanics* **38**: 291-353.

Yim, M., Roufas, K., Duff, D., Zhang, Y., Eldershaw, C. and Homans, S. 2003. Modular reconfigurable robots in space applications. *Autonomous Robots* **14**: 225-237.

Yu, J., Tan, M., Wang, S. and Chen, C. 2004. Development of a biomimetic robotic fish and its control algorithm. *IEEE Transactions on Systems, Man and Cybernetics - Part B. Cybernetics* **34**: 1798-1810.

Chapter 2

The biology of errant polychaetes in the family Nereididae

2 The biology of errant polychaetes in the family Nereididae

2.1 Classification and phylogeny

The polychaetes (bristle worms) belongs to the phylum Annelida (segmented worms) together with oligochaetes (earthworms) and leeches, although recent research indicates that the latter two, grouped together in the Clitellata, are in fact a subgroup of the Polychaeta (see Westheide *et al.* 1999 for a discussion). Around 9000 species of mainly marine worms have been described in Polychaeta. The classification and taxonomic relationship of the 54 families in Polychaeta remains debatable (Rouse and Fauchald 1997), but it is generally agreed that all families of errant polychaetes can be found in the group Aciculata (Fig. 2.1). Errant polychaetes are defined as being active worms with well-developed parapodia and a distinct head region bearing sensory structures. An errant lifestyle is found in several distant related families within the Aciculata, which supports the hypothesis that the ancestral polychaete was morphologically similar to some extant errant polychaete groups and that sedentary forms have evolved independently several times from this stem group (Purschke 2002; Westheide *et al.* 1999).

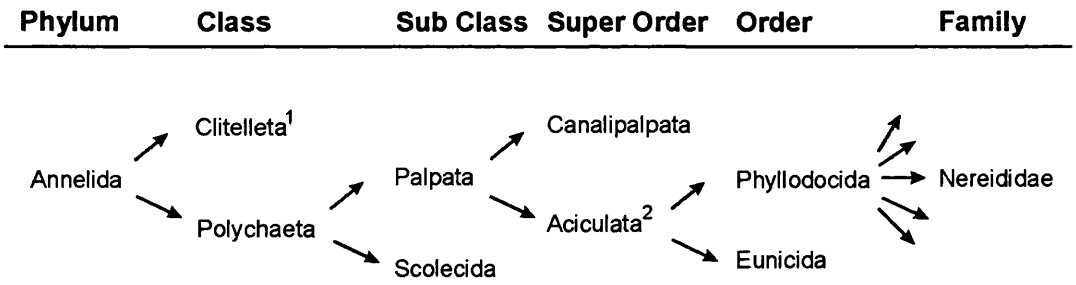

Fig. 2.1. The location of the family Nereididae in the taxonomic hierarchy of the Annelida based on the classification given by Rouse and Fauchald (1997). Note that the arrows from Phyllodocida represent many families. 1) Clitellata encompasses both the earthworms (Oligochaeta) and the leeches (Hirundea). Current research suggests that the Clittellata is not an independent group but belongs in the Polychaeta (Westheide *et al.* 1999). 2) Aciculata encompasses all known families of errant polychaetes as well as some sedentary ones.

The familiy Nereididae is one of the largest families with over 540 species in 43 genera (Bakken and Wilson 2005). Three subfamilies are found within the family: Namanereidinae, Gymnonereidinae and Nereidinae (Fitzhugh 1987). In this PhD study only species from the latter subfamily were used. Controversy exists over the exact number of genera in the subfamily Nereidinae as well as the allocation of species to genera (Bakken and Wilson 2005; Chambers and Garwood 1992; Fitzhugh 1987), but a phylogenetic tree of the most widely accepted genera can be found in figure 2.2. One of the most common species in the subfamily Nereidinae and the model organism used throughout this PhD project is the common ragworm *Nereis diversicolor*. The exact status of this species remains unresolved, but the majority of taxonomists now place it in the genus *Hediste* and thus it should be named *Hediste diversicolor* (Bakken and Wilson 2005; Scaps 2002; Sato 1999). However, as the name *Nereis diversicolor* is still the most widely recognised and the one most frequently used by ecologists (Nielsen *et al.* 1995; Golding and Yuwono 1994), I have decided to use it throughout this thesis, except in chapter 3, where the precise taxonomic relationships are of some importance. The phylogenetic relationships of the five species used in chapter 3 are the most widely accepted. However, very recent research suggests that the species *Neanthes succinea* and *Nereis virens* both belong in the new genus *Alitta* (Bakken and Wilson 2005). The results presented in this thesis, however, will not be affected by the taxonomic status of the species investigated.

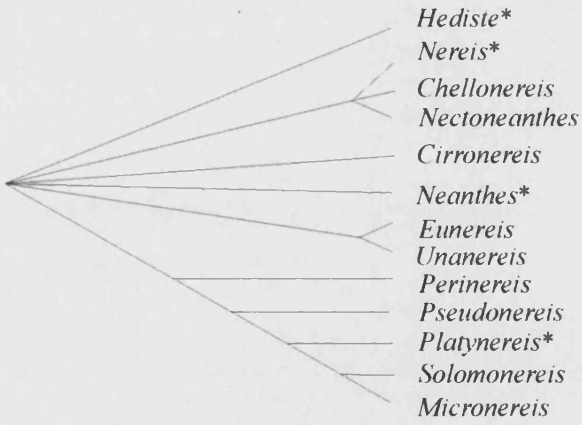

Fig. 2.2. Phylogenetic tree of the genera in the subfamily Nereidinae (Nereididae: Polychaeta). The stars indicate genera used in this PhD study. Simplified after Fitzhugh (1987).

2.2 Morphology and anatomy

Like all members of the Annelida, the body of errant polychaetes is divided into identical segments each bearing a pair of lateral appendages called parapodia (Fig. 2.3). The only exceptions are the two most anterior segments and the most posterior one (Fig. 2.3). The anterior segment is called the prostomium and bears the main sensory structures (more about them in section 2.3). The peristomium lies just behind the prostomium and includes the mouth and 4 head cirri. The last segment is the pygidium, which carries the anus and two pygidial cirri. The jaws are attached to the pharynx and are usually found inside the peristomium, however the anterior part of the pharynx, the proboscis, is eversible (Fig. 2.3).

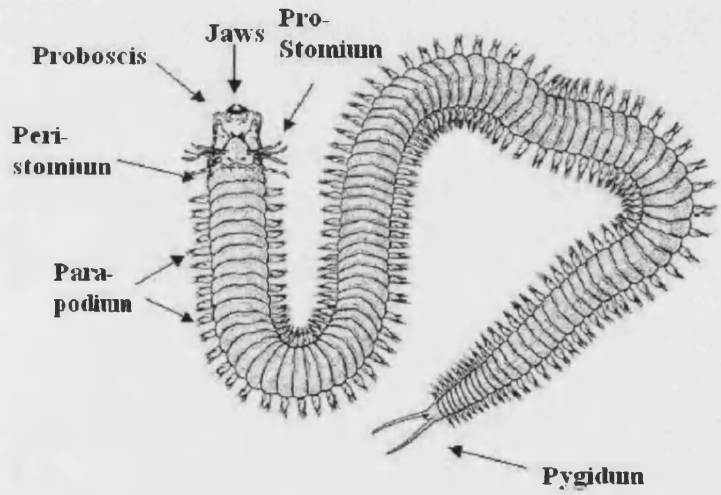

Fig. 2.3. Drawing of a typical *Nereis* with its proboscis protracted. Arrows point at the jaws on the protracted proboscis, at the prostomium (or head), at the peristomium and at a few of the parapodia extending lateral from both sides of each segment. Finally an arrow point at the pygidium.

Not only the external morphology is segmented, the internal structures also show compartmentalization. The body cavity takes up most of the volume, except in the first 10 segments where the foregut fills most of the available space. The body cavity is filled with coelomic fluid, which forms the hydrostatic skeleton. In nereidids, as in most other annelids, the isolation of coelomic fluid in one segment from that in other segments can be achieved by means of a septum (Mettam 1967). The intestine, blood vessels and nervecords are not segmented, but run continuously throughout the entire

length of the worm. The excretory system, however, is segmented with typically one pair of metanephridia per segment. The muscular system in errant polychaetes is segmented, and each segment has a pair of dorsal and ventral longitudinal muscle blocks, and circular muscles lining the body wall as well as several muscles protruding into the parapodia (Mettam 1967).

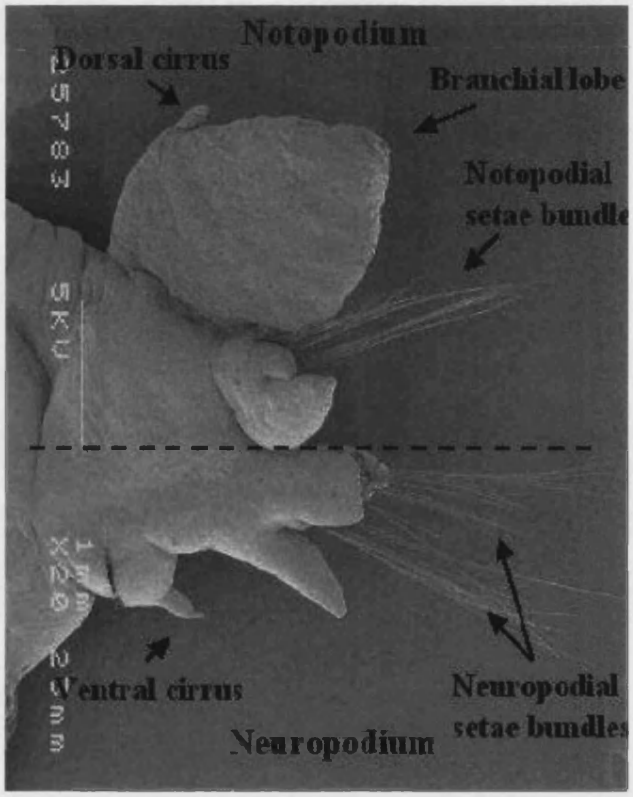

Fig. 2.4. A SEM photograph of a posterior parapodium in *Nereis virens*. The vertical bar on the left side of the photo is 1 mm long. The dashed line shows the approximate delimitation between the notopodium and neuropodium. The upper arrows point at the dorsal cirrus, the branchial lope (or gills) and the notopodial seta-bundle. The lower arrows point at the ventral cirrus and the two neuropodial seta-bundles.

Returning to the external morphology of errant polychaetes, the well-developed pair of parapodia on each body segment demands a closer examination. The parapodium consists of two parts of soft fleshy lobes, the dorsal one is called the notopodium and the ventral one is called the neuropodium (Fig. 2.4). Each part has an internal semi-rigid chitinous structure, the aciculum, and a small external sensory organ, the cirrus. The notopodium additionally has a large branchial lope which functions as a gill. In the notopodium the setae originate in a single bundle above the aciculum, whereas two

bundles, one above and one below the aciculum, are found in the neuropodium (Chamber and Garwood 1992). Several muscles run from the body segment to the parapodium, which enable it to move backward and forward (Mettam 1967). Other muscles from the body segment attach to the acicula, where they allow the parapodium to retract into the body. The exact morphology and size of the parapodium varies depending on position along the length of the body (Chambers and Garwood 1992). Especially the two most anterior pairs of parapodia are reduced in size and possess only the neuropodial aciculum and subsequently lack one bundle of setae (Chambers and Garwood 1992).

The seta-bundles consist of numerous individual setae. The simple seta is a non-jointed shaft tapering towards the end (Fig 2.5A). This type is very rare in the nereidids (Chambers and Garwood 1992). All other setae found in the errant polychaetes are compound setae, which consist of two parts: a shaft and a blade. The joint between these allows independent movement of the blade relative to the shaft, although a boss and a ligament restrict the degrees of freedom (Fig. 2.6). There are no muscles in the seta, so the blade has no intrinsic power and all movement occurs passively in response to external forces (Gustus and Cloney 1973). The shape of the joint in compound setae is either hetero- or homogomph. A homogomph seta has a symmetrical even joint, whereas on a heteregomph seta one side is longer than the other (Figs. 2.5 and 2.6). Setae are, furthermore, referred to as falcigers or spinigers depending on the shape of the blade. A falciger has a blunt or hooked tipped blade, while on a spiniger the blade tapers (Fig. 2.5). Falcigers are rare and restricted to neuropodial bundles (chapter 3; Gustus and Cloney 1973). The last type of setae is the paddle setae (Fig. 2.5F), which are exclusively found in the heteronereis, the sexual active stage in the life cycle of nereidids (see section 2.4). Although there are no muscles leading to the individual setae, the seta-bundle sacs have both retractor and protractor muscles associated with them (Mettam 1967).

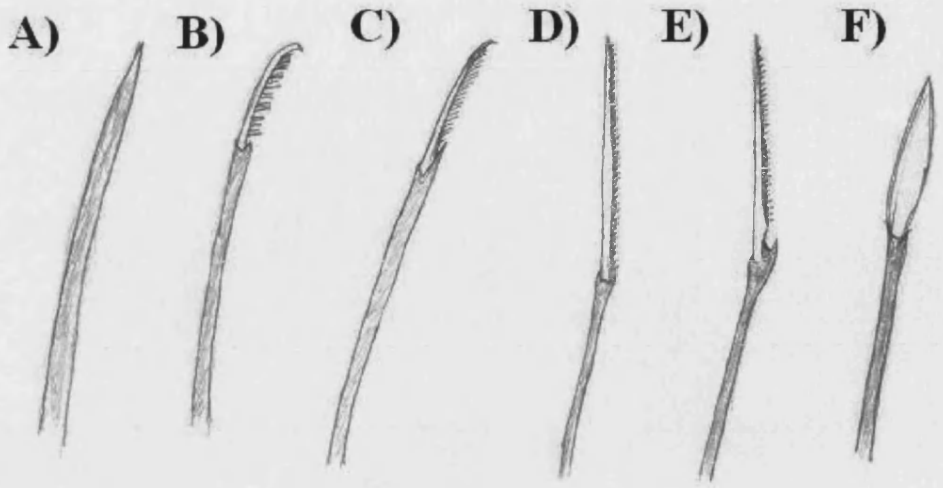

Fig. 2.5. The different types of setae. A) Simple seta. B) Homogomph falciger. C) Heterogomph falciger. D) Homogomph spiniger. E) Heterogomph spiniger . F) Paddle seta.

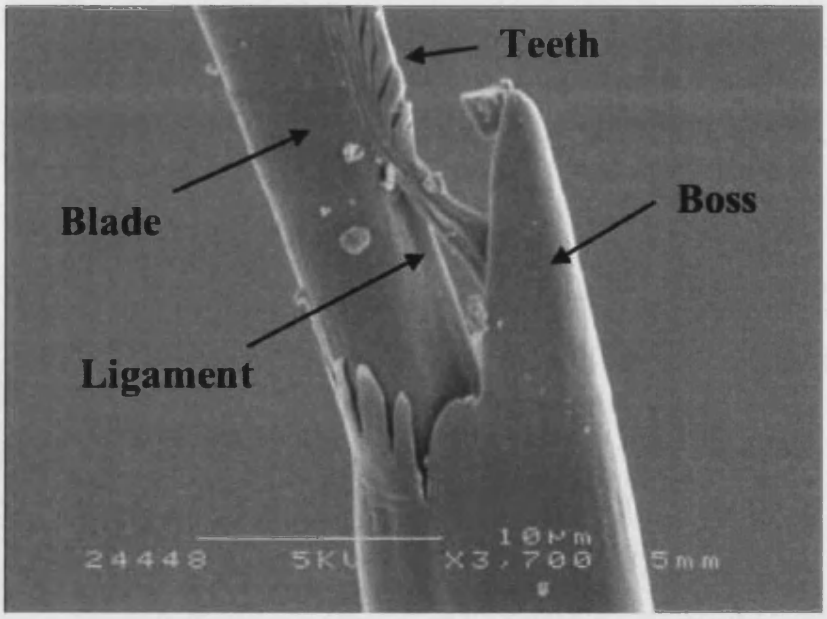

Fig. 2.6. The setal joint of a heterogomph spiniger from *Nereis virens*. Arrows indicate the position of the blade, the blade teeth, the ligament and the boss. The white horizontal bar at the bottom of the SEM photograph is 10 µm long.

2.3 The nervous and sensory system

The main part of the central nervous system in the Nereididae is the bilobed supra-oesophageal ganglion (the actual "brain" or the cerebral ganglion) located above

the pharynx (hence the name supra-oesophageal ganglion) in the prostomium (Fig. 2.7B). Below the gut, in the peristomium, is the sub-oesophageal ganglion, which can be considered as the anterior end of the nerve cord (Fig. 2.7). The two ganglia are connected to each other through the circum-oesophageal connectives (Orrhage 1993). 14 pairs of major nerves extending from the supra-oesophageal ganglion have been reported in *N. virens* (Orrhage 1993; Hamaker 1898). These nerves are labelled I to XIV in figure 2.7A. Nerves I and V innervate the proboscis. Nerve II goes to the antenna. Nerve III runs to the dorsal wall of the prostomium. Nerves IV, VI and VII innervate the palps. The three small nerves VIII, IX and X connect the circum-oesophageal connectives with the supra-oesophageal ganglion. Nerves XI and XII are the optic nerves and innervate the anterior and posterior eye respectively. Nerve XIII innervates the nuchal organs, while nerve XIV goes to the dorsal side of surface of the prostomium. Many questions remain about the morphology and not least function of the various parts of the brain in polychaetes. One issue that is important for understanding the evolutionary origin of the polychaetes, but has remained unresolved for the past 100 years, is whether the supra-oesophageal ganglion is fused together from different segments or if it is non-segmented (Orrhage and Müller 2005).

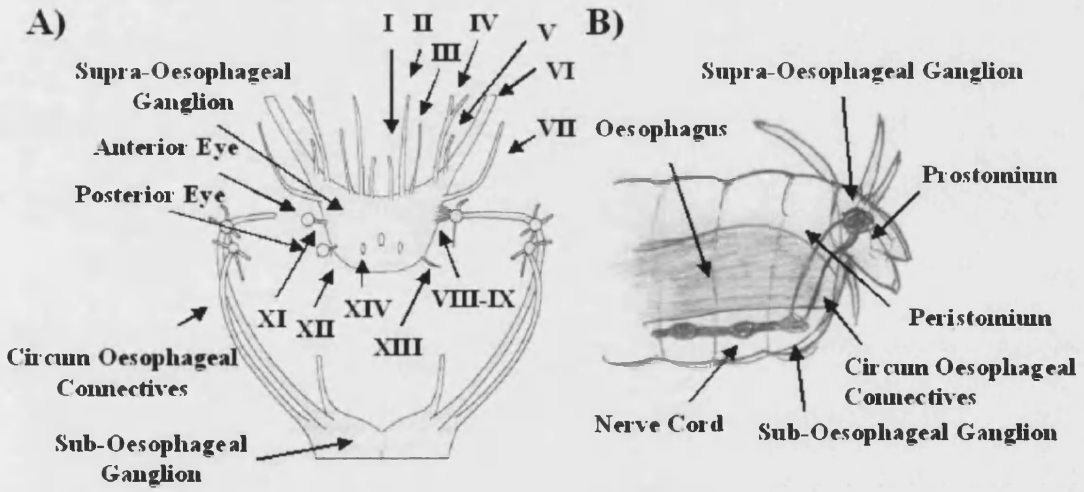

Fig. 2.7. The cephalic nervous system in nereidids. A) A dorsal view showing the 14 nerves (numbered I – XIV) that extend from the supra-oesphageal ganglion (or the actual "brain"). Modified after Orrhage (1993). B) Lateral view showing the spatial location of the supra and sub-oesophageal ganglions.

The annelid ventral nerve cord is a rope-ladder-like system, similar, but more variable, to what is seen in the arthropods and it is believed that both groups have inherited this structure from a common ancestor (Orrhage and Müller 2005). The nerve cord consists of one ganglion per segment, which is connected to its neighbours by thinner connectives (Fig. 2.8). The peripheral nerves in each segment arise from the intersegmental ganglia (Smith 1957). The nerve cord possesses two kinds of fibres, the giant fibres and the fine fibres. The giant fibres have rapid connections with motor and sensory pathways, and are primarily excited during escape and withdrawal behaviour (Dorsett 1964). In the fine fibres, two types of interneurons can be identified. The long axon neurons that transfer excitation to distant parts of the cord and the short-axon neurons, only found in the intersegmental ganglia, for local diffuse transfer of excitation (Smith 1957). Four pairs of peripheral nerves, extending from the intersegmental ganglia, are found in each segment (Fig. 2.8). Each nerve pair contains both motor and sensory pathways (Smith 1957). Nerve I terminates in the dorsal integument where it innervates the longitudinal muscles. Nerve II is the largest of the nerves and runs to the parapodium where it branches out and connects to sensory cells and innervates the intrinsic muscles in the parapodium. Nerve III is the smallest of the nerves and runs along the longitudinal muscles, where it connects to its counterpart in the next segment and thus form a lateral nerve that extends from the first to the last of the parapodium bearing segments (Smith 1957). Its primary function seems to be that of proprioception. Nerve IV innervates the longitudinal muscles as well as the retractor and protractor muscles and is thus together with nerve I responsible for locomotory activity (Lawry 1970; Smith 1957).

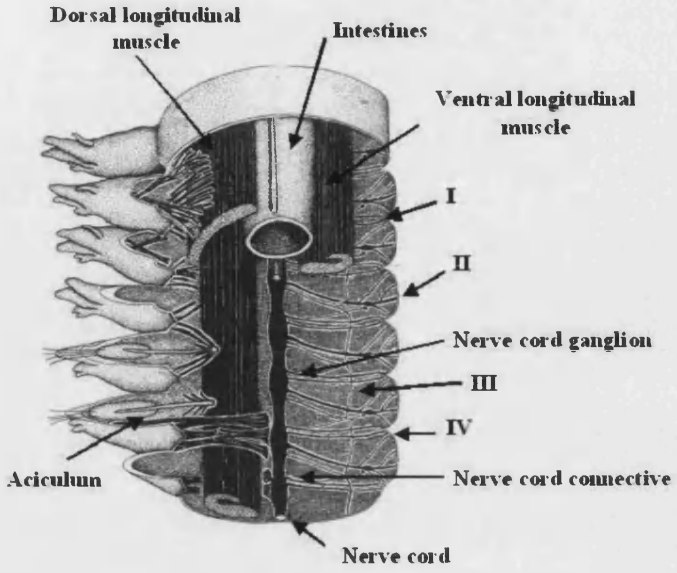

Fig. 2.8. Seven body segments of *Nereis virens*. Arrows point at the segmental nerves (I-IV) as well as other internal structures. Modified after Smith (1957).

All members of the family Nereididae have an active life style with a well-developed head region bearing most of the sensory organs (Fig. 2.9). Two relatively large palps and two small antennae are found at the anterior region of the prostomium. They have some chemoreceptors, but mainly possess mechanoreceptors and are probably primarily excited by physical contact with stimuli. Special retractable organs, the so-called nuchal organs are located on the dorsal side of the prostomium below the peristomium (Purschke 1997). These consist of a pair of ciliated sensory slits directly innervated from the brain. They contain a high concentration of chemoreceptors and their primary function is to detect food (Purschke 1997). Two pairs of eyes are also found on the prostomium. The eyes belong to the retinal cup (everted) type, and are covered with a lens (Yingst *et al.* 1972). They cannot, however, form any image, but they allow the animal to detect the direction and intensity of a light source (Cronin 1986). There is some indication that the *Nereis* eyes have a wider range of spectral sensitivity than many other marine animals (Yingst *et al.* 1972). Photoreceptors are also found distributed along the length of the body (Verger-Bocquet 1992). On the peristomium there are four pairs of cirri, primarily thought to possess touch receptors (Chambers and Garwood 1992).

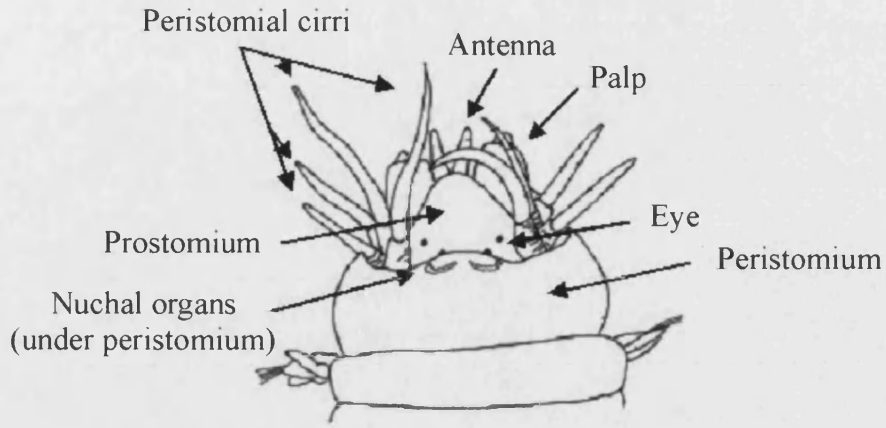

Fig 2.9. The anterior region of a nereidid showing the cephalic structures and sense organs.

Although the highest density of sensory cells is found in the head region, many are distributed around the body surface, especially in the parapodia, and a surprisingly high number of sensory cells are found in the pygidium and the pygidial cirri (Smith 1957). The reason that a substantial amount of mechanoreceptors and some chemoreceptors are found in the posterior region is probably that errant polychaetes are capable of, and quite frequently do, crawl and swim backwards (*Pers. obs.*). On the parapodium special sensory structures, the dorsal and ventral cirrus, are found (Fig. 2.4). The cirrus is mainly composed of epithelial and mucus cells (Smith 1957). In between these are numerous bipolar sensory cells oriented parallel to the epithelial cells. There is also an indication that the cirri contain proprioceptor cells that register the movements of the cirri (Dorsett 1964). Small clusters of specialised compound sensory organs are found distributed throughout all surfaces of the body, but more numerous in the head region and on the parapodia (Fig 2.10a) (Dorsett and Hyde 1969).The sensory structure has a diameter of 4-8 μm and consists of a cluster of 10 to 20 individual papilla with a diameter of less than 0.5 μm (Fig. 2.10b). The precise function of the compound sense organ remains controversial, but it consists most likely predominantly of mechanoreceptors and some chemoreceptors (Jouin *et al.* 1985; Dorsett and Hyde 1969).

Above we have focused on the major types of receptors and sense organs found in the Nereididae. However, although still not very well documented, it is likely that the worms also have other sense organs such as statocysts. Statocysts, are known from other polychaete families where they are used to detect the direction of gravity during burrowing (Verger-Bocquet 1992). Recently, speculation about whether marine

invertebrates possess electroreceptors similar to the ones found in fish has appeared in the literature (Bullock 1999). Such a sense would be useful in invertebrates to detect approaching predators even if much less sensitive than what is found in fish. However, as yet no evidence has been presented that errant polychaetes possess electroreception, but it remains a fascinating possibility.

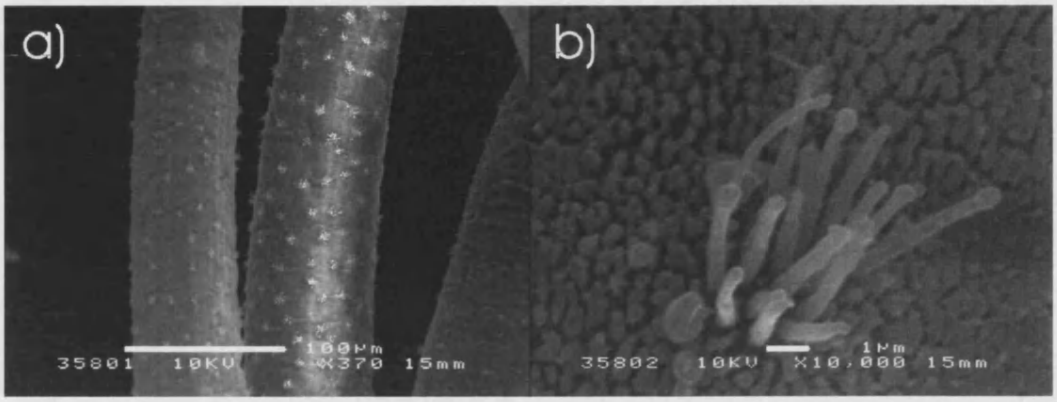

Fig. 2.10. SEM photos of sensory structures in the errant polychaete *Platynereis dumerilii*. a) A close-up of the head cirri. The white areas are individual compound sensory structures. The white bar is 100 µm long. b) A single compound sensory structure from the head cirrus. The white bar is 1 µm long.

2.4 Ecology and behaviour

Out of an estimated total diversity of 540 species in the family Nereididae, 12 can be found in the UK (Chambers and Garwood 1992). The nereidids have a worldwide distribution and can be found in nearly all coastal areas. Habitats range from beaches to the sea floor with some inhabiting fresh water and a few are even considered terrestrial (see references in Clark 1961). The British species show a wide range of habitats with species living on both hard and soft substrate in shallow or deeper waters. One species, *Neanthes fucata*, is a commensal and is mostly found sharing large shells occupied by hermit crabs (Goerke 1971b; Gilpin-Brown 1969). In a study of 5000 hermit crabs almost 30% of them were inhabited by *N. fucata* (Goerke 1971b). *Nereis diversicolor* and *Nereis virens* are both found in softer habitats in estuaries or along sandy or muddy coastlines (Scaps 2002; Bass and Brafield 1972), whereas *Neanthes succinea* and *Platynereis dumerilii* can be found in deeper waters associated with rocks, mussels or algal holdfasts (Chambers and Garwood 1992; Banse 1954). Similar

variations are found in other parts of the ecology, so a complete description of the ecology of the Nereididae is beyond the scope of this chapter. Instead, I will in the following concentrate mainly on *N. diversicolor* (the common ragworm), since I have primarily used this species in the studies presented in this thesis.

N. diversicolor is among the most common polychaetes in European waters, where it occurs as an infaunal species in coastal zones, although it can be found in the upper and less saline waters of estuaries (Scaps 2002). One of the main reasons for the wide distribution and occurrence of *N. diversicolor* is its ability to tolerate large environmental fluctuations. It can withstand salinities up to 200% of normal seawater as well as survive for up to two months in normal pond water (Oglesby 1970). The common ragworm usually inhabits sandy mud, but can be found in a wide range of habitats, including clay and turf (Clay 1967), where it constructs its burrow. The burrow is U- or Y-shaped and the walls are lined with mucus secreted by the worms (Fig. 2.11). *N. diversicolor* is primarily a nocturnal species and spends most of the day inactive in its burrow (Evans *et al.* 1974). It can, however, occasionally be seen projecting half of its body out of the burrow in search of food (Clay 1967). At night it sometimes completely abandons its burrow in a more active search of food. The common ragworm is an omnivore, but is also an active predator (Scaps 2002). It may act as a deposit feeder, collecting food near the burrow opening or it can subsist as a filter-feeder by generating a water flow through the burrow (Nielsen *et al.* 1995; Harley 1950). *N. diversicolor* has many natural enemies. Especially the overwintering and migrating waterfowls and waders can have a large impact on the population of ragworms, but also shrimps and small fish are important predators (Scaps 2002). Occasionally cannibalism can be observed as well as predation from larger or more aggressive nereidids, such as *N. virens* and *N. succinea* (Goerke 1971a). Its great palatability also benefits humans. Together with its larger relative *N. virens*, the common ragworm is an important bait species in recreational fishing. The European bait worm market in 1999 was estimated to have a value of €200 million (Olive 1999).

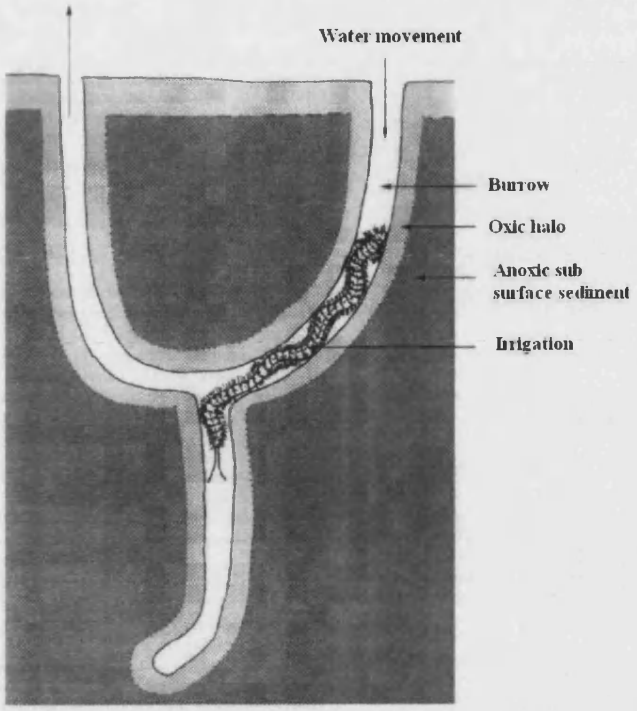

Fig. 2.11. The common ragworm irrigating its burrow. Modified from Scaps (2002).

As we saw in section 2.3, the "brain" of the Nereididae, although being one of the best developed among annelids, is a rather simple structure. Yet the nereidid species show a large variety of different behaviours ranging from irrigation over fighting behaviour to reproductive behaviour. Although the nereidids belong to the group of errant polychaetes, they spend most of their time inactive in their burrows punctuated by bouts of various spontaneous activities (Evans *et al.* 1974). These activities include searching behaviour, i.e. extending the anterior part of the body from the burrow. This is sometimes followed by rapid withdrawal if a potential threat is detected (Evans 1969). Another common activity is irrigation behaviour, used to ventilate the burrow, which consists of dorsal-ventral undulating movements where the wave travels from head to tail (Evans *et al.* 1974). This is interesting as it differs from normal locomotory activity that consists of lateral undulating waves that travel from tail to head (see next section). Other spontaneous activities include reversal in the burrow and deposit of waste products at the entrance to the burrow. All these activities have been monitored and classified in a dominance hierarchy, where withdrawal behaviour takes precedence over all other activities (Evans and Downie 1986). However, more complicated behaviour is also found in the Nereididae. Defence of the burrow has been reported in both *N. diversicolor* and *N. virens* (Miron *et al.* 1992). This includes threatening display

by everting the proboscis towards intruders, which occasionally escalates into pushing and biting behaviour. Usually the contest ends with the resident evicting the intruder, but occasionally the original resident withdraws (Miron *et al.* 1992). *N. diversicolor* also shows anti-predator behaviour and has in the presence of the nemertine *Lineus viridis* (a predatory unsegmented ribbon-worm) been observed, in the laboratory, to swim for more than an hour (Thiel and Reise 1993). Most of the behavioural repertoire found in errant polychaetes is of a rather stereotypic nature with little or no feedback and plasticity. For instance, shell entry behaviour in *N. fucata*, a commensal in the shell of the hermit crab, consists of a fixed sequence of detecting the approach of the crab, crawl onto the shell and locate its aperture and enter the shell (Cram and Evans 1980; Gilpin-Brown 1969). This behaviour is well-adapted but relies little on actual feedback since the worm will respond similarly to the shore crap and even attempt to enter its gill chamber in the belief it is the aperture as well as it accepts any kind of artificial holes made in the shell (Cram and Evans 1980). However, the nereidids do show some plasticity and also have the ability to learn. Habituation is readily observed in the lab, when the worms, after an acclimatization period, cease to show withdrawal behaviour to the approach of the investigator when feeding (*Pers. obs.*; Evans 1969). More complicated forms of learning have also been demonstrated in *N. diversicolor* and *N. virens*, such as navigation in T-mazes and the avoidance of channels with electrodes from environmental and idiothetic cues (Evans 1963a, b).

The common ragworm, like most polychaetes, is diocious unlike the hermaphroditic earthworms. However, the reproduction of *N. diversicolor* is in many ways atypical. Unlike most other members of the family Nereididae, the common ragworm does not metamorphose into a distinct sexual stage (Scaps 2002). In other species the reproductive stage or heteronereis is reached by both external and internal changes in the juvenile worm. Changes in morphology include modification of the parapodium and the replacement of normal setae with special paddle formed setae (Figs. 2.5F, 2.12). Internal changes include development of the respiratory system, enlargement of parapodial muscles and improvements of the sensory organs (Clark 1961). The cost of these changes is histolysis of the body wall and the gut. The most significant difference from the juvenile stage, however, is the change in behaviour (Clark 1961). The heteronereis is an active swimmer and most nereidids only swim in this stage. During reproduction the heteronereis of most species gather in large swarms near the surface where spawning takes place. Nearly all polychaetes have external

fertilisation of the gametes taking place in the water. The exact cues that determine the onset of swarming are still poorly understood, but it seems that environmental cues, reinforced by chemicals secreted by already swarming individuals, are the main reason that a large proportion of the heteronereis of the same species swarms on the same days (Hardege 1999; Hardege and Bartels-Hardege 1995). The swarming behaviour usually consists of a so-called nuptial dance, which is characterized by the sexual partners swimming around each other in decreasing circles until the gametes are released. This release is primarily controlled by sex pheromones (Hardege 1999). After the release of gametes the females drop to the ocean floor and dies. The males continue swarming somewhat longer before they too die. In contrast, *N. diversicolor* does not metamorphose into a heteronereis and only experience a modest histolysis of the somatic tissue (Scaps 2002). Furthermore, it does not swarm, instead the female lays her eggs inside her burrow with the male releasing its sperm in front of the burrow. Irrigating behaviour by the female then brings the gametes into contact. The common ragworm also exhibits some brood care, with the female guarding the eggs inside her burrow for a period before she dies (Scaps 2002).

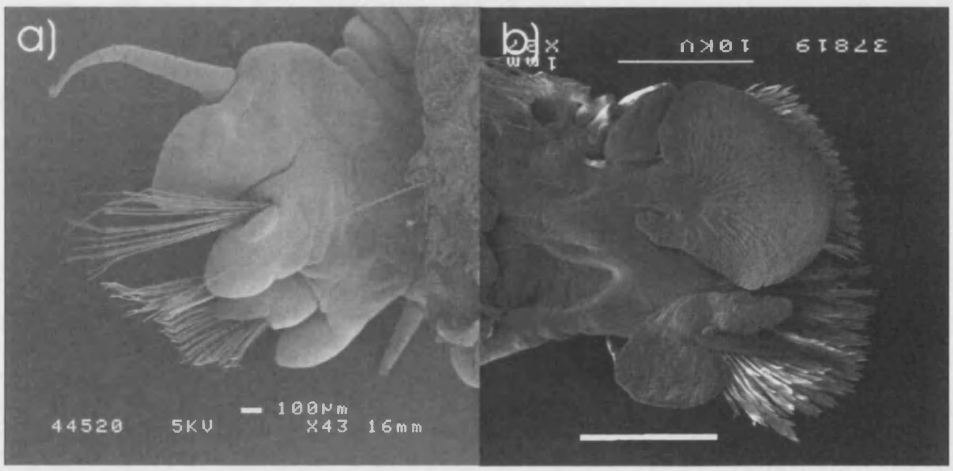

Fig 2.12. SEM photo of the parapodium of *Neanthes fucata* in different life stages. a) Parapodium of a juvenile. The white bar is 0.1 mm long. b) Parapodium of a heteronereis. The white bar is 1 mm long.

2.5 Locomotion

The swimming of errant polychaetes was scientifically described around the beginning of the last century (see references in Foxon 1936), but a description of the

crawling mechanism, using cinematographic methods, was first given 30 years later by Foxon (1936). In his classical paper, Gray (1939) refines and combines the previous work into a complete description of *Nereis* locomotion.

Three distinct types of gaits are found in the errant polychaetes (Fig. 2.13). During slow crawling no (or only very insignificant) lateral undulations of the body are observed and each parapodium functions similar to a leg in terrestrial animals. It is lifted from the ground and drawn inwards and forwards in the recovery stroke where after the tip of the parapodium touches the ground and forms a fulcrum (although some slippage is normally observed), around which the parapodium turns during the power stroke and thus advances the segment (Mettam 1967; Gray 1939; Foxon 1936). Each parapodium is out of phase with its neighbours on the ipsilateral side. This results in a wave of parapodial activity progressing toward the head on each side of the body. In an example of slow walking in *Nereis virens* the parapodia on each segment were found to be 180° out of phase with every 4th parapodium of the ipsilateral side in phase (Dorsett 1966). However, the exact number of segments between synchronized parapodia depends both on species and speed of crawling (*Pers. obs.*; Merz and Edwards 1998).

In fast crawling, the above described parapodial movement is coupled with lateral undulations of the body travelling in a posterior-anterior direction. The tip of the parapodium touches the ground as the segment on which it is attached approaches the crest of the body wave, so that the backward power stroke of the parapodium coincides with the crest of the body wave. This means that the force, generated during the power stroke, does not only stem from the parapodial muscles but is amplified by the longitudinal muscles and their resulting body movements (Mettam 1967, Gray 1939). There are a relatively small number of segments in each complete wave and the amplitude of the sinusoid wave is small compared to when swimming.

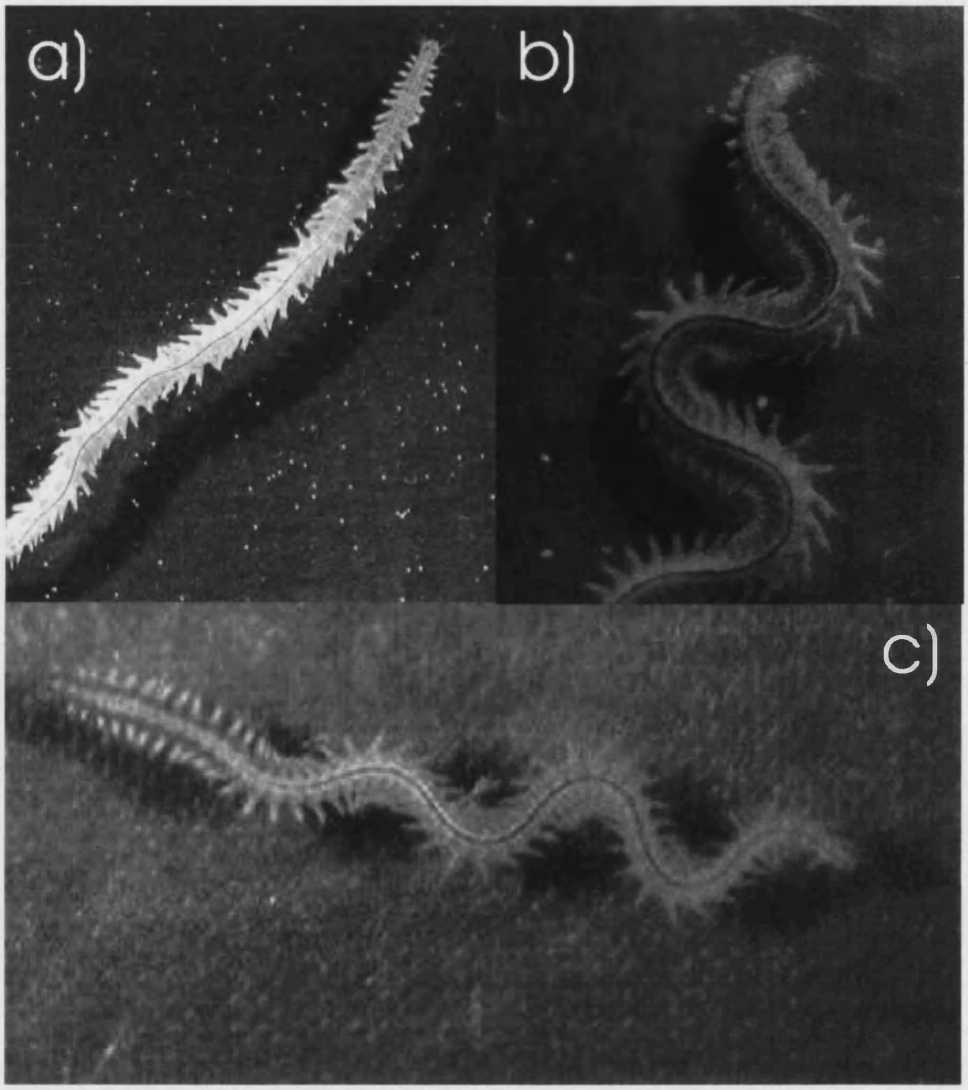

Fig. 2.13. The three gaits found in errant polychaetes. All photos here are of *Nereis diversicolor*. a) Slow crawling. b) Swimming. c) Fast crawling.

During swimming the body is no longer in contact with the substrate and the number of body waves along the body decreases and show larger amplitudes. Similar to fast crawling, the body undulations and parapodial movements are coupled during swimming. Swimming by means of undulatory body waves has been adopted by a large diversity of animals and is an effective locomotory mechanism for a wide range of Reynolds numbers and body sizes (Lighthill 1983). In his classical study the physicist Sir Geoffrey Taylor initiated the hydrodynamical study of undulatory locomotion by analysing elongated animals exhibiting several complete waves along their body (Taylor 1952). His studies on long narrow cylinders let him to propose that the

tangential and normal components of the resistive forces depend on the relative velocity of the cylinder through water. This is now known as the resistive theory of aquatic locomotion and the force-velocity dependence is linear at low Reynolds numbers but quadratic at high Reynolds numbers (Wu 2001). The undulatory swimming found in polychaetes is unusual since the body waves are moving in an anterior direction from tail to head, contrary to what is found in most other undulatory swimmers, such as eels and snakes, where the body waves move from head to tail (Tytell and Lauder 2004; Gillis 1998). Taylor (1952) expanded his theoretical model by analysing the forces on rough cylinders and found that in some circumstances propulsive forces could be generated by a rough cylinder when the body waves were moving in an anterior direction. By using data of a swimming *Nereis* from Gray (1939), which fitted with his model he concluded that the role of the parapodia in the errant polychaetes during swimming is entirely passive and only necessary for giving the body the required roughness (Taylor 1952). However, further data from a larger group of swimming nereidids disagreed with the Taylor model and instead a much more active role for the parapodia was suggested (Clark 1976; Clark and Tritton 1970). This also agrees more with observations of the elaborate movement of the parapodia during swimming. The length of the parapodia varies during swimming so that the maximum length is reached at the crest of the body wave thereby maximising the drag on the parapodia (chapter 6). As this coincides with the power stroke, i.e. the parapodia moves backwards relative to the direction of movement of the animal, it results in maximum thrust production. In contrast the parapodia have their minimum length and are closest together during the recovery stroke, where they move in the same direction as the body, and thus minimise their drag. The role of the parapodia during swimming can therefore be likened to a paddle and the role of the body wave is to enhance the function of the parapodia (Clark and Tritton 1970). In chapter 6 of this thesis I present experimental kinematic data of the swimming of *N. diversicolor* as well as evidence of previously unknown distinct jets in the wake of the swimming worm, thereby showing that the interaction of multiple parapodia results in a jet-like type of propulsion in swimming juvenile errant polychaetes.

Most studies on locomotion in nereidids concentrate on swimming, which is somewhat misleading, since the primary mode of locomotion is that of crawling over the substratum. As we saw in the previous section most errant polychaetes swim only in the heteronereis stage, and the few that do swim in the juvenile stage, do so only rarely

and then mainly to escape from certain predators (Thiel and Reise 1993). Underwater walking differs from swimming in that contact with the substrate is essential for generating thrust, resulting in major importance of factors such as buoyancy and friction (Martinez 1996). However, in general it seems like the field of underwater walking has been neglected, with very few studies published and predominantly on crabs (Wootton 1999; Martinez 1996). In chapter 5, where we compare the effect of seta-ablation on locomotion over two substrates I give experimental kinematic data of some overall crawling parameters.

Burrowing, although strictly speaking more a form of construction behaviour, can be regarded as a locomotory mechanism. This is evident when observing how fast *N. diversicolor* can dig and disappear into the sediment when surprised in daylight (*Pers. obs.*). Polychaetes mainly burrow by use of direct peristaltic waves (Elder 1973). *N. diversicolor* buries its anterior segments by lateral movements of the head and forward crawling by the posterior segments (Trevor 1977). When the first few anterior segments are buried the worm starts to dig by everting its pharynx. In later stages when the worm is more than half buried it uses peristalsis to progress the body (Trevor 1977), although the parapodia also seems to be involved (Mettam 1967). A recent study show that the everted pharynx instead of working as an anchor, as previously thought, might instead be used to propagate cracks through the sediment thus making burrowing more mechanically efficient (Dorgan *et al.* 2005).

As we saw in section 2.2, the structural complexity of the small setae protruding distally from the parapodium is very high. It is therefore likely that they play a significant functional role during locomotion in errant polychaetes. The existence of acicular muscles capable of protracting and retracting the seta-bundles, lends support to this notion (Mettam 1967). When the worm is engaged in slow or fast crawling the setae are protracted during the power stroke and retracted during the recovery stroke. The function of the passive setal joints is probably to enhance the contact area between the sediment and the fine teeth on the seta-blade and thus to increase friction (Gustus and Cloney 1973). This hypothesis is supported by experimental data, which show that trimming of the setae and removal of the joints decrease both slow and fast crawling speeds (Merz and Edwards 1998) and the ablation study presented in chapter 5. The function of the setae during swimming is less clear. A theoretical analysis, supported by experimental evidence, demonstrate that rows of small hairs or setae can have such

small amounts of water flowing through the hairs that they practically act as paddles (Koehl 2001; Cheer and Koehl 1987).

The Cheer and Koehl (1987) model show that the leakiness, i.e. the ratio of water passing through to what goes around it, for a pair of cylinders, depends on the diameter of the cylinders, the distance between them and the Reynolds number (Fig. 2.14). Theoretical calculations based on the conditions found in the seta-bundles of errant polychaetes suggest that they have a rather low leakiness (see chapter 3). Thus the functional role of setae during swimming could be to increase the thrust generating area of the parapodium during the power stroke. However, experimental data show that simply trimming the setae has no effect, only when the joints are also removed is a negative effect on swimming speed observed (Merz and Edwards 1998). No clear effect of removing the entire neuropodial seta-bundles was, furthermore, found on swimming performance in the study presented in chapter 5. The setae of tube dwelling polychaetes function like hooks and are used primarily to resist removal of worms from their burrows (Woodin and Merz 1987). It is likely that a similar function exists in the parapodial setae of errant polychaetes. Furthermore, they probably increase the grip to the sediment during burrowing (Mettam 1967).

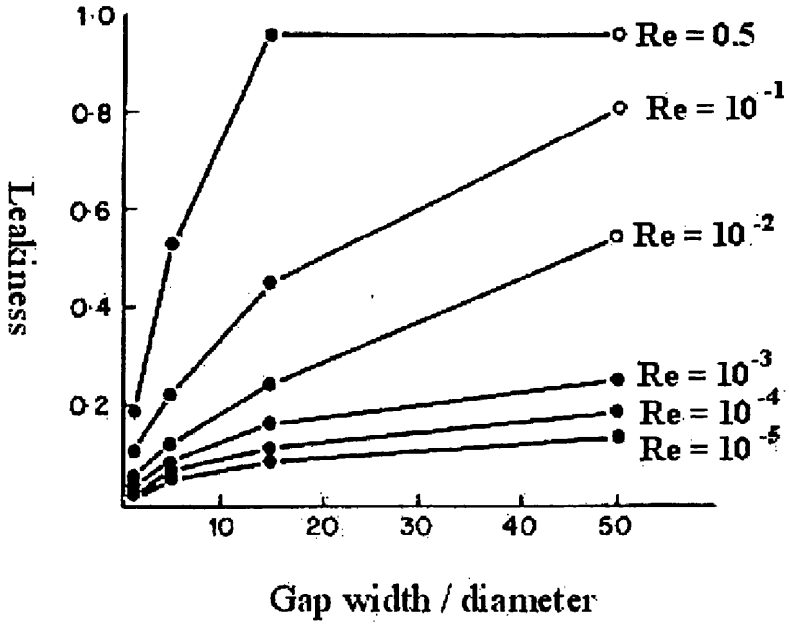

Fig. 2.14. Leakiness of a pair of cylinders, in relation to the width of the gap between them divided by their diameter, as predicted by the Cheer and Koehl model. Each curve corresponds to a different Reynolds number. After Cheer and Koehl (1987).

References

Bakken, T. and Wilson, R. S. 2005. Phylogeny of nereidids (Polychaeta, Nereididae) with paragnaths. *Zoologica Scripta* **34**: 507-547.

Banse, K. 1954. Über Morphologie und Larvalentwicklung von *Nereis* (*Neanthes*) *succinea* (LEUCKART) 1847 (Polychaeta errantia). *Zoologische Jahrbuch Abteilung für Anatomie* **74**: 160-171.

Bass, N. R. and Brafield, A. E. 1972. The life-cycle of the polychaete *Nereis virens*. *Journal of the Marine Biological Association* **52**: 701-726.

Bullock, T. H. 1999. The future of research on electroreception and electrocommunication. *Journal of Experimental Biology* **202**: 1455-1458.

Chambers, S. and Garwood, P. 1992. *Polychaetes in Scottish Waters. A Guide to Identification. Part 3 Family Nereidae*. National Museums of Scotland.

Cheer, A. Y. L. and Koehl, M. A. R. 1987. Paddles and rakes: fluid flow through bristled appendages of small organism. *Journal of Theoretical Biology* **129**: 17-39.

Clark, R. B. 1961. The origin and formation of heteronereis. *Biological Reviews* **36**: 199-236.

Clark, R. B. 1976. Undulatory swimming in polychaetes. In *Perspectives in experimental biology*. (Ed. Davies, P. S.). Pergamon Press. Oxford. Vol 1: 437-446.

Clark, R. B. and Tritton, D. J. 1970. Swimming mechanisms in nereidiform polychaetes. *Journal of Zoology* **161**: 257-271.

Clay, E. 1967. Literature survey of the common fauna of estuaries. *Imperial Chemical Industries Ltd. Brixham Laboratory* **1**: 1-28.

Cram, A. and Evans, K. E. 1980. Shell entry behaviour in the commensal ragworm *Nereis fucata*. *Marine Behaviour and Physiology* **7**: 57-64.

Cronin, T. 1986. Photoreception in marine invertebrates. *American Zoologist* **26**: 403-415.

Dorgan, K. M., Jumars, P. A., Johnson, B., Boudreau, B. P. and Landis, E. 2005. Burrow extension by crack propagation. *Nature* **433**: 475.

Dorsett, D. A. 1964. The sensory and motor innervation of *Nereis*. *Proceedings of the Royal Society of London. B.* **159**: 652-667.

Dorsett, D. A. 1966. Overlapping sensory fields of *Nereis*, and their possible role in locomotion. *Proceedings of the Royal Society of London* **164**: 615-623.

Dorsett, D. A. and Hyde, R. 1969. The fine structure of the compound sense organs on the cirri of *Nereis diversicolor*. *Zeitschrift für Zellforschung* **97**: 512-527.

Elder, H. Y. 1973. Direct peristaltic progression and the functional significance of the dermal connective tissues during burrowing in the polychaete *Polyphysia crassa* (Oersted). *Journal of Experimental Biology* **58**: 637-655.

Evans, S. M. 1963a. The effect of brain extirpation on learning and retention in nereid polychaetes. *Animal Behaviour* **11**: 172-178.

Evans, S. M. 1963b. Behaviour of the polychaete *Nereis* in T-mazes. *Animal Behaviour* **11**: 379-392.

Evans, S. M. 1969. Habituation of the withdrawal response in nereid polychaetes 1. The habituation process in *Nereis diversicolor*. *Biological Bulletin* **137**: 95-104.

Evans, S. M., Cram, A. and Rogers, F. 1974. Spontaneous activity and responses to stimulation in the polychaete *Nereis diversicolor* (O. F. Müller). *Marine Behaviour and Physiology* **3**: 35-58.

Evans, S. M. and Downie, P. J. 1986. Decision-making processes in the polychaete *Platynereis dumerilii*. *Animal Behaviour* **34**: 472-479.

Fitzhugh, K. 1987. Phylogenetic relationships within the Nereididae (Polychaeta): implications at the subfamily level. *Bulletin of the Biological Society of Washington* **7**: 174-183.

Foxon, G. E. H. 1936. Observations on the locomotion of some arthropods and annelids. *The Annals and Magazine of Natural History* **18**: 403-419.

Gillis, G. B. 1998. Environmental effects of undulatory locomotion in the american eel *Anguilla rostrata*: kinematics in water and on land. *Journal of Experimental Biology* **201**: 949-961.

Gilpin-Brown, J. B. 1969. Host-adoptation in the commensal polychaete *Nereis fucata*. *Journal of the Marine Biological Association* **49**: 121-127.

Goerke, H. 1971a. Die Ernährungsweise der *Nereis*-arten (Polychaeta, Nereidae) der deutchen küsten. *Veröffentlichungen der Institut für Meeresforschung in Bremerhaven* **13**: 1-50.

Goerke, H. 1971b. *Nereis fucata* (polychaeta, nereidae) als kommensal von *Eupagurus bernhardus* (Crustacea, Paguriedae). Entwicklung einer population und

verhalten der art. *Veröffentlichungen der Institut für Meeresforschung in Bremerhaven* **13**: 79-118.

Golding, D. W. and Yuwono, E. 1994. Latent capacities for gametogenic cycling in the semelparous invertebrate *Nereis*. *Proceedings of the National Academy of Science* **91**: 11777-11781.

Gray, J. 1939. Studies in animal locomotion. VII. The kinetics of locomotion of *Nereis diversicolor*. *Journal of Experimental Biology* **16**: 9-17.

Gustus, R. M. and Cloney, R. A. 1973. Ultrastructure of the larval compound setae of the polychaete *Nereis vexillosa* Grube. *Journal of Morphology* **140**: 355-366.

Hamaker, J. I. 1898. The nervous system of *Nereis virens* Sars. *Bulletin from the Museum of Comparative Zoology* **32**: 89-135.

Hardege, J. 1999. Nereidid polychaetes as model organisms for marine chemical ecology. *Hydrobiologia* **402**: 145-161.

Hardege, J. and Bartels-Hardege, H. 1995. Spawning behaviour and development of *Perinereis nuntia* var. *brevicirrus* (Annalida: Polychaeta). *Invertebrate Biology* **114**: 39-45.

Harley, M. B. 1950. Occurrence of a filter-feeding mechanism in the polychaete *Nereis diversicolor*. *Nature* **165**: 734-735.

Jouin, C., Tschernigovtzeff, C., Baucher, M. F. and Toulmond, A. 1985. Fine structure of probable mechano- and chemoreceptors in the caudal epidermis of the lugworm *Arenicola marina* (Annelida, Polychaeta). *Zoomorphology* **105**: 76-82.

Koehl, M. A. R. 2001. Transitions in function at low Reynolds number: hair-bearing animal appendages. *Mathematical methods in the applied sciences* **24**: 1523-1532.

Lawry, J. V. 1970. Mechanisms of locomotion in the polychaete, *Harmothoe*. *Comparative Biochemistry and Physiology* **37**: 167-179.

Lighthill, J. 1983. Aquatic animal locomotion: a survey of recent theoretical developments. In *Mathematical Biofluiddynamics* (Ed. Lighthill, J.). Society for Industrial and Applied Mathematics. Philadelphia: 117-139.

Martinez, M. M. 1996. Issues for aquatic pedestrian locomotion. *American Zoologist* **36**: 619-627.

Merz, R. A. and Edwards, D. R. 1998. Jointed setae - their role in locomotion and gait transitions in polychaete worms. *Journal of Experimental Marine Biology and Ecology* **228**: 273-290.

Mettam, C. 1967. Segmental musculature and parapodial movement of *Nereis diversicolor* and *Nephthys hombergi* (Annelida: Polychaeta). *Journal of Zoology* **153**: 245-275.

Miron, G., Desrosiers, G. and Retiere, C. 1992. Organization of fighting in the polychaete *Nereis virens* (Sars) and the effects of residency and orientation. *Behaviour* **121**: 20-34.

Nielsen, A. M., Eriksen, N. T., Iversen, J. J. L. and Riisgaard, H. U. 1995. Feeding growth and respiration in the polychaetes *Nereis diversicolor* (facultative filter-feeder) and *N. virens* (omnivorous) - a comparative study. *Marine Ecology and Progress Series* **125**: 149-158.

Oglesby, L. C. 1970. Studies on the salt and water balance of *Nereis diversicolor*-I. Steady-state parameters. *Comparative Biochemistry and Physiology* **36**: 449-466.

Olive, P. J. 1999. Polychaete aquaculture and polychaete science: a mutual synergism. *Hydrobiologia* **402**: 175-183.

Orrhage, L. 1993. On the microanatomy of the cephalic nervous system of nereidae (polychaeta), with a preliminary discussion of some earlier theories on the segmentation of the polychaete brain. *Acta Zoologica* **74**: 145-172.

Orrhage, L. and Müller, M. C. M. 2005. Morphology of the nervous system of Polychaeta. *Hydrobiologia* **535/536**: 79-111.

Purschke, G. 1997. Ultrastructure of the nuchal organs in polychaetes (annelida) - new results and review. *Acta Zoologica* **78**: 123-143.

Purschke, G. 2002. On the ground pattern of Annelida. *Organisms Diversity & Evolution* **2**: 181-196.

Rouse, G. W.; Fauchald, K. 1997. Cladistics and polychaetes. *Zoologica Scripta* **26**: 139-204.

Sato, M. 1999. Divergence of reproductive and developmental characteristics in *Hediste* (Polychaeta: Nereididae). *Hydrobiologia* **402**: 129-143.

Scaps, P. 2002. A review of biology, ecology and potential use of the common ragworm *Hediste diversicolor* (O.F. Müller) (Annelida: Polychaeta). *Hydrobiologia* **470**: 203-218.

Smith, J. E. 1957. The nervous anatomy of the body segments of nereid polychaetes. *Philosophical Transactions of the Royal Society of London. Series B.* **350**: 135-196.

Taylor, G. 1952. Analysis of the swimming of long and narrow animals. *Proceedings of the Royal Society of London. A.* **214**: 158-183.

Thiel, M. and Reise, K. 1993. Interaction of nemertines and their prey on tidal flats. *Netherlands Journal of Sea Research* **31**: 163-172.

Trevor, J. H. 1977. The burrowing of *Nereis diversicolor* O. F. Müller, together with some observations on *Arenicola marina* (L.) (Annelida: Polychaeta). *Journal of Experimental Marine Biology and Ecology* **30**: 129-145.

Tytell, E. D. and Lauder, G. V. 2004. The hydrodynamics of eel swimming. I. Wake structure. *Journal of Experimental Biology* **207**: 1825-1841.

Verger-Bocquet, M. 1992. Polychaeta: sensory structures. In *Microscopic Anatomy of Invertebrates. Vol. 7. Annelida* (Eds. Harrison, F. W. and Gardiner, S. L.). Wiley-Liss Inc. Vol. 7: 181-196.

Westheide, W., McHugh, D., Purschke, G. and Rouse, G. 1999. Systematization of the Annelida: different approaches. *Hydrobiologia* **402**: 291-307.

Woodin, S. A. and Merz, R. A. 1987. Holding on by their hooks: anchors for worms. *Evolution* **41**: 427-432.

Wootton, R. J. 1999. Invertebrate paraxial locomotory appendages: design, deformation and control. *Journal of Experimental Biology* **202**: 3333-3345.

Wu, T. Y. 2001. On theoretical modeling of aquatic and aerial animal locomotion. *Advances in Applied Mechanics* **38**: 291-353.

Yingst, D. R., Fernandez, H. R. and Bishop, L. G. 1972. The spectral sensitivity of a littoral annelid: *Nereis mediator*. *Journal of Comparative Physiology* 77: 225-232.

Chapter 3

A comparative study on the functional morphology of parapodia and setae in nereidids (Polychaeta: Nereididae)

Published in Animal Biology.

Hesselberg, T. and Vincent, J. F. V. 2006 A comparative study on the functional morphology of parapodia and setae in nereids (Polychaeta: Nereididae). *Animal Biology* **56**: 103-120.

3 A comparative study of the functional morphology of parapodia and setae in nereidids (Polychaeta: Nereididae)

Hesselberg, T. and Vincent, J. F. V.

Centre for Biomimetic and Natural Technologies. Department of Mechanical Engineering. The University. Claverton Down. BA2 6AY. Bath. UK.

Abstract: Errant polychaetes of the family Nereididae can be found in a wide range of sub- and intertidal habitats. They can burrow, crawl and swim. The latter two behaviours are primarily achieved by the use of parapodia and their attached setae. Here we compare the parapodia and setae of five species of atoke nereidids living in either soft or hard substrate in a scanning electron microscopy (SEM) study. Three types of setae, found in all the worms examined, were consistently different across species, allowing us to compare setal distribution. However, neither distribution nor number of setae, or intersetal gap, showed a clear dependence on substrate. Thus it appears that the morphology is not adapted to a specific substrate. This might be because both the parapodia and the setae serve multiple functions in the living animal. Location of the parapodium and the size of the intersetal gap showed some dependence on whether the atoke stage swims. However, neither the area of the parapodium nor of the setal bundles seems to relate to swimming. Phylogenetic relationships amongst the examined species, from three genera all in the subfamily Nereidinae, did not significantly influence either of the morphological parameters investigated. This study indicates that the morphology of the parapodia and setae of nereidids is not adapted to any specific function, instead they are presumably important for a variety of tasks performed by the worms.

KEYWORDS: functional morphology, locomotion, setae, Nereididae, Polychaeta

3.1 Introduction

Despite the common use of parapodial and setal morphology to classify and identify nereidids (Chambers and Garwood 1992; Fitzhugh 1987), very few studies have attempted to link morphology to function (Dorgan *et al.* 2005; Merz and Edwards 1998). We investigated if the detailed morphology of the parapodia and the setae could be correlated to habitat and locomotory behaviour.

Nereidid polychaetes are active marine worms which can burrow, crawl and swim (Trevor 1977; Clark and Tritton 1970; Gray 1939), although they spend most of the time inactive in their burrows (Evans *et al.*, 1974). On each segment nereidids bear a

pair of appendages – the parapodia. The parapodium is biramous with a notopodium (dorsal) and a neuropodium (ventral), except for the uniramous 1st and 2nd parapodia (Chambers and Garwood 1992). Each part has an internal semi-rigid chitinous structure, the aciculum, and an external sensory organ, the cirrus (Smith 1957). In the notopodium the setae originate in a single bundle above the aciculum, whereas two bundles, one above and one below the aciculum, are found in the neuropodium (Chambers and Garwood 1992). Several muscles run from the body segment to the parapodium, which move it backwards and forwards. Other muscles from the body segment attach to the acicula, where they retract part of the parapodium into the body (Mettam 1967). These muscles move the parapodium in a leg-like mode during crawling and in a paddle-like mode during swimming (Gray 1939). The morphology and size of the parapodium vary along the length of the body (Chambers and Garwood 1992).

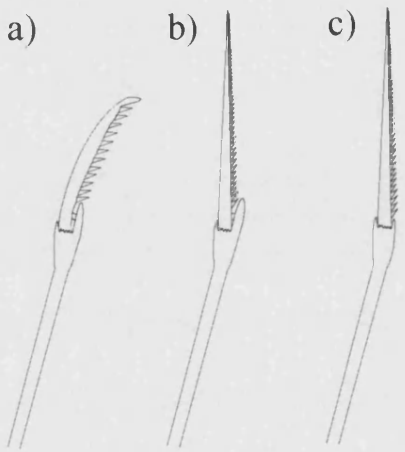

Fig. 3.1. Schematic drawing of the three seta-types found in this study. a) The heterogomph falciger. b) The heterogomph spiniger. c) The homogomph spiniger.

Six types of seta can be found in nereidids (Chambers and Garwood 1992) of which three were found in this study (Fig. 3.1). All of them were compound setae, which have a shaft and blade coupled together in a joint cup (Fig. 3.2). The blade is held in place by a boss and the attachment to the joint cup via a ligament allows the blade to move independently of the shaft, but restricts the degrees of freedom. There are no muscles or nerve cells in the seta, so all movement is passive (Gustus and Cloney 1973). The three setal types observed in this study were the heterogomph falciger (the boss extends beyond the collar and the blade has a blunt tip); the heterogomph spiniger (the

boss extends beyond the collar and the blade has a long tapering tip); and the homogomph spiniger (the boss is in line with the collar and the blade has a long tapering tip). The setal bundle sacs have retractor and protractor muscles (Mettam 1967). This, together with the serrated blades (Fig. 3.2), suggests that setae can increase the friction between the worm and the substrate during locomotion (Merz and Edwards 1998; Gustus and Cloney 1973; Foxon 1936). If this were so one would expect to see substrate-specific adaptations of distribution and morphology of the setae. The main aim of the current study was to examine whether such adaptations could be found in five species of nereidids found along the coast of Northern Europe. A further aim was to look for evident morphological adaptations to swimming in the parapodium and setae.

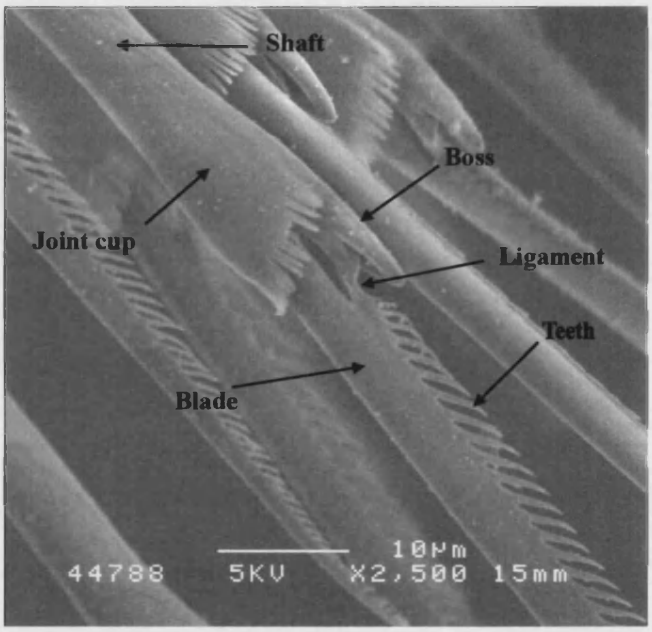

Fig. 3.2. A SEM photo of a heterogomph spiniger in the lower neuropodial bundle of *Neanthes succinea*. Arrows point to the important setal characteristics. The white bar in the lower part of the photo is 10 µm long.

Five species of ragworms in the subfamily Nereidinae (family Nereididae) were used in this study. *Hediste diversicolor* (O. F. Müller, 1776) - formerly known as *Nereis diversicolor* - is found in shallow waters in estuaries, where it lives in a wide range of soft substrates, predominantly in mud but also in sand and gravel (Scaps 2002; Clay 1967). *Neanthes fucata* (Savigny, 1818) - formerly known as *Nereis fucata*- is found in the subtidal zone, where it lives as a commensal on gastropod shells associated with hermit crabs (Goerke 1971b). *Neanthes succinea* (Leuckart, 1847) - formerly known as

Nereis succinea - is found along the shoreline, where it predominantly inhabits hard substrate, under rocks or mussels, but can also be found in sandy mud (Detwiler *et al.* 2002; Banse 1954). *Nereis virens* Sars, 1835 - formerly known as *Neanthes virens* - is found in the intertidal zone, where it lives in soft substrates such as mud and sand (Bass and Brafield 1972). *Platynereis dumerilii* (Audouin and Milne Edwards, 1833) is found in the intertidal and subtidal zones, where it is associated with hard substrates, rocks and algal holdfasts (Chambers and Garwood 1992). Table 3.1 shows the main ecological and behavioural differences between the five species relevant for a morphological analysis of locomotion and figure 3.3 shows the taxonomic relationships. Parapodial and setal morphology are important characteristics for both generic and specific identification (Sato 1999; Chambers and Garwood 1992; Fitzhugh 1987). However, all species examined are closely related and belong to the subfamily of Nereidinae (Fig. 3.3) and, except for *Platynereis dumerilii*, they have at some stage been placed in the genus *Nereis* (Chambers and Garwood 1992).

Table 3.1. Habitat and swimming ability in five species of nereidids

	Preferred substrate	Swimming[1]	References
Hediste diversicolor	Soft	Yes	Scaps 2002, Gray 1939
Neanthes fucata	Hard	No	Goerke 1971a,b
Neanthes succinea	Soft/Hard	No	Banse 1954, Goerke 1971a
Nereis virens	Soft	Yes	Bass and Brafield 1992, Goerke 1971a
Platynereis dumerilii	Hard	Yes	Chambers and Garwood 1992, Pers. Obs.

1) Note: swimming is here defined as showing coordinated body undulations, as described by Clark and Tritton (1970), in the atoke stage. All species that metamorphose into a heteronereis are capable of rapid swimming (Clark 1961).

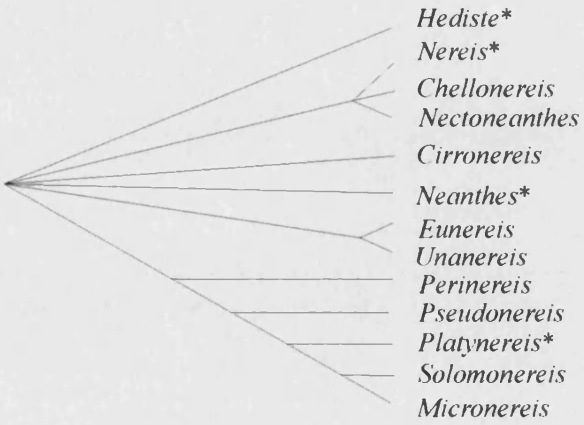

Fig. 3.3. Phylogenetic tree of the genera in the subfamily Nereidinae (Nereidae: Polychaeta). The stars indicate genera used in this study. Simplified after Fitzhugh (1987).

3.2 Materials and methods

3.2.1 Examined species

We used undamaged specimens (except for a few that were missing the pygidium) of a similar size. 6 immature *H. diversicolor* and 7 immature *N. virens* were obtained live from SeaBait Ltd., Northumberland, UK. 7 immature *N. fucata* were obtained fixed in glutaraldehyde from The Biological Institute on Helgoland, Germany. 5 immature *N. succinea* were obtained fixed in glutaraldehyde from Dr. Carsten Müller, University of Cardiff, Wales, UK. 6 immature *P. dumerilii* were obtained live from Dr. Hardege, University of Hull, Humberside, UK. All specimens except *H. diversicolor* and *N. virens* from SeaBait were wild caught. However, the morphology of cultured specimens are unlikely to differ from wild ones, as the worms at SeaBait were cultured in a natural sand habitat with wild sperm occasionally added (P. Olive *Pers. comm.*).

3.2.2 Scanning electron microscopy

Living worms were anaesthetized in 7.5% magnesium chloride and their length was measured and the number of segments counted before they were killed in 2% glutaraldehyde. Several days later the 15th segment and the 16th-18th segments of the worms were dissected. The 15th segment was selected as representative in this study, because it occurs in the largest region of the body (Chambers and Garwood 1992), which is therefore arguably the most important region for locomotion. However, since the SEM mounting restricted the view of the parapodium, it was not possible to obtain all the morphological data from segment 15. Segment 17 was used to obtain data from a different view. The dissected specimens were rinsed with a PBS-buffer and placed in 1% osmium tetroxide before water was extracted in an acetone gradient (20% → 50% → 60% → 70% → 80% → 90% → 95% → 100%). The specimens were then dried in a critical point drier and mounted. Single segments provided a frontal view of the parapodium (Fig. 3.4b). The 3-segments specimens were mounted to give a ventral view (Fig. 3.4a). The specimens were then covered with a thin layer of gold by a sputter coater (Edwards S150B Gold Sputter Coater) and examined in a scanning electron microscope (JEOL JSM6310). Care was taken through out the whole process to avoid shrinkage or deformation of the original samples. However, some shrinkage especially during the drying out phase was un-avoidable. The values of the measurements

described below might therefore be a slight under estimate of the real values. But since all specimens were in the same size range and treated exactly the same, this should not influence the result of the comparative study conducted here.

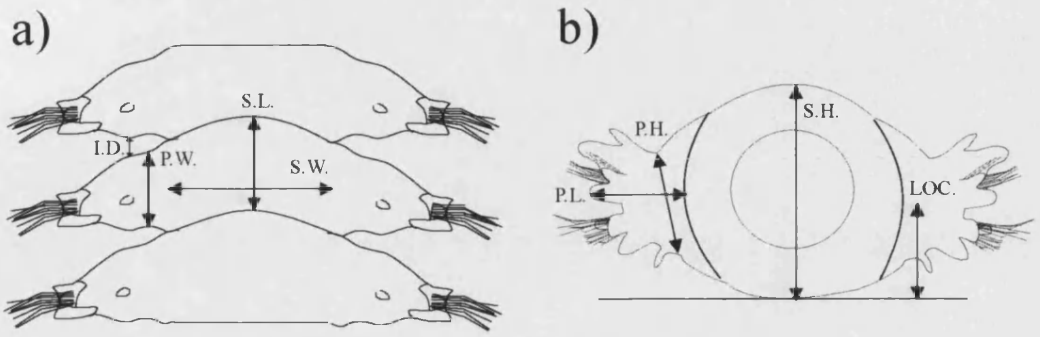

Fig. 3.4. Schematic drawing of the 16-18th segment seen from above (a), and the 15th segment viewed from the front (b). The abbreviations used are: I.D. (interparapodial distance), LOC. (parapodial location), P.H. (parapodial height), P.L. (parapodial length), P.W. (parapodial width), S.H. (segment height), S.L. (segment length), S.W. (segment width).

3.2.3 Morphological parameters

Digital SEM images were analysed with ImageJ 1.29x (NIH, USA). Measurements were only performed on features that were viewed directly or almost directly from above in order to minimise any apparent distortion. Note that where not specifically mentioned the measurements came from segment 15.

Segment length: The length of segment 17 measured from below as the distance between the segment's most posterior and anterior part (Fig. 3.4a).

Segment width: The width of segment 17 was measured from below as the distance from the left side parapodial base to the right side (Fig. 3.4a).

Segment height: The height of the segment measured from a frontal view. (Fig. 3.4b).

Parapodial length: The distance from the base of the parapodium to the distal end (Fig. 3.4b).

Parapodial height: The distance from the trough behind the neuropodial cirrus to the trough behind the notopodial cirrus (Fig. 3.4b).

Parapodial width: The distance from the anterior to the posterior end of the parapodium on segment 17 as seen from below (Fig. 3.4a).

Interparapodial distance: The distance between neighbouring parapodia measured as an average of the distance from the 16th to the 17th and from the 17th to the 18th parapodia (Fig. 3.4a).

Total number of setae: The total number of setae from all three setal bundles on the parapodium.

Setal bundle area: The area of the specified setal bundle as a proportion of the total area of the parapodium and all three setal bundles.

Intersetal gap (*G*): The spacing between individual seta in the bundle (*S*), at the height of the seta-joints, divided by the setal diameter (*d*), derived from the following equation.

$$G = S/d = (w - N_{het-fal}d_{het-fal} - N_{het-spin}d_{het-spin} - N_{\text{hom}-spin}d_{\text{hom}-spin})/(N-1)\bar{d}$$

where w is width of the setal bundle at the same average distance from the base as the setal joints. $N_{\text{het-fal}}$ is the number of heterogomph falciger setae in the bundle and $d_{\text{het-fal}}$ is the average shaft diameter (see below) of all heterogomph falcigers for the particular species (data from Table 3.4). $N_{\text{het-spin}}$, $d_{\text{het-spin}}$ and $N_{\text{hom-spin}}$, $d_{\text{hom-spin}}$ are the same for the heterogomph and homogomph spinigers, respectively. N is the total number of setae in the bundle and $\bar{d}$ is the weighted average shaft diameter of the bundle. Note that the setae were not always placed in rows; sometimes the setal spacing was negative. In these cases the intersetal gap was set to zero.

Parapodial area: This is the frontal area of both parapodia as a proportion of the total cross-sectional area of the body including both parapodia. It was assumed that the right and left parapodia had equal areas, so only one parapodium was measured. Only segments not disfigured or excessively wrinkled had their cross-sectional area measured.

Parapodial location: This is the height of the midpoint of the parapodium above the base line of the segment, measured as a proportion of segment height (Fig. 3.4b).

Shaft diameter: A maximum of five setae were randomly selected from each setal bundle and measured. The diameter of the shaft was measured just below the beginning of the joint cup (see Fig. 3.2)

Blade length: All setae with an unobstructed view of the entire blade were measured.

Teeth density: A maximum of five setae were randomly selected from each setal bundle and the number of teeth per distance length of the blade was measured. The 10 teeth from number 6 to 15 counting from the setal joint were divided by the distance between them. Where fewer than 10 teeth were visible and in the heterogomph falcigers

of *Platynereis dumerilii*, which did not have 15 teeth on the blade, fewer than 10, but never fewer than 6 teeth, were used.

3.2.4 Statistics

The relative parapodial parameters (parapodial area and parapodial location) were compared across species with a one-way ANOVA. If the assumption of equal variances was violated, a logarithmic transformation of the data was performed to obtain normality and equal variances. A two-way ANOVA was used for comparisons of relative setal bundle area and intersetal gap with location of setal bundle and species as fixed factors. The data was transformed logarithmically before testing in order to achieve normality and equal variances. For the comparison of the setal parameters (shaft diameter, blade length and tooth density) a preliminary correlation analysis (Pearson) between segment height and the setal parameters for all species combined gave a significant result (9 tests, R^2 and P values are not given). This suggests that size of the worm, and thus the individual, had an effect on the setal parameters. In order to test and control for this a two-way ANOVA with setal type and individual as fixed factors were used to analyse the setal parameters. Logarithmic transformations of the setal parameters yielded an approach to normality and equal variances.

Since several tests were performed on the same datasets, a sequential Bonferroni adjustment was made to minimise type I errors (Rice, 1989). Two separate Bonferroni adjustments were made, one for the parapodial and setal bundle parameters (data in Table 3.3 and Fig. 3.6) and one for the setal parameters (data in Table 3.4). In the Bonferroni adjusted tests the actual significance level is written after the P-value, except in Table 3.4. The initial significance level was set at 5%. All statistical tests were performed using SPSS 12.0 (SPSS Inc. 2003).

3.3 Results

The parapodia of the five species were biramous, with two aciculae dividing the parapodium into notopodium and neuropodium. They had four ligules on the parapodium and a cirrus on both the neuro- and the notopodium (Fig. 3.5). All parapodia, with the possible exception of *N. succinea*, were asymmetrical with the notopodium slightly larger than the neuropodium (Fig. 3.5). The parapodia of *N.*

succinea (Fig. 3.5c) were more slender than those of the other four species and the cirri of *H. diversicolor* (Fig. 3.5a) and *N. virens* (Fig. 3.5d) were shorter than the cirri of the other three species.

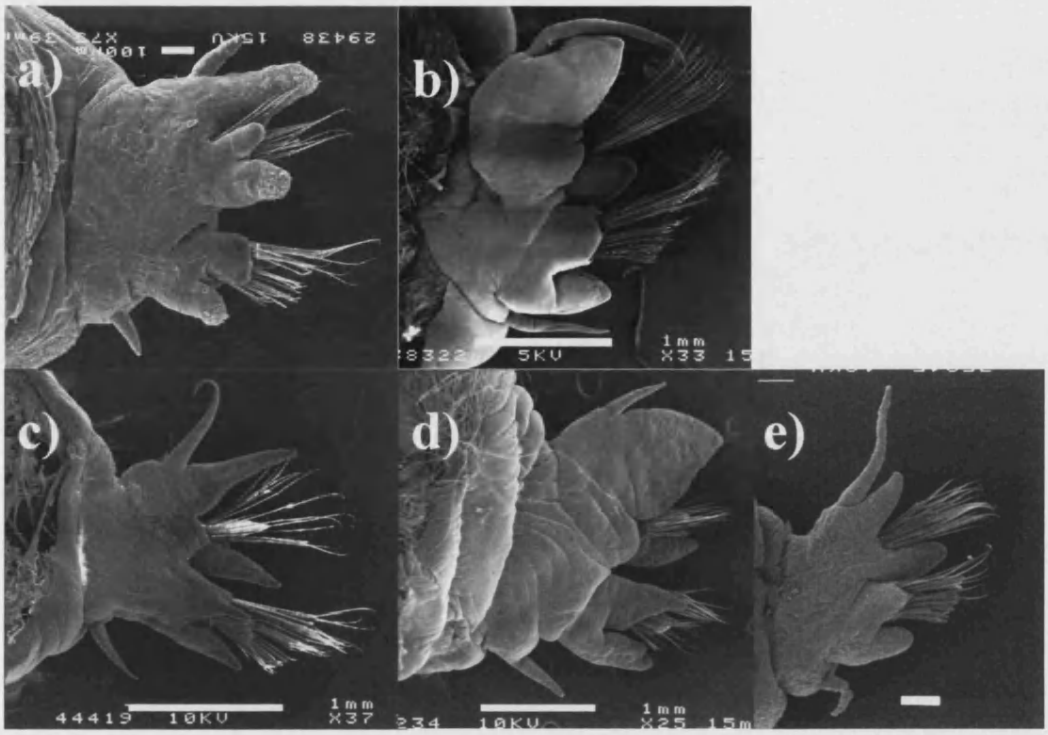

Fig. 3.5. SEM photos of the parapodium on the 15th body segment; the neuropodium is in the lower part of the photo and the notopodium in the upper. a) *Hediste diversicolor*. scale 100 µm. b) *Neanthes fucata*. scale 1 mm. c) *Neanthes succinea*. scale is 1 mm. d) *Nereis virens*. scale 1 mm. e) *Platynereis dumerilii*. scale 100 µm.

Table 3.2. Size parameters

	H. diversicolor	*N. fucata*	*N. succinea*	*N. virens*	*P. dumerilii*
Body length	(6) 50.7 ± 9.3	(4) 66.0 ± 12.5	(5) 37.3 ± 11.1	(7) 149.5 ± 17.9	(6) 32.3 ± 4.9
Number of segments	(6) 69.7 ± 5.3	(4) 108.3 ± 3.8	(5) 91.6 ± 13.1	(7) 106.3 ± 11.1	(6) 86.3 ± 10.7
Segment length	(6) 0.66 ± 0.13	(7) 0.60 ± 0.20	(5) 0.49 ± 0.13	(7) 1.30 ± 0.18	(6) 0.37 ± 0.07
Segment width	(6) 1.73 ± 0.29	(7) 3.68 ± 0.95	(5) 2.16 ± 0.50	(7) 3.95 ± 0.47	(6) 1.06 ± 0.16
Segment height	(6) 1.75 ± 0.35	(5) 3.10 ± 0.72	(5) 2.00 ± 0.56	(7) 4.06 ± 0.33	(6) 0.96 ± 0.17
Parapodial length	(6) 0.76 ± 0.11	(7) 1.70 ± 0.35	(5) 1.08 ± 0.28	(7) 1.79 ± 0.15	(6) 0.49 ± 0.10
Parapodial width	(6) 0.54 ± 0.10	(7) 0.53 ± 0.17	(5) 0.32 ± 0.09	(7) 0.69 ± 0.10	(6) 0.21 ± 0.03
Parapodial height	(6) 0.75 ± 0.12	(7) 1.23 ± 0.29	(5) 0.77 ± 0.20	(7) 1.81 ± 0.13	(6) 0.37 ± 0.06
Interparapodial distance	(6) 0.18 ± 0.05	(5) 0.13 ± 0.08	(5) 0.19 ± 0.05	(7) 0.46 ± 0.14	(7) 0.18 ± 0.09
Number of setae	(6) 39.8 ± 6.1	(7) 63.7 ± 17.8	(5) 58.2 ± 17.9	(7) 89.6 ± 2.9	(6) 37.7 ± 6.1

Values are given as: (sample size) mean ± standard deviation.

All measurements are in mm.

The general size and other parameters for the five species examined in this study are given in Table 3.2. Ideally the five species used here should have been of similar size. However, it was considered more important that all species had roughly the same maturity level (large juveniles). The species can be grouped into large species (*N. fucata* and *N. virens*) and small species (*H. diversicolor*, *N. succinea* and *P. dumerilii*). *P. dumerilii* was considerably smaller than the other two species in the "small" group (Table 3.2). *H. diversicolor* had fewer segments and, together with *P. dumerilii*, fewer setae on the parapodium. The distance between neighbouring parapodia was more than twice as large in *N. virens* as in the other four species.

Table 3.3. Parapodial parameters

	H. diversicolor	*N. fucata*	*N. succinea*	*N. virens*	*P. dumerilii*
Parapodial area	(6) 0.31 ± 0.03	(5) 0.32 ± 0.05	(5) 0.41 ± 0.06	(7) 0.35 ± 0.03	(5) 0.39 ± 0.11
Parapodial Location	(6) 0.48 ± 0.04	(5) 0.38 ± 0.04	(5) 0.38 ± 0.06	(7) 0.41 ± 0.03	(6) 0.44 ± 0.05

Values are given as: (sample size) mean ± standard deviation.

Parapodial area is given as a proportion of cross-sectional area and location of the parapodium as a proportion of segment height.

Table 3.3 gives the area of the parapodium and the location of the parapodium (see Fig. 3.4b) relative to the size of the worm. There was no significant difference between the relative areas of the parapodia across the five species (one-way ANOVA: $F_{(4,23)} = 2.86$, $P = 0.05 > 0.017$). However, there was a significant difference between the relative location of the parapodium (one-way ANOVA: $F_{(4,24)} = 5.41$, $P = 0.003 < 0.013$). A *post hoc* Tukey HSD test revealed that *H. diversicolor* had the parapodium placed significantly higher than *N. fucata* and *N. succinea*.

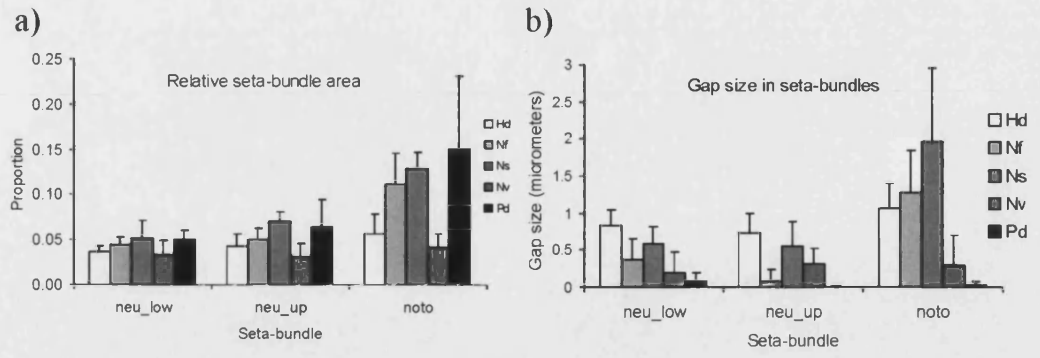

Fig. 3.6. Relative setal bundle characteristics of the three setal bundles for all species. Neu-low is the lower neuropodial seta-bundle, neu-up is the upper neuropodial setal bundle and noto is the notopodial setal bundle. a) The relative setal bundle area as a proportion of total parapodial area. Sample sizes ranged from n = 5 to n = 7. b) The gap-size between setae in the setal bundles. Sample sizes ranged from n = 5 to n = 7. The white column represents *Hediste diversicolor* (Hd), the light grey column represents *Neanthes fucata* (Nf), the grey column represents *Neanthes succinea* (Ns), the dark grey column represents *Nereis virens* (Nv) and the black column represents *Platynereis dumerilii* (Pd). The error bars show the standard deviation.

The relative setal bundle area of the notopodial bundle was larger than each of the two neuropodial bundle areas (Fig. 3.6a). This was because the gap between neighbouring setae in the bundle was larger in the notopodial bundle than in the two neuropodial bundles (Fig. 3.6b). Both the location of the setal bundle (two-way ANOVA, $F_{(2,69)} = 32.76$, $P = 10^{-10} < 0.007$) and the species ($F_{(4,69)} = 20.87$, $P = 10^{-11} < 0.006$) were significant, whereas the interaction between them was not ($F_{(8,69)} = 1.79$, $P = 0.093$). A *post hoc* Tukey HSD test revealed that the notopodial setal bundle was significantly larger than the lower and upper neuropodial bundles. *H. diversicolor* and *N. virens* had significantly smaller relative setal bundles than the other three species. Intersetal gap varied with the location of the setal bundle (two-way ANOVA, $F_{(2,50)} = 10.53$, $P = 10^{-4} < 0.01$) and the species (two-way ANOVA, $F_{(4,50)} = 18.58$, $P = 10^{-9} < 0.008$), although the interaction between species and location was not significant (two-way ANOVA, $F_{(8,50)} = 1.75$, $P = 0.11$). A *post hoc* Tukey HSD test showed that the notopodial setal bundles had a significantly larger gap than the two neuropodial setal bundles. It also showed that the species can be divided into 3 distinct groups, with *P. dumerilii* as the species with the smallest gap, then follows *N. virens* and lastly the group with the largest gap; *N. succinea* and *H. diversicolor*. *N. fucata* had a gap that was not significantly different from either of the other two groups.

The distribution of the three kinds of setae across the setal bundles was similar for the three smaller species – *H. diversicolor*, *N. succinea* and *P. dumerilii* - which all had a 70%-80% to 20%-30% distribution of heterogomph falcigers to heterogomph spinigers in the lower neuropodial setal bundle and a similar distribution of homogomph spinigers to heterogomph falcigers in the upper neuropodial setal bundle (Fig. 3.7a, c, e). Only homogomph spinigers were found in the notopodial setal bundle (Fig. 3.7). The larger *N. fucata* had a slightly different distribution with a 95% to 5% of heterogomph falcigers to heterogomph spinigers in the lower neuropodial setal bundle (Fig. 3.7b). However, the large *N. virens* had the opposite distribution of the other four species in the lower neuropodial setal bundle with a 10% to 90% of heterogomph falcigers to heterogomph spinigers (Fig. 3.7d). There was also a difference in the upper neuropodial setal bundle where *N. virens* had a 5% to 95% distribution of heterogomph falcigers to homogomph spinigers.

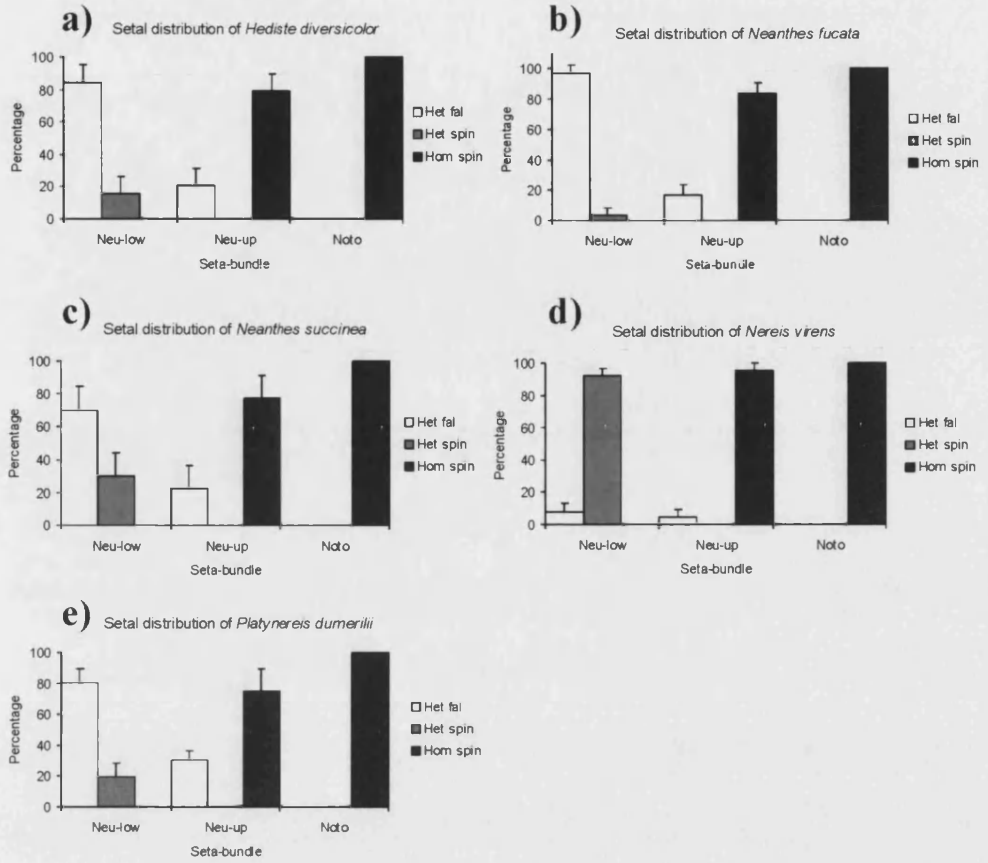

Fig. 3.7. The setal distribution of the three types of setae in the three setal bundles. The distribution is measured as percentage of a given setal type in the bundle. a) *Hediste diversicolor* (n = 6). b) *Neanthes fucata* (n = 7). c) *Neanthes succinea* (n = 5). d) *Nereis virens* (n = 7). e) *Platynereis dumerilii* (n = 6). The white columns represent the heterogomph falcigers (Het fal), the grey columns represent the heterogomph spinigers (Het spin) and the black columns represent the homogomph spinigers (Hom spin). The error bars indicate the standard deviation.

The setal parameters for each setal type and for each species are shown in Table 3.4. A two-way ANOVA showed that none of the interactions was significant and the individual worms showed an effect for blade length in *N. succinea* only. There was a significant difference in shaft diameter between the three setal types in *N. fucata*, *N. virens* and *P. dumerilii* (Table 3.4). The heterogomph falciger had the largest diameter and the homogomph spiniger the smallest, with the heterogomph spiniger in between. However, in *N. virens* the heterogomph spiniger had the largest diameter, but that was probably due to a very small sample size for the heterogomph falciger (Table 3.4). The heterogomph falciger had the shortest blade, the homogomph spiniger the longest and the heterogomph spiniger was in between. For teeth density all the species again

showed a significant difference between the setal types. The heterogomph falciger had the highest teeth density (effectively it had more slender teeth that were closer together) compared to the other two setal types (Table 3.4). However, *N. virens* showed the opposite pattern with the heterogomph falciger having a significant lower teeth density than the other two setal types. But this might be ascribed to a very small sample size of heterogomph falcigers in this species.

Table 3.4. Setal parameters

	Het-fal[1]	Het-spin[2]	Hom-spin[3]	Statistics[4]	P-value[5]	Individual[6]	Interaction[7]
H. diversicolor							
Shaft diameter (µm)	(26) 6.2 ± 1.1	(4) 6.2 ± 0.8	(48) 5.7 ± 0.7	$F_{(2,63)} = 2.0$	0.15	no	no
Blade length (µm)	(38) 34 ± 7	(8) 143 ± 19	(56) 198 ± 30	$F_{(2,86)} = 1207$	10^{-63} (*)	no	no
Teeth density (μm^{-1})	(19) 0.9 ± 0.1	(1) 0.7	(40) 0.5 ± 0.1	$F_{(2,47)} = 94$	10^{-17} (*)	no	no
N. fucata							
Shaft diameter (µm)	(24) 12.7 ± 1.6		(51) 9.7 ± 2.0	$F_{(1,61)} = 48$	10^{-9} (*)	no	no
Blade length (µm)	(70) 62 ± 9	(3) 119 ± 22	(102) 236 ± 36	$F_{(2,158)} = 2043$	10^{-113} (*)	no	no
Teeth density (μm^{-1})	(32) 0.8 ± 0.1		(54) 0.7 ± 0.1	$F_{(1,72)} = 26$	10^{-6} (*)	no	no
N. succinea							
Shaft diameter (µm)	(16) 7.2 ± 1.3	(7) 7.1 ± 0.9	(24) 7.6 ± 1.6	$F_{(2,34)} = 0.3$	0.75	no	no
Blade length (µm)	(45) 54 ± 10	(13) 154 ± 49	(76) 251 ± 80	$F_{(2,120)} = 349$	10^{-50} (*)	yes	no
Teeth density (μm^{-1})	(20) 0.6 ± 0.1	(7) 0.6 ± 0.1	(25) 0.5 ± 0.1	$F_{(2,38)} = 11.8$	10^{-4} (*)	no	no
N. virens							
Shaft diameter (µm)	(2) 8.9 ± 1.6	(24) 9.6 ± 0.9	(49) 8.0 ± 0.6	$F_{(2,60)} = 30$	10^{-9} (*)	no	no
Blade length (µm)	(9) 115 ± 35	(43) 329 ± 73	(85) 372 ± 69	$F_{(2,119)} = 124$	10^{-29} (*)	no	no
Teeth density (μm^{-1})	(6) 0.5 ± 0.1	(23) 0.6 ± 0.1	(48) 0.6 ± 0.1	$F_{(2,60)} = 8.2$	0.0007 (*)	no	no
P. dumerilii							
Shaft diameter (µm)	(12) 8.1 ± 1.2	(4) 5.5 ± 0.6	(29) 6.2 ± 0.8	$F_{(2,30)} = 19.9$	10^{-6} (*)	no	no
Blade length (µm)	(52) 23 ± 4	(9) 132 ± 13	(58) 178 ± 28	$F_{(2,101)} = 2481$	10^{-86} (*)	no	no
Teeth density (μm^{-1})	(21) 1.3 ± 0.3	(6) 0.7 ± 0.1	(37) 0.6 ± 0.1	$F_{(2,46)} = 115$	10^{-18} (*)	no	no

1) (n) mean ± std. dev. of the heterogomph falcigers.
2) (n) mean ± std. dev. of the heterogomph spinigers.
3) (n) mean ± std. dev. of the homogomph spinigers.
4) F-statistics for the fixed factor setal type in the two-way ANOVA.
5) P value for the fixed factor setal type in the two-way ANOVA.
6) Indicating if the P-value is significant for the fixed factor individual in the two-way ANOVA.
7) Indicating if the interaction between setal type and individual is significant in the two-way ANOVA.

Note that all P-values, including the ones for the individual and the interaction were tested against a Bonferroni adjusted significance level.

3.4 Discussion

There is an inherent danger of relating morphology to function or ecology, when in fact it might relate to traits shared by a common ancestor. Therefore knowledge of

taxonomy is important for making considered conclusions. However, in many groups of invertebrates the taxonomy is poorly known (Willmer 1990). This is especially the case for the Annelida, which have unresolved questions at all phylogenetic levels, from classes (Purschke 2002; Westheide *et al.* 1999), through families (Dahlgren *et al.* 2000; Fauchald and Rouse 1997) to genera (Bakken and Wilson 2005, Chambers and Garwood 1992, Fitzhugh 1987). Whatever the true phylogenetic relationships they seem to be of little relevance to the morphological aspects examined here. The species with the most similar setal distribution - *Hediste diversicolor*, *Neanthes succinea*, *Platynereis dumerilii* – belong to different genera (Fig 3.7) and the two species with the smallest intersetal gap– *Nereis virens* and *Platynereis dumerilii* – belong to different genera (Fig. 3.6b). None of the morphological parameters examined here seem to depend on the taxonomy of the species. All investigated morphological parameters, with the exception of setal distribution and intersetal gap, were normalised relative to size so that we could see whether any of the parameters varied with the size of the species. However, with the possible exception of setal distribution (Fig. 3.7), no variation was found. Thus we found no effects of either phylogeny or size in the morphology of the parapodia and setae.

The same three setal types were found in all species examined here, although only very few heterogomph falcigers and spinigers were found in *N. virens* or *N. fucata* respectively (Fig. 3.7b, d). All setal parameters depended on the size of the species but, with the exception of shaft diameter in *N. succinea*, showed no correlation with intra-specific size variation (Table 3.4).

540 species are described in the family Nereididae inhabiting a range of environments from aquatic habitats via coastal waters to the sea floor (Hutchings *et al.* 2000, Chambers and Garwood 1992). Given the important functional role of setae in generating friction between the substrate and the worm during crawling (Merz and Edwards 1998; Gustus and Cloney 1973), morphological adaptation to the habitat of the parapodia and setae was expected. However, such a hypothesis is not supported by our findings. Neither the number of setae (Table 3.2) nor their distribution and type (Fig. 3.7) nor the size of the intersetal gap (Fig. 3.6b) shows any variation with type of substrate. Perhaps setae play no role during locomotion on the substrate. However, observations, both personal and in the literature (Gustus and Cloney 1973; Gray 1939; Foxon 1936) on the movement of the parapodia, as well as experiments with setal ablation (Merz and Edwards 1998) strongly suggest otherwise. Furthermore,

experiments with a physical model employing nereidid-like crawling motion on dry substrate show that setae increase thrust compared to plain parapodia and, on certain substrates, also compared to an added plate of the same area (chapter 4; La Spina *et al.* 2005).

The parapodia and the setae have several other functions. They are used during burrowing (Trevor 1977), and the setae hook the worm to the burrow walls (Woodin and Merz 1987), thus allowing rapid withdrawal (Clark 1960) and making it more difficult for a predator to pull the worm out of its burrow (Woodin and Merz 1987; Knight-Jones and Fordy 1979). During swimming the parapodia generate thrust (Clark and Tritton 1970; Gray 1939). Experimental data from a setal ablation study indicates that setae play a role during swimming (Merz and Edwards 1998). In the swimming species the parapodium is closer to the midpoint of the body (Table 3.3), which presumably increases stability. However, neither the area of the setal bundle (Fig. 3.6a) nor parapodial area (Table 3.3) was significantly larger in species swimming in the atoke stage compared to species not swimming in the atoke stage.

It is possible that the setal bundles act as plates during swimming similar to the second maxillae of copepods, which can act as either paddles or leaky sieves (Koehl 1993). The leakiness of an array of hairs is determined by the Reynolds number, the diameter of the hairs, and the distance between them (Cheer and Koehl 1987). The Reynolds number is defined as $Re = Ud/\nu$, where U is velocity, d is seta diameter and ν is kinematic viscosity. From high speed recordings of the swimming of *H. diversicolor* the parapodial tip speed relative to the water during the power stroke can be estimated as U = 80 mm/s (chapter 6). The seta shaft-diameter for *H. diversicolor* was d = 0.006 mm (Table 3.4) and the kinematic viscosity of sea water is 1.05 mm^2/s. This gives a Re = 0.5. Using figure 2.14 (chapter 2) and the seta gap sizes from figure 3.6b give a leakiness for the seta bundles of a swimming *H. diversicolor* of slightly less than 0.2, where 1 is a sieve with all water passing through the gaps and 0 is a plate with no water passing through the gaps. For all gap sizes given in figure 3.6b the seta bundles will thus function more as paddles than sieves at a Reynolds number of 0.5. However, the gap size values lie on the steep curve of figure 2.14, where slight changes in Reynolds number and gap size could give a significant difference in leakiness. Furthermore, the gap size used in this study is the gap size at approximately the midpoint of the seta-bundle and the setae diverge from their insertion points (Fig. 3.5). They will therefore

not leak at the base but would be more leaky at the distal end of the seta-bundle. Thus gap size is presumably of importance for the added thrust generated by the seta-bundles during swimming. Some support for this hypothesis was found in this study, since two of the species swimming in the atoke stage, *N. virens* and *P. dumerilii*, had significantly smaller distance between the setae in all setal bundles than the species not swimming in the atoke stage (Fig. 3.6b). The gap size of *H. diversicolor*, which also swims in the atoke stage, was, however, not different from the species not swimming in the atoke stage. The seta-bundle area and gap size will also be relevant for slower crawling locomotion. During crawling in semi-liquid muddy substrate the seta-bundles must, based on the above analysis, function as paddles since they will be operating at lower Reynolds numbers due to the higher viscosity medium and lower speed thus having much lower leakiness (Cheer and Koehl 1987).

The parapodia are essentially muscular hydrostats and can be subject to large deformations (Wootton 1999). Both the parapodia and the setal bundles retract during the recovery stroke and protract during the power stroke (Mettam 1967). It is possible that the static area measurements made in this study do not truly represent the dynamic situation in the moving worm. Swimming in juvenile nereidids, however, is rarely observed in nature even in the swimming species. Swimming of atoke worms is limited to migratory (Goerke 1971a) and escape (Thiel and Reise 1993) behaviours, which could be the reason for the small number of morphological adaptations observed. In the epitoke swimming is essential for reproductive success as most species swarm in the open water (Hardege and Bartels-Hardege 1995; Clark 1961). The worm undergoes morphological and anatomical changes from the atoke to the epitoke stage, most notably a change in muscle tissue and in the parapodia (Clark 1961). Special paddle-shaped setae replace the normal setae described in this study (Clark 1961).

The multifunctional nature of the parapodia and setae can partly explain the results given here, since specific morphological adaptations to a single function, such as maximisation of thrust on different substrates or swimming, could have a negative impact on other functions. A further explanation for the lack of adaptation can be that the micro-habitat experienced by the five species does not differ as much as the macro-structure suggests. Hard substrates such as rocks and algal holdfast are interspersed with softer patches. Several of the species in this study can, furthermore, be found in both soft and hard substrate (Scaps 2002; Banse 1954). *N. fucata* lives in the early stage in a burrow in the mud, and waits for a passing hermit crab on whose shell it subsequently

lives (Cram and Evans 1980). Furthermore, the nereidids studied here spend most of their time in their burrows (Evans *et al.* 1974), which are lined with mucus (Defretin 1971). Mucous trails are also left by the worms when crawling especially in muddy substrate (*Pers. obs.*), thus it is possible that the worms experience the same micro-habitat, i.e. a mucous layer, disregarding the actual substrate. Further studies on the interaction between mucus, substrate and setae are necessary as well as dynamic studies on the locomotion in various substrates to resolve whether small morphological or behavioural adaptations to habitat exist in nereidids. But the present study indicates that no obvious morphological adaptations are found in errant polychaetes in the family Nereididae.

Acknowledgement:

We thank Torkild Bakken, Helmut Goerke, Jörg Hardege, Carsten Müller, Peter Olive and John Williams for their advice and comments. Thanks also to two anonymous referees for suggestions to improve the original manuscript. Invaluable technical help was given by Ursula Potter from the Centre for Optical Electron Studies at the University of Bath. This work was supported by the European Commision, in the framework of the BIOLOCH Project (IST FET Programme, IST-2001-34181).

References

Bakken, T. and Wilson, R.S. 2005. Phylogeny of nereidids (Polychaeta, Nereididae) with paragnaths. *Zoologica Scripta.* **34**: 507-534.

Banse, K. 1954. Über Morphologie und Larvalentwicklung von *Nereis* (*Neanthes*) *succinea* (LEUCKART) 1847 (Polychaeta errantia). *Zoologische Jahrbuch Abteilung für Anatomie* **74**: 160-171.

Bass, N. R. and Brafield, A. E. 1972. The life-cycle of the polychaete *Nereis virens*. *Journal of the Marine Biological Association* **52**: 701-726.

Chambers, S. and Garwood, P. 1992. *Polychaetes in Scottish waters. A guide to identification. Part 3 family Nereidae.* National Museums of Scotland, Edinburgh.

Cheer, A. Y. L. and Koehl, M. A. R. 1987. Paddles and rakes: fluid flow through bristled appendages of small organism. *Journal of Theoretical Biology* **129**: 17-

39.

Clark, R. B. 1960. Habituation of the polychaete *Nereis* to sudden stimuli. 2. Biological significance of habituation. *Animal Behaviour* **8**: 92-103.

Clark, R. B. 1961. The origin and formation of heteronereis. *Biological Reviews* **36**: 199-236.

Clark, R. B. and Tritton, D. J. 1970. Swimming mechanisms in nereidiform polychaetes. *Journal of Zoology* **161**: 257-271.

Clay, E. 1967. Literature survey of the common fauna of estuaries. *Imperial Chemical Industries Ltd. Brixham Laboratory* **1**: 1-28.

Cram, A. and Evans, K. E. 1980. Shell entry behaviour in the commensal ragworm *Nereis fucata*. *Marine Behaviour and Physiology* **7**: 57-64.

Dahlgren, T. G., Lundberg, J. Pleijel, F. and Sundberg, P. 2000. Morphological and molecular evidence of the phylogeny of Nereidiform polychaetes (Annelida). *Journal of Zoological Systematics and Evolutionary Research* **38**: 249-253.

Defretin, R. 1971. The tubes of polychaetes. *Comprehensive Biochemistry* **23C**: 713-747.

Detwiler, P. M., Coe, M. F. and Dexter, D. M. 2002. The benthic invertebrates of the Salton Sea: distribution and seasonal dynamics. *Hydrobiologia* **473**: 139-160.

Dorgan, K. M., Jumars, P. A., Johnson, B., Boudreau, B. P. and Landis, E. 2005. Burrow extension by crack propagation. *Nature* 433, 475.

Evans, S. M., Cram, A. and Rogers, F. 1974. Spontaneous activity and responses to stimulation in the polychaete *Nereis diversicolor* (O. F. Müller). *Marine Behaviour and Physiology* **3**: 35-58.

Fauchald, K. and Rouse, G. 1997. Polychaeta systematics: Past and present. *Zoologica Scripta* **26**: 71-138.

Fitzhugh, K. 1987. Phylogenetic relationships within the Nereididae (Polychaeta): implications at the subfamily level. *Bulletin of the Biological Society of Washington* **7**: 174-183.

Foxon, G. E. H. 1936. Observations on the locomotion of some arthropods and annelids. *The Annals and Magazine of Natural History* **18**: 403-419.

Goerke, H. 1971a. Die Ernährungsweise der *Nereis*-arten (Polychaeta, Nereidae) der deutchen küsten. *Veröffentlichungen der Institut für Meeresforschung in Bremerhaven* **13**: 1-50.

Goerke, H. 1971b. *Nereis fucata* (polychaeta, nereidae) als kommensal von *Eupagurus*

bernhardus (Crustacea, Paguriedae). Entwicklung einer population und verhalten der art. *Veröffentlichungen der Institut für Meeresforschung in Bremerhaven* **13**: 79-118.

Gray, J. 1939. Studies in animal locomotion. VII. The kinetics of locomotion of *Nereis diversicolor*. *Journal of Experimental Biology* **16**: 9-17.

Gustus, R. M. and Cloney, R. A. 1973. Ultrastructure of the larval compound setae of the polychaete *Nereis vexillosa* Grube. *Journal of Morphology* **140**: 355-366.

Hardege, J. and Bartels-Hardege, H. 1995. Spawning behaviour and development of *Perinereis nuntia* var. *brevicirrus* (Annalida: Polychaeta). *Invertebrate Biology* **114**: 39-45.

Hutchings, P. A., Wilson, R. S., Glasby, C. J., Paxton, H. and Watson Russell, C. 2000 Appendix 1. In *Polychaetes and Allies: the Southern Synthesis* (Eds. Beesley, P.L., Ross, G. J. B. and Glasby, C. J.). CSIRO Publishing, Melbourne: 242-243.

Knight-Jones, P. and Fordy, M. R. 1979. Setal structure, functions and interrelationships in Spirorbidae (Polychaeta, Sedentaria). *Zoologica Scripta* **8**: 119-138.

Koehl, M. A. R. 1993. Hairy little legs: feeding, smelling and swimming at low Reynolds numbers. *Contemporary Mathematics* **141**: 33-64.

La Spina, G., Hesselberg, T., Williams, J. and Vincent, J.F.V. 2005. A biomimetic approach to robot locomotion in unstructured and slippery environments. *Journal of Bionics Engineering*, **2**: 1-14.

Merz, R. A. and Edwards, D. R. 1998. Jointed setae - their role in locomotion and gait transitions in polychaete worms. *Journal of Experimental Marine Biology and Ecology* **228**: 273-290.

Mettam, C. 1967. Segmental musculature and parapodial movement of *Nereis diversicolor* and *Nephthys hombergi* (Annelida: Polychaeta). *Journal of Zoology* **153**: 245-275.

Purschke, G. 2002. On the ground pattern of Annelida. *Organisms Diversity & Evolution* **2**: 181-196.

Rice, W. R. 1989. Analyzing tables of statistical tests. *Evolution* **43**: 223-225.

Sato, M. 1999. Divergence of reproductive and developmental characteristics in *Hediste* (Polychaeta: Nereididae). *Hydrobiologia* **402**: 129-143.

Scaps, P. 2002. A review of biology, ecology and potential use of the common ragworm *Hediste diversicolor* (O.F. Müller) (Annelida: Polychaeta). *Hydrobiologia* **470**: 203-218.

Smith, J. E. 1957. The nervous anatomy of the body segments of nereid polychaetes. *Philosophical Transactions of the Royal Society of London. Series B.* **350**: 135-196.

Thiel, M. and Reise, K. 1993. Interaction of nemertines and their prey on tidal flats. *Netherlands Journal of Sea Research* **31**: 163-172.

Trevor, J. H. 1977. The burrowing of *Nereis diversicolor* O. F. Müller, together with some observations on *Arenicola marina* (L.) (Annelida: Polychaeta). *Journal of Experimental Marine Biology and Ecology* **30**: 129-145.

Westheide, W., McHugh, D., Purschke, G. and Rouse, G. 1999. Systematization of the Annelida: different approaches. *Hydrobiologia* **402**: 291-307.

Willmer, P. 1990. *Invertebrate relationships - Patterns in animal evolution.* Cambridge University Press. Cambridge.

Woodin, S. A. and Merz, R. A. 1987. Holding on by their hooks: anchors for worms. *Evolution* **41**: 427-432.

Wootton, R. J. 1999. Invertebrate paraxial locomotory appendages: design, deformation and control. *Journal of Experimental Biology* **202**: 3333-3345.

Chapter 4

A biomimetic approach to robot locomotion in unstructured and slippery environments

Published in Journal of Bionics Engineering.

La Spina, G., Hesselberg, T., Williams, J. and Vincent, J. F. V. 2005. A biomimetic approach to robot locomotion in unstructured and slippery environments. *Journal of Bionics Engineering* **2**: 1-14.

4 A biomimetic approach to robot locomotion in unstructured and slippery environments

Giovanni La Spina[1], Thomas Hesselberg[2], John Williams[2], Julian FV Vincent[2]

[1] Scuola Superiore Sant'Anna, Polo Sant'Anna Valdera, CRIM Lab, Viale Rinaldo Piaggio, 34, 56025 - Pontedera (Pisa), Italy; E-mail: giannilaspina@crim.sssup.it.

[2] Centre for Biomimetic and Natural Technologies, Department of Mechanical Engineering, University of Bath, Bath, BA2 7AY.

Abstract: While much attention has been given to bio-robotics in recent years, not much of this has been given to the challenging subject of locomotion in slippery conditions. This study begins to rectify this by proposing a biomimetic approach to generating the friction required to give sufficient propulsive force on a slippery substrate. We took inspiration from a successful biological solution – that of applying hair-like structures to the propulsive appendages, similar to the setae found in nereidid polychaetes living in muddy habitats. We began by examining the morphology and the mean locomotion parameters of one of the most common nereidids: *Nereis diversicolor*. Following this study, we designed and fabricated a robotic system with appendages imitating the biological shape found in the worm. A flexible control system was developed to allow most of the locomotion parameters observed in the real worm to be applied to the robot. Experiments on three different natural substrates ranging from fine sand to gravel showed that, whereas a plate attached to the appendage generated most thrust on a small particle substrate, a bundle of artificial setae attached to the appendage generated most thrust on a large particle substrate. On all types of substrate tested, an appendage without any attachment did significantly worse than one with. This suggests that hair-like structures can be advantageous.

KEYWORDS: bio-robotics, biomimetics, polychaeta, thrust generation, friction.

4.1 Introduction

The field of robotics has in recent years been looking more towards animal locomotion. While the wheel remains the optimal solution for locomotion on flat level surfaces, biologically-inspired robots are being developed for locomotion on more structurally complex terrains. The hexapod design inspired by insects is the most promising one for fast locomotion on rugged terrain (Delcomyn 2004). The cockroach, especially, has been used as a model organism for several biomimetic studies, ranging

from mechanical parameters (Quinn and Ritzmann 1998) via leg sensors and design (Delcomyn and Nelson 2000) to control (Delcomyn 1999).

However, despite the increased attention on bio-robotics, most research has focused on locomotion over firm ground, as described above, or on underwater locomotion (Safak and Adams 2002; Liu *et al.* 2004; Yu *et al.* 2004). Scant attention has been given to locomotion in tortuous and slippery environments, such as muddy terrain, sewage pipes and organic environments. An example of the latter that has substantial biomimetic potential is locomotion inside the human body. Current endoscopic practice consists of pushing relatively stiff structures through the body cavities. This procedure can cause considerable discomfort to the patient. Steps are, therefore, currently being taken to develop self-moving endoscopes both by employing a traditional engineering approach (Lim et al, 2001) and by using a biomimetic approach (Kim *et al.* 2002; Menciassi and Dario 2003). Both approaches, however, suffer from problems with generating enough friction between the device and the mucous-lined tract wall.

In this study we start to address the problem of generating friction in slippery environments by looking at nature for inspiration. One group of animals that successfully navigate in such environments is the ragworms of the polychaete family Nereididae. Throughout this study we focus on the common ragworm *Nereis diversicolor*, which is found in estuaries and shallow coastal waters in the Northern Temperate Zone (Scaps 2002). It is found in habitats ranging from sandy mud, and gravel to clay (Clay 1967), where it can be found at a density of up to several thousand individuals per square meter (Scaps 2002).

What makes this species particularly useful from a biomimetic perspective is the diverse ways in which it can move through the medium. *N. diversicolor* is capable of burrowing through the substrate, crawling over the substrate and swimming in open water. During fast crawling and swimming the body undulates from side to side with each body wave moving from the posterior region to the anterior (Taylor 1952). Lateral appendages – the parapodia – are synchronised with the body waves and aid in thrust generation by acting as paddles during swimming (Clark and Tritton 1970) and legs during crawling (Gray 1939). During slow crawling no or only small amplitude, body waves are present and thrust is generated by the parapodia (Gray 1939).

Protruding distally from each parapodium are three bundles of setae, which are the structures that allow the worm to crawl effectively in slippery substrates (Merz and

Edwards 1998; Foxon 1936). Each seta consists of a shaft and a serrated blade which are jointed and allow movement of the blade relative to the shaft in a limited number of directions (Gustus and Cloney 1973). This movement is entirely passive and presumably allows the seta to interact with the surroundings and maximise friction (Gustus and Cloney 1973). In this study we first looked at the morphological parameters of the parapodium-seta system and the dynamic parameters of the crawling worm. We then used the results obtained to design and test a robotic seta-like appendage, attached to a servomotor imitating the movement of the parapodia, against control appendages over a range of substrates. Our objective was to analyse why setae might be more advantageous than either no setae at all or simply larger parapodia.

4.2 Biological data

4.2.1 Materials and methods

Large juvenile *Nereis diversicolor* (length ~ 50 mm and weight ~ 150 mg) were used in this study. For the scanning electron microscopy (SEM), worms were obtained from SeaBait Ltd., Northumberland, UK, whereas the worm used in the dynamic analysis was collected in the Severn Estuary, South Gloucestershire, UK.

Specimens were prepared for the SEM by placing them in 2% glutaraldehyde for several days. The 15th segment and the 16th-18th segment were then dissected into two pieces. The dissected specimens were rinsed with a PBS-buffer and placed in 1% osmium tetroxide before being dried in a sequence of acetone: water of increasing concentration. The specimens were then completely dried using a critical point drier and mounted. The single segment specimens were mounted to provide a frontal view of the parapodium. The three-segment specimens were mounted on the dorsal side so that a ventral view was possible. The specimens were then covered with a thin layer of gold by a sputter coater (Edwards S150B Gold Sputter Coater). Hereafter the specimens were ready for examination in the scanning electron microscope (JEOL JSM6310).

The following data were extracted from the specimens. The digital images were analysed with ImageJ 1.29x (NIH, USA). Note that all measurements of seta-bundle and setal area come from the lower half of the parapodium, whereas the data on setal morphology come from setae in both the lower and upper halves of the parapodium.

SEM - segment no. 15

Parapodial length: The distance from the base of the parapodium to the distal end.

Parapodial height: The distance from the trough behind the neuropodial cirrus to the trough behind the notopodial cirrus.

Parapodial area: The area of the entire parapodium including the setal bundles.

Bundle area: The area covered by the setae of the lower and upper neuropodial bundles.

Number of setae: The number of setae in the lower and upper neuropodial bundles.

Intersetal distance: The average distance between neighbouring setae in a bundle. Calculated using the following equation:

$$D = (W - Nd)/(N - 1)$$

where W is width of the bundle 100 μm distally from the base. N is the number of setae in the bundle and d is the average diameter of all setae, disregarding setal type, measured in this study (5.9 μm ± 0.9 μm). Note that the setae were not always placed in rows; sometimes the setal distance equation gave a negative value. In these cases the intersetal distance was set to zero.

Seta type: From the images of the joint region of individual seta it was possible to classify the setae into either heterogomph falcigers, heterogomph spinigers or homogomph spinigers.

Shaft length: The visible length of the setal shaft protruding from the parapodium.

Shaft diameter: The diameter of the setal shaft 15 μm below the setal joint.

Blade length: The length of the setal blade.

Blade diameter: The diameter of the setal blade 15 μm above the setal joint.

SEM - segments nos. 16-18

Parapodial width: The distance from the front to the end of the parapodium as seen from below.

Interparapodial distance: The distance between neighbouring parapodia. This measurement is an average of the distance from the 16th to the 17th segment and the distance from the 17th to the 18th segment.

To get information about the kinematics of crawling *N. diversicolor*, a worm was placed in a Petri dish filled with artificial seawater and, while crawling slowly, it was recorded with a digital high speed camera (The *Motion*Scope 2000S, Redlake MASD, Inc.) at 125 frames/sec.

4.2.2 Results

SEM photos at low magnification revealed the overall shape of the parapodium (Fig. 4.1). The parapodia are asymmetrical with the upper part of the parapodium larger than the lower and with many protruding parts (Fig. 4.1a), some of which are sensory organs (Smith 1957). Also conspicuous are the three protruding bundles of setae, one in the upper part and two close together in the lower (treated as a single bundle in the rest of this paper). A ventral view of the parapodium revealed that they are slightly tapering towards the distal end (Fig. 4.1b).

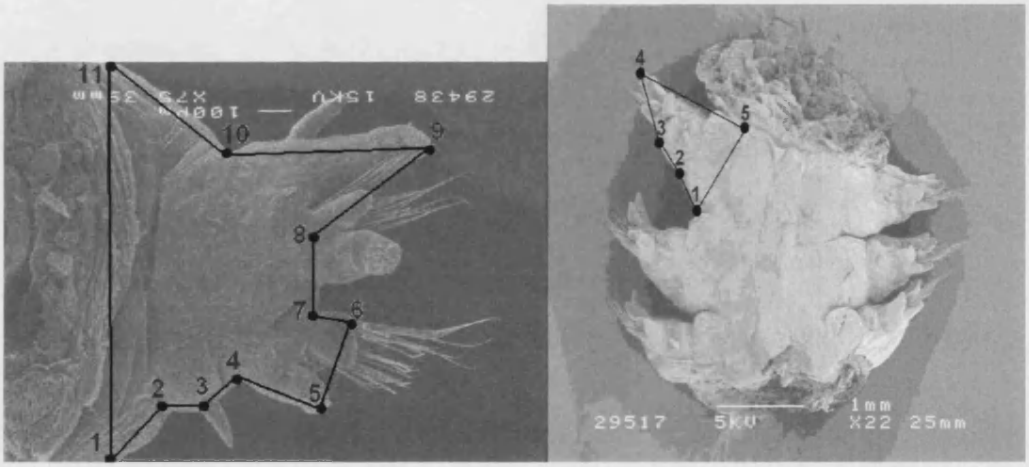

Fig. 4.1. SEM photos of *Nereis diversicolor*. a) Frontal view of one of the parapodia of the 15th segment. The white scale bar in the upper part of the picture is 0.1 mm long. b) Ventral view of segments 16 to 18. The white scale bar in the lower part of the picture is 1.0 mm long. Numbered points and connecting lines define geometry of artificial parapodium (See section 4.3.1).

Measurements on SEM photos of various magnifications were performed (see Table 4.1). These showed that the parapodia are on average as long as they are high, with a width of 0.5 mm and spaced 0.2 mm apart. The lower seta-bundle covers almost 8% of the entire area of the parapodium and consists of 25 setae spaced 2 μm apart. Three different seta-types were found in the two seta-bundles: Heterogomph falcigers, which can be identified by having an asymmetrical collar around the joint between shaft

and blade and a blunt ending of the blade; heterogomph spinigers, which also have an asymmetrical collar, but have a tapering end of the blade; homogomph spinigers, which have a symmetrical collar and a tapering end of the blade. All three types had similar shaft diameters and length as well as similar blade diameters, but the blade lengths were different, shortest for heterogomph falcigers and longest for homogomph spinigers (Table 4.1).

Table 4.1. Morphological data from the parapodium and setae of *Nereis diversicolor*

	Sample Size	**Mean**	**Standard deviation**
Parapodial length (mm)	6	0.76	0.11
Parapodial width (mm)	6	0.54	0.1
Parapodial height (mm)	6	0.75	0.12
Interparapodial distance (mm)	6	0.18	0.1
Parapodial area (mm^2)	6	0.64	0.18
Bundle area (mm^2)	6	0.05	0.01
Number of Setae	6	25.2	2.3
Intersetal distance (μm)	6	1.9	1
Heterogomph falciger			
Shaft length (μm)	32	154.9	46
Shaft diameter (μm)	25	5.9	1.3
Blade length (μm)	32	33.4	7.4
Blade diameter (μm)	26	5.6	1
Heterogomph spiniger			
Shaft length (μm)	7	156.1	32.2
Shaft diameter (μm)	4	6.1	0.7
Blade length (μm)	7	141.6	17.3
Blade diameter (μm)	4	5.4	1
Homogomph spiniger			
Shaft length (μm)	48	139.3	58.1
Shaft diameter (μm)	56	5.9	0.8
Blade length (μm)	48	191.6	36
Blade diameter (μm)	56	5.3	0.6

4.3 Modelling parapodium and setae

4.3.1 Modelling biological shapes

The worm parapodium was replicated using a dimension rapid prototyping machine. The exact form of the parapodium was strictly not important for the experiments conducted but the replication was undertaken as an exercise in producing biological shapes. In common with many biological forms, the parapodium of *N. diversicolor* is extremely complex. In order to obtain an acceptable model of this appendage, it was necessary to simplify its geometry. A Pro/Engineer 2001® part was sketched starting from pictures captured through the scanning electron microscope.

Eleven key points were marked out on the photo of the transverse section of a real worm (Fig. 4.1a). An interpolating spline was traced to get a similar cross-section border. The same method was used to generate a longitudinal profile (Fig 4.1b). The achieved cross-section was extruded along the longitudinal profile. In this way, a three-dimensional shape was obtained with proportions very similar to the natural appendage of the real nereidid. It is important to note, however, that the hydrostatic skeleton of the real worm allows its parapodia to change size and shape during the course of its motion (Wootton 1999). The worm, furthermore, has muscles that enable it to retract the parapodium during the recovery stroke and protract it again for the power stroke (Mettam 1967). Neither of these effects could be captured by the simplified robotic model.

Fabricating an artificial parapodium was the objective of this modelling. Once built, the parapodium had to be inserted into an actuated mechanism, able to replicate the principal nereidid locomotion gaits. Additional features were added to the natural geometry to make such an assembly technically feasible. These supplementary features did not interfere with the substrate, but facilitated interfacing to the servomotor. Figure 4.2 shows the geometry of the artificial parapodium.

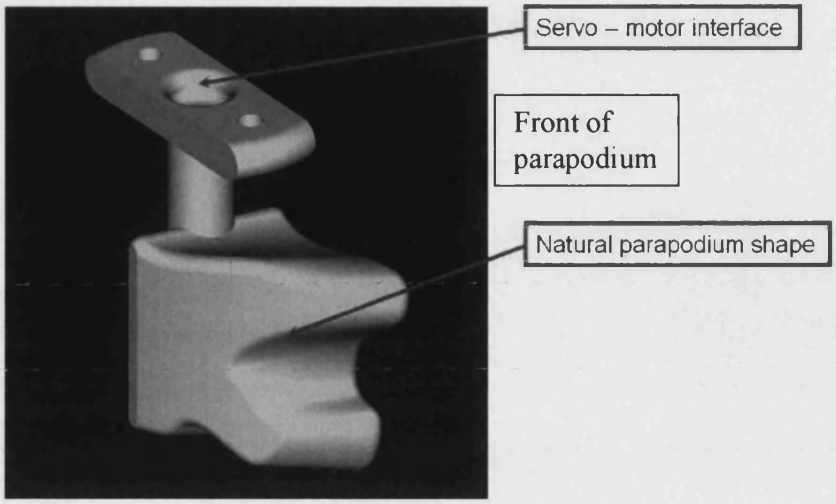

Fig. 4.2. A CAD drawing showing the design of the artificial parapodium and its interface with the servomotor.

One set of parapodia was constructed without setae. A second set of parapodia was fitted with setae modelled using 0.4 mm diameter piano wire. Five lengths of piano wire were glued onto each parapodium to give a setal bundle area somewhat larger, in relative terms, than that of the lower setal bundles of the real worm. The relative setal area was increased so as to amplify any measured differences in the performance of the setal configurations. Unlike the real worm setae, the experimental setae were not jointed. A third set of parapodia was fitted with extension plates, where each plate covered the full area of the sector of the circle over which the piano wire setae had been distributed when constructing the second parapodia set. This area was approximately 22% of the plain parapodium area. The three setal configurations are shown in figure 4.3.

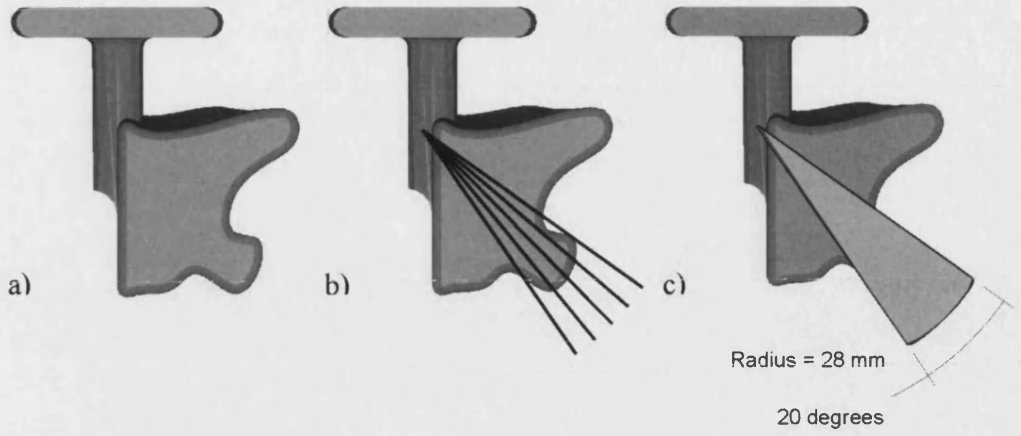

Fig. 4.3. The three setal configurations tested (viewed from rear): a) Plain parapodium; b) Parapodium with 0.4 mm piano wire setae; c) Parapodium with extension plate.

4.3.2 Modelling Polychaeta gaits

From observations of nereidids moving in their natural environment, locomotion gaits were derived. During fast crawling and swimming, the parapodia move with the same frequency of oscillation as the body wave, timed so that the power stroke of each parapodium is coincident with the crest of a passing body wave (Gray 1939). The current work focused on the effectiveness of the parapodia without a body wave. The worm employs this type of locomotion gait during slow crawling. From video recordings of slow crawling worms we found that each parapodium had an angular stroke of approximately 90°, as shown in figure 4.4.

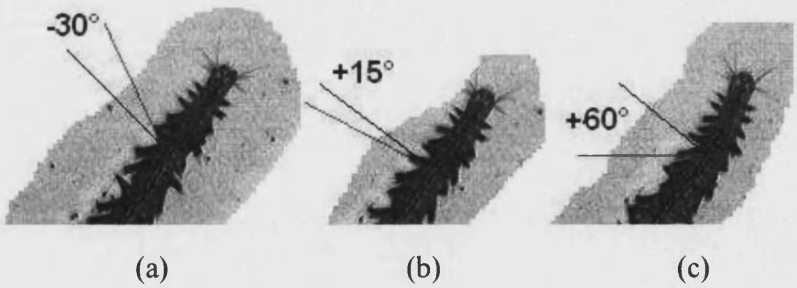

Fig. 4.4. Three snap-shot photos showing the parapodium position relative to the body during slow crawling in *Nereis diversicolor*. a) The beginning of the power stroke; b) the middle of the power stroke; c) the end of the power stroke.

The sixth parapodium on the left was recorded in three positions: the extreme forward position, the intermediate position and then the extreme backward position. By analysing the video recordings of crawling worms, a mean parapodial frequency of 1-1.25 Hz was observed. The rowing-like movement of a parapodium can be divided into two phases: during the first phase the appendage is pushing the nereidid body forward (power stroke) and during the second phase the parapodium returns to its original position (recovery stroke) (Gray 1939).
We found the duration of the power stroke to be approximately twice that of the recovery stroke. An entire cycle of the rowing-like movement lasted approximately 0.8 seconds, with the power stroke lasting approximately 0.5 s and the recovery stroke approximately 0.3 s.

Two main strategies were observed: "step-like" and "row-like" locomotion. "Step-like" locomotion occurred during slow crawling. Successive parapodia oscillate with a phase difference of approximately 25 degrees. The result is an apparent similarity with the walking of bipeds and quadrupeds, with the additional benefit of the body adjusting to the surrounding environment (Weingarten *et al.* 2004). "Row-like" locomotion is instead a synchronised waving of parapodia, just like oars in a boat, and occurs during fast crawling and swimming in water (Clark and Tritton 1970).

4.4 Robotic prototype

4.4.1 Fabrication of components

The robot frame and parapodia were designed using Pro/Engineer 2001® and Solid Edge® Version 14 CAD software and manufactured in ABS plastic on a dimension rapid prototyping machine. The robot frame was designed to accommodate a maximum of eight parapodia (four on each side of the frame), each driven directly by a GWS miniature servomotor. The dimensions of the worm parapodia were increased by a scale factor of 25 to give the dimensions of the robot parapodia. The inter-parapodial spacing with eight parapodia fitted was designed to the same scale and was equal to 18 mm and 47 mm in the axial and transverse directions respectively. Figure 4.5 shows the robot fitted with four parapodia in the corner positions of the frame, giving an axial inter-parapodial spacing of 54 mm.

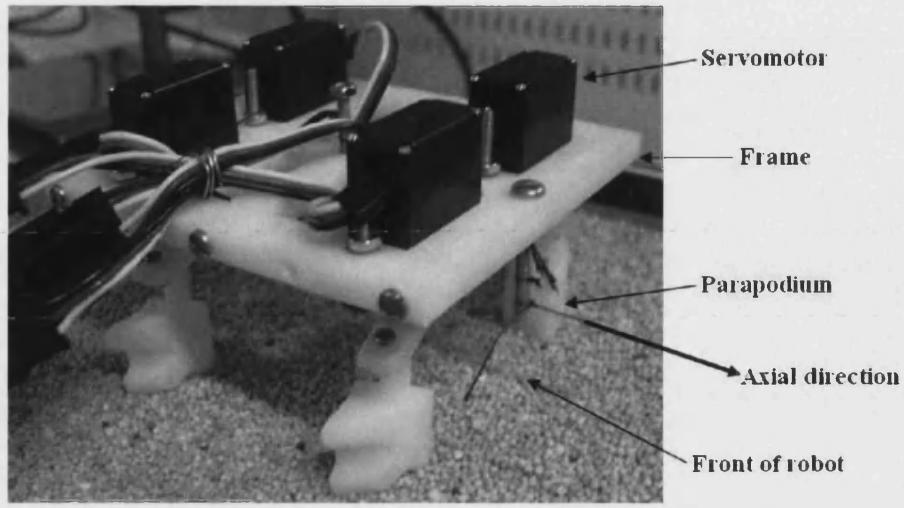

Fig. 4.5. Robot Assembly

4.4.2 Computer interface

The servomotors were controlled by a Pololu 16-servo controller connected to the USB interface of a personal computer. A Visual Basic® interface (test-bench) was written to give maximum control over the locomotion parameters. The implemented gaits emulated the fluctuating movement of real parapodia. The parapodial movement is defined by posterior to anterior metachronal waves (Gray 1939). The parameters that characterise these waves are the frequency, the angular amplitude, the phase difference between neighbouring parapodia and the zero-position about which the parapodia rotate equally in either direction by an amount equal to the angular amplitude. The frequency defines the parapodial sweep speed, which was constrained by the Visual Basic® software to be the same during the power and recovery strokes. Although the parameters that characterise the wave of a real worm parapodium are almost constant, the test-bench software was designed to be able to vary the parameters over a wide range of values, in order (in future work) to extract the best mix of variables able to determine the behaviour of an efficient and environment-adaptive robot.

The main window of the test-bench user interface is shown in figure 4.6. An additional control allows "step-like" or "row-like" locomotion to be introduced immediately with biomimetic parameters. These parameters were determined in section 6.3.2 and consist of frequency = 1 Hz, amplitude = 45° (overall stroke = 90°) and zero-position = -15° (i.e. each parapodium swings about a central position shifted towards the robot's rear by 15° with respect to the normal to the body's axis). The associated phase-

delays are 25° and 0° respectively. Controls allow each of the parameters to be adjusted independently and, in addition, the starting position of one of the front parapodia can be specified, with the other parapodial starting positions then defined by the specified phase difference. After the motion is stopped, the parapodia can be made to return to either their zero positions or their starting positions. Servo offsets can be slightly adjusted in order to correct small assembly errors and eight dynamic scroll-bars visualise the expected movement of the artificial parapodia in real time.

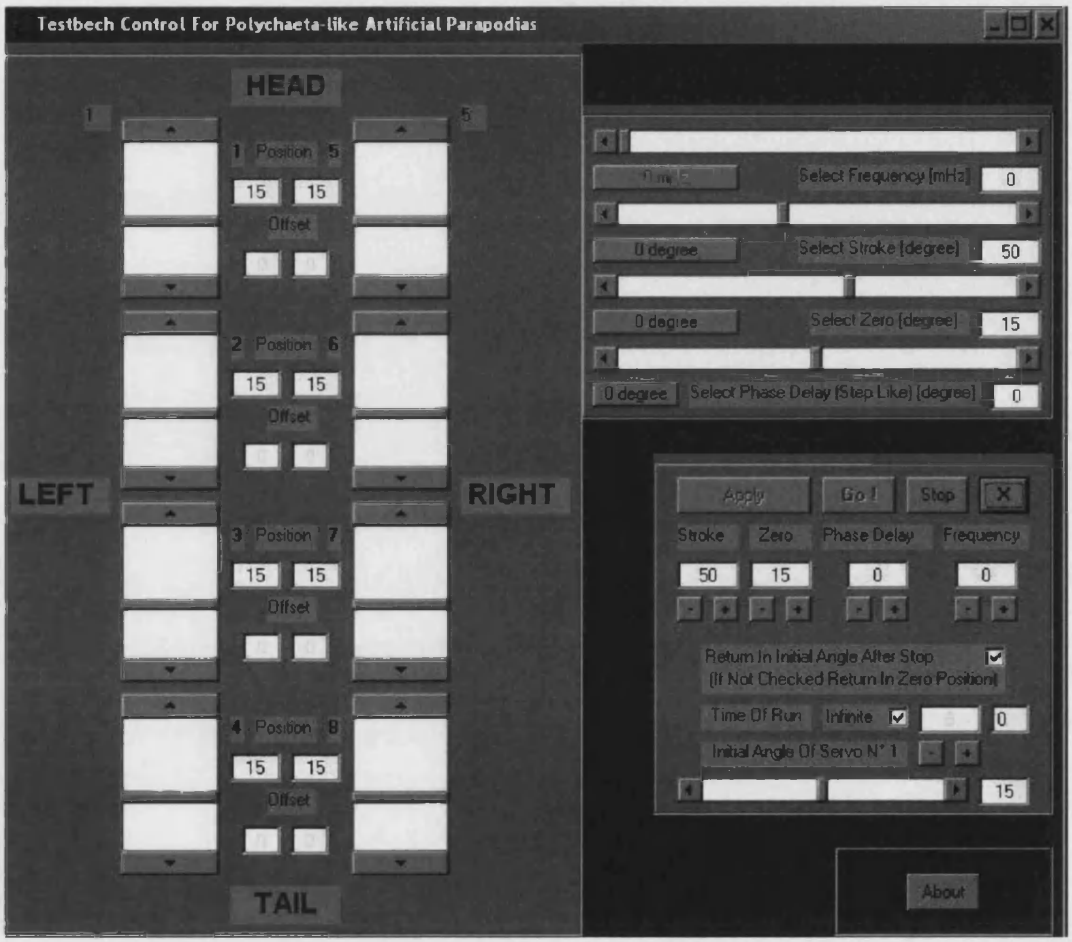

Fig. 4.6. The main window of the test-bench user interface

4.4.3 Measurement system

The horizontal thrust of the robot was measured using a piezoresistive force sensor with a maximum range of zero to 500 g (Honeywell part no. FSL05N2C). The robot was tethered to the end of an arm pivoted about a vertical axis, which also rested in contact with the force sensor (Fig. 4.7). This arrangement gave a variable gain

mechanical amplifier, the gain of which was set by choosing the distance of the force sensor from the pivot of the arm. Since the force sensor operates only in compression and the robot generated thrust in both the forward and backward directions, it was necessary to pre-load the force sensor by attaching the front of the robot to a vertically suspended weight via a thread running over a pulley. Unlike the worm, the robot generated thrust in both directions because the robot parapodia did not lift away from the substrate during the recovery stroke.

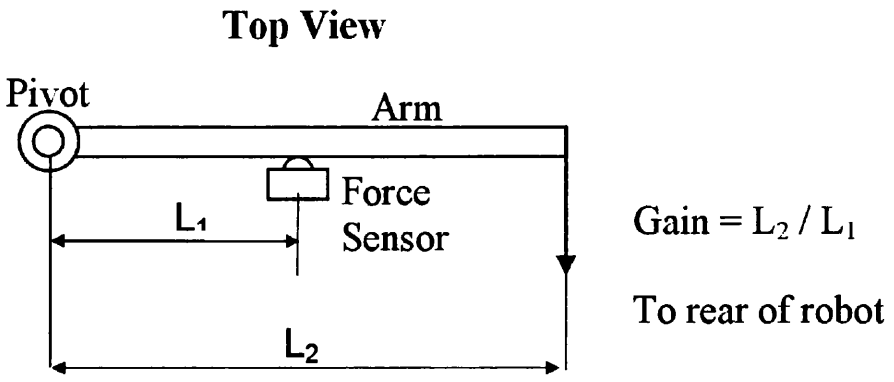

Fig. 4.7. Arrangement for horizontal thrust measurement

The force sensor contains a Wheatstone bridge circuit and was connected to a differential amplifier, the gain of which was adjusted to give a zero to 10 V output over the required thrust range. A data acquisition unit (Measurement Computing part no. PMD1208FS) recorded the amplifier output voltage over a period of 10 seconds at a sampling rate of 1000 samples per second, using LabVIEW® software. A set of weights was used to calibrate the force sensor before and after conducting the experiments. Both linearity and repeatability were found to be good and a mean sensitivity of 42 mV/g was used to convert acquired voltages to thrust in grams.

4.5 Experiments

4.5.1 Materials and methods

In all experiments, the robot was configured with four parapodia (two on each side of the frame, as in figure 4.5) operating in phase (i.e. "row-like" locomotion) at a frequency of approximately 1 Hz. Relative to the parapodial dimensions, the inter-parapodial spacing was therefore larger than that of the worm, since four rather than

eight parapodia were fitted. The angular amplitude of the parapodial motion was 25 degrees either side of a zero position 15 degrees rearward of the normal to the side of the robot body.

The angular amplitude was smaller than that of the real worm parapodia (section 4.3.2). This was to allow comparison with future experiments with eight parapodia fitted to the robot frame, under which conditions the angular amplitude is limited to 25 degrees by mechanical interference between neighbouring parapodia. The power and recovery strokes were of equal duration as stated in section 4.4.2. Prior to an experiment, each parapodium was moved to the position of the start of the power stroke, i.e. 10 degrees forward of the normal to the side of the robot body. To perform an experiment, the robot was then lowered gently onto the required substrate using a vertical suspension thread to minimise the introduction of horizontal frictional forces between the robot and the substrate. These frictional forces had the effect of changing the measured pre-load on the robot imposed by the attached vertically suspended weight. Data acquisition was then started and, after an interval of approximately one second, the robot motion initiated. The robot was stopped after eight seconds and the data acquisition terminated approximately one second thereafter. In this way, data was captured for around seven full cycles of the robot parapodia. Acquiring some data immediately before and after initiating the robot motion allowed the values of the static pre-load on the force sensor to be observed. Each experiment was repeated twenty times under identical conditions.

The two experimental variables investigated were substrate particle diameter and setal configuration. The three substrates used were fine sand with a mean particle diameter of 0.5 mm ± 0.2 mm (sample size = 84, measured from SEM photos), coarse sand with a mean particle diameter of 1.4 mm ± 0.2 mm (sample size = 34, measured from SEM photos) and gravel with a mean particle diameter of 6.2 mm ± 1.6 mm (sample size = 158, measured from digital photos). The three setal configurations consisted of plain parapodium with no setae, parapodium with piano wire setae and parapodium with extension plate, as described in section 4.3.1.

Data analysis concentrated on the first power stroke of the robot motion for two reasons. Firstly, the depth of parapodial penetration into the substrate could not be guaranteed to be consistent between repeated experiments at the start of any power stroke other than the first, since the robot rapidly sank into the substrate during its

motion. This sinking was a result of the absence of a robot body in contact with the substrate and was thus unrepresentative of the worm's behaviour. Secondly, since the robot did not lift its parapodia during the recovery stroke and the inter-parapodial spacing was not to scale and the durations of the power and recovery strokes were equal, the state of the substrate might not have been representative of that encountered by the worm except during the first power stroke of the robot motion. Concentrating on the first power stroke also meant that the shape of the front surface of the parapodium was not critical.

A data analysis program was written in FORTRAN 77 to extract from the acquired data the peak value of thrust during the first power stroke of each experiment and record the time relative to the start of the stroke at which this peak occurred. The mean peak thrust was then calculated for each set of twenty experiments performed under identical conditions. The mean peak thrust was then plotted as a function of substrate particle diameter for each of the three setal configurations.

The thrusts generated for all parapodial configurations and substrates were analysed using a two-way ANOVA with the substrate particle size and parapodial configuration as fixed factors. Data was logarithmically transformed to achieve normality, but equal variances were not achieved. The Tamhane's T2 test, which assumes unequal variances, was therefore employed for *post hoc* comparisons. Similarly statistics were used to compare the time from the beginning of the power stroke until the maximum thrust was reached. Here, substrate and parapodial configuration served as fixed factors. For all tests a significance level of $\alpha = 0.01$ was chosen. Tests were performed with SPSS 12.0 for Windows (SPSS Inc., 2003).

4.5.2 Results

All three parapodial configurations showed a general trend of an increase in thrust with an increase in particle size (Fig. 4.8). Here, the peak thrust during the first power stroke of the parapodial motion has been plotted; similar trends are observed if the mean thrust over the power stroke is plotted instead. Statistically significant effects of both particle size (Two-way ANOVA: $F_{(2,171)} = 145.4$, $P < 0.01$) and parapodial configuration (Two-way ANOVA: $F_{(2,171)} = 147.1$, $P < 0.01$) were found. A significant effect of the interaction between those was also observed (two-way ANOVA: $F_{(4,171)} = 18.8$, $P < 0.01$). From figure 4.8 it can be seen that the setal configuration showed a

steeper increase in thrust with increasing particle size than both the plain – and plate configurations. The setal configuration outperformed the plate configuration at the largest particle size. The *post hoc* Tamhane's T2 test revealed that the plate and setal configurations outperformed the plain configuration across all particle sizes. It also showed that significantly higher thrust was generated in the gravel substrate compared to the two other substrates.

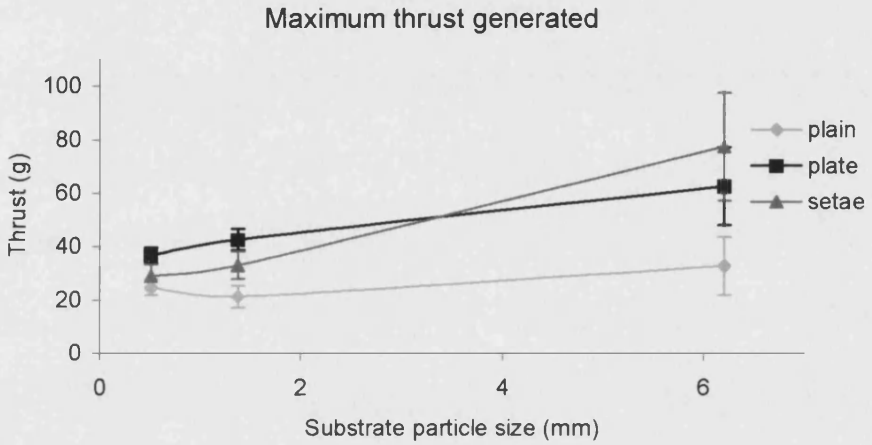

Fig. 4.8. The maximum thrust generated by the worm robot over one power stroke for each parapodium configuration and as a function of substrate particle size. The sample size for each point is n = 20. The 3 particle sizes were 0.5 mm (fine sand), 1.4 mm (coarse sand) and 6.2 mm (gravel). The error bars indicate the standard deviation.

A closer examination of the behaviour of the thrust generated in the three substrates revealed that the maximum thrust generally was generated 200-300 ms into the power stroke (Fig. 4.9). However, the same pattern was observed for all substrates, with the plain configuration reaching the maximum faster than the setal configuration and the plate configuration reaching its maximum later than the other two. A statistical test confirmed that the effect of parapodium configuration was significant (Two-way ANOVA: $F_{(2,171)} = 13.6$, $P < 0.01$), whereas neither the effect of substrate (Two-way ANOVA: $F_{(2,171)} = 4.6$, $P = 0.01$) nor the interaction between the two effects (Two-way ANOVA: $F_{(4,171)} = 2.4$, $P = 0.06$) were significant. The *post hoc* Tamhane's T2 comparison revealed that the only significant difference was found between the plate and the plain configurations. However, both the difference between plain and setal configurations and the difference between fine sand and gravel were close to being significant.

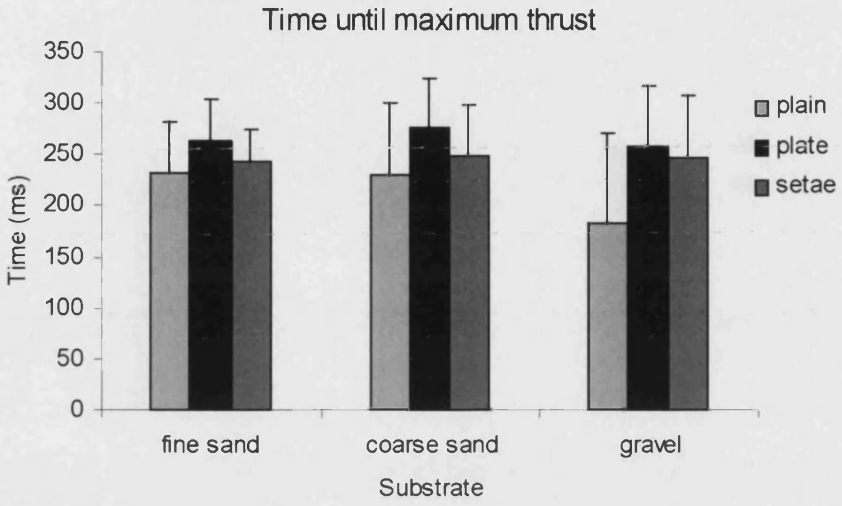

Fig. 4.9. The time from the beginning of the power stroke until the maximum thrust is generated for each parapodial configuration and substrate. Each column represents the mean of 20 samples and the error bars indicate the standard deviation.

4.6 Discussion

Thrust is generated by the appendages pushing against the substrate, both in our robotworm and in the real nereidid worm (Gray 1939; Foxon 1936). It was therefore expected that adding area to the appendage would give increased thrust. This was confirmed by our study showing a significantly lower thrust production in plain parapodia as compared to when an attachment was added (Fig. 4.8). However, more surprising was that the results of the preliminary experiments described in section 4.5 suggest that, as the substrate particle diameter is increased, a point is reached where the robotworm generates more thrust by having setae attached to its parapodia than would be the case were the parapodia simply enlarged to cover the setal area. Dimensional analysis can be used to predict the substrate particle diameter at this crossover point for the worm, based on the experimental data. The crossover particle diameter can then be compared to the particle diameters of the substrates in which the worm operates to see what benefit the setae may have.

When the substrate particle diameter is small compared with the setal diameter, it is suggested that the setae simply slide between the substrate particles thus generating

little thrust. In the limit of infinitesimal substrate particle diameter, setae might be expected to offer no benefit at all, which figure 4.8 appears to suggest. Under these conditions, larger parapodia would still be expected to offer a benefit, which is also suggested by figure 4.8. When the substrate particle diameter is large compared with the setal diameter, the setae are unlikely to slide between substrate particles, but instead the setae will generate thrust as a result of the resistance of the substrate particles. It is unclear exactly why the thrust should be larger with setae than with parapodia enlarged to cover the setal area but it is likely that the setae are better able to conform to the substrate particle shape. Particles with diameters larger than the spacing between the setae can be trapped between these and thus not roll out of the way of the moving setal configuration as easily as with the moving plate configuration. It is known from both theoretical analyses (Umemura 1982; Cheer and Koehl 1987) and experiments (Koehl 1995) that the spacing of hair-like cylinders is important for their function in aquatic environments.

Hair-like structures similar to the setal bundles found in nereidids have been found to work either as sieves or as plates depending on the spacing and Reynolds number at which they operate in a range of organisms, including copepod suspension feeding (Koehl 2004), sniffing in silk moths (Loudon and Koehl 2000) and swimming in mosquito larvae (Brackenbury 2001). It is possible that the spacing of hair-like structures plays an equally important role in a slippery substrate consisting of small particles. Further experiments with varying the setal spacing/particle size ratio are needed to determine this. The real compound seta found in errant polychaetes consists of two parts, a blade that can move independently of a shaft, and this probably allows the setae to conform to the substrate in a way that the stiff one-part setae used in the experiments presented here cannot (Gustus and Cloney 1973). Experiments conducted by Merz and Edwards (1998) show that worms with both the setal blade and the joint ablated crawl slower than worms with only the blade ablated. Experiments that compare two-part artificial setae with rigid setae are needed to determine whether higher conformity to the substrate would result in higher thrust generation in our robot.

The above discussion suggests that the relevant dimensionless group should be the ratio of the substrate particle diameter (d_{sub}) to the setal diameter (d_{set}). Table 4.2 shows values of this parameter for the experimental and worm environments. *N. diversicolor* can be found in a range of substrates (Clay 1967); here only two particle diameters, mud and fine sand, are included. Considering these results together with

those of figure 4.8 implies that setae will contribute differently to the thrust when the worm is operating in mud, since this is approximately equivalent to fine sand in the experimental environment, compared to when the worm is operating in fine sand. The crossover point in figure 4.8 occurs at a substrate diameter of approximately 3.4 mm in the experimental environment, which corresponds to a diameter of approximately 50 μm in the worm environment. This diameter is an order of magnitude larger than the mud particle diameter and an order of magnitude smaller than the fine sand particle diameter. However, some caution is necessary when transferring the result found here for robotic locomotion on a dry substrate to the marine environment of the real worms. Muddy cohesive sediments are known to behave like an elastic solid (Dorgan *et al.* 2005) and this will probably change the quantitative findings presented in this study although most likely not the qualitative ones. Further data from thrust generation on wetted substrates, and not least from studies on the locomotory behaviour of real worms in various substrates, are needed to determine the precise functional relationship between seta diameter and substrate particle diameter in errant polychaetes.

The difference between the stiffness of the worm setae and the artificial setae can be determined by calculating the bending stiffness in each case. The bending stiffness, k, is defined by the following equations:

$$k = E\,I$$

$$I = \pi\,(d_o^4 - d_i^4) / 64$$

where E is the Young's Modulus of the material and I is the second moment of area about its axis of a hollow circular shaft with inner and outer diameters d_i and d_o respectively. The displacement, y, of the setal tip under a point force, F, applied at the tip is then given by the following equation:

$$y = F\,L^3 / (3\,k)$$

where L is the setal length. This equation can be re-cast in the following form:

$$y / F = 1 / k'$$

where $1 / k' = L^3 / (3\,k)$ is a measure of the displacement per unit force such that k' is a measure of the effective bending stiffness. Assuming that a seta is made up of one third chitin and two thirds protein (Schroeder 1984) with Young's Moduli of 150 GPa and 10 GPa respectively (Xu 1994; Vogel 2004), then the Young's Modulus of the seta can be estimated to be 50 GPa from a simple rule of mixtures. Gustus and Cloney (1973) studied setae of 1 μm inner diameter and 2 μm outer diameter. Taking the outer

diameter of the *N. diversicolor* seta to be 6 μm (Table 4.1) and assuming the same inner-to-outer diameter ratio gives a k' of 0.33 N / m for a setal length of ~ 300 μm (Table 4.1). Assuming a Young's modulus of 200 GPa for the artificial setae constructed from 0.4 mm diameter solid steel piano wire with length ~ 10 mm gives a k' for the artificial seta of 750 N / m. The experimental setae were therefore very much stiffer than the worm setae and were thus less able to conform to the substrate. However, they were still useful for a first understanding of the role of setae in thrust generation.

Figure 4.9 shows that the time into the power stroke at which the maximum thrust occurred did not show substrate dependence but that there was a consistent variation with setal configuration. The maximum thrust was reached earliest when there were no setae, slightly later with setae and slightly later still with plates. A time of 250 ms into the power stroke corresponded approximately to the parapodial mid-position, i.e. 15 degrees back from the normal to the side of the robot frame. It is interesting to note that the maximum thrust did not occur when the parapodium passed through the normal to the side of the robot frame, as might be expected since the thrust vector would then be pointing directly rearwards. No data on thrust generation is available from the real worm, however. The observations relating to the time at which the maximum thrusts occurred are currently not fully understood.

The power input to the robot was not measured during the experiments so it is not possible to compare the efficiencies of the three setal configurations. Efficiency calculations would, however, not be trivial since the size and weight penalties associated with the different setal configurations would also have to be considered. The objective of the experiments was simply to determine if setae offered any advantages over larger parapodia in terms of thrust generation, and the results of this study suggest that such advantages can be found for relatively large-particle substrates.

Table 4.2. The ratio of substrate particle diameter to setal diameter on various substrates for both the worm robot and the real worm.

Experimental Environments:	d_{sub} (mm)[1]	d_{set} (mm)[2]	(d_{sub}/d_{set})
Fine Sand	0.5	0.4	1.3
Coarse Sand	1.4	0.4	3.5
Gravel	6.2	0.4	16
Worm Environments:			
Mud[3]	0.005	0.006	0.83
Fine Sand	0.5	0.006	83

1) The diameter of the substrate particles.
2) The diameter of the seta. For the real worms it represents an average value for the shaft diameter of all setal types combined.
3) The measure of mud particle diameter comes from a sample of clay-like mud collected from the Severn Estuary, South Gloucestershire, UK. Measurements were made from SEM photos.

4.7 Conclusion

This paper addresses the problem of generating friction in slippery substrates by taking inspiration from ragworms. Polychaetes can be found in a great variety of environments, which range from the depths of the ocean (swimming) to the sand of the seashore (crawling). Their versatile structure is a direct consequence of their adaptation to such diverse habitats and therefore they can be exploited as a model for a new generation of self-adaptive walking robots.

In particular, large juvenile *N. diversicolor* were studied with scanning electron microscopy and a digital high-speed camera, with the purpose of extracting morphological and kinematics data from the specimens. Scaled worm parapodia were replicated using a rapid prototyping machine and a robotic model was fabricated, after the necessary simplification of the complicated appendage geometry and of their complex biomechanics. Three sets of parapodia were constructed (without setae, with five stiff setae and fitted with extension plates) to determine if setae offered higher thrust over larger appendages. A computer interface able to control the main key parameters (frequency, amplitude, phase-delay and zero-position) was written and a

measurement system using a pre-loaded force sensor and a data acquisition unit was conceived and set-up.

Experiments, which were performed on three different substrates (fine and coarse sand and gravel) and with the above three parapodial configurations, showed that the thrust increases with particle size. Furthermore, with sufficiently coarse gravel, the robot generates more thrust with setae attached to its parapodia than with parapodia enlarged to cover the setal area. This suggests larger parapodia offer most benefits when particle diameter is small compared with setae size.

The results obtained in this study indicate that robots required to move in a slippery substrate, consisting of small particles, could enhance their thrust production by employing small hair-like structures at the ends of the propulsive appendages. Thus such structures should be considered in self-moving endoscopes or robots needed to inspect sewage pipes or explore sandy areas. Although setae are better than a simple extension of the propulsive appendage only at relative large particle diameters, they confer an advantage over large appendages in that they can more easily be retracted or folded away when not in use, such as during the recovery stroke or locomotion in less slippery terrain.

Future work will comprise experiments varying the setal spacing/particle-size ratio in order to determine the exact role of hair-like structure spacing in slippery substrates. In addition, the fabrication of new artificial setae that are more biomimetic is required. In fact, a real biological seta consists of two parts, a shaft and a blade elastically connected to each other, unlike the artificial setae considered in this paper. Such a jointed structure allows biological setae to conform better to the surrounding environment. Furthermore, worm setae are much less stiff than the artificial ones which we used. Finally, experiments with an eight-parapodia-robot will be performed and a deeper study of the single setal shape will be made. The fact that unexpected benefits were found even for such crude artificial setae as were used in this study provides considerable justification for more detailed work in this area.

Acknowledgements

The work presented in this paper has been carried out with the support of the European Commission, in the framework of the BIOLOCH Project (BIOmimetic structures for LOComotion in the Human body, IST FET Programme, IST-2001-34181). The authors wish to thank Ursula Potter from the Centre for Electron Optical

Studies at the University of Bath for technical help with SEM. Assistance from Dr. Adrian Bowyer, 'H' Jones, Vijay Rajput and Keith Paskins at the University of Bath is also gratefully acknowledged.

References

Brackenbury, J. 2001. The vortex wake of the free-swimming larva and pupa of *Culex pipiens* (Diptera). *Journal of Experimental Biology* **204**: 1855-1867.

Cheer, A. Y. L. and Koehl, M. A. R. 1987. Paddles and rakes: fluid flow through bristled appendages of small organism. *Journal of Theoretical Biology* **129**: 17-39.

Clark, R. B. and Tritton, D. J. 1970. Swimming mechanisms in nereidiform polychaetes. *Journal of Zoology* **161**: 257-271.

Clay, E. 1967. Literature survey of the common fauna of estuaries. *Imperial Chemical Industries Ltd. Brixham Laboratory* **1**: 1-28.

Delcomyn, F. 1999. Walking robots and the central and peripheral control of locomotion in insects. *Autonomous Robots* **7**: 259-270.

Delcomyn, F. 2004. Insect walking and robotics. *Annual Review of Entomology* **49**: 51-70.

Delcomyn, F. and Nelson, M. E. 2000. Architectures for a biomimetic hexapod robot. *Robotics and Autonomous Systems* **30**: 5-15.

Dorgan, K. M., Jumars, P. A., Johnson, B., Boudreau, B. P. and Landis, E. 2005. Burrow extension by crack propagation. *Nature* **433**: 475.

Foxon, G. E. H. 1936. Observations on the locomotion of some arthropods and annelids. *The Annals and Magazine of Natural History* **18**: 403-419.

Gray, J. 1939. Studies in animal locomotion. VII. The kinetics of locomotion of *Nereis diversicolor*. *Journal of Experimental Biology* **16**: 9-17.

Gustus, R. M. and Cloney, R. A. 1973. Ultrastructure of the larval compound setae of the polychaete *Nereis vexillosa* Grube. *Journal of Morphology* **140**: 355-366.

Kim, B., Lim, H.-Y., Kim, K.-D., Jeong, Y. and Park, J.-O. 2002. A locomotive mechanism for a robotic colonoscope. *IEEE. International Conference on Intelligent Robots and Systems*, Lausanne, Switzerland.

Koehl, M. A. R. 1995. Fluid flow through hair-bearing appendages: feeding, smelling and swimming at low and intermediate Reynolds numbers. In *Biological Fluid Dynamics* (Eds. Ellington, C. P. and Pedley, T. J). The Society for Experimental Biology: 157-182.

Koehl, M. A. R. 2004. Biomechanics of microscopic appendages: functional shifts caused by changes in speed. *Journal of Biomechanics* **37**: 789-795.

Lim, Y. M., Lee, J., Park, J., Kim, B., Park, J.-O., Kim, S. H. and Hong, Y.-S. 2001. A self propelling endoscope. *International Conference on Intelligent Robots and Systems*, Maui, Hawaii, USA.

Liu, J., Dukes, I., Knight, R. and Hu, H. 2004. Development of fish-like swimming behaviours for an autonomous robotic fish. *Control 2004*. University of Bath. Bath.

Loudon, C. and Koehl, M. A. R. 2000. Sniffing by a silkworm moth: wing fanning enhances air penetration through and pheromone interception by antennae. *Journal of Experimental Biology* **203**: 2977-2990.

Menciassi, A. and Dario, P. 2003. Bio-inspired solutions for locomotion in the gastrointestinal tract: background and perspectives. *Philosophical Transactions of the Royal Society of London. Series A.* **361**: 2287-2298.

Merz, R. A. and Edwards, D. R. 1998. Jointed setae - their role in locomotion and gait transitions in polychaete worms. *Journal of Experimental Marine Biology and Ecology* **228**: 273-290.

Mettam, C. 1967. Segmental musculature and parapodial movement of *Nereis diversicolor* and *Nephthys hombergi* (Annelida: Polychaeta). *Journal of Zoology* **153**: 245-275.

Quinn, R. D. and Ritzmann, R. E. 1998. Construction of a hexapod robot with cockroach kinematics benefits both robotics and biology. *Connection Science* **10**: 239-254.

Safak, K. K. and Adams, G. G. 2002. Dynamic modeling and hydrodynamic performance of biomimetic underwater robot locomotion. *Autonomous Robots* **13**: 223-240.

Scaps, P. 2002. A review of biology, ecology and potential use of the common ragworm *Hediste diversicolor* (O.F. Müller) (Annelida: Polychaeta). *Hydrobiologia* **470**: 203-218.

Schroeder, P. C. 1984. Chaetae. In *Biology of the Integument. Vol. I. Invertebrates* (Eds. Bereiter-Hahn, J., Matoltsy, A. G. and Richards, K. S.). Springer-Verlag. New York: 297-309.

Smith, J. E. 1957. The nervous anatomy of the body segments of nereid polychaetes. *Philosophical Transactions of the Royal Society of London. Series B.* **350**: 135-196.

Taylor, G. 1952. Analysis of the swimming of long and narrow animals. *Proceedings of the Royal Society of London. A.* **214**: 158-183.

Umemura, A. 1982. Matched-asymptotic analysis of low-Reynolds-number flow past two equal circular cylinders. *Journal of Fluid Mechanics* **121**: 345-363.

Vogel, S. 2004. *Comparative biomechanics : life's physical world.* Princeton University Press. Princeton.

Weingarten, J. D., Lopes, G. A. D., Buehler, M., Groffj, R. E. and Koditschek, D. E. 2004. Automated gait adaptation for legged robots. *Robotics and Automation, 2004.* Proceedings. ICRA '04. IEEE International Conference: 2153 – 2158.

Wootton, R. J. 1999. Invertebrate paraxial locomotory appendages: design, deformation and control. *Journal of Experimental Biology* **202**: 3333-3345.

Xu, W. 1994. *Biological applications of scanning tunneling microscopy and scanning force microscopy.* Ph.D. Thesis. University of Dalhousie.

Yu, J., Tan, M., Wang, S. and Chen, C. 2004. Development of a biomimetic robotic fish and its control algorithm. *IEEE Transactions on Systems, Man and Cybernetics - Part B. Cybernetics* **34**: 1798-1810.

Chapter 5

The function of parapodial setae in an errant polychaete moving on two different substrates

Accepted by the Journal of Experimental Marine Biology and Ecology.

Hesselberg, T. and Vincent, J. F. V. The function of parapodial setae in a nereidid polychaete moving on two different substrata. *Journal of Experimental Marine Biology and Ecology*. In press.

5 The function of parapodial setae in an errant polychaete moving on two different substrates

Thomas Hesselberg and Julian F. V. Vincent

Centre for Biomimetic and Natural Technologies. Department of Mechanical Engineering. University of Bath. Claverton Down. BA2 6AY. Bath. UK.

Abstract: Errant polychaetes of the family Nereididae possess a large number of compound setae originating in seta-bundles at the distal end of the parapodium. Here we investigate the functional role of the setae in *Nereis diversicolor* by comparing the locomotor performance of neuropodial seta-ablated worms with normal (control, non-ablated) worms moving on sand and mud. No differences between worms crawling on sand and mud were found, except that they were more submerged in the latter substrate. On both substrates a similar decrease in forward speed and increase in wave speed and slip were found in seta-ablated worms. However, this was not associated with any changes in gait, since both amplitude and wavelength were similar for seta-ablated and normal worms. This suggests that the setae are not adapted to a specific habitat. The same parameters were compared between seta-ablated and normal worms swimming over the substrate, but no significant differences were found, indicating that the setae are not as important during swimming as previously thought.

KEYWORDS: Polychaeta, Nereididae, setae, crawling, swimming

5.1 Introduction

Small hairs or setae can enhance the friction between a surface and animals such as insects (Gorb *et al.* 2002; Beutel and Gorb 2001) and geckos (Autumn *et al.* 2000). However, although the function of arrays of hairs has been extensively studied in filter feeding animals (Stamhuis *In press*; Koehl 2004; 1993), not much information is available about setae which increase friction or drag in an aquatic environment (but see Merz and Edwards 1998; Woodin and Merz 1987). Walking under water is more complicated than on land due to the higher density and viscosity of water compared to air which results in greater hydrodynamic and buoyant forces (Martinez 1996). This gives a smaller ground reaction force to propel the animal forward (Wootton 1999; Martinez 1996) as well as creating stability problems for the animal from wave action,

tides and currents (Ayers 2004). However, underwater walking is the main form of locomotion in a range of aquatic animals, including the errant polychaetes.

Nereidids are active marine worms, with a well developed head and sensory organs, capable of burrowing, crawling and swimming (Trevor 1977; Gray 1939). They spend the majority of their time inactive in their burrows (Evans *et al.* 1974), but emerge at night to crawl around on the substrate in search of food. The common ragworm *Nereis diversicolor* can be found in the intertidal zone in estuaries and shallow coastal regions, where it inhabits a range of substrates such as gravel, sand, mud and clay (Scaps 2002; Clay 1967). It is an omnivore, but may be a predator, a detritus feeder and even, occasionally, a filter feeder (Scaps 2002; Harley 1950). On each segment, except the two most anterior; the prostomium and the peristomium, and the most posterior; the pygidium, the errant polychaetes possess a pair of parapodia. The parapodium is a laterally extending biramous appendage, with an upper (notopodial) part and a lower (neuropodial) part. Each part has an external sensory organ, the cirrus, and an internal chitinous rod-like structure, the aciculum (Chambers and Garwood 1992; Smith 1957). Muscles run from the parapodium wall to the body wall, which allow forward and backward movement of the parapodium, and from the aciculum to the body, which enable the parapodium to be retracted into the body (Mettam 1967). Other muscles run from the notopodial aciculum to the single notopodial seta-bundle sac or from the neuropodial aciculum to the two neuropodial seta-bundle sacs, which allow the worm to retract and protract the seta-bundles (Mettam 1967). In *N. diversicolor* the notopodial bundle consists of around 15 long bladed setae (homogomph spinigers) and the neuropodial bundles consist of a mixture of around 25 short bladed (heterogomph falcigers) and long bladed (heterogomph spinigers) setae (chapter 3; Hesselberg *Unpublished data*; Hesselberg and Vincent 2006). All the setae in juvenile ragworms are compound setae consisting of a shaft and a serrated blade hinged with a ligament, and a boss to restrict movement of the blade (chapter 3; Hesselberg and Vincent 2006). The setae are not innervated and have no muscles, so all movement of the blade relative to the shaft is passive in response to external forces (Gustus and Cloney 1973).

The number of setae, their location on the appendages and the serrations on the blade suggest a role in increasing friction with the substrate either as hooks (Woodin and Merz 1987) and/or during locomotion (Gustus and Cloney 1973; Foxon 1936). Ragworms exhibit three gaits: slow walking, fast walking and swimming. During slow

walking the body is held rigid while the parapodia act as legs pushing the body forward, whereas small amplitude body waves are sent forward to aid the power stroke of the parapodia during fast walking (Gray 1939). The term crawling used in the present study refers to fast walking. In the crawling ragworm, the setae are protracted during the power stroke of the parapodium and the seta-joint presumably allows the blade to conform to the substrate to increase the contact area and thus the friction (Gustus and Cloney 1973; Mettam 1967). Merz and Edwards (1998) showed that the ablation of the distal portion of setae (the joints and blades) reduced the speed of the errant polychaete *Ophiodromus pugettensis*.

In an earlier study we compared setal and parapodial morphology in a range of ragworms inhabiting different substrates (chapter 3; Hesselberg and Vincent 2006). We found no obvious adaptations of the setae to the type of substrates encountered, thus suggesting a more multifunctional role of the setae. However, a study conducted with a physical model in a dry habitat, where arrays of artificial setae were placed on mechanical oscillating parapodium-shaped appendages, showed that the amount of extra thrust generated by the artificial setae depended on the size of the particles in the substrate (chapter 4; La Spina *et al.* 2005).

In the present study we compare the locomotory function of setae in *N. diversicolor* on two types of substrate by comparing kinematic parameters of ablated and non-ablated worms crawling on either mud or sand.

Some ragworms, including *N. diversicolor*, can swim in the juvenile stage, but this is infrequent and primarily an escape response (Thiel and Reise 1993). Most errant polychaetes, although not *N. diversicolor*, undergo metamorphosis into a reproductive active adult stage, the heteronereis, where changes in musculature and parapodial and setal morphology enable them to swim fast and extensively during swarming and the nuptial dance (Hardege and Bartels-Hardege 1995; Clark 1961). During swimming in juveniles body waves of large amplitude move from tail to head and are coupled to parapodia movement, such that the power stroke occurs at the crest of the wave where drag, and thus thrust generation, is maximised, and the recovery stroke occurs at the trough, where drag is minimised (Clark and Tritton 1970). Arrays of fine hairs act as sieves or plates depending on the distance between the hairs and the Reynolds number (Cheer and Koehl 1987), and there is some theoretical evidence that, at least the basal part if not the whole of, the seta-bundles may function as plates during swimming (chapter 3; Hesselberg and Vincent 2006). Edward and Merz (1998) substantiate this

claim by showing that blade and joint ablation, but not blade ablation alone, slows swimming in *O. pugettensis*. Here we investigate this further by comparing the swimming kinematics of normal and ablated worms.

5.2 Materials and methods

5.2.1 Crawling and swimming

Juvenile *N. diversicolor* were collected in the Severn Estuary, near Bristol, U. K. and placed in large mud-filled containers in a climate cabinet at 10°C for up to four weeks, during which they were fed TetraMIN Pro flakes twice a week. One week prior to experimental treatment worms were placed individually in open sand-filled containers in an aerated tank containing artificial sea water (salinity 22 ppt) at room temperature. Hereafter the worms that looked and behaved normally were anaesthetised with 7.5% MgCl and their length measured before they were transferred to a special 'cutting' bed made of ABS plastic, consisting of two square 'holding' areas interconnected by a narrow rectangular area with a semi-circular groove in the middle of diameter 1 mm (Fig. 5.1a). The bed was 70 mm long and glued to a Petri dish. Anaesthetised worms were placed in the bed with the ventral side up such that the body was resting in the groove with the parapodia sticking out on each side. The whole Petri dish was filled with 7.5% MgCl in artificial sea water up to the height of the bed, so that the parapodia were below the water level thereby giving easy view of, and access to, the setae. The neuropodial seta-bundles were ablated as close to the parapodial base as possible with iridectomy scissors under a dissection microscope (Fig. 5.1b).

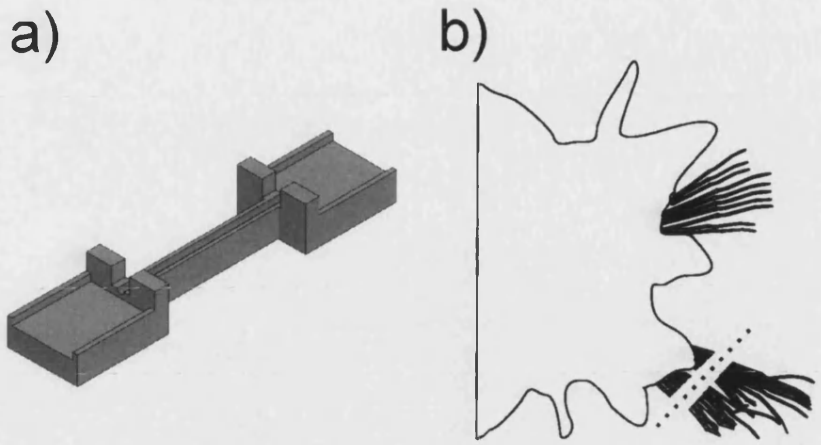

Fig. 5.1. a) The cutting bed used for seta-ablation. b) A schematic drawing of a parapodium of *Nereis diversicolor* showing the notopodial seta-bundle (upper) and the neuropodial seta-bundles (lower). The dotted line shows where the setae were ablated.

The worms were allowed to recover in artificial seawater. The whole operation including initial anaesthesia lasted 37 min ± 10 min (n = 61) for both ablated and non-ablated worms and never lasted longer than 60 min. The non-ablated control worms were treated in exactly the same manner, i.e. anesthetised and placed on the cutting bed under the dissection microscope, except that no setae were ablated. The ablated and non-ablated worms were anaesthetised for a similar length of time. After recovery the worms were returned to their sand-filled containers and allowed 24 hours to recover further before they were recorded. Regeneration and/or replacement of lost setae presumably occurs naturally (Schroeder 1984), so 24 hours was chosen to make sure no regeneration had taken place. This was confirmed by dissection of a few worms several days after ablation where no sign of regeneration or replacement was visible. Only worms that had successfully made a new burrow during the 24 hours and that moved and behaved normally were recorded.

Worms were transferred to the experimental arena (a rectangular 200 x 60 x 15 mm arena with upwards sloping ends made of Plexiglass) where their movement was filmed from above with a digital high speed camera (The MotionScope 2000S, Redlake MASD, Inc) fitted with a 25 mm Cosmicar Pentax lens. Recordings were made at 125 frames per second with a shutter speed of 1/1250 s. The arena contained a ~ 2 mm thick layer of substrate and artificial seawater (salinity 22 ppt). Recordings where the worms penetrated so far into the substrate that they touched the arena bottom were excluded from the analysis. The substrate was either mud collected at Severn Beach with a

particle diameter of 0.0051 mm ± 0.0034 mm, n = 69 (measured in a Scanning Electron Microscope) or commercially available garden sand with a particle diameter of 0.94 mm ± 1.08 mm, n = 140 (measured in a Scanning Electron Microscope). The worms were allowed to acclimatise to the experimental arena for 15 minutes, but were not recorded if they had not shown the desired locomotion type (normal fast walking or swimming) within 30 minutes of being introduced into the experimental arena. One measurement of walking was recorded for each worm followed (if the worm cooperated) by one recording of swimming.

Kinematic values were found by digitising the recordings with a custom made LabVIEW (Version 7.1, National Instruments, 2004) program (appendix B), which allowed an arbitrary number of points to be manually digitised in each frame. For the recordings of crawling behaviour this included the anterior point of the prostomium (excluding the cirri and antennae), and the posterior most 5-8 body crests – only the most posterior body waves were used as they were more stable and complete (Fig. 5.2a). For the recordings of swimming, the anterior point of the prostomium (excluding the cirri and antennae), the posterior point of the pygidium (excluding the cirri) and all body wave crests were digitised (a total of between 5 and 6 body digitisation points) (Fig. 5.2b). The digitisation points on the wave crests were placed in the middle of the segment. Analysis was done with MATLAB (Version 7.0, The MathWorks Inc., 2004) (appendix B). Amplitude and wavelength of crawling worms were measured using a local regression line calculated from the 5-8 digitisation points in each frame, whereas the fewer digitisation points for swimming worms meant that a global regression line was calculated from all digitisation points in all frames. To get a more reliable estimate of the forward speed and the wave speed, we used the global regression line calculated from all points digitised in the recording for both crawling and swimming worms. To minimise further the variance of the speed values (a slight scatter of digitisation points due to imprecise clicking was unavoidable) only every 10^{th} frame was used for the crawling recordings and every 5^{th} frame for the swimming recordings.

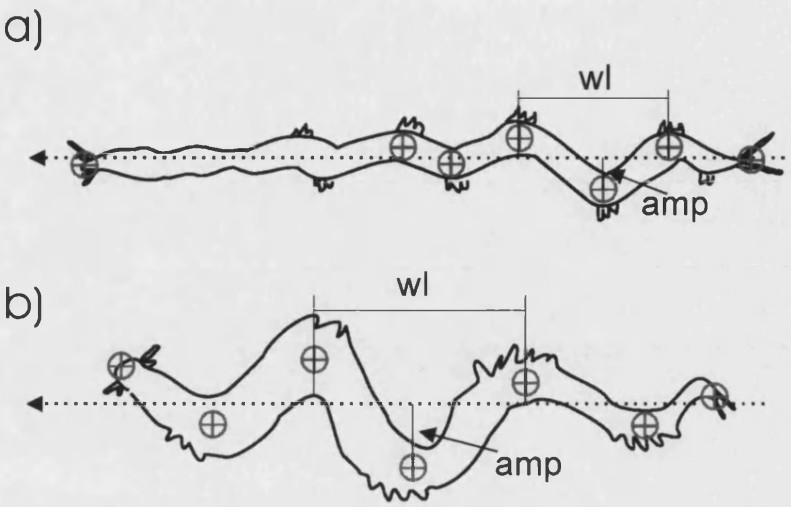

Fig. 5.2. Locomotion in nereidids. a) fast walking. b) swimming. The cross hairs show possible digitisation points. A measure of amplitude (amp) and a measure of wavelength (wl) is also shown. The dashed line gives the direction of movement.

The following kinematic parameters were extracted from the recordings of crawling and swimming.

Amplitude: The distance between the peak of the body wave crest and its position projected onto the local (crawling) or global (swimming) regression line and averaged over all frames (Fig. 5.2).

Wavelength: The distance between the body wave crest and its neighbouring ipsilateral crest (in the anterior direction). Distance was found from the crests projected onto the local (crawling) or global (swimming) regression line and averaged over all frames (Fig. 5.2).

Wave speed: The difference in projected crest position relative to projected prostomium position between every 10^{th} (crawling) or 5^{th} (swimming) frame was multiplied by the framing rate (125 fps) divided by 10 or 5 and averaged over all frames used. To minimise variation only the second body wave crest was used during swimming, since it is the largest and therefore arguably most important for locomotion. During crawling all the posterior body waves were of similar amplitude and shape so an average of them all was used. Note that wave speed is expressed in the reference frame of the worm and not the global reference frame.

Speed: The speed of the crawling worms was found by taking the difference in projected prostomium position between every 10th frame and multiplying it by the framing rate (125 fps) divided by 10 and averaged over all frames used. Since the head oscillates from side to side during swimming, even occasionally resulting in the head moving backward relative to the whole worm, another method of finding the forward speed was used. The speed of the swimming worm was found by taking the difference in position between every 5th frame of the point midway between the projected prostomium and pygidium positions and multiplying it by the framing rate (125 fps) divided by 5 and averaged over all frames.

U/V: The ratio between the forward speed of the worm (U) and the speed of the body wave (V) is also referred to as slip (Müller *et al.* 2002). A lower U/V ratio indicates a higher slip, where less of the thrust produced by the wave is translated into forward speed. Although thrust is generated by the parapodia and not by the body waves (Clark and Tritton 1970), there is such a tight coupling between parapodial and body waves that the U/V can be used as an indication of slip.

A 6 marker calibration grid was filmed after each recorded swimming event using the Two-Dimensional Direct Linear Transformation method (appendix A; Brewin and Kerwin 2003).

5.2.2 Lateral view

Another group of juvenile *N. diversicolor* worms collected in the Severn Estuary, near Bristol, U.K. was treated and recorded as described above, except that no ablation occurred and they were filmed from the side in an experimental arena (500 x 45 x 25 mm made of Plexiglass). The arena contained a ~ 2 mm thick layer of substrate and artificial seawater (salinity of 22 ppt) up to a height of 15-17 mm. Again sand and mud was used as substrate. Worms that did not show the desired locomotion type and were not recorded successfully within 30 minutes after being introduced into the experimental arena were discarded. After a successful recording, the worm was anaesthetised in 7.5% MgCl and its length was measured.

For the lateral view recordings the points digitised included the anterior point of the prostomium (excluding the cirri and antennae), and then 3-7 further points along the length of the body depending on the degree of horizontal movement displayed by the worm. Analysis was done in a spreadsheet. The substrate level was found by digitising

two points on each side of the recording at the interface between substrate and water. From these two points a linear equation describing the substrate surface was found, which was subtracted from the digitised point on the worm to get the height above the substrate. This was done to ensure accurate measurements of height even in the cases where the substrate or the camera was not completely horizontal.

A 6 marker calibration grid was filmed after each recorded swimming event using the Two-Dimensional Direct Linear Transformation method (appendix A; Brewin and Kerwin 2003).

The following kinematic parameters were extracted from the lateral view recordings.

Speed: The speed of the worm was found by taking the difference in position of the prostomium between the first and the last frame in the recording multiplied by the framing rate (125 fps) and divided by the number of frames between the first and the last frame in the recording.

Head height: The average vertical distance between the anterior part of the prostomium and the substrate for all frames of the recording.

Body height: The average vertical distance between all digitised points on the body (including the head) and the substrate for all frames of the recording.

5.2.3 Statistics

All parameters for both crawling and swimming worms were correlated pair-wise using Pearson's correlation test. For crawling all pair-wise correlations were made separately for seta-ablated and for control worms. Note that the correlation coefficient and significance are reported only for the significant cases.

For the data from crawling worms two different substrates (sand and mud) and two different treatments (ablated and non-ablated) were used. Since the sample size for each of these factors, furthermore, was unequal it proved unfeasible to use a nested ANOVA to test for differences within and among substrates. Instead a two-way ANOVA was used with amplitude, wavelength, wave speed, speed or U/V as dependent variables and substrate and treatment as fixed factors. The interaction between the factors showed whether the effect of seta-ablatation depended on the substrate.

The average parameters found for swimming worms and the crawling parameters taken from lateral views of the worms were compared between ablated and non-ablated worms for the former and between mud and sand for the latter by applying the two-tailed Student t-test.

Since several tests were performed on the same datasets, a sequential Bonferroni adjustment was made to minimise type I errors (Rice 1989). Five separate Bonferroni adjustments were made, one for each set of correlations (crawling and swimming), one for the crawling data, one for the swimming data and one for the lateral view data. The initial significance level was set at 5%. All statistical tests were performed using SPSS 12.0 (SPSS Inc. 2003).

5.3 Results

The nereidid worms showed only relatively short periods of continuous steady locomotion and were especially reluctant to swim despite being encouraged to do so by prodding them with disposable plastic pipettes. However, most of the worms did show short bursts of steady locomotion. The recordings that were included in this study had between 100 and 250 frames (0.8 to 2 sec) of steady crawling and between 50 and 125 frames (0.4 to 1 sec) of steady swimming

5.3.1 Crawling

Out of the 20 pair wise correlations done on the five crawling parameters (length, amplitude, wavelength, wave speed and forward speed) for both ablated and non-ablated recordings, only 5 were significant after the sequential Bonferroni adjustments to the significance level. Wavelength vs. amplitude showed correlations for both ablated (Pearson's correlation coefficient $r = 0.61$, $N = 21$, $P = 0.004$) and non-ablated worms (Pearson's correlation coefficient $r = 0.68$, $N = 24$, $P = 10^{-4}$) as did wavelength vs. wave speed (ablated: Pearson's correlation coefficient $r = 0.84$, $N = 21$, $P = 10^{-6}$, non-ablated: Pearson's correlation coefficient $r = 0.76$, $N = 24$, $P = 10^{-5}$). Furthermore, amplitude vs. wave speed was significantly correlated for the non-ablated worms (Pearson's correlation coefficient $r = 0.59$, $N = 24$, $P = 0.003$). It is presumably an artefact of the low sample size that not more parameters were interdependent.

The amplitude of the body wave was similar for both ablated and non-ablated worms (Fig. 5.3a, Two-way ANOVA, $F_{(1,41)} = 0.02$, $P = 0.87 > 0.017$) and for both substrates (Two-way ANOVA, $F_{(1,41)} = 6.77$, $P = 0.012 > 0.004$). The interaction between the substrate and treatment was also not significant (Two-way ANOVA, $F_{(1,41)} = 0.56$, $P = 0.46 > 0.007$). For the length of the body wave neither differences between

treatments (Fig. 5.3b, Two-way ANOVA, $F_{(1,41)} = 0.02$, $P = 0.89 > 0.025$) nor differences between substrates (Fig. 5.3b, Two-way ANOVA, $F_{(1,41)} = 0.36$, $P = 0.55 > 0.01$) were found. The interaction between substrate and treatment was not significant (Two-way ANOVA, $F_{(1,41)} = 0.17$, $P = 0.68 > 0.013$). Differences were found between treatments for the speed of the body wave (Fig. 5.3c). The wave speed of ablated worms was significantly higher than for non-ablated worms independent of substrate (Two-way ANOVA, $F_{(1,41)} = 9.76$, $P = 0.003 < 0.013$). However, no differences were found between the substrates (Two-way ANOVA, $F_{(1,41)} = 0.39$, $P = 0.53 > 0.008$) nor any interaction between substrate and treatment (Two-way ANOVA, $F_{(1,41)} = 0.009$, $P = 0.92 > 0.05$). Ablated worms moved slower than non-ablated worms (Two-way ANOVA, $F_{(1,41)} = 17.63$, $P = 10^{-4} < 0.004$), whereas neither differences between substrates (Two-way ANOVA, $F_{(1,41)} = 4.11$, $P = 0.049 > 0.006$) nor the interaction between substrate and treatment (Two-way ANOVA, $F_{(1,41)} = 4.09$, $P = 0.050 > 0.005$) proved to be significant. A similar pattern was observed for the ratio between forward speed and wave speed (Fig. 5.3e), with significantly lower ratios and thus higher 'slip' for ablated compared to non-ablated worms (Two-way ANOVA, $F_{(1,41)} = 48.66$, $P = 10^{-8} < 0.003$). No statistically significant difference between the substrates was found (Two-way ANOVA, $F_{(1,41)} = 4.56$, $P = 0.04 > 0.005$) and no interaction was found (Two-way ANOVA, $F_{(1,41)} = 2.50$, $P = 0.12 > 0.006$).

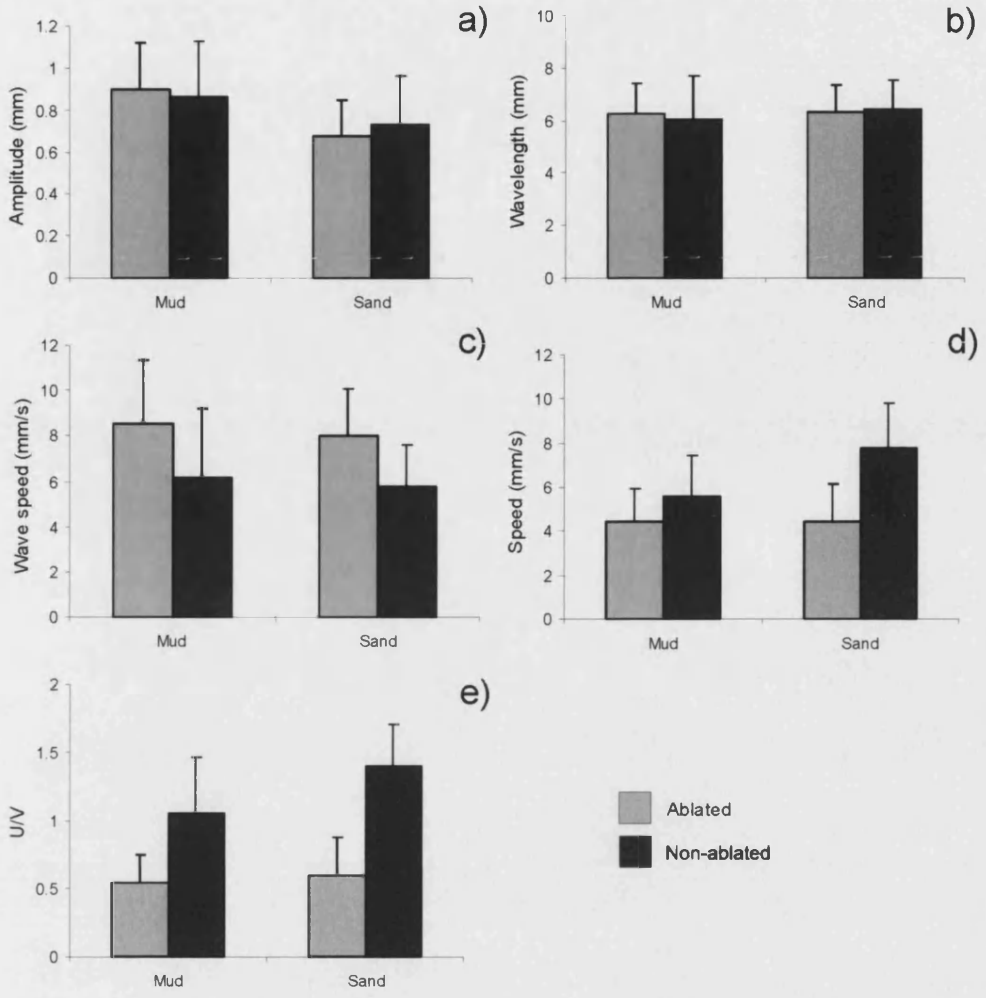

Fig. 5.3. Crawling parameters of ablated and non-ablated worms moving on sand or mud. The light grey columns represent ablated worms and the darker grey columns represent non-ablated worms. The sample size was 9 for mud ablated (length L = 47.4 ± 6.8 mm, mean ± std. dev.), 10 for mud non-ablated (length L = 48.6 ± 8.3 mm, mean ± std. dev), 12 for sand ablated (length L = 53.7 ± 7.2 mm, mean ± std. dev) and 14 for sand non-ablated (length L = 53.8 ± 10.0 mm, mean ± std. dev). The error bars indicate the standard deviation. a) Amplitude of the body wave in mm. b) Wavelength of the body wave in mm. c) Wave speed in relation to head position in mm/s. d) Forward speed of the worm in mm/s. e) The ratio of wave speed to forward speed (U/V) or 'slip'.

5.3.2 Swimming

During swimming the body was clear of the substrate, with the exception of the head that sometimes was in close contact with the substrate, and no significant differences in swimming parameters were found between the substrates. To get a decent

sample size we therefore pooled the recordings together into ablated and non-ablated ignoring the substrate over which they swam.

The five parameters of swimming (length, amplitude, wavelength, wave speed, forward speed) examined in this study were pair-wise correlated with each other, but only amplitude vs. speed (Pearson's correlation coefficient $r = 0.66$, $N = 15$, $P = 0.008$), showed significant correlation. This is surprising as most parameters were expected to depend on each other. However, the failure to find more significant correlations can probably be ascribed to the low sample size and the selection for low variance in length.

No significant differences were found between ablated and non-ablated worms for any of the swimming parameters analysed (Table 5.1). There were indications of higher wave speed and lower overall speed in ablated worms compared to non-ablated. This resulted in a larger 'slip' (U/V) for the former, although the high individual variation meant that this difference was not significant (Table 5.1).

Table 5.1. Kinematic parameters of swimming *Nereis diversicolor*

	Ablated	Non-ablated	df	t	P*
Sample size	12	15			
Length (mm)	49.4 ± 9.1	54.3 ± 9.6			
Amplitude (mm)	2.6 ± 0.6	3.2 ± 0.7	25	-2.02	0.054 > 0.01
Wavelength (mm)	10.6 ± 3.4	9.2 ± 2.2	25	1.31	0.202 > 0.025
Wavespeed (mm/s)	45.5 ± 4.9	42.3 ± 4.7	25	1.78	0.091 > 0.013
Speed (mm/s)	18.0 ± 6.2	21.2 ± 7.4	25	-1.20	0.241 > 0.05
U/V	0.40 ± 0.16	0.51 ± 0.20	25	-1.54	0.137 > 0.017

Values given as mean ± standard deviation.

* The significance values are compared to the Bonferroni adjusted significance level.

5.3.3 Lateral view

Measurements from the side of crawling worms revealed that there was a significant difference between sand and mud in the height of the body above the substrate (Table 5.2). In mud the dorsal part of the body was 0.9 mm above the substrate on average compared to 1.6 mm in sand. Assuming a segment height of 1.8 mm (chapter 3; Hesselberg and Vincent 2006) this means that the worms crawling on mud had half their body buried, whereas the worms on sand had only the ventral side of the body in contact with the sand. However, note the large variation on the means, which was a result of some worms deeply submerged in the substrate whereas others were barely in contact with it. No other significant differences were found between crawling

on sand and mud. In both cases the worms maintained a close contact between the sensory organs on the head and the substrate (Table 5.2). Note that despite the differences in methods used, the crawling speeds from the dorsal and lateral view were similar (Fig. 5.3d, Table 5.2).

Table 5.2. Kinematics parameters of crawling *Nereis diversicolor* measured from a lateral view

	Mud	Sand	df	t	P*
Sample size	13	14			
Length (mm)	49.1 ± 10.2	55.2 ± 16.9			
Head height (mm)	0.6 ± 0.5	0.8 ± 0.6	25	-1.01	0.32 > 0.025
Body height (mm)	0.9 ± 0.5	1.6 ± 0.4	25	-3.72	0.001 < 0.017
Speed (mm/s)	5.0 ± 1.2	4.6 ± 2.5	25	0.59	0.56 > 0.05

Values given as mean ± standard deviation.

* The significance values are compared with the Bonferroni adjusted significance level.

5.4 Discussion

Conventionally the function of structures or organs is studied by comparing the performance of whole animals with animals with the structure removed. In ragworms such studies involve the ablation of sensory organs to test their role in navigation and learning (Flint 1965) and the effect of extirpation of the supra-oesophageal ganglion on learning and memory (Evans 1963). However, one needs to be very cautious when interpreting the results of such ablation studies, as the operation and removal of integral structures are likely to affect the entire animal and not only the specific function of the structure in question. In the present study the ablation method is justified since the setae contain no living cells (Gustus and Cloney 1973) and thus the treatment should be no more traumatic than a hair-cut in humans. However, the anaesthetising and handling procedure used in this study might have a more drastic effect as a few worms never recovered from the anaesthetisation. But since ablated and non-ablated worms were treated similarly then, even if the anaesthesia and handling had an adverse effect on locomotion, this would not influence the comparative results presented here. It is, though, possible that the negative effects of seta-ablation on crawling speed found in this study were not the result of a loss of friction, but of another effect. The area around the seta-bundle sac is relatively rich in nerve receptors cells (Dorsett 1964; Hamaker

1898) and it is possible that the seta-bundles act as mechano-receptors. However, considering the rich morphological detail of the setae including the serrated blades, the primary function is more likely to be associated with generating friction. The nereidids, furthermore, possess special compound sense organs distributed throughout the body surface dedicated to chemo- and mechanoreception (Jouin et al. 1985; Dorsett and Hyde 1969).

From the lateral view recordings of crawling worms it could be observed that the worms held their prostomium, bearing most of the sensory organs (Verger-Bocquet 1992), in close contact with the substrate in both sand and mud (Table 5.2). This presumably provides the worm with continuous information about the substrate as well as allowing it to simultaneously search for food and be prepared to burrow rapidly (Trevor 1977; Flint 1965). Compared to crawling on sand, worms crawling on mud had more of the body submerged in the substrate (Table 5.2). It would, therefore, be expected that the worm would encounter more resistance from the mud and as a consequence move slower than on sand. However, no differences in crawling speed were observed between sand and mud in either the lateral view (Table 5.2) or the dorsal view experiments (Fig. 5.3d). One intrinsic problem with all locomotion studies at intermediate gaits is that the animal might have variable motivation for moving and might not actually move at its maximum speed. In the present study the worm was gently poked to provoke it to move away from the stimulus. However, one had to be gentle as the worm swam away from more persistent prodding, so it is possible that the worms were not crawling at their maximum speed. But considering the consistency across both experiments and the relatively large sample size the results presumably do reflect that crawling speed when half submerged in mud is not significantly reduced compared to crawling on sand. A possible explanation for this result is that, although *N. diversicolor* can be found in a wide range of substrates (Clay 1967), all the worms used in this study were collected on mud flats. It is possible that these worms were adapted for locomotion in mud and that different results would be obtained from worms collected from sandy habitats.

The dorsal view revealed no other differences between crawling on mud and sand in any of the crawling parameters investigated (Fig. 5.3). Neither were there any interactions between the substrate and the experimental treatment, meaning that ablating the setae had the same effect on the worms independent of the substrate on which they were crawling. This suggest that the physical model of La Spina and co-workers (2005),

which found differences in thrust generation by an array of artificial setae depending on the substrate, is not directly transferable to the situation in the real worm. One main difference is that the physical model was tested on dry substrates. The interactions between water and substrate particles experienced by the real setae coupled to the difference in scale might explain the observed differences. Furthermore, the worm, unlike the physical model, might be able to adapt behaviourally to the different substrates. Several muscles are attached to the seta-bundle sacs (Mettam 1967). Thus it is possible that the worms by retracting the setae or by other means can change the intersetal spacing in the seta-bundles thus optimising their function to the substrate.

In worms crawling on both mud and sand, removing the setae had significant effects on wave speed and forward speed (Fig. 5.3). Crawling speed was reduced and wave speed increased after seta-ablation. However, no changes were observed in the more gait-specific parameters (amplitude and wavelength). A much larger slip was observed in the ablated worms compared to the controls (Fig. 5.3e), which suggests that the worms were trying, unsuccessfully, to compensate for the lower thrust generated by ablated parapodia by increasing the speed, and thus the frequency, at which the body waves were sent forward. The reduced crawling speed of ablated worms agrees with an earlier study by Merz and Edwards (1998) who found reduced speeds for both slow and fast walking worms, where the seta-blades and joints were removed, but surprisingly enough no change was observed if most of the blade was removed. The reported increase in slip during swimming in the current study is, furthermore, mirrored in the Merz and Edwards (1998) study on the parapodial level. They found that seta-ablated worms showed a decrease in stride distance and a corresponding increase in stride frequency. They reported no other changes in parapodial gaits (Merz and Edwards 1998). It is also interesting to note that both crawling and swimming speeds of the small errant polychaete *Ophiodromus pugettensis* (L = 21 mm) were much higher than in *N. diversicolor* in the current study (Merz and Edwards 1998). It is, therefore, possible that *O. pugettensis* shows a different gait type, i.e. a substantial difference in amplitude and wavelength which they unfortunately did not investigate. It would have been interesting to include information on the behaviour of the parapodium during locomotion. However, it proved not feasible in this study as the parapodia were entirely submerged in the mud and thus not visible to the camera.

Whilst there is substantial experimental evidence from both the current study on whole body kinematics and the Merz and Edwards (1998) study on parapodial

kinematics that the setae play a functional role during walking, it remains unresolved whether they enhance thrust during swimming. Whereas Merz and Edwards (1998) found a significant reduction in swimming speed of worms which had the blade and joint ablated no significant decrease in swimming speed was found in the present study. However, a small reduction in speed was found for ablated worms and, although it was not significant, a relative large decrease in U/V (increase in slip) from 0.51 in controls to 0.40 in ablated worms was found (Table 5.2), thus suggesting some effect of seta-ablation on swimming. One major difference between the studies, other than the use of different species, is that in the present study only the neuropodial seta-bundles were ablated. The area of the notopodial seta-bundle is almost as large as the areas of the neuropodial bundles combined (chapter 3; Hesselberg and Vincent 2006). A similar study with larger sample sizes and ablation of all seta-bundles might show a significant decrease in swimming speed and a significant increase in slip. Theoretical calculations suggest that the seta-bundles operate at Reynolds numbers which together with the intersetal spacing result in a leakiness of less than 0.2 (chapter 3; Hesselberg and Vincent 2006). They function, therefore, mainly as plates, and since the parapodia act as drag-based paddles during swimming (Clark and Tritton 1970), the added area from the seta-bundles should contribute to the overall thrust generation. However, the results of the present study suggest that this contribution must be relatively small, at least from the neuropodial seta-bundles. Further studies are needed on the effect of the notopodial seta-bundle to fully analyse the function of the setae during swimming.

The results presented here suggest that the setae play an important role during crawling by increasing the friction between the parapodium and the substrate. They, furthermore, agree with morphological data (chapter 3; Hesselberg and Vincent 2006) in showing that the setae are not adapted to any specific habitat, but have a more multifunctional role.

Acknowledgements

The authors would like to thank 'H' Jones and Jackie Rawlings for technical help. The work was supported by the European Commission, in the framework of the BIOLOCH Project (IST FET Programme, IST-2001-34181).

References

Autumn, K., Liang, Y. A., Hsieh, S. T., Zesch, W., Chan, W. P., Kenny, T. W., Fearing, R. and Full, R. J. 2000. Adhesive force of a single gecko foot-hair. *Nature* **405**: 681-685.

Ayers, J. 2004. Underwater walking. *Arthropod Structure & Development* **33**: 347-360.

Beutel, R.G. and Gorb, S.N. 2001. Ultrastructure of attachment specializations of hexapods (Arthropoda): evolutionary patterns inferred from a revised ordinal phylogeny. *Journal of Zoological Systematics and Evolutionary Research* **39**: 177-207.

Brewin, M. A. and Kerwin, D. G. 2003. Accuracy of scaling and DLT reconstruction techniques for planar motion analyses. *Journal of Applied Biomechanics* **19**: 79-88.

Chambers, S. and Garwood, P. 1992. *Polychaetes in Scottish waters. A guide to identification. Part 3 family Nereidae*. National Museums of Scotland. Edinburgh.

Cheer, A. Y. L. and Koehl, M. A. R. 1987. Paddles and rakes: fluid flow through bristled appendages of small organisms. *Journal of Theoretical Biology* **129**: 17-39.

Clark, R. B. 1961. The origin and formation of heteronereis. *Biological Reviews* **36**: 199-236.

Clark, R. B. and Tritton, D. J. 1970. Swimming mechanisms in nereidiform polychaetes. *Journal of Zoology* **161**: 257-271.

Clay, E. 1967. Literature survey of the common fauna of estuaries. *Imperial.Chemical.Industries.Ltd. Brixham Laboratory* **1**: 1-28.

Dorsett, D. A. 1964. The sensory and motor innervation of *Nereis*. *Proceedings of the Royal Society of London. B.* **159**: 652-667.

Dorsett, D. A. and Hyde, R. 1969. The fine structure of the compound sense organs on the cirri of *Nereis diversicolor*. *Zeitschrift für Zellforschung* **97**: 512-527.

Evans, S. M., Cram, A. and Rogers, F. 1974. Spontaneous activity and responses to stimulation in the polychaete *Nereis diversicolor* (O. F. Müller). *Marine Behaviour and Physiology* **3**: 35-58.

Evans, S. M. 1963. The effect of brain extirpation on learning and retention in nereid polychaetes. *Animal Behaviour* **11**: 172-178.

Flint, P. 1965. The effect of sensory deprivation on the behavior of the polychaete *Nereis* in T-mazes. *Animal Behaviour* **13**: 187-193.

Foxon, G. E. H. 1936. Observations on the locomotion of some arthropods and annelids. *The Annals and Magazine of Natural History* **18**: 403-419.

Gray, J. 1939. Studies in animal locomotion. VII. The kinetics of locomotion of *Nereis diversicolor*. *Journal of Experimental Biology* **16**: 9-17.

Gorb, S. N., Beutel, R.G., Gorb, E.V., Jiao, Y. K., Kastner, V., Niederegger, S., Popov, V.L., Scherge, M., Schwarz, U. and Votsch, W. 2002. Structural design and biomechanics of friction-based releasable attachment devices in insects. *Integrative and Comparative Biology* **42**: 1127-1139.

Gustus, R. M. and Cloney, R. A. 1973. Ultrastructure of the larval compound setae of the polychaete *Nereis vexillosa* Grube. *Journal of Morphology* **140**: 355-366.

Hamaker, J. I. 1898. The nervous system of *Nereis virens* Sars. *Bulletin from the Museum of Comparative Zoology* **32**: 89-135.

Hardege, J. and Bartels-Hardege, H. 1995. Spawning behaviour and development of *Perinereis nuntia* var. *brevicirrus* (Annalida: Polychaeta). *Invertebrate Biology* **114**: 39-45.

Harley, M. B. 1950. Occurrence of a filter-feeding mechanism in the polychaete *Nereis diversicolor*. *Nature* **165**: 734-735.

Hesselberg, T. and Vincent, J. F.V. 2006. A comparative study of the functional morphology of parapodia and setae in nereids (Polychaeta: Nereididae). *Animal Biology* **56**: 103-120.

Jouin, C., Tschernigovtzeff, C., Baucher, M. F. and Toulmond, A. 1985. Fine structure of probable mechano- and chemoreceptors in the caudal epidermis of the lugworm *Arenicola marina* (Annelida, Polychaeta). *Zoomorphology* **105**: 76-82.

Koehl, M. A. R. 1993. Hairy little legs: feeding, smelling and swimming at low Reynolds numbers. *Contemporary Mathematics* **141**: 33-64.

Koehl, M. A. R. 2004. Biomechanics of microscopic appendages: functional shifts caused by changes in speed. *Journal of Biomechanics* **37**: 789-795.

La Spina, G., Hesselberg, T., Williams, J. and Vincent, J. F. V. 2005. A biomimetic approach to robot locomotion in unstructured and slippery environments.

Journal of Bionics Engineering **2**: 1-14.

Martinez, M. M. 1996. Issues for aquatic pedestrian locomotion. *American Zoologist* **36**: 619-627.

Merz, R. A. and Edwards, D. R. 1998. Jointed setae - their role in locomotion and gait transitions in polychaete worms. *Journal of Experimental Marine Biology and Ecology* **228**: 273-290.

Mettam, C. 1967. Segmental musculature and parapodial movement of *Nereis diversicolor* and *Nephthys hombergi* (Annelida: Polychaeta). *Journal of Zoology* **153**: 245-275.

Müller, U. K., Stamhuis, E. J. and Videler, J. 2002. Riding the waves: the role of the body wave in undulatory fish swimming. *Integrative and Comparative Biology* **42**: 981-987.

Rice, W. R. 1989. Analyzing tables of statistical tests. *Evolution* **43**: 223-225.

Scaps, P. 2002. A review of biology, ecology and potential use of the common ragworm *Hediste diversicolor* (O.F. Müller) (Annelida: Polychaeta). *Hydrobiologia* **470**: 203-218.

Schroeder, P. C. 1984. Chaetae. In *Biology of the Integument. Vol. I. Invertebrates* (Eds. Bereiter-Hahn, J., Matoltsy, A. G. and Richards, K. S.). Springer-Verlag. New York: 297-309.

Smith, J. E. 1957. The nervous anatomy of the body segments of nereid polychaetes. *Philosophical Transactions of the Royal Society of London. Series B.* **350**: 135-196.

Stamhuis, E. J. Basics and principles of particle image velocimetry (PIV) for mapping biogenic and biologically relevant flows. *Journal of Aquatic Ecology. In Press.*

Thiel, M. and Reise, K. 1993. Interaction of nemertines and their prey on tidal flats. *Netherlands Journal of Sea Research* **31**: 163-172.

Trevor, J. H. 1977. The burrowing of *Nereis diversicolor* O. F. Müller, together with some observations on *Arenicola marina* (L.) (Annelida: Polychaeta). *Journal of Experimental Marine Biology and Ecology* **30**: 129-145.

Verger-Bocquet, M. 1992. Polychaeta: sensory structures. In *Microscopic Anatomy of Invertebrates. Vol. 7. Annelida* (Eds. Harrison, F. W. and Gardiner, S. L).Wiley-Liss Inc. Vol 7: 181-196.

Woodin, S. A. and Merz, R. A. 1987. Holding on by their hooks: anchors for worms.

Evolution **41**: 427-432.

Wootton, R. J. 1999. Invertebrate paraxial locomotory appendages: design, deformation and control. *Journal of Experimental Biology* **202**: 3333-3345.

Chapter 6

Continuous jet-like propulsion in an errant polychaete

A shortened version is submitted to the Journal of Experimental Biology.

Hesselberg, T. Stamhuis, E. J., Williams, J. and Vincent, J. F. V. Continuous jet-like propulsion in an errant polychaete. *Journal of Experimental* Biology. In review.

6 Continuous jet-like propulsion in an errant polychaete

Thomas Hesselberg[1], Eize J. Stamhuis[2], John Williams[1] and Julian F.V. Vincent[1]

1. Centre for Biomimetic and Natural Technologies. Department of Mechanical Engineering. University of Bath. Claverton Down. BA2 6AY. Bath. UK.
2. Department of Marine Biology. Biological Centre. University of Groningen. Kerklaan 30. P.O.Box 14. 9750 AA Haren (Gn). The Netherlands

Abstract: Jet-propulsion is found in a range of animals, including jelly fish, salps and squids. Most, however, use the same mechanism of periodic jet-propulsion, where a body cavity ejects water during a power stroke and refills during a recovery stroke. Here we present evidence for a novel method of continuous jet-like propulsion generated by oscillating appendages in a swimming errant polychaete. Flow visualisation, using the digital particle image velocimetry (DPIV) method, revealed two long and narrow jets in the wake behind swimming juvenile *Nereis diversicolor*. The width of the jets did not significantly increase nor did the velocity of the fluid in the jets significantly decrease half a body length into the jet. Examination of the fluid flow around the crest of the body wave where the parapodial power stroke occurred and the kinematics of the parapodia confirmed that the jets were generated by the parapodia. Lateral views of the swimming worms indicated some movement in the third dimension, which probably explains the scattered patches of higher water velocity found along the jets.

KEYWORDS: kinematics, swimming, jet propulsion, DPIV, nereidids

6.1 Introduction

Propulsion under water is achieved by transferring momentum to the surrounding liquid. At higher Reynolds numbers the most common way is by undulating the whole or part of the body as found in insect larvae (Brackenbury 2004; 2002), fish (Müller *et al.* 2002; 2000; 1997), amphibians (Gillis 1997; Liu *et al.* 1996; Wassersug and Hoff 1985), reptiles (Graham *et al.* 1987) and marine mammals (Fish 2000). Undulatory locomotion has traditionally been divided into three broad categories (Breeder 1926). Ostraciform or thunniform mode seen in tuna and whales (Biewener 2003), where the body is rigid and only the tail is undulating. Carangiform mode seen in most fish such as cod and trout (Biewener 2003), where most of the body is rigid except the posterior part. Anguilliform mode seen in eels (Gillis 1998) and snakes (Graham *et al.* 1987), where most if not all of the body is undulating. Thrust is generated mainly by

drag in anguilliform swimmers and mainly by lift in carangiform and ostraciform swimmers (Biewener 2003). An alternative method of generating thrust at lower and intermediate Reynolds numbers is to oscillate one or several pairs of appendages as found for instance in insects (Nachtigall 1980), crustaceans (Williams 1994a), amphibians (Stamhuis and Nauwelaerts 2005), turtles (Pace *et al.*2001), during slow swimming and manoeuvring by the pectoral fins in fish (Drucker and Lauder 1999) and in penguins (Hui 1988). Thrust is generated by drag on the appendages, which typically function to maximise drag in the power stroke and minimise it in the recovery stroke by a change of effective area and/or by bending and torsion (Wootton 1999). A third way of generating thrust is jet propulsion. This involves ejecting a mass of water in the opposite direction of movement and is found in jellyfish (McHenry and Jed 2003; Colin and Costello 2002), scallops (Cheng and DeMont 1996) and squids (Bartol *et al.*2001). Most known instances of jet propulsion involve a cycle with a propulsive phase ejecting water from a body cavity and a recovery phase where water slowly refills the cavity. This is periodic jet propulsion (Weihs 1977). The only previously described example of continuous jet propulsion is found in pyrosomes, where ciliary activity in the individual zooids are responsible for generating jets (Bone 1998). Unfortunately no studies have yet been conducted on their swimming kinematics or their wake structure.

Common for the wake of most of these propulsive mechanisms is the shedding of individual vortex rings (Stamhuis *In press*; Linden and Turner 2004), whether it is two discrete rows of vortices as in the wake of the swimming damsel fly larvae (Brackenbury 2002), the reverse von Karman vortex street with alternate rotating vortices found in the wake of fish (Müller *et al.*1997; Blickhan *et al.*1992) or individual shedding of vortices in the wake of oscillating appendages such as the pectoral fin in fish (Drucker and Lauder 1999) and the hind legs in swimming frogs (Stamhuis and Nauwelaerts 2005). Swimming by jet propulsion generates vortices due to the periodic nature of the mechanism, in jelly fish shedding of individual vortex rings occurs at the beginning of both the propulsive and recovery phase (Dabiri *et al.*2005; Colin and Costello 2002).

Here we present evidence for a novel method of continuous jet-like propulsion in the errant polychaete *Nereis diversicolor*, generated not by ejection of water from a body cavity but by a conveyor belt-like action from a succession of appendages. Contrary to periodic jet propulsion and most other types of propulsion no vortices were observed in the wake of swimming worms, instead two long distinct jets were found.

The ragworm *N. diversicolor* is an errant polychaete with a well-developed head bearing sense organs and a pair of lateral appendages – the parapodia – on each segment. It inhabits U- or Y-shaped burrows in a range of estuarine substrates including sand and mud (Scaps 2002). The worm usually moves by slow or fast crawling when it emerges from its burrow to feed at night. During slow crawling the body is held rigid and the parapodia are oscillating in a leg-like fashion with contact to the substrate during the power stroke (Gray 1939). During fast crawling the parapodial cycle is coupled with small amplitude body undulations so that the power stroke occurs at the crest of the forward moving body wave (Gray 1939). The ragworms are also capable of swimming, but in the juveniles this gait is rarely used. However, it might be of vital importance in escaping from predators such as nemertines (Thiel and Reise 1993). In swimming the body waves travel in the same direction as the animal is moving (Clark and Tritton 1970; Taylor 1952; Gray 1939), contrary to what is found in other undulatory swimmers such as eels (Gillis 1998) and snakes (Graham *et al.* 1987) where the body waves travel from head to tail. Taylor (1952) showed that a rough cylinder can generate force in the opposite direction to that in which it is moving and proposed a model where the parapodia provide the roughness which increases the worm's longitudinal force coefficient and thus allows it to generate thrust when the body waves move from tail to head. However, such a model, where thrust is generated by the body with passive parapodia, is not supported by observations and data from a range of swimming errant polychaetes. Clark and Tritton (1970) proposed that the parapodia work as drag-based paddles and the body undulations enhance this action by coupling the parapodial cycle with the body wave so the power stroke occurs at the crest of the body wave where exposure to the water, and thus drag, is maximised and interference from neighbouring parapodia is minimised. The recovery stroke occurs at the trough where drag is minimised (Clark and Tritton 1970; Gray 1939). This effect is increased by muscles that retract the parapodium into the body during the recovery stroke and protract it during the power stroke (Mettam 1967).

The flow visualisation and kinematic data presented here show that the parapodia are the thrust producers, by linking the backward projected jets with the parapodial power strokes at the crest of the body wave.

Extruding laterally from the parapodia are bundles of setae, which are thought to function primarily to generate friction with the ground during crawling (chapter 3; Hesselberg and Vincent 2006; Gustus and Cloney 1973). Some evidence points to a

possible function of adding extra area to the parapodia and thus enhancing propulsive drag during the power stroke in swimming worms (chapter 3; Hesselberg and Vincent 2006; Merz and Edwards 1998), although other evidence suggests no such effect (chapter 5; Hesselberg and Vincent *In press*). However, due to the small size of the individual setae it was not possible to observe their function with the cameras and lenses used in this study. Therefore only kinematics of the parapodia themselves is included in the analysis presented here.

6.2 Materials and methods

6.2.1 Kinematics and flow visualisation

Juvenile *Nereis diversicolor* were collected in the Severn Estuary, near Bristol, U.K. and at the dikes near Delfzijl, The Netherlands. No differences in size or swimming behaviour were found between the two populations and no further distinction was therefore made between them in this study. At the laboratory the worms were housed in sand-filled containers placed in a tank with re-circulating artificial sea water (salinity of 30 ppt) in a room maintaining a stable temperature of 16.5 °C. Worms were kept between one and three weeks before being used in experiments. They were fed every second day with TetraMIN Pro flakes.

Worms were introduced to the experimental container one hour prior to experimentation to acclimatise to laboratory conditions (temperature around 20 °C). The experimental set-up consisted of a 240 x 240 x 55 mm glass container filled with 1 L of artificial sea water (salinity of 30 ppt) seeded with 25 μm Pliolite particles. A partition and two plastic blocks were placed in the container to direct the swimming nereidid to the camera focal area (Fig. 6.1). A CW Krypton Laser (Coherent Innova K, Coherent Lasers Inc., Santa Clara, California, USA, $\lambda = 647$ nm, $P_{max} = 1$ W), fitted with either optical lenses or a sheet probe, provided a homogenous 1 mm thick horizontal laser sheet inside the focal area. The height of the laser sheet depended on the swimming behaviour of the particular worm, but was usually set at 3-5 mm. A camera mounted above the focal area recorded the movement of the worm and the particles in the surrounding water. Two camera systems were used. For high resolution recordings of the whole worm and its wake a Kodak Model ES 1.0 digital camera (30 frames/sec at a resolution of 1024 x 1024 pixels) fitted with a Nikon zoom lens was used and for high speed recordings of the parapodial movement and the fluid flow around them a Kodak

MotionCorder high speed camera (250 frames/sec at a resolution of 512 x 480 pixels) fitted with a Nikon macro lens was used. The worms were kept in the experimental container for maximum one hour and, depending on how cooperative the worm was, up to three recordings were made per worm. Worms that were successfully recorded were then anaesthetised with clove oil and their length measured.

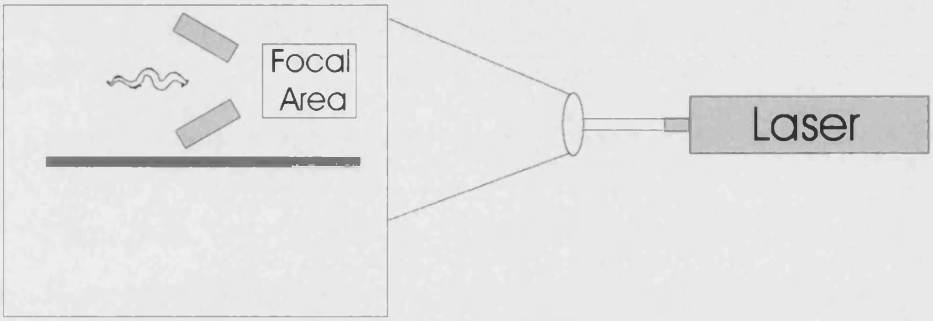

Fig. 6.1. The experimental set-up. Note that the camera placed above the focal area is not shown in this figure.

6.2.2 Analysis and kinematic parameters

The recorded frames with the illuminated particles were analysed pair wise using a commercial digital particle image velocimetry program (Swift 4.0. Originally developed at the University of Groningen. Dutch Vision Systems, Breda, The Netherlands). Image cross-correlation was performed with convolution filtering applying a 67 x 67 pixel interrogation area for the high resolution images and a 57 x 57 pixel interrogation area for the low resolution images. For both a 50% overlap was used and peaks were located using a COGW (centre of gravity weighed to grey value) method (Stamhuis *et al.*2002). Erroneous vectors and obvious outliers were removed manually and replaced using 2D spline interpolation (Stamhuis *In press*). The output from this analysis was colour coded velocity diagrams with the velocity vectors shown and a data file with the magnitudes of the velocity vectors and their corresponding x-y coordinates. The latter was analysed with a MATLAB (Version 7.0, The MathWorks Inc., 2004) routine to generate information on jet width and average jet speed as a function of distance from the beginning of the jet (appendix B).

Kinematic values were found by digitising the recordings with a custom made LabVIEW (Version 7.1, National Instruments, 2004) program, which allowed an arbitrary number of points to be manually digitised (appendix B). For the high

resolution recordings this included the anterior point of the prostomium (excluding the cirri and antennae), the posterior point of the pygidium (excluding the cirri) and all body wave crest peaks. Depending on the size and the speed of the swimming worm the number of digitised points per frame varied between 7 and 9. Since all points on the body of the worm were moving in both the x and y direction it was not possible to use reference points for calculating the kinematic values. Instead a MATLAB routine was used that found the global linear regression of all digitised points from all frames and then projected the digitised points from each frame onto the global regression line to obtain prostomium, crest and pygidium positions (appendix B). Only recordings in which the worm swam straight were used. For the high speed recordings one parapodium was followed through each frame with one digitised point at the base and one at the tip of the parapodium (excluding the setae).

A 6 marker calibration grid was filmed after each recorded swimming event and either the Simple Scaling Method (for the PIV analysis) or the Two-Dimensional Direct Linear Transformation method (for the kinematic analysis) was used (appendix A; Brewin and Kerwin 2003).

The following kinematic parameters were extracted from the recordings.

Speed: The speed of the worm was found by taking the difference in position between successive frames of the midpoint between the prostomium and pygidium positions projected onto the global regression line and multiplying with the frame rate (30 fps) and averaged over all frames.

Wave speed: To minimise variation and because it is the largest, and therefore arguably the most important in locomotion, the second body wave crest was chosen for analysis. The difference in crest position relative to prostomium projected onto the global regression line between each frame was multiplied with the frame rate (30 fps) and averaged over all frames. Note that wave speed was expressed in the reference frame of the worm and not in the global reference frame.

Amplitude: The distance between the peak of the second body wave crest and its position projected onto the global regression line and averaged over all frames.

Wavelength: The distance between the 2^{nd} and 4^{th} body wave crest projected onto the global regression line and averaged over all frames.

Reynolds number: Calculated from the following equation $Re = \rho l U / \mu$, where ρ is sea water density (1.022×10^3 kg m^{-3}), l is a characteristic linear dimension, here the length of either the whole worm or the parapodium, U is the average speed of either the worm or the parapodium tip during the power stroke and μ is the viscosity of sea water (1.072×10^{-3} kg $m^{-1}s^{-1}$).

Stroke frequency: The frequency of a parapodial cycle including power and recovery stroke. Measured from recordings where one parapodium was digitised for an entire cycle.

Power stroke: The power stroke was defined to start at the frame where the parapodium showed a clear difference in angle from the previous frame and ending when no clear difference in angle was visible. Angle differences were visibly assessed from figures of parapodial movement (see figure 6.2 for an example).

Duration: The duration of the power stroke.

Parapodium length: The length of the parapodium during the power stroke relative to its average length over the entire cycle. Length was measured as the distance between the digitised point at the base and the digitised point at the tip of the parapodium.

Tip velocity: The velocity of the tip of the parapodium during the power stroke. It was measured as differences in position of the tip from frame to frame multiplied with the frame rate (250 fps). Tip velocity, therefore, included movements in two dimensions.

Parapodial angle: The angle of the parapodium in the global reference system. Found with trigonometry from the x-y coordinates of the digitised point at the base and at the tip of the parapodium.

Stroke angle: The absolute difference in angle between the beginning and the end of the power stroke.

Angular velocity: The difference in angle of the parapodium from one frame to the next during the power stroke multiplied with the frame rate (250 fps).

Distance along jet: From the output images of the DPIV analysis lines were drawn around the most conspicuous of the two jets in the wake, or around the single jet immediately behind the body wave crest, with the first line indicating the start of the jet. The outer limits of the jet were located where the velocity gradient of the jet approached the background velocity gradient, which occurred at vector magnitudes of approximately 15% of the maximum vector magnitude found in the jet. Starting from

the first line a midline was drawn between the two outer limits of the jet until the end of the jet. Distance from the start of the jet was measured along this midline

Jet width: At specific distances along the jet midline the nearest point distance to both of the outer jet limits was measured and added together to give the width of the jet.

Jet speed: At specific intervals along the jet midline, the average jet speed of all the velocity vectors in the area enclosed by the nearest point line to both of the two outer jet limits, the outer limits of the jet and to the previous interval limits or the starting line.

6.2.3 Lateral view

Juvenile *N. diversicolor* were collected in the Severn Estuary, near Bristol, U.K. and placed in large mud filled containers in a climate cabinet at 10°C for a maximum of four weeks, during which they were fed TetraMIN Pro flakes twice a week. One week prior to experimentation worms were placed individually in sand-filled containers placed in an aerated tank containing artificial sea water (salinity of 22 ppt) maintained at room temperature. Each worm was fed one TetraMIN Pro flake every second day. Recording was done in a 150 x 85 x 100 mm clear plastic tank divided laterally by a black partition to give contrast between worm and background. The tank was filled with artificial seawater (salinity of 22 ppt) to a height of 40 mm. Swimming worms were recorded at 125 frames/sec at a resolution of 480 x 420 pixels with a digital high speed camera (The MotionScope 2000S, Redlake MASD, Inc) placed in front of the tank. Worms were prodded with a plastic pipette in order to facilitate swimming. Only worms that swam in a horizontal direction and showed normal swimming behaviour within 15 minutes of being introduced into the tank were recorded. After a successful recording the worm was anaesthetised with 7.5% MgCl and its length measured.

Kinematic values were found as described above. The digitised points included the anterior point of the prostomium (excluding the cirri and antennae), the posterior point of the pygidium (excluding the cirri) and all visible body wave crests. The number of digitised points per frame varied between 6 and 9 depending on the size and speed of the swimming worm. Analysis was done in a spreadsheet. Only recordings were used where the worm swam in a stable level direction. Calibration was done as described above.

The following kinematic parameters were extracted from the recordings.

Speed: The speed of the worm was found by taking the difference in position of the prostomium between the first and the last frame in the recording multiplied with the frame rate (125 fps) and divided by the number of frames between the first and the last frame in the recording.

Height above ground: The vertical distance between positions on the worm (prostomium, body and pygidium) and the bottom of the experimental tank. The distance was averaged over all digitised points in the recording (for the body also averaged between 4 and 7 points per frame) and then averaged over all recordings.

Height difference: The vertical distance between the highest and the lowest vertical position on the body of the swimming worm. The height above the ground was averaged for each point in the recording and the difference between the highest and the lowest point was then averaged for all recordings.

6.2.4 Statistics

The relations between distance and jet width and between distance and jet speed were analysed statistically by a one-way ANOVA using either jet width or jet speed as an independent variable with distance from the beginning of the jet as a factor. The initial significance level was set at 5%. The test was performed using SPSS 12.0 (SPSS Inc., 2003).

6.3 Results

Nereis diversicolor rarely swims spontaneously and does not respond well to being prodded. Therefore only a small fraction of all swimming bouts were recorded and due to turning or irregular swimming fewer than half the recordings were analysed.

6.3.1 Kinematics

The variation both between individual worms and between different recordings of the same individual was large (Table 6.1). This was partly due to the lack of fixed points on the worm body to digitise and partly due to differences in swimming parameters and the resulting kinematic values. The main reason for the latter was that when the worm was occasionally poked to make it swim its responses was very variable. The speed of the worm was approximately half of the wave speed and the

amplitude was around 1/5 of the wavelength. Reynolds numbers were between 800 and 2000.

During its power stroke the parapodium moves in the opposite direction to the worm with respect to the global reference system and the surrounding water (Fig. 6.2a), thereby allowing the parapodium to impart momentum to the water and thus to generate thrust. During the power stroke at the crest of the body wave the base of the parapodium was almost stationary with respect to the global reference system with the tip of the parapodium rotating around it (Fig. 6.2a). The opposite was seen in the trough of the body wave where the tip was almost stationary with the base rotating around it (Fig. 6.2a). Another conspicuous feature was the variation in parapodial length (Fig. 6.2b) as it was retracted into the body during the recovery stroke and protracted during the power stroke (Mettam 1967). During the power stroke the parapodium was more than 1/3 longer than the average length for the entire stroke cycle (Table 6.2). The parapodium was oscillating at 4 Hz and swept an angle of almost 80° during the power stroke (Table 6.2). The Reynolds number for the parapodium varied between 40 and 180 during the power stroke. All kinematic values are summarised in Table 6.2.

Table 6.1. Swimming kinematics

	Mean	n	Std. dev.
Length (mm)	62.0	4	7.0
Speed (mm/s)	22.4	8	5.8
Wave speed (mm/s)	42.1	8	11.2
Amplitude (mm)	2.5	8	0.5
Wave length (mm)	12.4	8	1.0
Reynolds number	1347	8	434

Table 6.2. Parapodium Kinematics

	Mean	n	Std. dev.
Worm length (mm)	85.3	3	24.6
Stroke frequency (s^{-1})	4.0	3	0.7
During the powerstroke			
Duration (ms)	38.3	7	6.9
Parapodium length*	136%	5	5%
Tip velocity (mm/s)	83.7	7	20.1
Stroke angle (degrees)	78	5	48
Angular velocity (degrees/s)	2432	7	421
Reynolds number	118	7	51

* The average length of the parapodium for the entire cycle was $l = 0.9 \pm 0.1$ ($n = 5$).

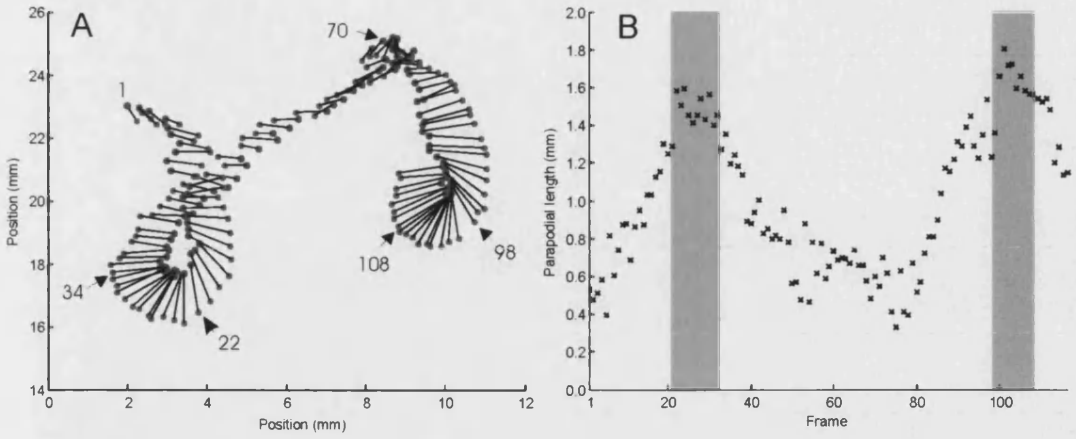

Fig. 6.2. The digitised single parapodium of a swimming *Nereis diversicolor*. a) Location of the parapodium in each frame in a global coordinate system (both axes in mm). The green circles indicate the base of the parapodium and the red circles indicate the tip of the parapodium. The arrows show the frame numbers at the beginning of the power stroke and at the troughs. The worm was moving from left to right. b) The length of the parapodium (in mm) as a function of frame number. The shaded area highlights the location of the power stroke.

6.3.2 Flow visualisation

Two distinct narrow bands of water with a significantly higher fluid velocity than the surroundings, were obvious from all the recordings (Figs. 6.3, 6.4). Any other fluid flow phenomena were irregular and infrequent, although sometimes water was pressed forward by the prostomium or dragged along by the pygidium (Fig. 6.4). By combining the strain rate and divergence outputs from the DPIV analysis it is possible to get an indication of the presence of any significant 3D flow components (Stamhuis *In press*). Using this method in the present study did not show any consistent out of plane fluid flow.

Close-up recordings of the fluid flow behind the body wave crest revealed that the jet was very conspicuous and originated immediately behind the crest where the power strokes of the parapodia took place (Fig. 6.5). The speed of the water was considerably higher in the vicinity of the parapodia than further along the jets in the wake of the swimming worm (Figs. 6.3, 6.4, 6.6). Except for minor rotational fluid flow in the troughs of the body wave (Fig. 6.5), no other fluid flow phenomena were visible in the recordings. As with the flow around the entire worm, no consistent out-of-plane movement of the water was indicated by the DPIV analysis in the flow close to the body.

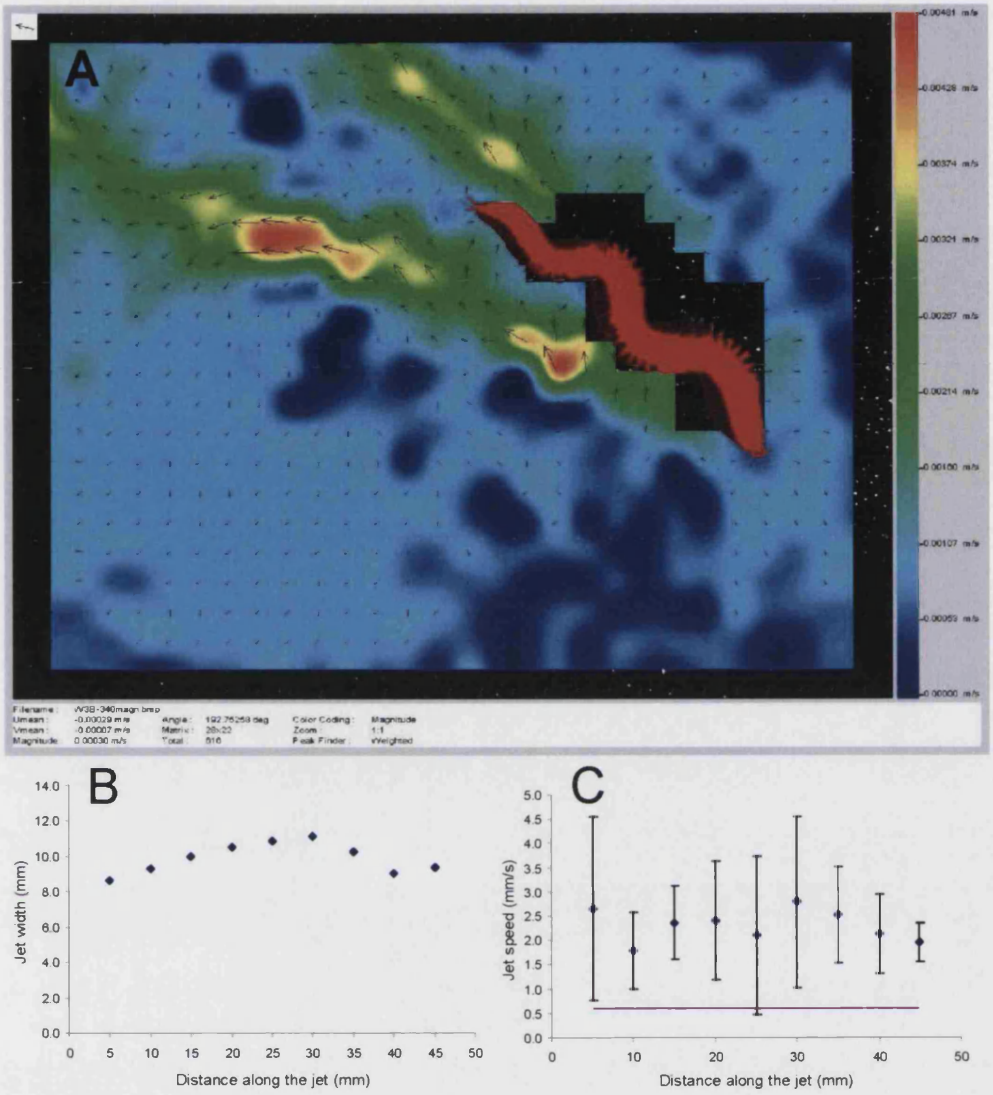

Fig. 6.3. The wake of a swimming *Nereis diversicolor*. a) Digital Particle Image Velocimetry results of two subsequent frames in a recording of a swimming worm. The worm was moving from the top left corner to the bottom right corner. The filled red areas show the position of the worm in the two successive frames used for DPIV analysis. The black area is where the body of the worm or the proximity to the frame limits prevented reliable velocity vectors. The colour gradient shows increasing velocities of the particles in the water from blue to red, with a maximum velocity of 5 mm/s. Individual velocity vectors are also shown. b) The width of the right hand jet as a function of distance along the jet. The x-axis gives the distance from the beginning of the jet in mm and the y-axis the width in mm. c) The average speed of the right hand jet as a function of distance along the jet. The x-axis gives the distance from the beginning of the jet in mm and the y-axis the average speed of the jet in mm/s. The dashed horizontal line shows the average speed of the background flow. The error bars indicate the standard deviation from the mean.

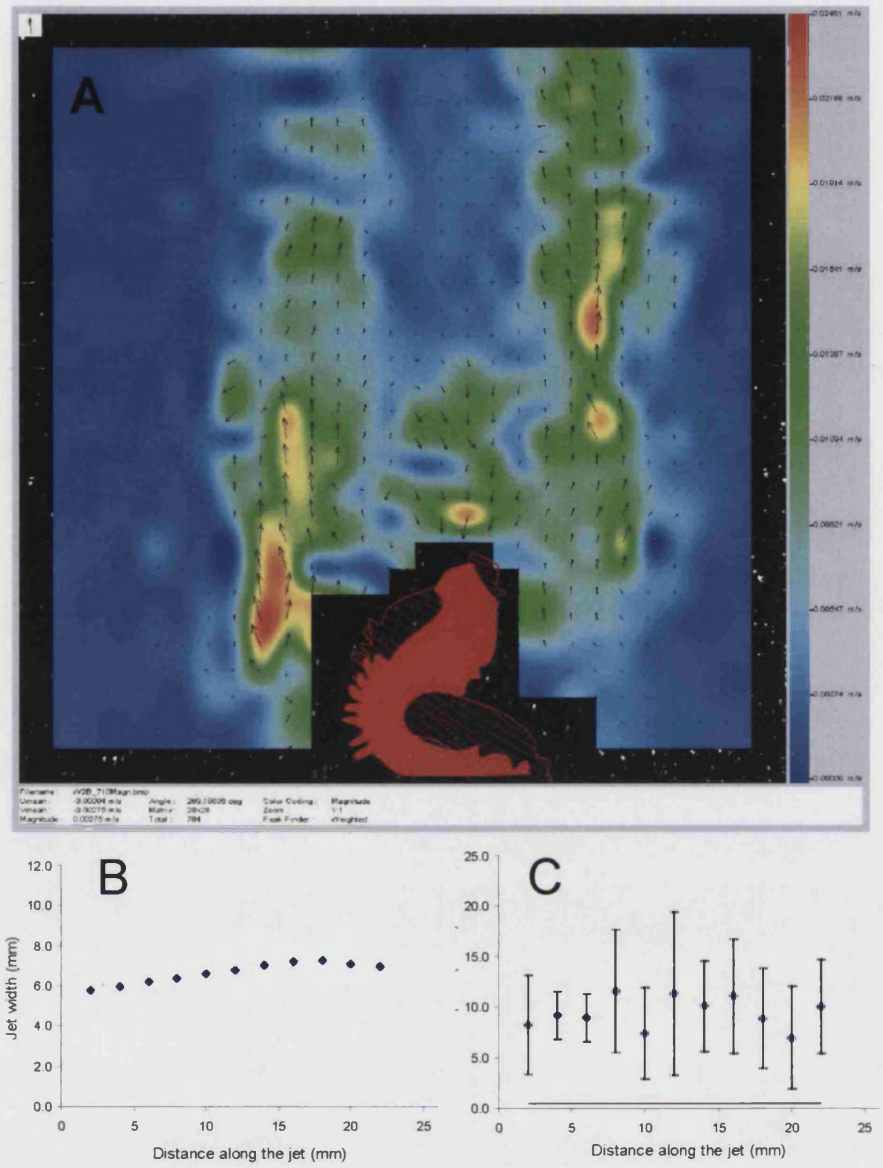

Fig. 6.4. The wake of a swimming *Nereis diversicolor*. a) Digital Particle Image Velocimetry results of two subsequent frames in a recording of a swimming worm. The worm was moving from the top to the bottom of the image and only the last third of the worm is visible. The filled red areas show the position of the worm in the two successive frames used for DPIV analysis. The black area is where the body of the worm or the proximity to the frame limits prevented reliable velocity vectors. The colour gradient shows increasing velocities of the particles in the water from blue to red, with a maximum velocity of 25 mm/s. Individual velocity vectors are also shown. b) The width of the left hand jet as a function of distance along the jet. The x-axis gives the distance from the beginning of the jet in mm and the y-axis the width in mm. c) The average speed of the left hand jet as a function of distance along the jet. The x-axis gives the distance from the beginning of the jet in mm and the y-axis the average speed of the jet in mm/s. The dashed horizontal line shows the average speed of the background flow. The error bars indicate the standard deviation from the mean.

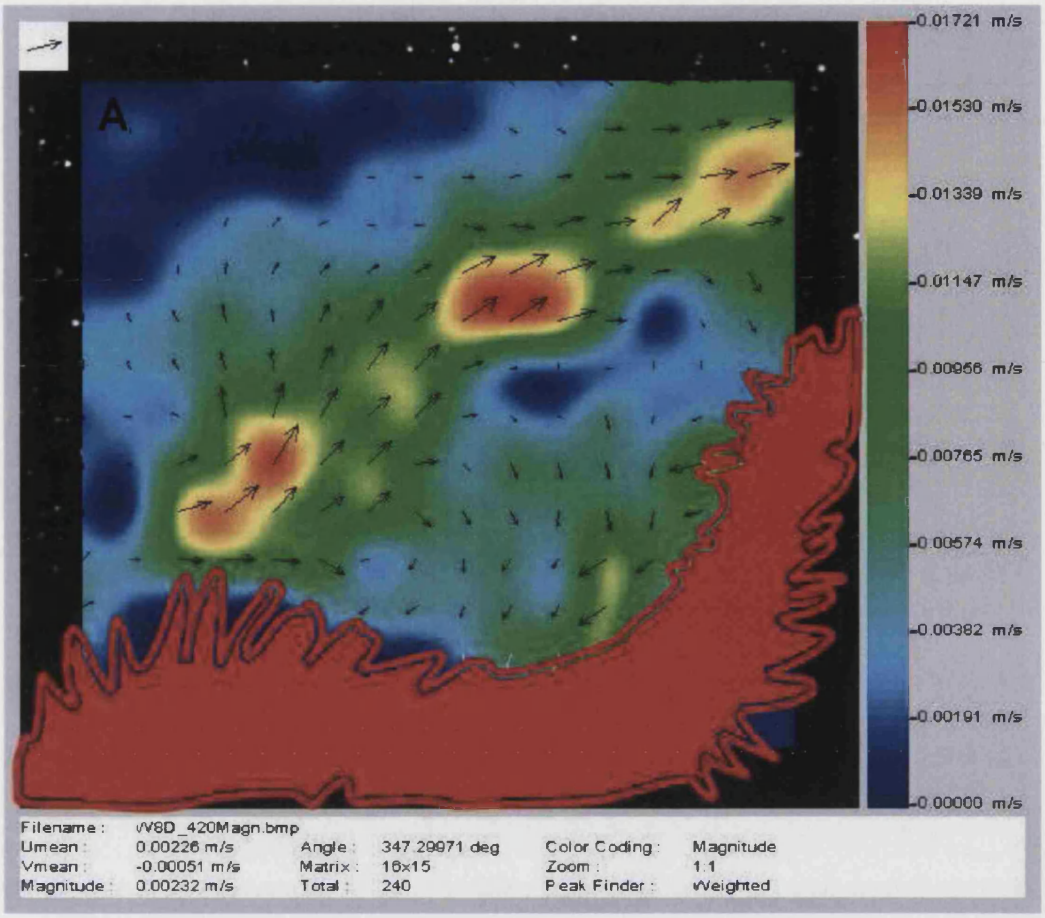

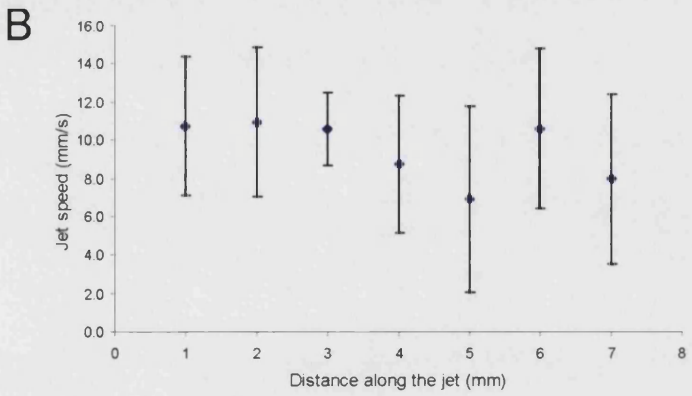

Fig. 6.5. The fluid flow around a body wave crest of a swimming *Nereis diversicolor*. a) Digital Particle Image Velocimetry results of two successive frames in a recording of a swimming worm. The worm was moving from the right to the left corner of the image. The filled red area shows the position of the worm. The colour gradient shows increasing velocity of the particles in the water from blue to red, with a maximum velocity of 17 mm/s. Individual velocity vectors are also shown. b) The average speed of the jet as a function of distance along the jet. The x-axis gives the distance from the beginning of the jet in mm and the y-axis the average speed of the jet in mm/s. The error bars indicate the standard deviation from the mean.

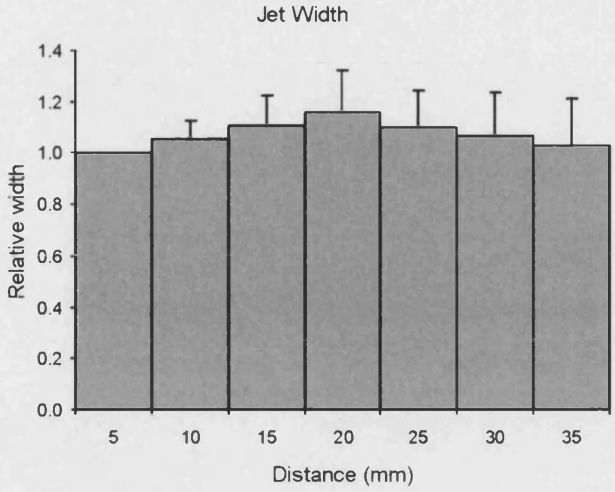

Fig. 6.6. The width of the jet in the wake of swimming *Nereis diversicolor* as a function of distance along the jet. The x-axis gives the distance in mm from the beginning of the jet and the y-axis gives the width in each distance interval relative to the width of the jet in the 0-5 mm interval. The mean of the first interval was 8.5 mm ± 1.7 mm (n = 11). For the other intervals the sample size varied between 4 and 11. The error bars indicate the standard deviation from the mean

One of the surprising outcomes of the DPIV analysis was that the jet did not spread in the immediate wake of the worm (Figs. 6.3, 6.4). If the initial 5 mm interval is set to 100% and the following intervals are re-calculated relative to it for all recordings, then a slight increase was observed in the following intervals, but no clear trend was observed (Fig. 6.6). A one-way ANOVA test performed on the actual widths showed no significant differences in jet width along the length of the jet ($F_{(6,55)} = 17.1$, $P = 0.23$).

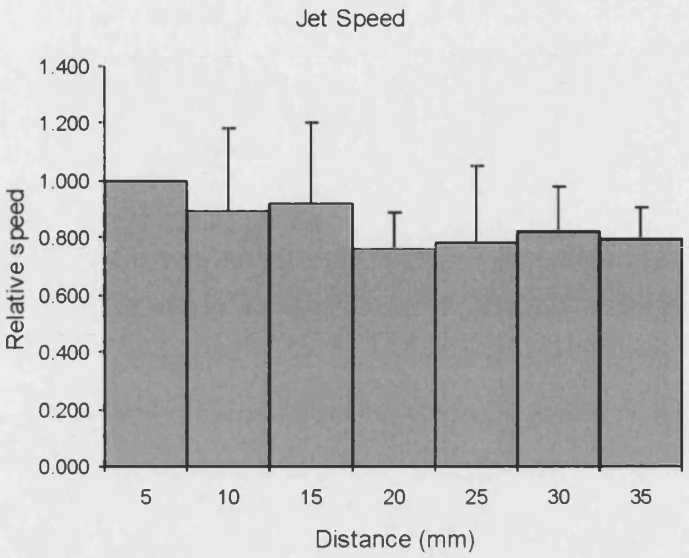

Fig. 6.7. The speed of the jet in the wake of swimming *Nereis diversicolor* as a function of distance along the jet. The x-axis gives the distance in mm from the beginning of the jet and the y-axis gives the jet speed in each distance interval relative to the speed of the jet in the 0-5 mm interval. The mean of the first interval was 5.2 mm/s ± 1.7 mm/s (n = 11). For the other intervals the sample size varied between 4 and 11. The error bars indicate the standard deviation from the mean.

The largest velocity vectors in the jets were found at the beginning (Figs. 6.3, 6.4). However, quite often further along the jet other areas of high velocity were found (Fig. 6.3). It was therefore not possible to assess the decrease of jet speed along the length of the jet. But if the initial 5 mm interval is set to 100% and the following intervals are re-calculated relative to it for all recordings, then a slight decrease of jet speed was visible along the length of the jet (Fig. 6.7). However, a one-way ANOVA performed on the actual jet speeds showed that this decrease was not significant ($F_{(6,55)} = 1.9$, $P = 0.10$).

This negligible decrease in speed of the jet was even more noticeable in the immediate vicinity of the power strokes on the crest of the body wave (Fig. 6.5). This time using intervals of 2 mm but otherwise again taking the relative jet speeds gave some variation along the length of the jet, but no overall decrease in jet speed (Fig. 6.8). A one-way ANOVA test confirmed this by showing that there were no significant differences in jet speed along the jet ($F_{(9,30)} = 0.8$, $P = 0.64$).

Recordings were done for a limited time after the worm had disappeared from the frame and no information is available on what the worms did after they disappeared

from the frame. In most cases, though, they probably ceased swimming as swimming bouts generally were short. Unfortunately, therefore, it was not possible to get quantitative data about the longevity of the jets in the wake of a swimming worm. However, in one case there were still visible jets 85 frames (2.6 sec) after the worm had disappeared. The average magnitude of the vectors in the most conspicuous jet was 45% of the jet speed immediately behind the swimming worm or 2.1 mm/s ± 1.0 mm/s (n = 91), which was significantly larger than the surrounding water velocity of 0.7 mm/s ± 0.3 mm/s (n = 44).

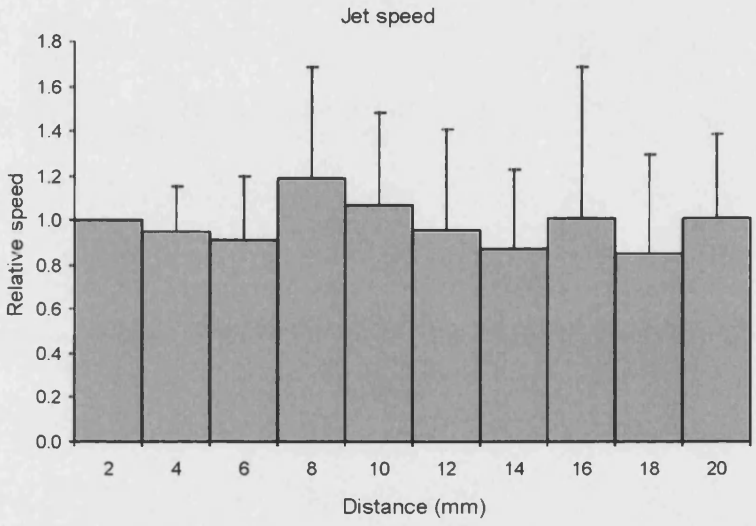

Fig. 6.8. The speed of the jet immediately behind a body wave crest of swimming *Nereis diversicolor* as a function of distance along the jet. The x-axis gives the distance in mm from the beginning of the jet and the y-axis gives the jet speed in each distance interval relative to the jet speed of the jet in the 0-2 mm interval. The mean of the first interval was 14.1 mm/s ± 2.6 mm/s (n = 5). For the other intervals the sample size varied between 3 and 5. The error bars indicate the standard deviation from the mean.

6.3.3 Lateral view

Side views of swimming worms revealed that they not only oscillated in two dimensions, but also oscillated somewhat in the lateral plane (Fig. 6.9). The average height difference between the highest and the lowest point on the body of the swimming worms was around 2 mm (Table 6.3). In most of the recordings both the prostomium and the pygidium of the worm were closer to the ground than the body (Table 6.3). In several cases it appeared as though the worm was actually making contact with the

bottom surface with its antennae and anterior cirri. The worms quite consistently preferred to swim close to the ground rather than in open water when swimming horizontally. However, in many cases, which were excluded from the present study, the worm swam upwards toward the surface and upon reaching it swam downwards. This change of direction between upwards and downwards swimming did frequently last for the entire swimming bout. The worms used for the lateral view recordings were slightly smaller than the ones used for the flow visualisation recordings but swam slightly faster (Table 6.1, 6.3).

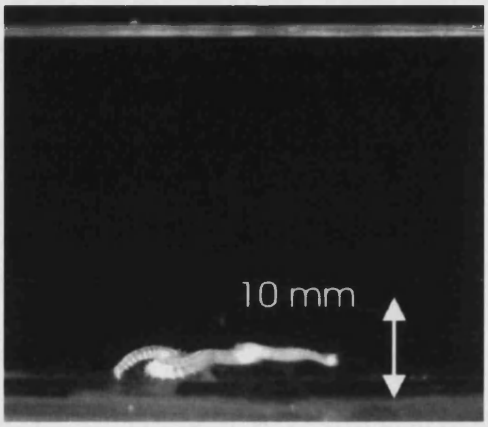

Fig. 6.9. Lateral view of a swimming *Nereis diversicolor*. The white arrow scale is 10 mm and the horizontal line in the upper part of the picture is the water surface.

Table 6.3. Swimming kinematics – Lateral View

	Mean	Std. dev.
Length (mm)	53.9	7.2
Speed (mm/s)	30.5	8.8
Height above ground		
Prostomium (mm)	2.2	0.7
Body (mm)	3.2	0.7
Pygidium (mm)	2.3	0.9
Height difference (mm)	2.2	0.9

All values were calculated from a sample size of 14

6.4 Discussion

We have found two distinct jets in the wake of swimming *Nereis diversicolor* juveniles. The velocity vectors from the DPIV revealed that the jets are long and narrow. Only an insignificant widening and a 20% decrease in water velocity were

observed in the first 35 mm of the jets. Unfortunately no information is available on the total length of the jet before it disintegrates, but jets were still visible 2.6 seconds after the worm had passed, which with an average swimming velocity of 22.4 mm/s (Table 6.1) gives a jet length of 58.2 mm. The jets were therefore visible at least one and most likely several body lengths away from the worm. This sends out a clear directional hydromechanical signal of the whereabouts of the swimming worm. Some animals use such hydromechanical signals to locate prey or mates (Kiørboe and Visser 2000, van Duren *et al.* 1998; Atema 1996) and this might therefore be one possible reason why the ragworms rarely swim in the wild.

Surprisingly, vortex traces are not visible in the wake, as might be expected from an animal moving in a fluid at intermediate or high Reynolds numbers (Linden and Turner 2004). Animals swimming by periodic jet propulsion, such as jelly fish, have start and stop vortices associated with the jet pulses (Dabiri *et al.* 2005; McHenry and Jed 2003). Oscillating appendages, such as the hind legs in swimming frogs (Stamhuis and Nauwelaerts 2005) and the pectoral fins in labriform swimming in fish (Drucker and Lauder 1999), result in shedding of a single or a pair of vortex rings. Such vortex rings were not found in the present study, probably because the short time between the power stroke of neighbouring appendages, and the presence of several simultaneous crests on the body of the worm, result in a conveyor-belt like action where the contribution of an individual appendage is masked by the overall flow generated. At the scale of the parapodia of the worm it might be beneficial to create a large flow street on each side of the worm and allow individual appendages to add momentum to it, instead of creating individual vortices that eventually merge, or probably decay before they merge. Thus momentum is added to the water without much immediate dissipation. This method of momentum transfer has not been found before in biological systems.

The first model of swimming in errant polychaetes proposed that thrust was generated by undulatory movement and that the parapodia function only in providing the required roughness to the body for the model to work (Taylor 1952). However, with more data it became clear that this model could not adequately explain swimming in these animals. Instead a model was proposed in which thrust is generated by the parapodia oscillating with the body undulations enhancing the function (Clark 1976; Clark and Tritton 1970). The wake of two distinct jets, cannot occur if the thrust is being produced by an undulating body. It must arise from being produced in a narrow region such as the parapodial power stroke on the crest of the body wave. Close-up DPIV data of the region around the crest of the body wave further supported this by indicating that the jets originate immediately behind the parapodial power stroke. The present study confirmed earlier observations on the behaviour of the parapodium during the locomotory cycle (Mettam 1967; Gray 1939). The base of the parapodium moved slightly backwards during the power stroke thus giving rise to loops in the path of parapodial movement. Furthermore, the length of the parapodium varied during the cycle. It was shortest around the troughs and longest during the beginning of the power stroke at the crest of the body wave. In the Clark and Tritton model (1970) the main rotational movement is presumed to be caused by muscles running from the parapodium to the body (Mettam 1967). However, J. Williams (*Unpublished*) showed theoretically by approximating the shape of the body undulations to semi-circles that the passive rotation due to each segment sliding along the body wave is enough to give a high rotational speed of the parapodium at the crest of the body wave. Using kinematic and morphological parameters for a swimming *N. diversicolor* similar to the ones found here, his model predicts an angular velocity of around 1100-4200 deg/s depending on the curvature of the crest (J. Williams *Unpublished*). Comparing it with the angular velocity of 2400 deg/s found in this study suggests that active rotation of the parapodia is not as important as previously believed. A more advanced computational model needs to be compared with a more extensive data set to determine the exact significance of active versus passive rotation of the parapodium

No direct force measurements were made here and, therefore, no detailed explanation can be given of how the forces that give rise to the jets were produced. But, as proposed by Clark and Tritton (1970) it is likely that the thrust is produced by the drag experienced by the backward moving parapodia during the power stroke. However, another force, the acceleration reaction, is also important for oscillating limbs (Daniel

1984). The acceleration reaction force opposes acceleration, where drag opposes velocity, and it arises from the force required to increase the kinetic energy of the fluid around the body whose speed is increasing (Daniel and Webb 1987). One measure of the importance of the acceleration reaction force is the reduced frequency parameter $\sigma = 2\pi fl/U$, where f is the oscillating frequency, l is the length of the limb and U is the forward speed of the animal. If the reduced parameter σ is greater than 0.5 then the acceleration reaction force is of importance (Martinez 1996). Using values given in Tables 6.1 and 6.2 the reduced frequency for a swimming *N. diversicolor* worm is: $\sigma = 2\pi \times 4\ s^{-1} \times 0.9$ mm / 22.4 mm/s = 1.0. The acceleration reaction force therefore appears to play an important role in thrust generation by the parapodia in swimming errant polychaetes. From some of the close-up DPIV images, which showed complex rotational fluid patterns in the troughs of the body wave, it is likely that other processes are occurring. One such process could be, as Clark (1976) suggested for the swimming in heteronereis, that water is being sucked into the parapodia as they start to separate on the leading edge on the body wave and then ejected on the crest. It is, furthermore, possible that the setae are of importance during swimming. Ablating the setae resulted in a reduced maximum swimming speed for the polychaete *Ophiodromus pugettensis* (Merz and Edwards 1998), although a recent study found no effect of ablating the neuropodial setae on swimming in *N. diversicolor* (chapter 5; Hesselberg and Vincent *In press*). The leakiness of an array of hairs is determined by the Reynolds number, the diameter of the hairs and the distance between them (Cheer and Koehl 1987). The setae are found in bundles on the parapodia and estimation of leakiness suggests that the setal bundles in errant polychaetes behave functionally as plates (chapter 5; Hesselberg and Vincent 2006). The setal bundles can retract and protract into the parapodium (Mettam 1967) and they could enhance the thrust generating effects of the drag and acceleration reaction forces acting on the parapodium. However, more detailed flow visualisation studies are needed to elucidate exactly how the parapodia and setae interact with the surrounding water during swimming.

No information is available on the energy usage or the power output of swimming errant polychaetes, so it is currently not possible to calculate the swimming efficiency of these animals. However, based on the complex swimming pattern involving both longitudinal and parapodial muscles and a swimming speed of only around 0.4 bodylength per second (data from Table 6.1), the swimming efficiency must be rather low. Compared to other anguilliform swimmers such as eels (1.4 BL/s - Tytell

and Lauder 2004), tadpoles (10 BL/s - Wassersug and Hoff 1985) and damselfly larvae (8 BL/s - Brackenbury 2002) juvenile nereidids are very slow swimmers. Most species of errant polychaetes swim very infrequently and usually only in response to certain predators or for reproducing (Thiel and Reise 1993; Clark 1961). The majority of nereidids metamorphose into a special reproductive stage, the heteronereis, which shows modifications of the parapodia by replacing normal setae with special paddle-shaped setae, enlargement of the parapodial muscles, histolysis of the body wall and the gut, development of special chemical sensory organs and enlargement of the eyes (Clark 1961). The heteronereis is adapted to continuous swimming during courtship and reproduction. It swims with small body amplitudes and powerful parapodial strokes and can reach speeds of up to 5 BL/s (Clark and Tritton 1970). This is more than 10 times faster than the speed of juvenile *N. diversicolor* measured in this study. Future studies on how the morphological and dynamical differences between the juvenile nereidid and the heteronereis affect the wake behind the swimming worms are necessary to further elucidate the interplay between the parapodia, the body wave and the surrounding fluid.

Previous studies on swimming in errant polychaetes assumed that they essentially undulate in the horizontal plane only (Merz and Edwards 1998; Clark and Tritton 1970; Gray 1939). The lateral views of the swimming worm presented here show that the difference between highest and lowest point on the worm body was 40% of that between a right and left hand body wave crest. This is not insignificant and presumably therefore 3D flow visualisation data is needed to get a full picture of the flow system over a swimming nereidid. Height differences in the power stroke as the crest moves forward probably explain the observed groups of higher velocity vectors along the length of the jets. If the 'jet motor' moves up and down then the maximum output velocity is only visible when the plane of the 'motor' and the plane of the DPIV laser sheet coincide. It is, however, unlikely that there was any strong 3D component in the flow around the swimming worm as it would then have been picked up during the analysis with the DPIV software. The lateral view observations, furthermore, showed that the worms prefer to swim in close proximity to the bottom and with the head often in direct contact with the substrate. It is possible that this provides the animal with extra lift by exploiting the ground effect (Martinez 1996). However, the most likely explanation for this behaviour is that the worms are continuously scanning the substrate for a suitable place to rapidly burrow as they are reluctant swimmers.

Jet-propulsion is defined as propulsion by ejecting a jet of fluid towards the rear which then generates thrust in the opposite direction by Newton's third law of motion. *N. diversicolor* is technically speaking, therefore, not swimming by jet-propulsion, since water is propelled backward in a jet by outside appendages. The mechanism described differs from jet propulsion in animals such as jelly fish (McHenry and Jed 2003; Colin and Costello 2002), scallops (Cheng and DeMont 1996) and squids (Bartol *et al.*2001), which all operate by periodically ejecting and refilling a body cavity with fluid. Periodic jet-propulsion has been shown theoretically to generate larger average thrust forces than continuous jet-propulsion for a given mass flux (Weihs 1977). Periodic jet-propulsion generates both start and stop vortices, which together with the intermittent backwards acceleration of water results in more diffuse and shorter jets than the narrow and long well-defined jets found here (Dabiri *et al.*2005; Colin and Costello 2002). The continuous jet-like propulsion mechanism described in this paper has not previously been found anywhere in the animal kingdom. Although this study only examined one species of the many errant polychaetes, it is likely that the jets are found in all of them. All of the errant polychaetes swim by a similar mechanism of body undulations coupled with parapodial oscillations (Clark and Tritton 1970). However, it would be interesting to compare the wake found here with that of errant polychaetes in other families. The errant polychaetes in the family Nephtyidae are more frequent and efficient swimmers than the nereidids and they perform the power stroke more localised exactly on the tip of the body wave crest (Mettam 1967). If it exists outside the errant polychaete group, a good place to search would be among animals propelling themselves with numerous oscillating appendages. One such candidate is *Artemia*, a group of small crustaceans where the antennae and the trunk limbs generate thrust via a drag based mechanism by oscillating their limbs in a coordinated metachronal rhythm (Williams 1994b). However, contrary to what appears to be the case for *N. diversicolor* then unsteady forces play an insignificant part in thrust production for *Artemia* larvae (Williams 1994a). Unfortunately no information is available on the structure of the wake behind swimming *Artemia*. Other possible candidates could be fish, such as the knife fish, that swims by undulation of a large ventral ribbon fin (Blake 1983). The ribbon fin might work by moving water backward in a similar conveyor-belt way to that of *N. diversicolor*. However, a single elongated fin is unlike to be able to generate the same high backward velocities as the individual parapodia generated in this study. Again, unfortunately no data on the wake of the knife fish is available.

More flow visualisation studies are needed to determine if continuous jet-like propulsion is truly unique to errant polychaetes or if a similar mechanism operates in *Artemia*, the knife fish or other groups of animals. However, the mode of locomotion described here in a juvenile swimming errant polychaete is unlikely to be widespread since it is less efficient than periodic jet-propulsion (Weihs 1977) and results in a long distinct wake, which essentially works as a hydromechanical advertisement signal for predators (Kiørboe and Visser 2000; Atema 1996).

Acknowledgement:
We thank William MeGill, Peter Müller and John Videler for their advice and comments on this study and manuscript. Invaluable technical assistance was given by 'H' Jones at the University of Bath and Jos de Wiljes at the University of Groningen. TH also thanks John Videler for his invitation to visit his group at the University of Groningen. This work was supported by the European Commission, in the framework of the BIOLOCH Project (IST FET Programme, IST-2001-34181).

References

Atema, J. 1996. Eddy chemotaxis and odor landscapes: exploration of nature with animal sensors. *Biological Bulletins* **191**: 129-138.

Bartol, I. K., Patterson, M. R. and Mann, R. 2001. Swimming mechanics and behavior of the shallow-water brief squid *Lolliguncula brevis*. *Journal of Experimental Biology* **204**: 3655-3682.

Biewener, A. A. 2003. *Animal locomotion*. Oxford University Press. Oxford.

Blake, R. W. 1983. Swimming in electric eel and knifefishes. *Canadian Journal of Zoology* **61**: 1432-1441.

Blickhan, R., Krick, C., Zehren, D. and Nachtigall, W. 1992. Generation of a vortex chain in the wake of a subundulatory simmer. *Naturwissenschaften* **79**: 220-221.

Brackenbury, J. 2002. Kinematics and hydrodynamics of an invertebrate undulatory swimmer: the damsel-fly larva. *Journal of Experimental Biology* **205**: 627-639.

Brackenbury, J. 2004. Kinematics and hydrodynamics of swimming in the mayfly larva. *Journal of Experimental Biology* **207**: 913-922.

Breeder, C. M. 1926. The locomotion of fishes. *Zoologica* **4**: 159-297.

Bone, Q. 1998. Locomotion, locomotor muscles, and buoyancy. In *Biology of Pelagic Tunicates* (Ed. Q. Bone). New York, Oxford University Press: 35-53.

Brewin, M. A. and Kerwin, D. G. 2003. Accuracy of scaling and DLT reconstruction techniques for planar motion analyses. *Journal of Applied Biomechanics* **19**: 79-88.

Cheer, A. Y. L. and Koehl, M. A. R. 1987. Paddles and rakes: fluid flow through bristled appendages of small organisms. *Journal of Theoretical Biology* **129**: 17-39.

Cheng, J.-Y. and DeMont, M. E. 1996. Jet-propelled swimming in scallops: swimming mechanics and ontogenetic scaling. *Canadian Journal of Zoology* **74**: 1734-1748.

Clark, R. B. 1961. The origin and formation of heteronereis. *Biological Reviews* **36**: 199-236.

Clark, R. B. 1976. Undulatory swimming in polychaetes. In *Perspectives in experimental biology*. (Ed. Davies, P. S.). Oxford, Pergamon Press. Vol 1: 437-446.

Clark, R. B. and Tritton, D. J. 1970. Swimming mechanisms in nereidiform polychaetes. *Journal of Zoology* **161**: 257-271.

Colin, S. P. and Costello, J. H. 2002. Morphology, swimming performance and propulsive mode of six co-occurring hydromeduase. *Journal of Experimental Biology* **205**: 427-437.

Dabiri, J. O., Colin, S. P., Costello, J. H. and Gharib, M. 2005. Flow patterns generated by oblate medusan jellyfish: field measurements and laboratory analyses. *Journal of Experimental Biology* **208**: 1257-1265.

Daniel, T. L. 1984. Unsteady aspects of aquatic locomotion. *American Zoologist* **24**: 121-134.

Daniel, T. L. and Webb, P. W. 1987. Physical determinants of locomotion. In *Comparative Physiology: Life in Water and on Land.* (Eds. Dejours, P. Bolis, L. Taylor, C. R. and Weibel, E. R.). Liviana Press. Padovia: 343-369.

Drucker, E. G. and Lauder, G. V. 1999. Locomotor forces on a swimming fish: three-dimensional vortex wake dynamics quantified using digital particle image velocimetry. *Journal of Experimental Biology* **202**: 2393-2412.

Fish, F. E. 2000. Biomechanics and energetics in aquatic and semiaquatic mammals:

Platypus to whale. *Physiological and Biochemical Zoology* **73**: 683-698.

Gillis, G. B. 1997. Anguilliform locomotion in an elongate salamander (*Siren intermedia*): effects of speed on axial undulatory movements. *Journal of Experimental Biology* **200**: 767-784.

Gillis, G. B. 1998. Environmental effects of undulatory locomotion in the american eel *Anguilla rostrata*: kinematics in water and on land. *Journal of Experimental Biology* **201**: 949-961.

Graham, J. B., Lowell, W. R., Rubinoff, I. and Motta, J. 1987. Surface and subsurface swimming of the sea snake *Pelamis platurus*. *Journal of Experimental Biology* **127**: 27-44.

Gray, J. 1939. Studies in animal locomotion. VII. The kinetics of locomotion of *Nereis diversicolor*. *Journal of Experimental Biology* **16**: 9-17.

Gustus, R. M. and Cloney, R. A. 1973. Ultrastructure of the larval compound setae of the polychaete *Nereis vexillosa* Grube. *Journal of Morphology* **140**: 355-366.

Hesselberg, T. and Vincent, J. F. V. 2006. A Comparative study of the functional morphology of parapodia and setae in nereids (Polychaeta: Nereididae). *Animal Biology* **56**: 103-120.

Hesselberg, T. and Vincent, J. F. V. The function of parapodial setae in nereidid polychaetes moving on two different substrata. *Journal of Experimental Marine Biology and Ecology*. In press.

Hui, C. A. 1988. Penguin swimming. I. hydrodynamics. *Physiological Zoology* **61**: 333-343.

Kiørboe, T. and Visser, A. W. 1999. Predator and prey perception in copepods due to hydromechanical signals. *Marine Ecology Progress Series* **179**: 81-95.

Linden, P. F. and Turner, J. S. 2004. 'Optimal' vortex rings and aquatic propulsion mechanisms. *Proceedings of the Royal Society of London. B.* **271**: 647-653.

Liu, H., Wassersug, R. J. and Kawachi, K. 1996. A computational fluid dynamic study of tadpole swimming. *Journal of Experimental Biology* **199**: 1245-1260.

Martinez, M. M. 1996. Issues for aquatic pedestrian locomotion. *American Zoologist* **36**: 619-627.

McHenry, M. J. and Jed, J. 2003. The ontogenetic scaling of hydrodynamics and swimming performance in jellyfish (*Aurelia aurita*). *Journal of Experimental Biology* **206**: 4125-4137.

Merz, R. A. and Edwards, D. R. 1998. Jointed setae - their role in locomotion and gait

transitions in polychaete worms. *Journal of Experimental Marine Biology and Ecology* **228**: 273-290.

Mettam, C. 1967. Segmental musculature and parapodial movement of *Nereis diversicolor* and *Nephthys hombergi* (Annelida: Polychaeta). *Journal of Zoology* **153**: 245-275.

Müller, U. K., Stamhuis, E. J. and Videler, J. 2002. Riding the waves: the role of the body wave in undulatory fish swimming. *Integrative and Comparative Biology* **42**: 981-987.

Müller, U. K., Stamhuis, E. J. and Videler, J. J. 2000. Hydrodynamics of unsteady fish swimming and the effects of body size: comparing the flow fields of fish larvae and adults. *Journal of Experimental Biology* **203**: 193-206.

Müller, U. K., van den Heuvel, B. L. E., Stamhuis, E. J. and Videler, J. J. 1997. Fish foot prints: morphology and energetics of the wake behind a continuously swimming mullet (*Chelon labrosus* Risso). *Journal of Experimental Biology* **200**: 2893-2906.

Nachtigall, W. 1980. Mechanics of swimming in water beetles. In *Aspects of animal movement* (Elder, H.Y. and Trueman, E. R.). Cambridge University Press. London: 107-124.

Pace, C. M., Blob, R. W. and Westneat, M. W. 2001. Comparative kinematics of the forelimb during swimming in red-eared slider (*Trachemes scripta*) and spiny softshell (*Apalone spinifera*) turtles. *Journal of Experimental Biology* **204**: 3261-3271.

Scaps, P. 2002. A review of biology, ecology and potential use of the common ragworm *Hediste diversicolor* (O.F. Müller) (Annelida: Polychaeta). *Hydrobiologia* **470**: 203-218.

Stamhuis, E. J. Basics and principles of particle image velocimetry (PIV) for mapping biogenic and biologically relevant flows. *Journal of Aquatic Ecology*. In press.

Stamhuis, E. J. and Nauwelaerts, S. 2005. Propulsive force calculations in swimming frogs II. Application of a vortex ring model to DPIV data. *Journal of Experimental Biology* **208**: 1445-1451.

Stamhuis, E. J., Videler, J. J., van Duren, L. A. and Müller, U. K. 2002. Applying digital particle image velocimetry to animal-generated flows: traps, hurdles and cures in mapping steady and unsteady flows in Re regimes between 10e-2 and 10e5. *Experiments in Fluids* **33**: 801-813.

Taylor, G. 1952. Analysis of the swimming of long and narrow animals. *Proceedings of the Royal Society of London. A.* **214**: 158-183.

Thiel, M. and Reise, K. 1993. Interaction of nemertines and their prey on tidal flats. *Netherlands Journal of Sea Research* **31**: 163-172.

Tytell, E. D. and Lauder, G. V. 2004. The hydrodynamics of eel swimming. I. Wake s tructure. *Journal of Experimental Biology* **207**: 1825-1841.

van Duren, L. A., Stamhuis, E. J. and Videler, J. J. 1998. Reading the copepod personal ads: increasing encounter probability with hydromechanical signals. *Philosophical transactions of the Royal Society of London. Series B.* **353**: 691-700.

Wassersug, R. J. and Hoff, K. v.-S. 1985. The kinematics of swimming in anuran larvae. *Journal of Experimental Biology* **119**: 1-30.

Weihs, D. 1977. Periodic jet propulsion of aquatic creatures. *Fortschritte der Zoologie* **24**: 171-175.

Williams, T. A. 1994a. Locomotion in developing *Artemia* larvae: Mechanical analysis of antennal propulsors based on large-scale physical models. *Biological Bulletins* **187**: 156-163.

Williams, T. A. 1994b. A model of rowing propulsion and the ontogeny of locomotion in *Artemia* larvae. *Biological Bulletins* **187**: 164-173.

Wootton, R. J. 1999. Invertebrate paraxial locomotory appendages: design, deformation and control. *Journal of Experimental Biology* **202**: 3333-3345.

Chapter 7

Discussion and conclusions

7 Discussion and conclusions

7.1 Results and discussion of the BIOLOCH project

7.1.1 Introduction

The BIOLOCH (BIOmimetic structures for LOComotion in the Human body) project officially ended in October 2005 and a brief account is given here on the most important results of the project. First a short summary of the results from each of the work packages described in section 1.4 (chapter 1) will be given, before two of the findings will be described in more detail. However, apart from the direct results of the project, it has also given the scientists in the consortium, and especially the PhD students, a fascinating insight into the nature of large international projects. The BIOLOCH consortium did not always work together harmoniously, and individual member groups occasionally pursued their own agenda instead of collaboratively working toward a common goal. However, the project provided valuable lessons on the interactions of scientists in international collaborations as well as the bureaucracy and culture behind the funding of research in the European Commission's Frame Work Programmes. I personally gained experience of interdisciplinary research culture by meeting with and reading about the research conducted by consortium members in a wide range of fields, including micro engineering, computer science and medicine. Participating in such a high profile international project, furthermore, gave me the opportunity to become involved in a number of public outreach and science communication activities, including to participate in both a British and a Korean TV science programme about biomimetics, a bionic exhibition at the Zoological Museum in Copenhagen and to write popular science articles for the museum exhibition catalogue, a Danish engineering weekly and proceedings of the Bath Royal Literary and Scientific Institution.

The information given in this section comes from presentations at bi-annual research meetings in the consortium and from review meetings with the European Commission as well as from written deliverables of the work packages, review reports and some of the more than 25 journal and conference papers resulting from the BIOLOCH project.

7.1.2 Results of the work packages

Work Package (WP) 1 comprised the study of locomotion and adhesion mechanism in lower animal forms. It focused on locomotion principles in aquatic and terrestrial invertebrates, but with the exclusion of wing or fin based propulsion. The adhesion of geckos by Van der Waals forces was also mentioned (see section 1.3 of this thesis) as was adhesion by suckers in octopuses and by byssys threads in mollusc. The review focused on undulatory locomotion found in snakes, oligochaetes and errant polychaetes (section 2.5). The preliminary review caused the consortium to pursue the oligochaete and polychaete locomotion principles as inspiration for the design of the robot locomotion units. The tiny hooks found in the mouth part of the human gut tape worm *Taenia solium* and the setae found in annelids (section 2.2 and chapter 3) were selected to provide inspiration for development of adhesion and friction structures enabling the robots to move in the slippery gut environment. The major scientific outcomes from WP1 were the discovery of a novel form of jet-like propulsion in errant polychaetes (chapter 6), an increased understanding of the function of parapodial setae in errant polychaetes (chapters 3, 4 and 5) and the development of a theoretical biomechanical model which provides a description and prediction of locomotion parameters in oligochaetes (Accoto *et al.*2004).

WP2 dealt with modelling and design of artificial structures. Together with WP6 this included the actual design and construction of the oligochaete and polychaete robots. The various robots developed throughout the BIOLOCH project are described more fully below. This work package also included research into the principles behind robotic implementation and together with WP5 resulted in the development of the SIMUUN (SIMUlator for UNdulatory locomotion) environment, which is also described more fully below.

WP3 focused on the principles and fabrication of biomimetic components such as actuators and sensors. A wide range of actuators was identified in this work package and incorporated into the design of the robots. Traditional electromechanical actuators (i.e. stepper and servo motors) were used in order to quickly create fully functional robots which could be used to test and implement the developed undulatory control mechanisms. However, one of the secondary aims of the BIOLOCH project was to develop and implement state-of-the-art technology throughout all phases of the project. Therefore, and because they better approximate biological function and design, more recent actuator technology such as shape memory alloys and ionic polymer metal

composites were implemented in the later robotic prototypes (see below). The consortium, furthermore, investigated the use of dielectric electroactive polymers (EAPs) as actuators. EAPs respond to external electrical stimulation by displaying a significant shape or size displacement. This resulted in the development of a new type of contractile polymer based electromechanical linear actuator (Carpi *et al.*2005). It comprises two helical compliant electrodes and an elastomeric silicone insulator interposed between them. Applying a voltage difference between the electrodes generates axial contractions (maximum axial strain of -5% at about 14 V μm^{-1}) as well as related radial expansions (Carpi *et al.*2005). This work package also looked into the fabrication of small adhesion and friction devices. Several techniques were looked at including micro-moulding which is derived from soft lithography and consists of producing microscopic patterns by placing a mask above a layer of photosensitive material and developing it with ultraviolet radiation. This technique gave a resolution of around one micrometer. Another technique, developed at the University of Pisa and known as pressure activated micro-syringe (PAM), involves extruding polymer through a thin glass syringe by applying a pressure. The system is connected to a computer that in real time controls the positioning of the syringe and the pressure applied. This gives resolutions between 5 and 20 micrometers. Lastly a novel technique for fabricating micro-hooks, called the liquid-bridge method, was developed (La Spina *et al.*2005b). This consists of melting a drop of polymer between two parallel planes and then taking advantage of surface tension and capillary forces to form biologically shaped hooks by slowly moving the plates apart (Fig. 7.1).

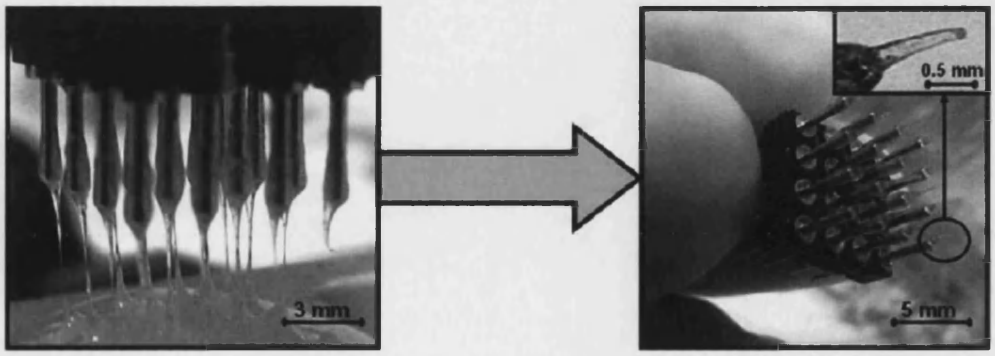

Fig. 7.1. Fabrication of micro-hooks using the 'Liquid bridge' technology. After La Spina *et al.*2005b.

WP4 comprised the understanding and replication of perception in lower animal forms. The main focus was on the structure of the nervous system and the resultant behaviour of errant polychaetes (sections 2.3, 2.4) and the computational models generated to control undulatory locomotion (see below). Biological control mechanisms, such as central pattern generators (CPGs), which generate metachronal rhythms were also looked at and incorporated into the control software. The endoscopic robots developed by the BIOLOCH project were ultimately designed to be controlled by a surgeon. However, some limited local control of the 'corridor-following' type was envisaged. To achieve this, a biomimetic approach was followed with focus on bees. Bees display a centring response and maintain equidistance to both walls while flying through tunnels. They achieve this by balancing the speed of images perceived by their two compound eyes (Srinivasan *et al.* 1996). This mechanism enabled a simulated polychaete robot to successfully navigate through a maze.

WP5 involved control strategy and control implementation. The output of this work package was the main undulatory simulation environment (SIMUUN) described below as well as specific control programmes for the individual robots, such as the one used to control the parapodial test bed described in chapter 6.

WP6 dealt with the actual fabrication of the biomimetic robots, which are described more fully below.

WP7 focused on the practical medical testing of the prototypes developed in WP6. This included some preliminary mechanical test of the human gastrointestinal (GI) tract such as friction values and elasticity of the bowel. However, the main focus was on the development of reliable and realistic test beds for evaluating the performance of the endoscopic robots developed by the consortium. The primary test bed developed was a biohybrid phantom box, which simulate the anatomy of the human GI tract and can be equipped with animal organs (primarily pig intestines) to approach the tissue properties of the human intestines (Fig. 7.2A). A sensor system, which can be attached to the phantom box, was also developed to measure the forces exerted on tubular organs by the locomotion device. For in vivo testing a standardised lab with living pigs were set up and an opportunity to test advanced prototypes in preserved human corpses was available. The Thiel method for preservation of corpses provided the best results with the lowest degree of discoloration and realistic mechanical properties of the tissue without shrinking or hardening. This test bed, however, was not used in the BIOLOCH project as none of the developed endoscopic robots was at a

stage advanced enough to justify the significant costs associated with this test bed. All test beds, though, were validated by trained surgeons with either biomimetic prototypes or traditional endoscopes (Fig. 7.2B).

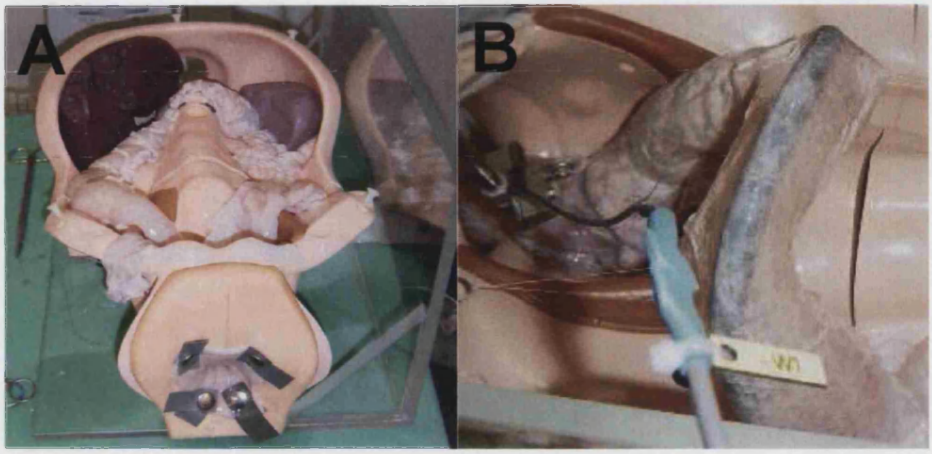

Fig. 7.2. Methods for testing the robotic prototypes. A. A humanoid phantom box replicating the anatomy of the human intestine using pig intestinal tissue. B. Validation of the test bed using a traditional endoscope.

7.1.3 Robotic prototypes

A preliminary demonstration robot was developed at the onset of the project to show how the undulatory mechanism works. This simple mechanical robot has an electrical motor driving a rotating helix, which sets a rubber band into undulatory motion (Fig. 7.3A). The rubber band pushes on rigid Perspex flanges, which simulates the action of the parapodium by performing power and recovery strokes, thus enabling the robot to crawl slowly forward. A miniaturized version using a gear mechanism instead of the rubber band was also developed, but the design had to be abandoned as it performed poorly due to too much internal friction.

However, several large robots were developed using traditional engineering techniques. These were primarily designed to test the method of locomotion and the control developed as well as testing various friction generating devices. These robots may also have a possible application as inspection or search and rescue robots. One of those is an eleven segment polychaete robot with 10 degrees of freedom (Fig. 7.3B). The undulatory wave is generated by a servomotor in each segment connected to neighbouring segments via bridges with a high stiffness to torque and high flexibility in the lateral plane. The length of the robot is 38 cm with a total weight of 360 g. A

satisfactorily progress was observed when crawling on sand by adding directional flanges or grooves to the base of the segments. The robot was designed so that it is possible to attach rigid parapodium-like appendages on the segment in future trials.

Another polychaete robot developed with parapodium-like structures is the 5-module SMA (shape memory alloy) artificial polychaete (Fig. 7.3C). It consists of a flexible skeleton made of silicone which is divided into 5 segments by rigid plastic blocks. SMA springs run between the blocks on both sides of the skeleton. SMAs are metals that, after being strained, at a certain temperature revert back to their original shape. Passing a current through the springs heats them up which makes them revert back to their contracted state thus bending the segment. The robot is 6 cm long and 2 cm wide and with small hooks attached to the base of the blocks it can reach a velocity of 1.3 mm/s on a flat surface applying a current of 170 mA.

A similar method of actuation is used in the 4-module SMA artificial oligochaete (Fig. 7.3D). Each segment consists of a silicone shell attached to two endplates. A SMA spring runs inside the segment between the endplates and contracts the whole segment when a current is applied. The robot crawls by sending a wave of contractions from the last segment to the first in a manner similar to what is found in earthworms (Accoto *et al.*2004). Passing a current of 300 mA through the SMA springs with a dimater of 600 μm, made of a wire 100 μm in diameter, results in a contraction of the segment of 2 mm or 20% of its length (Menciassi *et al.*2004). The whole robot has a length of 4 cm and a diameter of 1 cm and with small rigid hairs attached to the base of the segments it can reach a velocity of 2.5 mm/s on a flat surface.

The last robot that was developed by the BIOLOCH consortium is the IPMC (ionic polymer metal composite) polychaete robot. IPMCs are a type of EAPs that bend in response to an electrical activation as a result of the mobility of cations in the polymer network. They require relatively low voltages to stimulate a bending response (1-10 V) with frequencies below 1 Hz. The IPMC used for this robot is coated with platinum and has a thickness of 300 μm. A polychaete segment consists of a strip of IPMC with dimensions 20 mm x 4 mm x 0.3 mm and a clamp at each end. The findings reported by La Spina and co-workers (2005a) (and chapter 4 of this thesis) of the thrust enhancing effect of artificial setae and parapodia in crawling robots was applied and parapodium-like appendages with artificial setae were attached to the distal ends of the clamps. A square wave (with a 10 V dynamics from +5 V to -5 V) was chosen instead of a sine wave in order to simplify the electronic hardware that drives the robot. This

robot is still in development and no quantitative measurements of performance have yet been done, but a 4-segment prototype was made which replicated polychaete motion satisfactorily (Fig. 7.3E). One of the advantages of using IPMCs is that they like other EAPs can function both as actuators and as sensors.

The BIOLOCH consortium, furthermore, developed a completely different type of robot locomotion not inspired by annelids but by a combination of wriggling motion found in fly larvae and the directed motion in oat seeds (*Avena sativa*) caused by hairs providing directional friction. The SEMOR (SEnseless MOtion Robot) consists of a voice-coil which, powered by a small battery, generates mechanical vibration (Fig. 7.3F). An outer surface covered with skate-like structures provides directional friction that translates the vibration motion into forward locomotion. A velocity of 5.8 mm/s was achieved over velvet, rough rubber and sandpaper. SEMOR has a length of 7 cm and a diameter of 3 cm and is the only truly autonomous robot developed during the BIOLOCH project. A robot with these characteristics could be used as the propulsion system of a robot composed of two parts, one based on senseless motion and the other equipped with sensory systems for monitoring medical parameters.

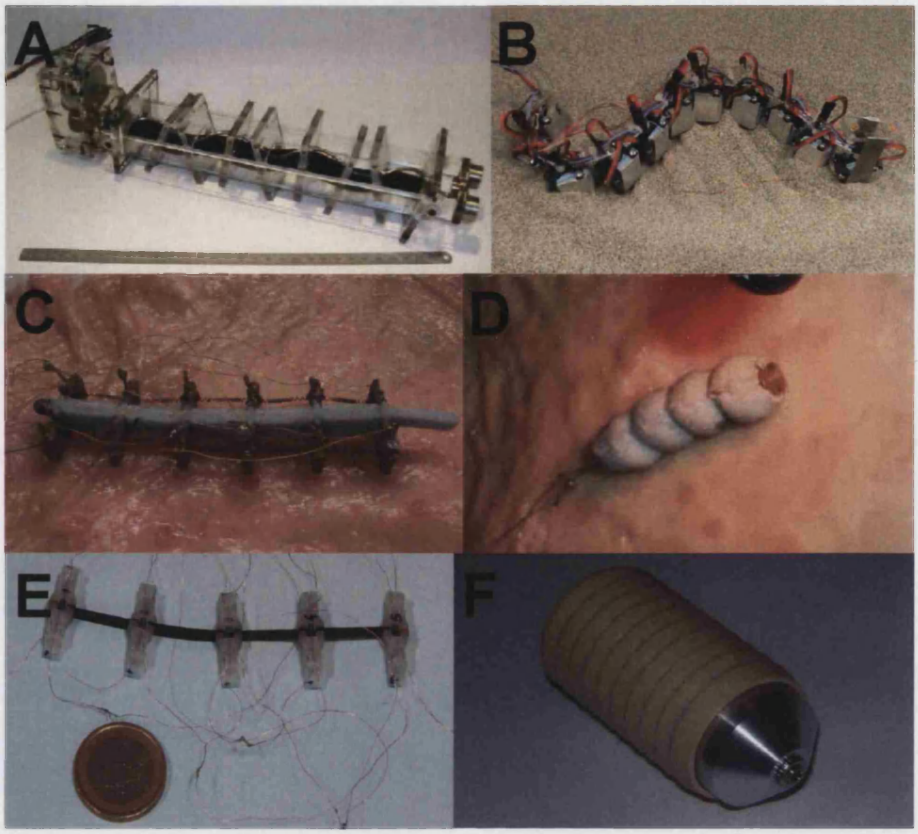

Fig. 7.3. The most important biologically inspired robots developed during the BIOLOCH project. A. The original mechanical polychaete model. B. The second mechanical smooth polychaete robot. C. The shape memory alloy (SMA) polychaete robot. D. The SMA oligochaete robot. E. The Ionic Polymer Metal Composite (IPMC) polychaete robot. F. The vibrating robot SEMOR.

7.1.4 The SIMUUN environment

The SIMUUN (SIMUlator for UNdulatory locomotion) environment is a block-based simulation environment developed for conducting research on undulatory locomotion from both a robotic and a biological perspective (Sfakiotakis and Tsakiris *In press*; 2004). SIMUUN has been created on top of the MATLAB/Simulink environment in order to take advantage of its block-based modular structure. It consists of three components. The body mechanical model, the body shape control model and the force model of the body's interaction with the environment (Fig. 7.4A). The body mechanics are modelled using the SimMechanics toolbox in Simulink, which allows blocks to represent physical components and their geometric and kinematics relationships (Sfakiotakis and Tsakiris *In press*). The blocks are serially linked to each other with joint angles between them. The shape control model was done in two ways. The first and most straightforward way to generate a travelling wave is to have the joint angles

vary sinusoidally by controlling them directly with equations. Another more biologically inspired body shape control method is based on central pattern generators (Sfakiotakis and Tsakiris 2004). A connectionist CPG circuit, modelled as a chain of identical segmental oscillators, properly interconnected to generate a wave of joint activation was used. The oscillators comprise interneurons and motoneurons, which are all modelled as leaky integrators. Leaky integrators work by slowly 'forgetting' bad initial conditions and numerical errors, so that they do not continue the build up forever. The interaction with the environment is modelled for both terrestrial and aquatic habitats. In terrestrial habitats a general friction model was developed, which combines stiction, Coulomb and viscous damping as well as the Stribeck effect and anisotropic characteristics, in an attempt to cover the wide range of tribological phenomena encountered during terrestrial ground locomotion (Sfakiotakis and Tsakiris *In press*). A fluid drag model is used in SIMUUN to simulate the interaction of undulatory mechanisms with the aquatic environment. The model assumes that the fluid forces are mainly inertial ($400 < Re < 4 \times 10^5$), the fluid is stationary so that its force on a single link is due only to the motion of that link and that the tangential and normal force components are decoupled. The forces are calculated using Taylor's (1952) resistive analysis of elongated animal swimming, where the forces are proportional to the squared swimming speed of the animal (section 1.2). Since the assumptions of this model restricts its scope to the inviscous swimming of elongated animals it cannot be used for the undulatory swimming of micro-organisms or fish swimming.

The SIMUUN environment was validated against both robotic and biological data. The performance of a simulated 7-link robot was compared with the performance of one of the electromechanical artificial polychaetes developed by the BIOLOCH consortium (Tsakiris *et al.*2005). A good qualitative agreement was found of the motion patterns and trajectory plots between the simulation and the robot (Fig. 7.4B, C). The mean velocities achieved by the robot (30-50 mm/s), furthermore, compared favourably with the ones obtained from the simulations (35 – 55 mm/s) (Tsakiris *et al.*2005). The SIMUUN environment was also evaluated against biological data obtained from a swimming eel (Sfakiotakis and Tsakiris *In press*). A biomechanical eel model was constructed, composed of 20 cylindrical links of equal length and unequal radius, using morphological and kinematic data from D'Aout and Aerts (1999). Amplitude, wavelength and speed were compared between the model and the biological data. For

both forward and backward swimming the simulated values showed good agreement with the measured ones (Sfakiotakis and Tsakiris *In press*).

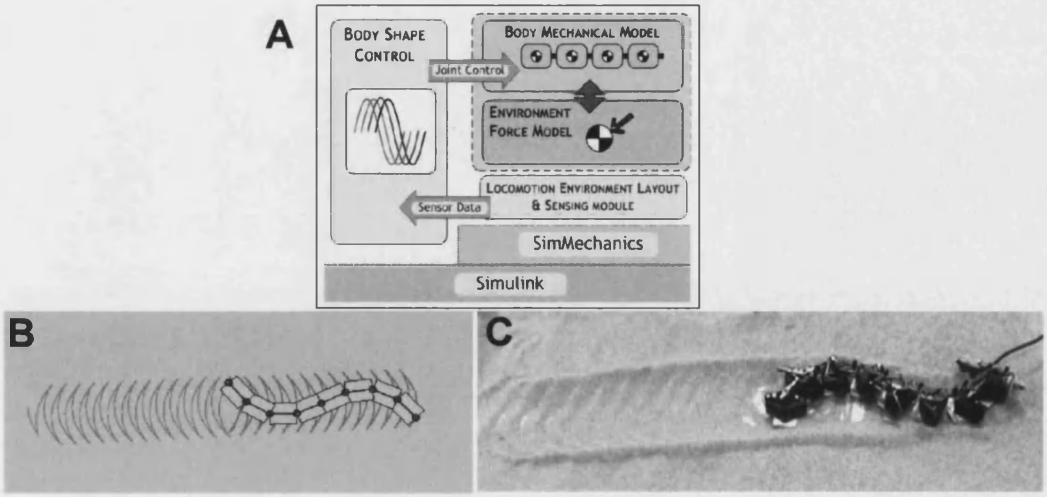

Fig. 7.4. The SIMUUN environment. A. The main components of the simulation environment. B. Artificial tracks left by the simulated movements of a smooth polychaete robot. C. Validation of SIMUUN by using one of the smooth polychaete robot prototypes developed in the BIOLOCH project.

It would have been very interesting to use SIMUUN in this PhD project to compare simulations to real measurements and learn more about the relationships between amplitude, wave length and forward speed described in chapters 5 and 6. However, although special blocks simulating parapodia have been developed for SIMUUN (Sfakiotakis and Tsakiris 2004), it was not possible to use them in comparisons with locomotion of real errant polychaetes. The reason is that SIMUUN only models frictional forces with the ground as is appropriate for terrestrial crawling whereas the worms crawl under water where hydrodynamical forces play a significant role (chapter 5). For swimming SIMUUN uses the resistive Taylor model for swimming in elongated animals (Taylor 1952). However, as was shown in chapter 6 then the body undulations themselves provide little if any of the actual thrust produced during swimming. This is instead generated by the parapodia as is evident from the two distinct jet produced in the wake. Furthermore, the SIMUUN environment does not model unsteady forces such as the acceleration reaction and there are strong indications that the acceleration reaction is important for swimming in errant polychaetes (chapter 6). However, it should be possible to include these modifications in future versions of

SIMUUN and thus make it a useful tool to further the study of locomotion in errant polychaetes.

9.1.5 Conclusion

The BIOLOCH project did not develop a fully functional biomimetic endoscope and substantial problems including low locomotion speed, friction and steering need to be solved before any of the prototypes described above will be of any medical use. However, the goal of the BIOLOCH project was not to produce a commercial product, but to explore the possibilities of developing a biomimetic endoscope and applying new technology to the field of medical engineering. The technological and scientific breakthroughs of the project included, as described above, the development of; an undulatory simulation environment, a biohybrid phantom box for evaluating the damage on the intestines by endoscopic devices, novel methods of fabricating micro-hooks, vibratory direction movement and the use of helical EAPs and IPMC in actuation and sensing. Lastly as described in this thesis the BIOLOCH project advanced our knowledge of the biology of locomotion in errant polychaetes and led to the discovery of a novel form of continuous jet-like propulsion in swimming juvenile errant polychaetes.

One patent was generated on a new configuration of elastomeric actuator and sensor (Patent n. PCT/IB2004/001868) and the technological results were transferred to the German company Novineon Healthcare Technology Partners in a collaboration on evaluating the market potential of biomimetic robots. The BIOLOCH project, furthermore, generated significant public interest and was featured in newspaper articles, TV programmes and museum exhibitions and provided training for a total of 9 PhD students in 4 of the 6 participating institutions. The project was, therefore, positively evaluated by the reviewers from the European Commission.

9.2 Discussion and conclusion of PhD

The most significant scientific output of this PhD project is the discovery of a novel type of continuous jet-like propulsion in swimming juvenile *Nereis diversicolor* (chapter 6). Jet propulsion is well known in the animal kingdom from groups such as squids, jellyfish and dragonfly larvae (Colin and Costello 2002; Bartol *et al.*2001).

However, all of these groups use a discontinuous form of jet propulsion where water is ejected from a body cavity, which needs to be refilled before the next propulsive bout thus resulting in punctuated thrust production. The use of appendages to generate the jets in a way that can be likened to a conveyor belt, where each parapodium contributes with a small package of water to the overall flow, has to my knowledge not been found anywhere else in nature. The swimming in juvenile nereidids is, furthermore, unique in not resulting in the shedding of any individual vortices in its wake. Shedding of individual or chains of vortices is a common feature in most forms of swimming (Stamhuis *In press*; Linden and Turner 2004; 2001). It is found as chains of vortices behind undulatory swimming in both fish (Müller *et al.* 1997) and invertebrates (Brackenbury 2004; 2002), as individual vortices behind oscillating appendages (Stamhuis and Nauwelaerts 2005) as well as start and stop vortices associated with periodic jet propulsion (Dabiri *et al.* 2005; Colin and Costello 2002).

Early on in this PhD project it became clear that one of the interesting aspects of the morphology of errant polychaetes is the setae. The setae have a serrated blade jointed to a shaft by a relatively complex joint that limits the degrees of freedom of the blade (chapter 2). This combined with the fact that all motion of these setae occurs passively, since no muscles or neurons are present in the seta (Gustus and Cloney 1973), as a response to external factors make them highly interesting from both a biomechanical and biomimetic perspective. Several scientists claim that this passive response to the substrate gives the setae a significant role in increasing the friction between the parapodia and the substrate (Gustus and Cloney 1973; Mettam 1967; Foxon 1936). Experimental results support this claim (Merz and Edwards 1998), but also suggest that setae play a role during swimming (Merz and Edwards 1998) and as hooks (Woodin and Merz 1987). Shedding further light on the question of the functional role of setae in errant polychaetes especially from a locomotory perspective was, therefore, made one of the cornerstones of this PhD project. The comparative study described in chapter 3 examined whether the morphology and distribution of the parapodia and setae were correlated to habitat. Five closely related species in the subfamily Nereidinae, of which two inhabit soft substrates and three hard substrates, were compared. However, although significant differences were found in number of setae, seta location, size related parameters and the distribution of setae, no correlation with either species size, ability to swim in the juvenile stage or habitat was found. This study thus suggests that the setae (and the parapodia) are not adapted to any specific habitat. The variance found

among swimming polychaetes as well as the distribution of setae and the direction in which their teeth are pointing, furthermore, indicate that the setae have more functions than just increasing the friction between the parapodium and the substrate. A simplified mechanical model of oscillating parapodia was developed (chapter 4) and used to investigate whether there were any potential benefits of having setae attached to parapodia during crawling locomotion. Three parapodial configurations, plain, plate and setae consisting of 5 piano wires, were tested on three substrates differing in particle size. As expected the plain configuration generated less thrust than the other two. However, the artificial setal configuration generated more thrust than the plate configuration at the largest particle size tested (gravel with a particle diameter of 6.2 mm). The results obtained from the simple mechanical model, therefore, support the hypothesis that setae play an important role in enhancing thrust during crawling. In the last study regarding the significance of setae, conducted during this PhD, we conducted a classical ablation experiment, where the locomotion performance of worms with their setae removed was compared to control worms (chapter 5). Crawling performance was tested on both mud and sand, but no differences were found between the two substrates in how worms respond to seta-ablation. However, differences in wave and crawling speed were found on both substrates between control and ablated worms with the latter moving slower over the substrate but with a higher body wave speed. Kinematics and morphological data suggest according to the Cheer and Koehl (1987) model that seta-bundles mainly function as plates and, therefore, aid the parapodia in thrust production during swimming (chapters 2, 3). However, no difference in swimming performance was found between seta-ablated worms and control worms in the study described in chapter 5. This disagrees with an earlier study on seta-ablation (Merz and Edwards 1998), but since we only ablated the neuropodial seta-bundle it remains possible that the notopodial seta-bundle is important during swimming. The study on seta-ablation thus supports the comparative morphology study in concluding that the setae are not adapted to any specific substrate but rather seem to be multifunctional in nature. It, furthermore, supports the results of the mechanical study that setae play a significant role during crawling, while it does not indicate any role of setae during swimming.

Apart from the scientific results mentioned above this PhD also generated other output. A detailed investigation of the various methods to transform image coordinates into real world coordinates was conducted. A comparison between the simple scaling method and the more complicated two-dimensional direct linear transformation methods

(2D-DLT) was performed (appendix A). A marker board was recorded with different angles of tilt and pan and significant smaller reconstruction errors were found with the 2D-DLT methods at higher angles. Overall the 2D-DLT method with 9 parameters showed the smallest reconstruction error and was used in the experiments described in chapter 5 and 6. 2D-DLT methods are primarily used in sports science (Brewin and Kerwin 2003), although some biological 3-D kinematic studies use it (de Groot et al. 2004; Kram et al. 1997). Appendix A shows its potential for 2-D studies on animal locomotion. However, considering the overall large variations found in swimming worms and the substantial digitising inaccuracies when trying to digitise moving body wave crests, it presumably would not have made much difference if the simple scaling method had been used throughout this study. But once the equations are understood and incorporated into the digitising software and a suitable marker-board designed and fabricated no extra work is associated with using the 2D-DLT method compared to the simple scaling method. The exercise has, furthermore, provided me with a useful tool for future kinematic studies.

This PhD resulted in the development of the digitising software, Nereis.vi, specifically designed for use with undulatory locomotion in elongated animals (appendix B). An initial evaluation of current commercial software packages was done, but due to high prices and restrictions on the number of digitising points allowed per frame, it was decided to write a digitising programme. LABVIEW was chosen as the programming language due to its modular structure and graphical interface as well as the pre-programmed image analysis libraries found in the add-on IMAQ Vision. However, plans to automate the digitising process had to be abandoned due to the constant shape changes in the swimming undulatory worms and the low contrast between worm and background especially when the worm was moving in mud and sand. Although, Nereis.vi was specifically designed for use with swimming worms, it can with minor modifications be used for other digitising purposes.

From a biomimetic perspective the interesting results of this PhD project is the potential application for artificial setae in enhancing friction with slippery substrates. Even the very simple representation of setae using piano wires described in chapter 4 showed significant potential in increasing the friction between robot and substrate. A slightly more morphologically complex representation was attached to the latest IPMC robot developed by the BIOLOCH consortium with encouraging results (previous

section). Artificial setae, with the passive action of the joint between shaft and blade incorporated, presumably has further potential for biomimetic exploitation.

The locomotion method employed by errant polychaetes of sending body waves in an anterior direction and using appendages to aid locomotion is used extensively in the polychaete robots designed by the BIOLOCH consortium. The general locomotion method found in errant polychaetes has, furthermore, significant potential for multifunctional robots since the worms are capable of crawling and swimming using the same mechanism and applying the same neuronal circuitry thus reducing the complexity of control in a robot. The worm is also capable of burrowing using the everted pharynx and the hydrostatic skeleton (Trevor 1977). A recent study show that the larger *Nereis virens* uses it everted pharynx to propagate cracks in muddy cohesive sediments (Dorgan *et al.*2005). Incidentally, a method which in itself is worth investigating in more detail from a biomimetic perspective. With an extra layer of morphological detail (such as an artificial eversible pharynx or a hydrostatical skeleton) a robot based on the nereidid design would be able to burrow, crawl and swim in a wide range of habitats requiring relatively simple control mechanisms. The function of the oscillating parapodia in generating a distinct jet of water as described in chapter 6 has non-locomotory biomimetic potential. Instead of propelling a robot forward artificial parapodia can be used as a pump to generate a flow of water. Such a pump would work well with viscous fluids or mixtures of liquid and particulate matter. In an undergraduate project at the Centre for Biomimetic and Natural Technologies at the University of Bath, it was proved theoretically that a system with multiple artificial parapodia would generate flow rates comparable to other displacement pumps (Cummings 2004). A prototype was, furthermore, built which proved the mechanism in practise although it generated rather low flow rates and had no ability to overcome pressure differences, mainly due to slip between the parapodium gaps (Cummings 2004). Improving the design of the prototype could result in a commercially viable biomimetic pump mechanism.

The biologically inspired robot community will hopefully find the kinematic data presented in chapter 5 and 6 (and hopefully soon to be published in biological journals) of potential interest. The studies presented in this thesis provide the most detailed morphological and kinematic data yet published on nereidid locomotion. Only a study on seta-ablation on the hesionid polychaete *Ophiodromus pugettensis* provide similar kinematic data, but with more focus on the parapodial kinematic than the overall

worm kinematic (Merz and Edwards 1998). However, the smaller *O. pugettensis* employ a different and more efficient mode of locomotion than *N. diversicolor*, with fast crawling speeds of 21 - 22 mm/s and swimming speeds of 43 - 50 mm/s of the former compared to crawling speeds of 5 – 8 mm/s and swimming speeds of 21 – 30 mm/s given in this thesis (chapters 5, 6). In the earlier studies of locomotion in errant polychaetes not much kinematic data is given in the papers (Clark 1976; Clark and Tritton 1970; Gray 1939). However, Clark and Tritton (1970) found forward speed / wave speed (U/V) ratios of 0.2 – 1.0 with an average around 0.6, which corresponds well to the average U/V ratios found here of 0.51 – 0.53 (chapters 5, 6). Faith in the kinematic values presented in this thesis also comes from the very good correspondence between the main swimming parameters of the ablation experiment described in chapter 5 and the PIV study described in chapter 6. The ablation study (n = 15) gave the following average swimming parameters (for control worms); speed of 21.2 mm/s, wave speed of 42.3 mm/s, wavelength of 9.2 mm and amplitude of 2.6 mm compared to the average parameters found in the PIV study (n= 8); speed of 22.4 mm/s, wave speed of 42.1 mm/s, wavelength of 12.4 mm and amplitude of 2.5 mm.

Locomotion in errant polychaetes is a vast subject and has, despite the findings presented here, barely been touched upon. The experiments described in this thesis have answered many questions but like all science have also given rise to many further questions. One of the most interesting avenues to pursue in future research projects is to conduct flow visualisation studies across a range of errant polychaetes. It would be of particular interest to obtain flow visualisation data on the swimming of heteronereis worms. Most nereidids, although not *N. diversicolor*, metamorphose into an adult heteronereis stage prior to reproduction. This involves an enlargement of parapodial muscles, improvements of the sensory organs, histolysis of the body wall and morphological changes of the parapodia and setae (Clark 1961). The heteronereis is a more efficient and faster swimmer than *N. diversicolor* and produces smaller body undulations (*Pers. obs.*). The parapodia and setae are, furthermore, more paddle-shaped (Clark 1961). It would, therefore, be interesting to see how these morphological changes affect both the generated flow and the kinematics of swimming. The fact that the setae changes into special paddle-shaped setae (see chapter 2, Fig. 2.5f) suggests that they play a significant role in generating thrust during swimming in the heteronereis. Seta-ablation studies similar to the one described in chapter 5 could resolve this issue.

In the present project we studied the functional role of setae during crawling and swimming. However, it would be interesting to investigate its role during burrowing and rapid withdrawal. Polychaete setae have been shown to function as hooks to lock the worm in its burrow (Woodin and Merz 1987). This function is presumably also found in errant nereidids and could be used to secure the posterior part of the worm in the burrow while the anterior part search for food. The setae would thus play an important role during the rapid withdrawal behaviour found in response to threats (Evans 1969). An interesting experiment would be to ablate the setae in the posterior part and compare their rapid withdrawal behaviour to worms where the setae were ablated in the anterior part and to control worms. If mechanical vibrations where used as threat signals this would, furthermore, show if the setae also function as mechanoreceptors. Preliminary experiments using a high speed camera to record the rapid withdrawal behaviour in juvenile *N. diversicolor* were performed as part of this PhD. However, due to problems with successfully enticing the worms to emerge from their burrows in the experimental set-up and time constraints, this line of research was abandoned.

Originally the seta-ablation study (chapter 5) was designed to look at crawling performance on a wide range of substrates including smooth and hard substrates such as rock and stainless steel. However, due to time constraints this was abandoned. It would, though, be interesting from a biomimetic perspective to test the thrust enhancing effects of setae on substrates on which the worm is not found naturally. A large comparative study using the same species as in the comparative morphology study (chapter 3), where the locomotion performance of species occurring on hard substrate is compared to species on soft substrates for both control and seta ablated worms, would generate further insights into the function of setae during crawling. Similar more extended studies using more species and removing the setae either exclusively from the notopodial seta-bundle or in combination with removing them from the neuropodial seta-bundles would resolve the question of whether setae play a role during swimming in juvenile nereidids.

A different approach, to elucidate the function of setae and their interplay with parapodial movement, not pursued in this PhD project is the use of computer modelling. Techniques such as computational fluid dynamics (CFD) and finite element analysis (FEA) are potentially powerful tools to increase our knowledge of locomotion in errant polychaetes. However, I decided early on not to pursue these techniques further in this

project since the kinematics of the parapodia and setae as well as their mechanical performance is poorly known and because using CFD or FEA is a PhD project in itself. More information of the constituent material and mechanical properties of the setae would be interesting and useful in determining their function. The cortex of setae is a composite consisting of longitudinal polysaccharide chitin fibres and a protein matrix interspersed with 20-30 longitudinally orientated tubular channels (Schroeder 1984; Gustus and Cloney 1973). However, no studies are available on the bending stiffness, probably because of the technical difficulties of measuring mechanical properties of something this small. However, with modern technologies such as micro manipulators and laser displacement sensors it should now be possible to attempt such measurements. More detailed studies of the function of the seta-joint as well as the material and elasticity of the ligament would generate interesting results from both a biological and biomimetic perspective.

The results of this PhD project should be compared to the objectives stated in chapter 1. The first objective was: *To investigate the kinematic variables and gait types employed by the ragworm Nereis diversicolor as it moves on and through different substrates. To relay this information to the BIOLOCH consortium and subsequently derive an optimal design for a robotic worm required to move inside the slippery human gut.* This objective was covered in the experiment that compared locomotion performance of seta-ablated worms on two substrates (chapter 5), although it proved not to be feasible to record worms as they burrowed through the substrate. A test rig consisting of sand placed between two Perspex plates in close proximity unfortunately did not give results as the worms did not display normal behaviour in the test rig. The kinematic data found in the seta-ablation and the PIV studies (chapters 5, 6) was relayed to the BIOLOCH consortium and incorporated into various robot designs, including the parapodial test bed described in chapter 4, although it proved most useful in developing and validating the SIMUUN environment (see previous section). The second objective was: *To analyse the flow around both the entire ragworm and the individual parapodium in order to verify and update the current theories of swimming in these worms.* The PIV study visualised the flow around the whole worm and around the crest and revised the theory by showing that the worm swim by jet-like propulsion (chapter 6). Unfortunately the PIV method did not allow flow visualisation around a single parapodium as the laser light reflected from the body and parapodium disrupted the

detection of the suspended particles in the vicinity of the body and parapodia. In order to do so a more powerful zoom-lens and smaller particles are necessary, but it would still be difficult to record one parapodium in the small focal area. Recording the flow around the crest as described in chapter 6 was already cumbersome and time-consuming. The last objective was: *To conduct a comparative study of the morphology and function of the parapodial setae in various species of errant polychaetes adapted to different habitats. Furthermore, to assess the relevance of seta-like structures on a robotic worm required to move inside the human gut.* This objective was fully covered in the comparative morphology study, the seta-ablation study and the robotic test-bed study (chapters 3, 4, 5). In conclusion the objectives set out at the beginning of this PhD project have been almost completely met by the experiments described in this thesis.

The overall results of this PhD project is the discovery of a novel way of continuous jet-like propulsion in errant polychaetes and evidence for a less specialised and more multifunctional role of parapodial setae during crawling. Artificial setae have, furthermore, been shown to possess biomimetic potential.

References

Accoto, D., Castrataro, P. and Dario, P. 2004. Biomechanical analysis of oligochaeta crawling. *Journal of Theoretical Biology* **230**: 49-55.

Bartol, I. K., Patterson, M. R. and Mann, R. 2001. Swimming mechanics and behavior of the shallow-water brief squid *Lolliguncula brevis*. *Journal of Experimental Biology* **204**: 3655-3682.

Brackenbury, J. 2002. Kinematics and hydrodynamics of an invertebrate undulatory swimmer: the damsel-fly larva. *Journal of Experimental Biology* **205**: 627-639.

Brackenbury, J. 2004. Kinematics and hydrodynamics of swimming in the mayfly larva. *Journal of Experimental Biology* **207**: 913-922.

Brewin, M. A. and Kerwin, D. G. 2003. Accuracy of scaling and DLT reconstruction techniques for planar motion analyses. *Journal of Applied Biomechanics* **19**: 79-88.

Carpi, F., Migliore, A., Serra, G. and De Rossi, D. 2005. Helical dielectric elastomer

actuators. *Smart Materials and Structures* **14**: 1-7.

Cheer, A. Y. L. and Koehl, M. A. R. 1987. Paddles and rakes: fluid flow through bristled appendages of small organisms. *Journal of Theoretical Biology* **129**: 17-39.

Clark, R. B. 1961. The origin and formation of heteronereis. *Biological Reviews* **36**: 199-236.

Clark, R. B. 1976. Undulatory swimming in polychaetes. In *Perspectives in experimental biology*. (Ed. Davies, P. S.). Pergamon Press. Oxford. Vol. 1: 437-446.

Clark, R. B. and Tritton, D. J. 1970. Swimming mechanisms in nereidiform polychaetes. *Journal of Zoology* **161**: 257-271.

Colin, S. P. and Costello, J. H. 2002. Morphology, swimming performance and propulsive mode of six co-occurring hydromeduase. *Journal of Experimental Biology* **205**: 427-437.

Cummings, B. 2004. A biomimetic pump based on the fast-swimming locomotive mechanism of *Nereis diversicolor*. Final Year Report. Department of Mechanical Engineering. University of Bath.

Dabiri, J. O., Colin, S. P., Costello, J. H. and Gharib, M. 2005. Flow patterns generated by oblate medusan jellyfish: field measurements and laboratory analyses. *Journal of Experimental Biology* **208**: 1257-1265.

D'Aout, K. and Aerts, P. 1999. A kinematic comparison of forward and backward swimming in the eel *Anguilla anguilla*. *Journal of Experimental Biology* **202**: 1511-1521.

Dorgan, K. M., Jumars, P. A., Johnson, B., Boudreau, B. P. and Landis, E. 2005. Burrow extension by crack propagation. *Nature* **433**: 475.

Evans, S. M. 1969. Habituation of the withdrawal response in nereid polychaetes 1. The habituation process in *Nereis diversicolor*. *Biological Bulletins* **137**: 95-104.

Foxon, G. E. H. 1936. Observations on the locomotion of some arthropods and annelids. *The Annals and Magazine of Natural History* **18**: 403-419.

Gray, J. 1939. Studies in animal locomotion. VII. The kinetics of locomotion of *Nereis diversicolor*. *Journal of Experimental Biology* **16**: 9-17.

de Groot, J. H., van der Sluijs, I., Snelderwaard, P. C. and van Leeuwen, J. L. 2004. A three-dimensional kinematic analysis of tongue flicking in *Python molurus*.

Journal of Experimental Biology **207**: 827-839.

Gustus, R. M. and Cloney, R. A. 1973. Ultrastructure of the larval compound setae of the polychaete *Nereis vexillosa* Grube. *Journal of Morphology* **140**: 355-366.

Kram, R., Wong, B. and Full, R. J. 1997. Three-dimensional kinematics and limb kinetic energy of running cockroaches. *Journal of Experimental Biology* **200**: 1919-1929.

La Spina, G., Hesselberg, T., Williams, J. and Vincent, J. F. V. 2005a. A biomimetic approach to robot locomotion in unstructured and slippery environments. *Journal of Bionics Engineering* **2**: 1-14.

La Spina, G., Stefanini, C., Menciassi, A. and Dario, P. 2005b. A novel technological process for fabricating micro-tips for biomimetic adhesion. *Journal of Micromechanics and Microengineering* **15**: 1576-1587.

Linden, P. F. and Turner, J. S. 2001. The formation of 'optimal' vortex rings, and the efficency of propulsion devices. *Journal of Fluid Mechanics* **427**: 61-72.

Linden, P. F. and Turner, J. S. 2004. 'Optimal' vortex rings and aquatic propulsion mechanisms. *Proceedings of the Royal Society of London. B.* **271**: 647-653.

Menciassi, A., Gorini, S., Pernorio, G. and Dario, P. 2004. A SMA actuated artificial earthworm. *IEEE International Conference on Robotics and Automation*, New Orleans, USA, IEEE.

Merz, R. A. and Edwards, D. R. 1998. Jointed setae - their role in locomotion and gait transitions in polychaete worms. *Journal of Experimental Marine Biology and Ecology* **228**: 273-290.

Mettam, C. 1967. Segmental musculature and parapodial movement of *Nereis diversicolor* and *Nephthys hombergi* (Annelida: Polychaeta). *Journal of Zoology* **153**: 245-275.

Müller, U. K., van den Heuvel, B. L. E., Stamhuis, E. J. and Videler, J. J. 1997. Fish foot prints: morphology and energetics of the wake behind a continuously swimming mullet (*Chelon labrosus* Risso). *Journal of Experimental Biology* **200**: 2893-2906.

Schroeder, P. C. 1984. Chaetae. In *Biology of the Integument. Vol. I. Invertebrates*. (Eds. Bereiter-Hahn, J., Matoltsy, A. G. and Richards, K. S.). Springer-Verlag. New York: 297-309.

Sfakiotakis, M. and Tsakiris, D. P. 2004. A simulation environment for undulatory locomotion. *International Conference on Applied Simulation and Modelling*,

Rhodes, Greece, IASTED.

Sfakiotakis, M. and Tsakiris, D. P. SIMUUN: a simulation environment for undulatory locomotion. *International Journal of Modelling and Simulation*. In press.

Srinivasan, M. V., Zhang, S. W., Lehrer, M. and Collett, T. S. 1996. Honeybee navigation en route to the goal: visual flight control and odometry. *Journal of Experimental Biology* **199**: 237-244.

Stamhuis, E. J. Vortices rule the wake: structure and Reynolds' scaling of animal generate wake. In *Flow phenomena in Nature*. (Ed. Liebe, R.). WIT Press. In press.

Stamhuis, E. J. and Nauwelaerts, S. 2005. Propulsive force calculations in swimming frogs II. Application of a vortex ring model to DPIV data. *Journal of Experimental Biology* **208**: 1445-1451.

Taylor, G. 1952. Analysis of the swimming of long and narrow animals. *Proceedings of the Royal Society of London. A.* **214**: 158-183.

Trevor, J. H. 1977. The burrowing of *Nereis diversicolor* O. F. Müller, together with some observations on *Arenicola marina* (L.) (Annelida: Polychaeta). *Journal of Experimental Marine Biology and Ecology* **30**: 129-145.

Tsakiris, D. P., Sfakiotakis, M., Menciassi, A., La Spina, G. and Dario, P. 2005. Polychaete-like undulatory robotic locomotion. *International Conference on Robotics and Automation*, Barcelona.

Woodin, S. A. and Merz, R. A. 1987. Holding on by their hooks: anchors for worms. *Evolution* **41**: 427-432.

Appendix A

A comparison of different methods to convert digitised image coordinates into real world coordinates

Appendix A A comparison of different methods to convert digitised image coordinates into real world coordinates

Abstract: An important step in any kinematical analysis of video recordings is the transformation of the digitised image coordinates into real world coordinates. In this study the reconstruction errors of four calibration methods - the simple scaling method and three variations of the two-dimensional direct linear transformation (2D-DLT) - were compared for both pan and tilt over a range of angles. It was found that both the 9-parameter 2D-DLT and the 8-parameter 2D-DLT with 6 calibration points performed significantly better than the other two methods. Since the former had a slightly better overall performance, the 9-parameter 2D-DLT was chosen at the method of calibration for recordings of nereidid locomotion.

A.1 Introduction to calibration

Kinematical studies are done by first collecting the data (i.e. recording a movement sequence) and then analysing the collected data. However, some intermediate steps need to be taken before an analysis can be carried out. The points of interest in the sequence need to be digitised either manually or automatically, so that these points can be expressed in a coordinate system. A proper quantification of the movement, such as speed and distance, can then be done. However, if these image measurements are to make sense they have to be converted into real world measurements. The simplest way of transforming pixel coordinates obtained from a recording into real world coordinates is the scaling method. This technique simply consists of placing a scale bar of known length in the recordings. However, it is only accurate if the camera is placed directly perpendicular and horizontally levelled to the activity plane (Brewin and Kerwin 2003). Even small rolls and tilts of the camera can have significant negative effects on reconstruction errors (Brewin and Kerwin 2003). Instead another technique, two-dimensional direct linear transformation (2D-DLT) where several calibration points are distributed over the entire field of view, can be used. This method provides much more accurate positional data independent of camera position (Brewin and Kerwin 2003). The 2D-DLT method, furthermore, automatically

incorporates separate horizontal and vertical scale factors which have been shown to provide better accuracy in the scaling method.

In this thesis there is a need for calibration of high-speed recordings of the locomotion of the marine worm *Nereis diversicolor*. This worm primarily moves by crawling over the substrate (Gray 1939), however, it is also capable of swimming (Clark and Tritton 1970), especially when threatened (Thiel and Reise 1993). Crawling over a flat surface is horizontal locomotion, but the worm also displays level or near level movement during swimming (chapter 6). Traditionally locomotion has, therefore, been analysed as movement in the horizontal plane only (Clark and Tritton 1970, Gray 1939). Thus only two-dimensional calibration methods are necessary to study locomotion in nereidids. However, more complicated, three-dimensional calibration can be done using very similar techniques. The three-dimensional direct linear transformation method is essential the same as the below mentioned 2D-DLT method, except that more linear equations need to be solved as a result of the extra z-coordinate (Shapiro 1978).

In the present study variations of the 2D-DLT method were compared with the simple scaling method under realistic field conditions to locate the most suitable method (i.e. the one showing the smallest reconstruction error) to calibrate the recordings of nereidid worm locomotion.

A.2 Simple scaling

The simple scaling method is the most simple, and probably therefore the most common, method to use when converting image coordinates into real world coordinates. It consists of using a linear equation to describe the relation between the image and the real world coordinates.

$$\begin{bmatrix} x \\ y \end{bmatrix} = \begin{bmatrix} a_x & \\ & a_y \end{bmatrix} \begin{bmatrix} u \\ v \end{bmatrix} + \begin{bmatrix} b_x \\ b_y \end{bmatrix}. \qquad \text{(A.1)}$$

Where, a_x, a_y, b_x and b_y are constants.
To find the constants two calibration points with known real world coordinates (x_1,y_1) and (x_2,y_2) and known image coordinates (u_1,v_1) and (u_2,v_2) are needed. From (A.1) it follows that the a_x and a_y constants can be found this way

$$\begin{bmatrix} x_1 \\ y_1 \end{bmatrix} - \begin{bmatrix} x_2 \\ y_2 \end{bmatrix} = \begin{bmatrix} a_x \\ a_y \end{bmatrix} \left(\begin{bmatrix} u_1 \\ v_1 \end{bmatrix} - \begin{bmatrix} u_2 \\ v_2 \end{bmatrix} \right) \Leftrightarrow$$
$$\begin{bmatrix} a_x \\ a_y \end{bmatrix} = \begin{bmatrix} (x_1 - x_2)/(u_1 - u_2) \\ (y_1 - y_2)/(v_1 - v_2) \end{bmatrix} \quad \text{(A.2)}$$

Similarly the b_x and b_y constants can be found from (3.1) in this way

$$\begin{bmatrix} a_x \\ a_y \end{bmatrix} = \left(\begin{bmatrix} x_1 \\ y_1 \end{bmatrix} - \begin{bmatrix} b_x \\ b_y \end{bmatrix} \right) / \begin{bmatrix} u_1 \\ v_1 \end{bmatrix} = \left(\begin{bmatrix} x_2 \\ y_2 \end{bmatrix} - \begin{bmatrix} b_x \\ b_y \end{bmatrix} \right) / \begin{bmatrix} u_2 \\ v_2 \end{bmatrix} \Leftrightarrow$$
$$\begin{bmatrix} b_x \\ b_y \end{bmatrix} = \begin{bmatrix} (u_2 x_1 - u_1 x_2)/(u_2 - u_1) \\ (v_2 y_1 - v_1 y_2)/(v_2 - v_1) \end{bmatrix} \quad \text{(A.3)}$$

When the calibration has been done and the constants found from equation (A.2) and (A.3), the real world coordinates can be calculated from the image coordinates by using equation (A.1).

Note that in order to use equation (A.3) the two marker points must not form a horizontal or vertical line. However, in cases where this is unavoidable, the image pixels might be assumed to be square in which case the horizontal and vertical calibration parameters are equal (i. e. $a_x = a_y$ and $b_x = b_y$).

A.3 Two-dimensional direct linear transformation

The relationship between the real world coordinates (x,y) and the image coordinates (u,v) in the 2D-DLT method can be described with the following equations (Walton 1981 cited in Kwon 1999)

$$u = \frac{L_1 x + L_2 y + L_3}{L_7 x + L_8 y + 1}. \quad \text{(A.4)}$$

$$v = \frac{L_4 x + L_5 y + L_6}{L_7 x + L_8 y + 1}. \quad \text{(A.5)}$$

Where L_1, L_2,…., L_8 are the 2-D DLT parameters. These parameters can be found from a minimum of 4 calibration points and the above equations that can be rearranged as following, where n is the number of calibration points.

$$u_n = \frac{L_1 x_n + L_2 y_n + L_3}{L_7 x_n + L_8 y_n + 1} \Rightarrow u_n * (L_7 x_n + L_8 y_n + 1) = L_1 x_n + L_2 y_n + L_3$$

$$v_n = \frac{L_4 x_n + L_5 y_n + L_6}{L_7 x_n + L_8 y_n + 1} \Rightarrow v_n * (L_7 x_n + L_8 y_n + 1) = L_4 x_n + L_5 y_n + L_6$$

Introducing the vector $\vec{L} = (L_1, L_2, L_3, L_4, L_5, L_6, L_7, L_8)$ the above equations can be written as a set of linear equations.

$$u_1 + (0,0,0,0,0,0,u_1 x_1, u_1 y_1) \cdot \vec{L} = (x_1, y_1, 1, 0, 0, 0, 0, 0) \cdot \vec{L}$$
$$v_1 + (0,0,0,0,0,0,v_1 x_1, v_1 y_1) \cdot \vec{L} = (0,0,0, x_1, y_1, 1, 0, 0) \cdot \vec{L}$$
$$\vdots \qquad \vdots$$
$$u_n + (0,0,0,0,0,0,u_n x_n, u_n y_n) \cdot \vec{L} = (x_n, y_n, 1, 0, 0, 0, 0, 0) \cdot \vec{L}$$
$$v_n + (0,0,0,0,0,0,v_n x_n, v_n y_n) \cdot \vec{L} = (0,0,0, x_n, y_n, 1, 0, 0) \cdot \vec{L}$$

Subtracting the second term on the left hand side from the right hand side and using the distribution law for vectors, these sets of linear equations can be re-written as.

$$u_1 = (x_1, y_1, 1, 0, 0, 0, -u_1 x_1, -u_1 y_1) \cdot \vec{L}$$
$$v_1 = (0,0,0, x_1, y_1, 1, -v_1 x_1, -v_1 y_1) \cdot \vec{L}$$
$$\vdots \qquad \vdots$$
$$u_n = (x_n, y_n, 1, 0, 0, 0, -u_n x_n, -u_n y_n) \cdot \vec{L}$$

$$v_n = (0,0,0,x_n,y_n,1,-v_n x_n,-v_n y_n)\cdot \vec{L}.$$

This can be written as the following matrix equation and solved for $\vec{L}$.

$$\vec{c} = A\vec{L}. \qquad \text{(A.6)}$$

Where n ≥4 and $\vec{L} = \begin{bmatrix} L_1 \\ L_2 \\ L_3 \\ L_4 \\ L_5 \\ L_6 \\ L_7 \\ L_8 \end{bmatrix}, \vec{c} = \begin{bmatrix} u_1 \\ v_1 \\ . \\ . \\ . \\ . \\ u_n \\ v_n \end{bmatrix}, A = \begin{bmatrix} x_1 & y_1 & 1 & 0 & 0 & 0 & -u_1x_1 & -u_1y_1 \\ 0 & 0 & 0 & x_1 & y_1 & 1 & -v_1x_1 & -v_1y_1 \\ . & . & . & . & . & . & . & . \\ . & . & . & . & . & . & . & . \\ . & . & . & . & . & . & . & . \\ . & . & . & . & . & . & . & . \\ x_n & y_n & 1 & 0 & 0 & 0 & -u_nx_n & -u_ny_n \\ 0 & 0 & 0 & x_n & y_n & 1 & -v_nx_n & -v_ny_n \end{bmatrix}$.

Since n can be larger than 4, A is not necessarily a square matrix and hence is not always invertible. Instead $\vec{L}$ is found with a modification of the Gauss-Elimination technique (the '\' operator in MATLAB).

Once the 2D DLT parameters (L_1, L_2,…., L_8) have been found from equation (A.6), equations (A.4) and (A.5) can be used to transform the image coordinates (u,v) of the recording into the real world coordinates (x,y). From (A.4) x can be isolated.

$$x = \frac{L_2 y + L_3 - uL_8 y - u}{uL_7 - L_1}. \qquad \text{(A.7)}$$

Equation (A.7) can be inserted into (A.5) from which y can be isolated

$$y = \frac{(L_4 - vL_7)(L_3 - u) + (L_6 - v)(uL_7 - L_1)}{vL_7(L_2 - uL_8) - L_4(L_2 - uL_8) - (L_5 + vL_8)(uL_7 - L_1)}. \qquad \text{(A.8)}$$

Alternatively, a more computationally friendly method can be used to find the real world coordinates $\vec{r}$ = (x,y) from the image coordinates (u,v), which consists of solving the following linear equation (Brewin and Kerwin *Unpublished*)

$$\vec{q} = M\vec{r} \Leftrightarrow$$
$$\begin{bmatrix} u - L_3 \\ v - L_6 \end{bmatrix} = \begin{bmatrix} L_1 - L_7 u & L_2 - L_8 u \\ L_4 - L_7 v & L_5 - L_8 v \end{bmatrix} \begin{bmatrix} x \\ y \end{bmatrix}. \qquad \text{(A.9)}$$

As with equation (A.6) $\vec{r}$ is found by using a modification of the Gauss elimination technique (the '\' operator in MATlab).

A general method to estimate the accuracy of the calibration, not only for the 2D-DLT method, but for all calibration methods, is to calculate the reconstruction error. This is the distance between the original calibration points and the reconstructed calibration points and can be formally written as

$$\varepsilon_r = \frac{1}{n}\sum_{i=1}^{n}\sqrt{(rx_i - x_i)^2 + (ry_i + y_i)^2}\,. \qquad \text{(A.10)}$$

Where (x_i,y_i) is the original calibration point and (rx_i,ry_i) is the reconstructed and n is the total number of calibration points.

Note that when employing the 2D-DLT method the calibration points must not be collinear.

A.4 Two-dimensional direct linear transformation with 9 parameters

Recently a modification of the 2D-DLT method that corrects for lens distortion and therefore includes an extra 9th parameter in the L-vector was developed at the Department of Sport and Exercise Science at the University of Bath (Brewin and Kerwin *Unpublished*). Essentially the method works by evaluating the 8-parameter 2D-DLT, and obtaining estimates of the errors due to lens distortion by finding the difference between the real world and the reconstructed coordinates of the calibration points (Trewartha *Pers. comm.*). The modifications to equation (A.6) result in a new set of linear equations that can be written as follows.

$$\vec{c} = A\vec{L} \Leftrightarrow$$

$$\begin{bmatrix} u_1 \\ v_1 \\ \cdot \\ \cdot \\ \cdot \\ \cdot \\ u_n \\ v_n \end{bmatrix} = \begin{bmatrix} x_1 & y_1 & 1 & 0 & 0 & 0 & -mu_1x_1 & -mu_1y_1 & -u_1r_1 \\ 0 & 0 & 0 & x_1 & y_1 & 1 & -mv_1x_1 & -mv_1y_1 & -v_1r_1 \\ \cdot & \cdot & \cdot & \cdot & \cdot & \cdot & \cdot & \cdot & \cdot \\ \cdot & \cdot & \cdot & \cdot & \cdot & \cdot & \cdot & \cdot & \cdot \\ \cdot & \cdot & \cdot & \cdot & \cdot & \cdot & \cdot & \cdot & \cdot \\ \cdot & \cdot & \cdot & \cdot & \cdot & \cdot & \cdot & \cdot & \cdot \\ x_n & y_n & 1 & 0 & 0 & 0 & -mu_nx_n & -mu_ny_n & -u_nr_n \\ 0 & 0 & 0 & x_n & y_n & 1 & -mv_nx_n & -mv_ny_n & -v_nr_n \end{bmatrix} \begin{bmatrix} L_1 \\ L_2 \\ L_3 \\ L_4 \\ L_5 \\ L_6 \\ L_7 \\ L_8 \\ L_9 \end{bmatrix} \quad \text{(A.11)}$$

Where

$$r_i = u_i^2 + v_i^2$$
$$mu_i = u_i + L_9 r_i u_i$$
$$mv_i = v_i + L_9 r_i v_i$$

and n is the number of calibration point which, due to the extra parameter in the modified 2D-DLT, needs to be at least 5.

The modified 2D-DLT method works by finding the optimal 9th parameter (L_9) by an iteration method. The iteration needs to run 5-10 times to produce a stable L_9. The initial estimation of L_9 used in the first iteration is the square of the reconstruction error found by equation (A.10). The traditional 2D-DLT method therefore needs to be applied before the modified 2D-DLT method can be used.

When a satisfactory set of 2D-DLT parameters have been obtained these can be used to convert the image coordinates (u,v) into real world coordinates $\vec{r}$ = (x,y) by applying the following modified version of equation (A.9)

$$\vec{q} = M\vec{r} \Leftrightarrow$$
$$\begin{bmatrix} mu - L_3 \\ mv - L_6 \end{bmatrix} = \begin{bmatrix} L_1 - L_7 mu & L_2 - L_8 mu \\ L_4 - L_7 mv & L_5 - L_8 mv \end{bmatrix} \begin{bmatrix} x \\ y \end{bmatrix} \quad \text{(A.12)}$$

Where

$$r = u^2 + v^2$$
$$mu = u + L_9 ru$$
$$mv = v + L_9 rv$$

Note that similar to the 2D-DLT method with 8 parameters, the calibration points for the 2D-DLT method with 9 parameters must not be collinear.

A.5 Materials and methods

To compare the accuracy of the three methods, described in the previous sections, under realistic field situations, a marking board containing a set of calibration and reconstruction points was photographed at various angles of tilt and pan. Single photographs were taken with a digital high-speed camera (The *Motion*Scope 2000S, Redlake MASD, Inc.) yielding a resolution of 480 x 420 pixels for each image. A 25 mm lens was used and placed at a height of 50 cm above the marking board, but the actual distance between the lens and the marker board varied with tilt and pan angles. The marking board contained 10 points. Six of these were calibration points with the following real world coordinates in mm, C1: (5,55), C2: (15,5), C3: (30,25), C4: (35,45), C5: (50,15) and C6: (55,60). The last 4 were the reconstruction points with the following real world coordinates in mm, R1: (15,30), R2: (25,60), R3: (35,15) and R4: (40,35).

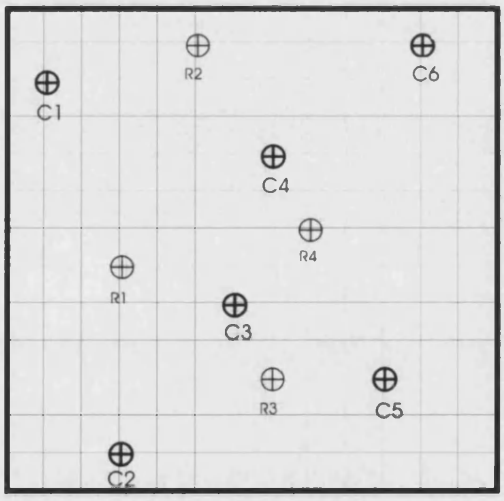

Fig. A.1. The Marking board with the 6 calibration points (C1-C6) and the 4 reconstruction points (R1-R4)

One photograph was taken at each of the following tilt angles 0°, 5°, 10° and 15° while keeping a constant pan angle of 0°. Furthermore, one photograph was taken at each of the following pan angles 0°, 5°, 10° and 15° while keeping a constant tilt angle

of 0°. This resulted in a total of 8 photographs. Each photograph was digitised 10 times using CaliDigitiser, a custom-built LabVIEW program (see appendix B). The digitised calibration coordinates were then used to obtain the calibration parameters (i.e. calculating the constants for the simple scaling method and the L-vector for the 2D-DLT methods) by using MethComp, a custom-built MATLAB program (see appendix B). MethComp was also used to convert the digitised image coordinates of the reconstruction points into real world coordinates. From the real world coordinates the reconstruction error was calculated using equation (A.10).

Four calibration methods were compared. The simple scaling method described in section A.2, where calibration points C1 and C5 were used, the 8 parameter 2D-DLT method described in section A.3 was used with both 4 calibration points (C1, C2, C5 and C6) and with all 6 calibration points (henceforth referred to as DLT84 and DLT86, respectively) and finally the 9 parameter 2D-DLT method described in section A.4 was used, again with all 6 calibration points (henceforth referred to as DLT9).

The data was analysed by first performing a logarithmic transformation of the data to obtain equal variances, except for a few cases where the original data showed equal variances and of combined data where a square-root transformation was necessary to obtain equal variances. The reconstruction error was then compared for each reconstruction point and for pan and tilt by using a two-way ANOVA with method and angle as fixed factors. Overall means of all angles were also compared for pan and tilt using a two-way ANOVA. For all individual reconstruction points a *post hoc* Tukey HSD test was performed to separately check for significant differences within all the combinations of the main effect angle and the main effect method. Note that the statistics of the Tukey HSD test is not shown to avoid large unnecessary tables. A one-way ANOVA was performed to investigate the effect of angle for each method separately for all reconstruction points combined. Significance level was set at $\alpha = 0.05$ and all tests were performed using SPSS for Windows version 11.0 (SPSS Inc. 2001).

A.6 Results

The largest difference between the minimum and maximum x-value for the same point was 2 pixels (n = 80) and for the y-value it was 4 pixels (n = 80). Overall the

average difference in percentage between the maximum and the minimum was for the x-value 0.6% (n = 80) and for the y-value it was 1.4% (n = 80).

Reconstruction Point 1:

Reconstruction point 1 was located close to the left border of the area spanned by the calibration points (Fig. A.1).

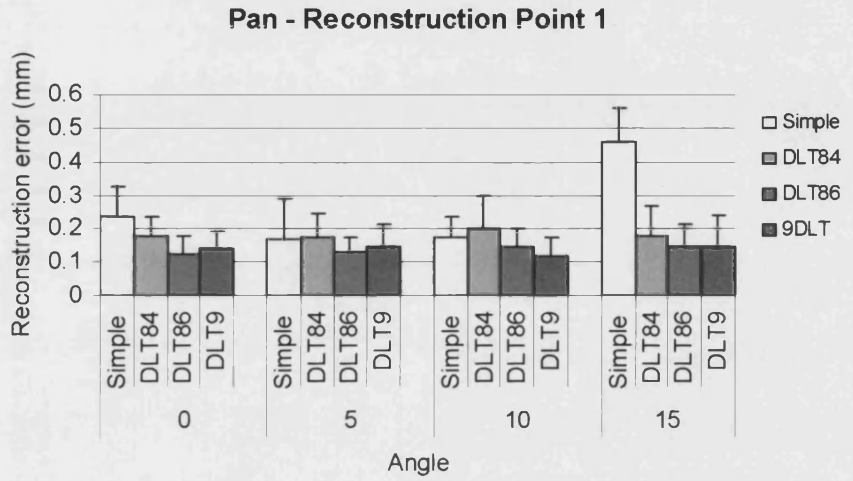

Fig. A.2. The reconstruction error of the 4 methods at increasing angles of pan. Simple is the simple scaling method, DLT84 is the 8-parameter 2D-DLT method using 4 calibration points, DLT86 is the 8-parameter 2D-DLT method using 6 calibration points, and DLT9 is the 9-parameter 2D-DLT method using 6 calibration points. Each bar represents the mean of 10 samples. The error bars indicate the standard deviation.

The four methods performed more or less similarly at the three lower pan angles, whereas the simple scaling method had a much higher reconstruction error at 15° than the other three methods (Fig. A.2). There was, however, no significant effect of angle (Two-way ANOVA: $F_{(3,159)} = 1.78$, $p = 0.15$). Furthermore, the DLT86 method and the DLT9 method consistently performed better than the other two methods. A statistical analysis revealed a significant effect of method (Two-way ANOVA: $F_{(3,159)} = 9.66$, $p < 0.05$). The interaction between the effects of angle and method was also significant (Two-way ANOVA: $F_{(9,159)} = 9.66$, $p < 0.05$). A *post hoc* Tukey HSD revealed a significant difference between the simple scaling method and both the DLT86 and the DLT9. A significant difference was also found between the DLT84 and the DLT9.

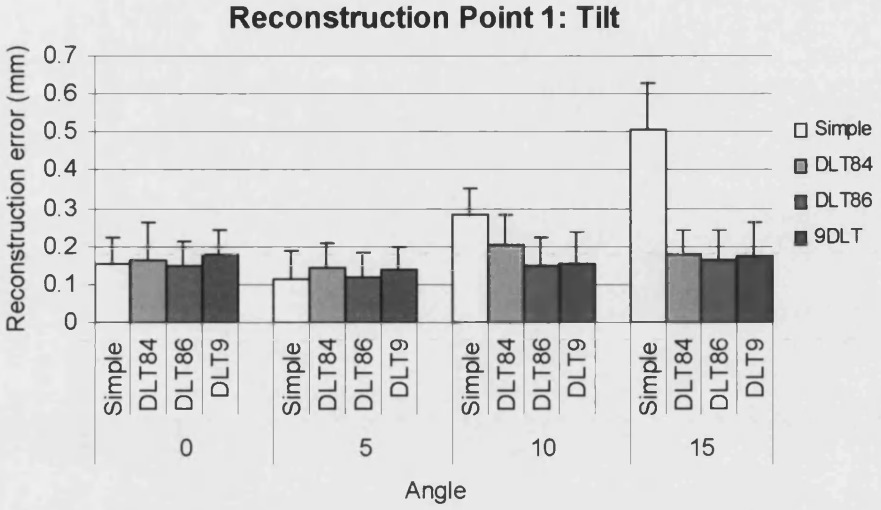

Fig. A.3. The reconstruction error of the 4 methods at increasing angles of tilt. Simple is the simple scaling method, DLT84 is the 8-parameter 2D-DLT method using 4 calibration points, DLT86 is the 8-parameter 2D-DLT method using 6 calibration points, and DLT9 is the 9-parameter 2D-DLT method using 6 calibration points. Each bar represents the mean of 10 samples. The error bars indicate the standard deviation.

The reconstruction error of the four methods was similar at the two lower angles of tilt, whereas the simple scaling methods had a higher reconstruction error at both 10° and 15° than the other three methods (Fig. A.3). Statistical tests revealed both a significant effect of angle (Two-way ANOVA: $F_{(3,159)} = 9.60$, $p < 0.05$) and of method (Two-way ANOVA: $F_{(3,159)} = 6.59$, $p < 0.05$). The interaction between the effects of angle and method was also significant (Two-way ANOVA: $F_{(9,159)} = 3.90$, $p < 0.05$). A *post hoc* Tukey HSD test showed there were significant differences between 15° and both 5° and 10°, as well as a significant difference between 5° and 10°. Similar significant differences were found between the simple scaling method and the rest of the methods, which did not differ from each other.

Reconstruction Point 2:

Reconstruction point 2 was located outside of the top border of the area spanned by the calibration points (Fig. A.1).

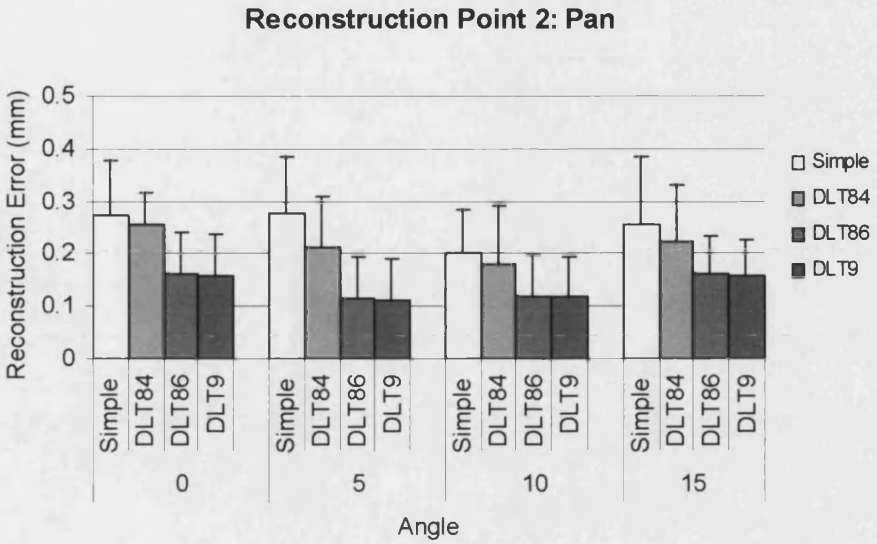

Fig. A.4. The reconstruction error of the 4 methods at increasing angles of pan. Simple is the simple scaling method, DLT84 is the 8-parameter 2D-DLT method using 4 calibration points, DLT86 is the 8-parameter 2D-DLT method using 6 calibration points, and DLT9 is the 9-parameter 2D-DLT method using 6 calibration points. Each bar represents the mean of 10 samples. The error bars indicate the standard deviation.

The simple scaling method and the DLT84 method performed consistently worse than the other two methods for all angles, whereas there appeared to be no effect of angle on any of the methods (Fig. A.4). Statistical tests confirmed these observations as a significant effect of method was found (Two-way ANOVA: $F_{(3,159)} = 11.83$, $p < 0.05$), but not of angle (Two-way ANOVA: $F_{(3,159)} = 2.36$, $p = 0.07$). No interaction was found between the effects of angle and method (Two-way ANOVA: $F_{(9,159)} = 0.58$, $p = 0.81$). A *post hoc* Tukey HSD test showed there were significant differences between the simple scaling method and both the DLT86 and the DLT9 method. Differences were also found between the DLT84 and both the DLT86 and the DLT9 method.

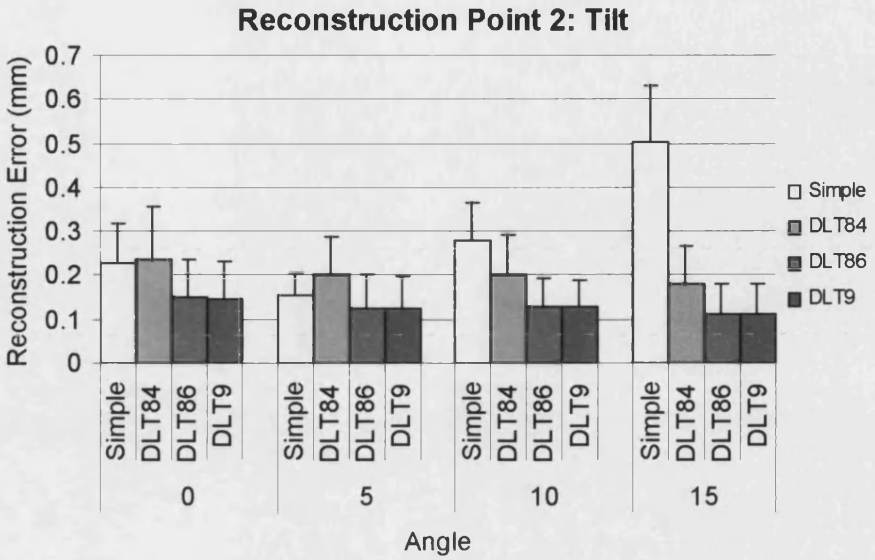

Fig. A.5. The reconstruction error of the 4 methods at increasing angles of tilt. Simple is the simple scaling method, DLT84 is the 8-parameter 2D-DLT method using 4 calibration points, DLT86 is the 8-parameter 2D-DLT method using 6 calibration points, and DLT9 is the 9-parameter 2D-DLT method using 6 calibration points. Each bar represents the mean of 10 samples. The error bars indicate the standard deviation.

Contrary to the situation for pan, tilt angle did affect the accuracy of the simple scaling method (Fig. A.5). The simple scaling method and the DLT84 method, furthermore, performed consistently worse than the other two methods for all angles investigated. Statistical tests revealed that there was a significant effect of both angle (Two-way ANOVA: $F_{(3,159)} = 5.20$, $p < 0.05$) and method (Two-way ANOVA: $F_{(3,159)} = 32.57$, $p < 0.05$). The interaction between them was also significant (Two-way ANOVA: $F_{(9,159)} = 9.01$, $p < 0.05$). A *post hoc* Tukey HSD test showed that there was a significant difference between the effect of angle at 5° and 15°, whereas the rest of the angles were not significantly different. A similar test done for the effect of method revealed that there were significant differences between all the methods except between DLT86 and DLT9.

Reconstruction Point 3:

Reconstruction point 3 was located below the centre of the area spanned by the calibration points (Fig. A.1).

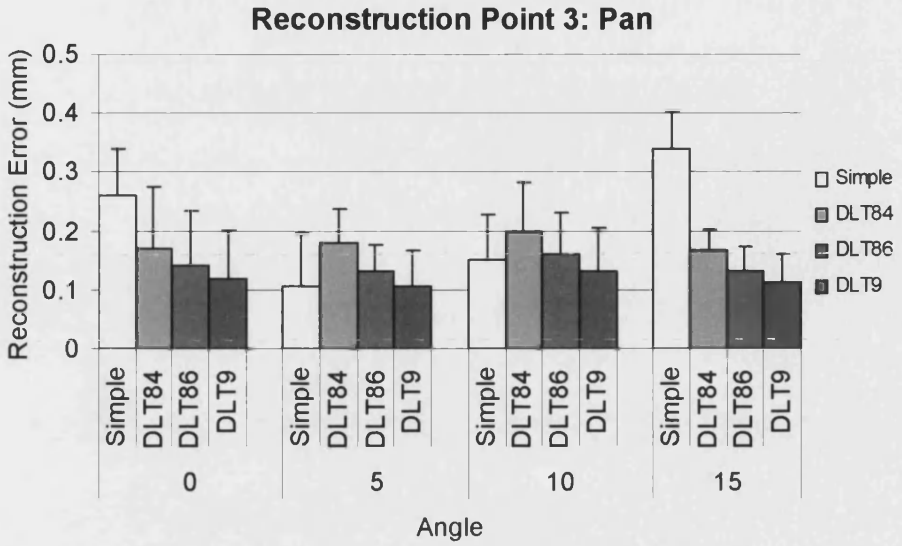

Fig. A.6. The reconstruction error of the 4 methods at increasing angles of pan. Simple is the simple scaling method, DLT84 is the 8-parameter 2D-DLT method using 4 calibration points, DLT86 is the 8-parameter 2D-DLT method using 6 calibration points, and DLT9 is the 9-parameter 2D-DLT method using 6 calibration points. Each bar represents the mean of 10 samples. The error bars indicate the standard deviation.

The three 2D-DLT methods were more or less constant at the four angles, whereas the simple scaling method showed some variation with the highest errors found at 0° and 15° (Fig. A.6). Statistical tests showed that there were both a significant effect of angle (Two-way ANOVA: $F_{(3,159)} = 4.23$, $p < 0.05$) and of method (Two-way ANOVA: $F_{(3,159)} = 14.07$, $p < 0.05$). The interaction between the effects was also significant (Two-way ANOVA: $F_{(9,159)} = 5.93$, $p < 0.05$). A *post hoc* Tukey HSD test showed a significant difference between 5° and 15°. Differences were also found between the simple scaling method and both the DLT86 method and the DLT9 as well as between the DLT84 and DLT9 method.

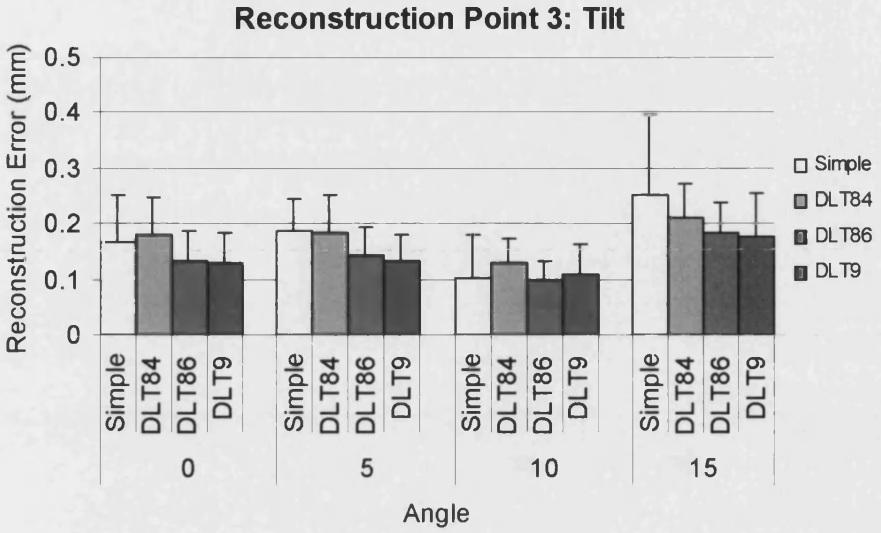

Fig. A.7. The reconstruction error of the 4 methods at increasing angles of tilt. Simple is the simple scaling method, DLT84 is the 8-parameter 2D-DLT method using 4 calibration points, DLT86 is the 8-parameter 2D-DLT method using 6 calibration points, and DLT9 is the 9-parameter 2D-DLT method using 6 calibration points. Each bar represents the mean of 10 samples. The error bars indicate the standard deviation.

There was a slightly smaller error at 10° and a slightly larger error at 15° than for the first two angles of tilt (Fig. A.7). It, furthermore, looked like there was a slightly larger error for the simple scaling method and for the DLT84 method than for the other two methods. Significant effects of both angle (Two-way ANOVA: $F_{(3,159)} = 10.00$, $p < 0.05$) and of method (Two-way ANOVA: $F_{(3,159)} = 3.46$, $p < 0.05$) were found, but the interaction between them was not significant (Two-way ANOVA: $F_{(9,159)} = 0.12$, $p = 0.99$). A *post hoc* Tukey HSD test revealed a significant difference between the angles of 0° and 15°, and between 5° and 10° as well as between 10° and 15°. There were also significant differences between the DLT9 method and both the simple scaling method and the DLT84 method.

Reconstruction Point 4:

Reconstruction point 4 was located close but slightly to the left of the centre of the area spanned by the calibration points (Fig. A.1).

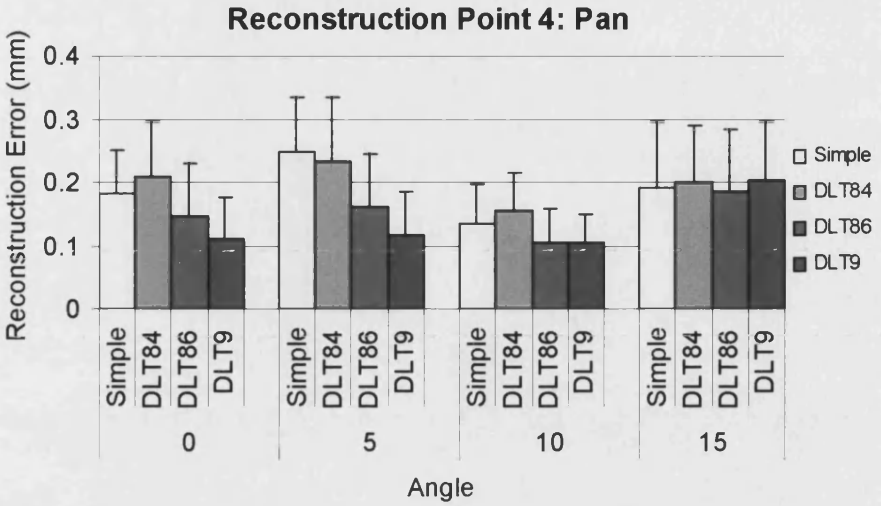

Fig. A.8. The reconstruction error of the 4 methods at increasing angles of pan. Simple is the simple scaling method, DLT84 is the 8-parameter 2D-DLT method using 4 calibration points, DLT86 is the 8-parameter 2D-DLT method using 6 calibration points, and DLT9 is the 9-parameter 2D-DLT method using 6 calibration points. Each bar represents the mean of 10 samples. The error bars indicate the standard deviation.

The simple scaling method and the DLT84 method performed worse than the other two methods at the two smaller angles of pan, whereas all four methods showed the same performance for the two larger angles (Fig. A.8). Both the effects of angle (Two-way ANOVA: $F_{(3,159)} = 4.06$, $p < 0.05$) and of method (Two-way ANOVA: $F_{(3,159)} = 5.66$, $p < 0.05$) were statistically significant, but the interaction of the effects was not (Two-way ANOVA: $F_{(9,159)} = 1.18$, $p = 0.31$). A *post hoc* Tukey HSD test showed significant differences between 10° and both 5° and 15°. Significant differences were also found between the DLT9 method and both the simple scaling method and the DLT84.

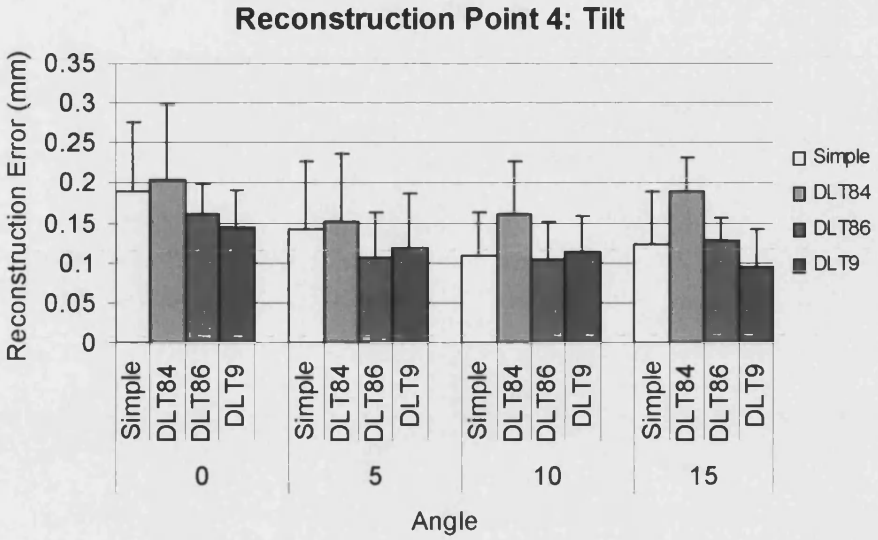

Fig. A.9. The reconstruction error of the 4 methods at increasing angles of tilt. Simple is the simple scaling method, DLT84 is the 8-parameter 2D-DLT method using 4 calibration points, DLT86 is the 8-parameter 2D-DLT method using 6 calibration points, and DLT9 is the 9-parameter 2D-DLT method using 6 calibration points. Each bar represents the mean of 10 samples. The error bars indicate the standard deviation.

There was little difference between the tilt angles, except possibly a slightly larger error at 0° (Fig. A.9). The DLT84 method with 4 calibration points consistently performed worse than the other three methods. Statistical tests revealed that both the effect of angle (Two-way ANOVA: $F_{(3,159)} = 4.19$, $p < 0.05$) and of method (Two-way ANOVA: $F_{(3,159)} = 4.64$, $p < 0.05$) were significant. The interaction of the effect was not significant (Two-way ANOVA: $F_{(9,159)} = 0.67$, $p = 0.74$). A *post hoc* Tukey HSD test showed significant differences between the angles of 0° and both 5° and 10°. Significant differences were also found between the DLT84 and both the DLT86 and DLT9 model.

Overall: Lastly the data from the four points were pooled together in order to get an estimate of the performance of each method in the whole focus area.

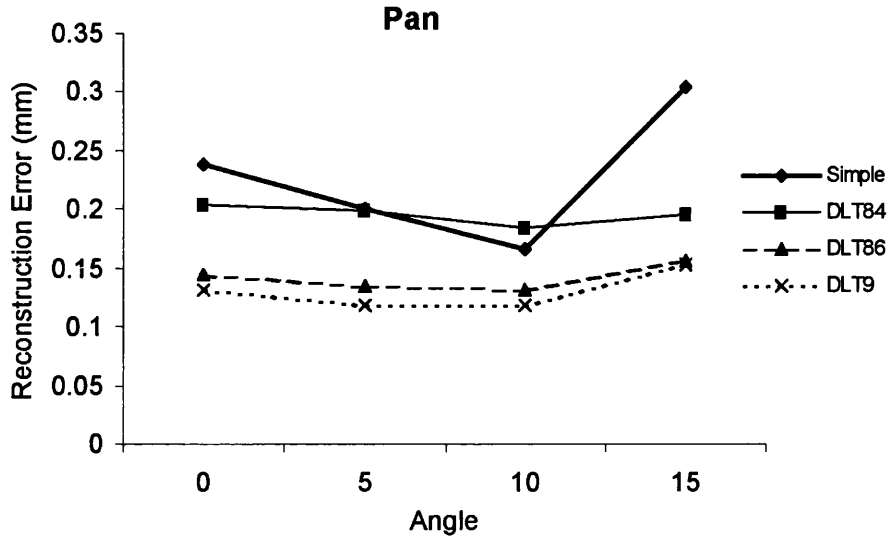

Fig. A.10. The performance of each method for all reconstruction points combined as a function of pan angle. Simple is the simple scaling method, DLT84 is the 8-parameter 2D-DLT method using 4 calibration points, DLT86 is the 8-parameter 2D-DLT method using 6 calibration points, and DLT9 is the 9-parameter 2D-DLT method using 6 calibration points. Each point represents the mean of 40 samples.

For the combined data on pan there was a significant effect of method (Two-way ANOVA: $F_{(3,639)} = 39.03$, $p < 0.05$) and from figure A.10 it follows that the DLT9 method and the DLT86 method had the smallest reconstruction errors for all pan angles investigated. A significant effect was also found of angle (Two-way ANOVA: $F_{(3,639)} = 8.71$, $p < 0.05$), however further statistical tests revealed that only the simple scaling method showed varied performance with different angles (One-way ANOVA: $F_{(3,159)} = 8.71$, $p < 0.05$), whereas the other three methods showed constant performance over the angles investigated (8DLT84: One-way ANOVA: $F_{(3,159)} = 0.39$, $p = 0.76$, 8DLT86: One-way ANOVA: $F_{(3,159)} = 0.85$, $p = 0.47$, DLT9: One-way ANOVA: $F_{(3,159)} = 1.62$, $p = 0.19$). The interaction between the effect of angle and the effect of method was significant (Two-way ANOVA: $F_{(9,639)} = 2.38$, $p < 0.05$).

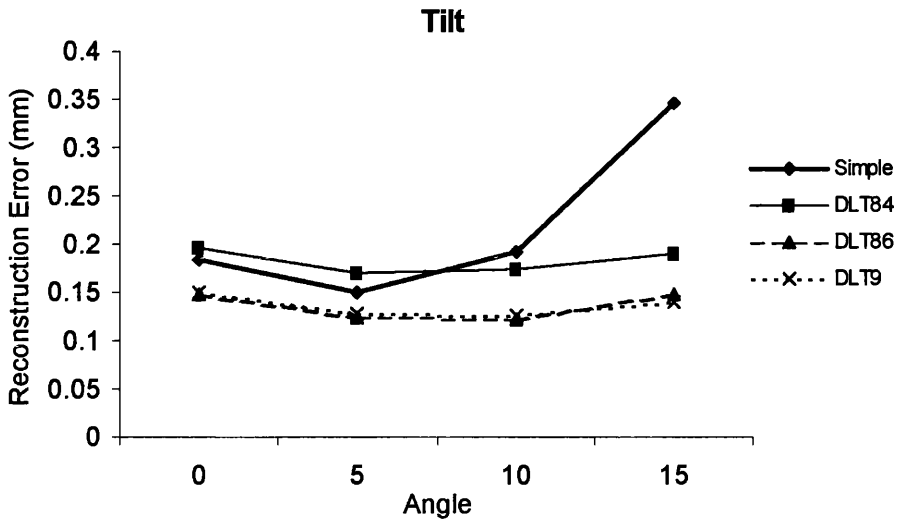

Fig. A.11. The performance of each method for all reconstruction points combined as a function of tilt angle. Simple is the simple scaling method, 8DLT4 is the 8-parameter 2D-DLT method using 4 calibration points, 8DLT6 is the 8-parameter 2D-DLT method using 6 calibration points, and 9DLT is the 9-parameter 2D-DLT method using 6 calibration points. Each point represents the mean of 40 samples.

The responses of the methods to increasing angles of tilt were similar to that observed for pan. The DLT9 method and the DLT86 again had the smallest reconstruction errors for all tilt angles investigated (Fig. A.11). The simple scaling method gave the largest reconstruction error at the higher angles. Both the effect of angle (Two-way ANOVA: $F_{(3,639)} = 11.55$, $p < 0.05$) and of method (Two-way ANOVA: $F_{(3,639)} = 25.11$, $p < 0.05$),) were statistically significant, as were the interaction between them (Two-way ANOVA: $F_{(9,639)} = 4.81$, $p < 0.05$). Angle had no significant influence on the reconstruction errors for all three 2D-DLT methods at the tilt angles investigated (8DLT84: One-way ANOVA: $F_{(3,159)} = 0.69$, $p = 0.56$, 8DLT86: One-way ANOVA: $F_{(3,159)} = 2.06$, $p = 0.11$, DLT9: One-way ANOVA: $F_{(3,159)} = 0.54$, $p = 0.66$)m whereas there was a significant influence for the simple scaling method (One-way ANOVA: $F_{(3,159)} = 9.56$, $p < 0.05$).

A. 7 Discussion

The reason for choosing and individually analysing four reconstruction points in this study, was to investigate whether any clear differences in reconstruction error were

evident between the reconstruction points. The reconstruction points were chosen such that point R3 and R4 were located near the centre of the area spanned by the calibration points, whereas point R1 and R2 were located on the borders of that area. However, as can be seen on the overview figure (Fig. A.12), only the simple scaling method showed any visible difference in reconstruction error between the various points. For the other three methods there seemed to be no effect of location of the points on the reconstruction error for either tilt or pan. It is, though, important to note that none of the reconstruction points were very far away from the calibration points. In general, extrapolation to points lying outside the calibration area results in a significant increase in the reconstruction error (Brewin and Kerwin 2003; Choo and Oxland 2003).

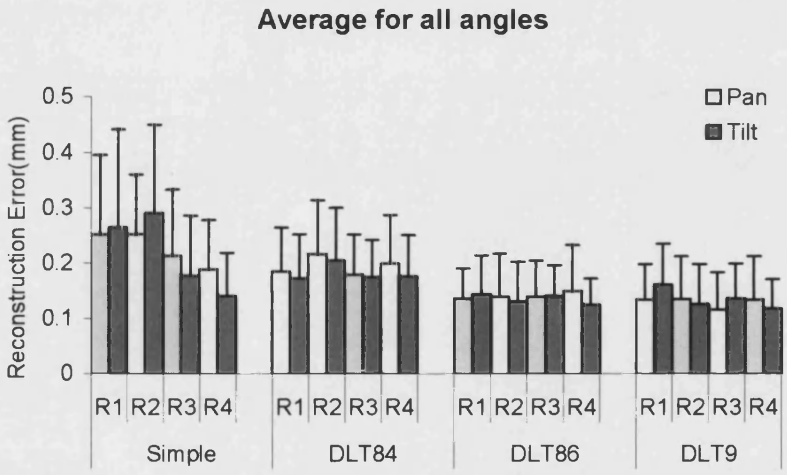

Fig. A.12. The reconstruction errors for each method and point averaged for all angles. Simple is the simple scaling method, DLT84 is the 8-parameter 2D-DLT method using 4 calibration points, DLT86 is the 8-parameter 2D-DLT method using 6 calibration points, and DLT9 is the 9-parameter 2D-DLT method using 6 calibration points. Each bar is mean of 40 samples. The error bar represents the standard deviation

In the present study the effects of tilt and pan were investigated. They both showed similar reconstruction errors for all four methods (Fig. A.12). A more detailed analysis revealed that the effects of pan and tilt as a function of angle resulted in only minor differences between the distributions of reconstruction error among the four methods (see Figs A.2 – A.9). A third effect of roll, the rotation of the camera, was not treated here, despite its alleged influence on the reconstruction error (Brewin and

Kerwin 2003). However, corrections for roll, like for pan and tilt, are inherent in the direct linear transformation methods and since Brewin and Kerwin (2003) have already investigated the difference between the simple scaling method with and without roll, it was decided not to look at roll in the present study. Furthermore, roll has most influence in points placed in the periphery of an image and in the present study most points were placed relatively close to the image centre.

The study of Brewin and Kerwin (2003) compared the accuracy of the scaling method and the 2D-DLT method for various degrees of tilt. In accordance with the results presented here, they found that the 2D-DLT method outperformed the scaling method and that the reconstruction error of the scaling method increased with angle, whereas the reconstruction error of the 2D-DLT was independent of angle. However, in their study they found a much higher sensitivity of the scaling method to angle as they saw a significant increase in reconstruction error from 0° to 6° (Brewin and Kerwin 2003), where the error, in this study, first significantly increased at 10° and above (Fig. A.11). Another difference is that Brewin and Kerwin (2003) only investigated the difference between the scaling method and the DLT84 method, which they found to be significant. In the present study only at reconstruction point 2 was the DLT84 performing significantly better than the simple scaling method (Figs A.2, A.3) and there seemed to be no discernible difference between the two methods for all the points combined except at higher angles (Fig. A.11). The reason for these differences is probably the much higher degree of accuracy that Brewin and Kerwin (2003) employ for both the measurement of angles and the digitising of the calibration and reconstruction points. Such a high degree of accuracy was deemed unnecessary in the study presented here, since the aim was to test the methods under realistic experimental conditions, where it would be too time-consuming to achieve a high degree of precision during the digitising process.

Table A.1. Ranking of the four calibration methods

Point		Significant differences[1]	Interaction[2]
R1	Pan	DLT9 > DLT84, Simple DLT86 > Simple	Yes
	Tilt	DLT9, DLT86, DLT84 > Simple	Yes
R2	Pan	DLT9, DLT86 > DLT84, Simple	No
	Tilt	DLT9, DLT86 > DLT84 > Simple	Yes
R3	Pan	DLT9 > DLT84, Simple DLT86 > Simple	Yes
	Tilt	DLT9 > DLT84, Simple	No
R4	Pan	DLT9 > DLT84, Simple	No
	Tilt	DLT9,DLT86, Simple > DLT84	No

1) The '>' signifies that the methods on the left of the sign have significantly lower reconstruction error than the methods on the right side. Simple is the simple scaling method, DLT84 is the 8-parameter 2D-DLT method using 4 calibration points, DLT86 is the 8-parameter 2D-DLT method using 6 calibration points, and DLT9 is the 9-parameter 2D-DLT method using 6 calibration points.

2) The interaction column displays if the interaction between the effects of angle and method was significant.

The statistical tests conducted revealed whether or not there was a significant interaction between the effects of angle and method. In other words if there were any differences in the way the methods reacted to a change in angle. Since none of the three 2D-DLT methods reacted to angle for either pan or tilt (Figs A.10, A.11), this interaction results from the reaction of the simple scaling method. In half of the cases this was adequate to cause a significant interaction (Table A.1).

The main aim of this study was to identify the most suitable method to use as a calibration method for recordings of locomotion of marine worms. So which method resulted in the smallest reconstruction error? From figures A.10 and A.11 it is evident that the 9-parameter 2D-DLT with 6 calibration points and the 8-parameter 2D-DLT with 6 calibration points performed consistently better than the other two methods for both tilt and pan as well as over all angles tested. A closer look at the results of the individual reconstruction points shows that in none of the cases were there any significant difference between the DLT9 method and the DLT86 method (Table A.1). However, it also reveals that the former method performed slightly better against the DLT84 method and the simple scaling method (Table A.1). Furthermore, since both

methods require 6 calibration points and the only difference lies in the computation (which the computer takes care of), it makes sense to use the DLT9 method. The conclusion of the present study is therefore that the 9-parameter 2D-DLT method will, where possible, be applied to the calibration of all recordings of nereidid locomotion presented in this thesis.

References

Brewin, M. A. and Kerwin, D. G. 2003. Accuracy of scaling and DLT reconstruction techniques for planar motion analyses. *Journal of Applied Biomechanics* **19**: 79-88.

Choo, A. M. and T.Oxland, T. R. 2003. Improved RSA accuracy with DLT and balanced calibration marker distributions with an assessment of initial-calibration. *Journal of Biomechanics* **36**: 259-264.

Clark, R. B. and Tritton, D. J. 1970. Swimming mechanisms in nereidiform polychaetes. *Journal of Zoology* **161**: 257-271.

Gray, J. 1939. Studies in animal locomotion. VII. The kinetics of locomotion of *Nereis diversicolor*. *Journal of Experimental Biology* **16:** 9-17.

Kwon, Y-H. 1999. Object plane deformation due to refraction in two-dimensional underwater motion analysis. *Journal of Applied Biomechanics* **15**: 396-403.

Shapiro, R. 1978. Direct linear transformation method for three-dimensional cinematography. *The Research Quarterly* **49**: 197-205.

Thiel, M. and Reise, K. 1993. Interaction of nemertines and their prey on tidal flats. *Netherlands Journal of Sea Research* **31**: 163-172.

Appendix B

Description and design of software applications written in LABVIEW and MATLAB

Appendix B Description and design of software applications written in LABVIEW and MATLAB

B.1 Introduction and requirements

In experimental sciences, and especially in comparative biomechanics, the manner of extracting and analysing accumulated data often requires almost as much thought as the design of the experiment itself. Sometimes the extraction of data can be done with readily available software such as spreadsheets and statistical packages. This is the case for one of five data chapters in this thesis. In chapter 3 where the morphology of parapodia and setae are compared across species the data is the digital images taken by the scanning electron microscope. Morphological parameters were derived from these images by using the shareware ImageJ 1.29x (National Institutes of Health, USA) and analysed using Microsoft Excel and SPSS (SPSS Inc., 2003). In chapter 4 where the biomimetic potential of artificial hairs was investigated the software controlling the robotic test bed was written in Visual Basic by Gianni La Spina. A LABVIEW example programme was used to extract data from the force sensor and this data was analysed with a FORTRAN 77 routine written by John Williams. Since these programmes were not written by me they are not described in this chapter. However, the remaining two data chapters (chapters 5, 6) and appendix A make use of both LABVIEW and MATLAB programmes specifically written for this PhD project.

Data in these chapters consists mainly of high speed recordings or other types of digital images, so the primary requirements for analysis is a programme that can digitise points of interest in these images. Several such programmes are available commercially. However, due to the unique nature of the animals investigated here, where up to 10 digitised points are necessary to capture all body wave peaks, and the high price of commercially available programmes, I decided to write my own programme. The resultant application Nereis.vi allows an arbitrarily large number of points on each image to be manually digitised and converts the image coordinates of these points into real world coordinates. It is described in some detail in the following section. Attempts were made to automate the digitising process, but due to the complicated sinusoid shape of the moving worm where all points of the body oscillate

and the low contrast between worm and substrate in the recordings of chapter 5, it proved to be too complicated and time consuming to realise within the framework of this PhD. A precursor programme used to digitise single images for the comparison of calibration methods described in appendix A and a modification of it used to extract jet-data from the PIV images in chapter 6 are described in section B.3. The intention was to integrate the data analysis into the LABVIEW digitising process thus making the analysing process simple, fast and user friendly. However, it transpired that the exact way of analysing the digitised data depends on the experimental design thus making it impossible to use a generic method for all experiments. Instead a number of small purpose-built MATLAB routines were written to analyse the real world data extracted by the digitising software. These routines are described in some detail in section B.4. As the project described in this thesis is not a computer science project the main emphasis in the following is on how the programmes work and what they do. Therefore, only a very brief overview with just a few main commands mentioned is given on the actual source code

B.2 The digitising application Nereis.vi

Nereis.vi is a digitising application for video recordings. VI stands for Virtual Instrument and is the file extension used by the object orientated graphical programme language LABVIEW (National Instruments, 2004), and is used throughout this chapter to describe programmes and subprogrammes written in LABVIEW, although in the case of Nereis.vi an actual stand alone executable application was built and used for the digitising process. All programmes used in this PhD project were written with LABVIEW 7.1 (National Instruments, 2004) using commands from the add-on IMAQ Vision (National Instruments, 2003). Nereis.vi consists of a main menu written as a parent VI for four semi-independent SubVIs (Fig. B.1). The main menu allows the user to select the image format of the recording (the individual frames in a recording need to be saved as images in the format 'imagename00xx' for the programme to work) and the SubVI to be executed. It, furthermore, transfers all the file and data parameters from SubVI to SubVI using Shift Registers. The umbrella VI runs in a While Loop and uses the Menu Ring variable to enter the If Boxes that execute the SubVI. The load

function is incorporated into the parent VI and asks the user to select one of the frame images in the recording sequence and supply information about the length of the root image name (the offset), the number of frames in the sequence and the frame rate (this is not used by the programme but gives useful information about the recording sequence for later data analysis). From this the programme identifies the image name and the frame number using the image extension name and the Match Pattern.vi command with '0' as the string to be matched. A very basic help-text and a short about-text are also available from the main menu.

Fig. B.1. A screenshot of the software application Nereis.vi being used to digitise points on a swimming *Nereis diversicolor*. Arrows point to the digitised points on the worm and the three open windows are highlighted. The sub programme Digitiser.vi is open.

The first SubVI NereisViewer.vi allows the user to play the recording back with a variable rate both forward and in reverse as well as manually going one frame back or forward (Fig. B.2). This is accomplished by having a frame number

variable connected to a Shift Register inside a While Loop. The frame number variable increases or decreases depending on the chosen action. After each change in the current frame number the IMAQ Create.vi is used together with the path and image information and the IMAQ Windraw.vi to display the current frame in an active window similar to what is shown in figure B.1. The total number of frames given by the user in the parent VI is here used to ensure that an increase in frame number does not occur after the maximum number has been reached. When the frame number is equal to the maximum frame number, the frame number is reset to the initial number resulting in the recording being played back in a loop. A similar mechanism operates when the recording is viewed in reverse order. There is also an option for the user to specify a given frame number to which the current frame number is then set, which results in the active window jumping to that frame in the recording. Lastly there is a function that allows the user to toggle between two frames (if the switch is positioned to the right the programme enters a nested While Loop), which is useful for visualising differences from frame to frame such as changes in tracer particles and thus water flow in the PIV method. This is accomplished by using Boolean logic to determine which of the two user-given frames is displayed after pressing the toggle bar.

Fig. B.2. The front panel menu for the sub programme NereisViewer.vi.

The second SubVI is the Calibration.vi where a separately loaded calibration image with known real world coordinates is digitised (Fig. B.3). The relation between real world and image coordinates is determined by the simple scaling method, the 2D-DLT with 8 parameters or the 2D-DLT with 9 parameters (see appendix A for a description and comparison of these methods). All functions are placed within a While Loop which terminates when the Exit button is pressed. The programme requires the user to load a single calibration image (in one of the following formats: JPEG, BMP, TIFF or PNG) and uses the IMAQ Create.vi, the IMAQ Readfile.vi and the IMAQ Windraw.vi commands to display the calibration image in the active window. It,

furthermore, creates a smaller zoom window by using the IMAQ Copy.vi and the IMAQ Windraw.vi with another window number (similar to the ones shown in Figs B.1 and B.4). The user can determine the zoom factor with a Horizontal Pointer Slide. When the cursor is in the active window the image coordinates of the cursor are displayed on the front panel. The SubVI has two functional modes, calibration and check mode, which can be switched between by using a Menu Ring variable. In calibration mode (shown in Fig. B.3) another Menu Ring variable allows the user to determine which of the three calibration methods mentioned above should be used to calculate the relation between image and real world coordinates. The variable Digipoint No keeps track of the number of digitisation points selected in the current session by increasing with one each time the mouse is pressed by using Shift Registers and the IMAQ WindLastEvent.vi. The simple scaling method requires two marker points and terminates automatically from the While Loop when Digipoint No reaches two. When the cursor is in the active window, during digitisation, a crosshair is shown in the zoom window to highlight the exact position of the cursor. The crosshair is drawn by using the IMAQ Overlay Oval.vi and the IMAQ Overlay Line.vi based on the cursor coordinates which are in the centre of the crosshair. It updates automatically every time the cursor is moved by deleting the old crosshair with IMAQ Clear Overlay before drawing a new one. When a point is digitised by pressing the mouse a crosshair is placed (until the beginning of a new digitising session) in the active window (See Fig B.4). Pressing the mouse also transfers the cursor coordinates into an Image array updated via Shift Registers. The user is then prompted for the real world coordinates corresponding to the digitised marker point. These coordinates are transferred into the Real array updated via Shift Registers. The same processes occur if the 2D-DLT with 8 or 9 parameters are chosen as calibration method except that the user is asked at the start to determine the number of marker points being digitised. When the number of digitised points reaches the given value (two in the case of the simple scaling method) the programme uses MATLAB code in a MATLAB Script to calculate the calibration parameters. In the case of the simple scaling method these are the b_x, b_y, a_x, a_y in a 4 x 1 array and for the 2D-DLT method these are the L_8 and L_9 vectors in a 8 x 1 and 9 x 1 array respectively (see appendix B for the mathematical equations that are used to calculate the calibration parameters).

In the check mode these calibration parameters can be checked against the calibration sheet in the active window to ensure that they convert image coordinates into real world coordinates with adequate precision. The menu on the right hand side of the front panel changes into check mode (not shown in Fig. B.3) by changing the visibility status on the Property Node of the variables. The active window and the zoom window are the same as in the calibration mode, however, when the user now presses the mouse a line is drawn using IMAQ Overlay Line.vi from the selected coordinates to the current position of the cursor. A recurring IMAQ Copy.vi command is used to ensure that only one line is shown at any given time independent of the position of the cursor. If the user presses the mouse a second time (registered by the IMAQ WindLastEvent.vi) the coordinates of the two selected points are converted into real world coordinates depending on the active calibration method using MATLAB code in a MATLAB Script (see appendix A for a description of the mathematical equations used). The distance between the two points is then calculated for the real world coordinates and can be compared with the known real world distance on the calibration sheet. The user can via a Menu Ring variable determine which calibration method will be used to convert from image to real world coordinates. The default method is the last one used in the calibration mode.

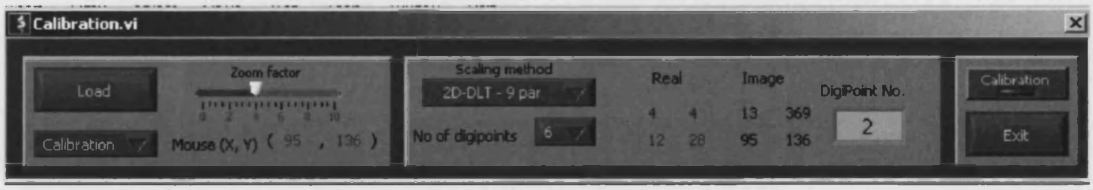

Fig. B.3. The front panel menu of the sub programme Calibration.vi in calibration mode.

The SubVI Digitiser.vi performs the actual digitising of the individual frames in the recording (Fig. B.1). The start frame is controlled by the current frame variable, which is the last active frame from NereisViewer.vi or if that has not been used the frame loaded in the parent VI. In Digitiser.vi there is also a go to function similar to the one in NereisViewer.vi that allows the user to jump to a specific frame. The active and the zoom windows work and make use of crosshairs in the same manner as described above for Calibration.vi. Before the user activates the digitising mode by pressing the

digitise button the number of points digitised needs to be given. The programme then allows the mouse to be pressed (controlled by IMAQ WindLastEvent.vi) the selected number of times in each frame before it advances to the next frame by adding one to the current frame number. Frame images are displayed with IMAQ Create.vi, IMAQ Readfile.vi and IMAQ Windraw.vi as described for NereisViewer.vi and Calibration.vi above. Each time a point is digitised the cursor coordinates are written into a data matrix (4000 x 13) and converted into real world coordinates by using the last calibration method used in Calibration.vi (the equations used to convert from image to real world coordinates are described in appendix A), which are then also added to the data matrix. The front panel contains an option to show the regression line of the selected points on the active window (using IMAQ Overlay Lines.vi) before the programme automatically advances to the next frame (Wait (ms).vi is used to pause the programme for one second). Originally the idea was to incorporate an automatic analysis of the points after each digitising session by finding a local regression line (either a normal regression using the MATLAB function Polyfit or a regression line starting from the last digitised point (i.e. the tail of the worm) and then finding a best fit slope by iterations of maximum and minimum slopes in a narrower and narrower area). Endpoints, midpoints, amplitude, wavelength and slope are then calculated from this regression line and added to the data matrix. However, the method of how this is done is not described here as the use of local regression lines was subsequently found to give too high variation and velocities (from midpoints and position of wave crests) and therefore not used in this project. Instead the locomotion parameters were derived from a global regression line of all digitised points (see section B.4 and chapters 5 and 6 for further details). The show regression line function was, however, found to be useful to give a quick first validation of the digitised points. After the user exits the SubVI and just before control returns to the parent VI, the programme automatically saves the data matrix in an Excel file with a time generated name file using a modified version of the Write to Spreadsheet.vi, which enables string headlines to be written in the first row of the Excel file, and the Format Date/Time String.vi. This is done as a safety precaution and backup to the manual save option given in the Datalog.vi described below.

The last SubVI is the Datalog.vi which displays the recording information and the calibration image and real world coordinates, the simple scaling or 2D-DLT parameters and all variables associated with the digitising process (frame number, digitised point number, image coordinates and real world coordinates). It, furthermore, allows the user to print the information (the content of the front panel of the Datalog.vi) using the Easy Print VI Panel or Documentation.vi or to save it in a text or Excel file using the modified Write to Spreadsheet.vi described above.

B.3 Smaller LABVIEW applications

Only the programmes used to analyse data are included in this chapter. A few smaller programmes were written to aid visualisation, such as a stand alone version of the SubVI NereisViewer.vi described above and a programme using IMAQ Avi Write Frame.vi that builds avi recordings from single image frames. However, two smaller LABVIEW programmes were written to extract digitised data from images. The first is Calidigitiser.vi which was used in appendix A to digitise the marker sheets (Fig. B.4). It is a precursor to the SubVI Calibration.vi described in the section above and can be viewed as a more basic version. The main difference is that the programme runs 10 continuous loops of manually digitising 4 or 6 calibration points (requires changes in the source code) and 4 reconstruction points and that it does not ask for the real world coordinates or calculate the calibration parameters. This is instead done with the MATLAB routine MethComp.m (see next section). Other differences include that the user is required to load the marker sheet image when the programme starts up and that output image coordinates are saved by the user when the programme terminates. The programme, furthermore, does not use IMAQ Overlay commands to draw the cross hair, but instead uses Draw Line.vi , Draw Circle by Radius.vi and the IMAQ AddPictToWindow.vi.

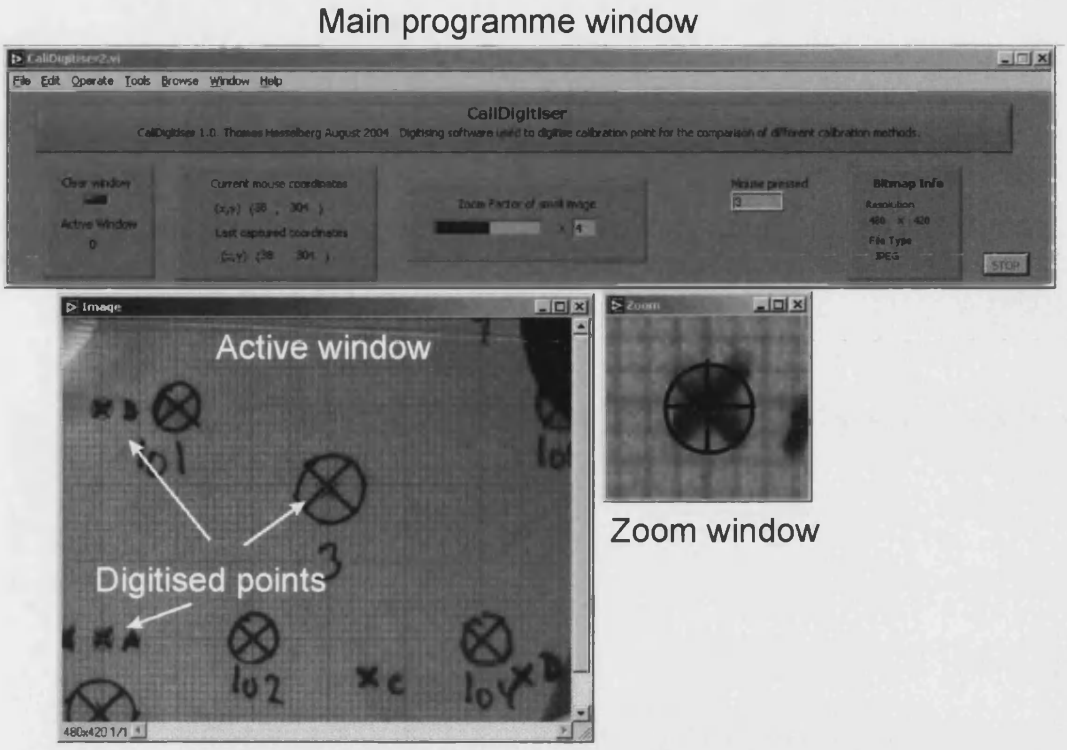

Fig. B.4. A screenshot of the programme Calidigitiser.vi being used to digitise points from a calibration sheet. The windows in the programme are highlighted and arrows point to the digitised points.

The second small programme PIVResAnal.vi is a modification of Nereis.vi which enables endpoints of lines to be digitised. This is useful for capturing the limits of the jets in the wake of the swimming worms (Fig. B.5). The VI differs from Nereis.vi in that more functions are carried out in the parent VI and that the menu options consist of buttons instead of a Menu Ring variable. The load and calibration function is similar to what is described for Nereis.vi in the previous section. The latter function opens the exact same SubVI (Calibration.vi). However, the Draw function, shows major differences to the SubVI Digitise.vi. No crosshairs are used, instead the end points of a line are digitised every time the user presses the mouse. The first line to be determined is a baseline that crosses the jet as close to the worm as possible (Fig. B.5). The lines are drawn with IMAQ Overlay Line.vi and after each drawn line (two clicks on the mouse button registered with IMAQ WindLastEvent.vi) the user is asked if a new line should be drawn or the programme terminated. All start and end coordinates of lines are continuously written into a data matrix (100 x 9) and when the user terminates the programme these image coordinates are converted into real world coordinates using the

last calibration method active in Calibration.vi and added to the data matrix. The front panel is designed with a Calculate function for analysing the digitised areas of the jets, but in the current version of the programme this function is empty as it proved easier and more flexible to write a separate MATLAB routine for analysing the digitised endpoints (see description of JetAnalyser.m in the next section).

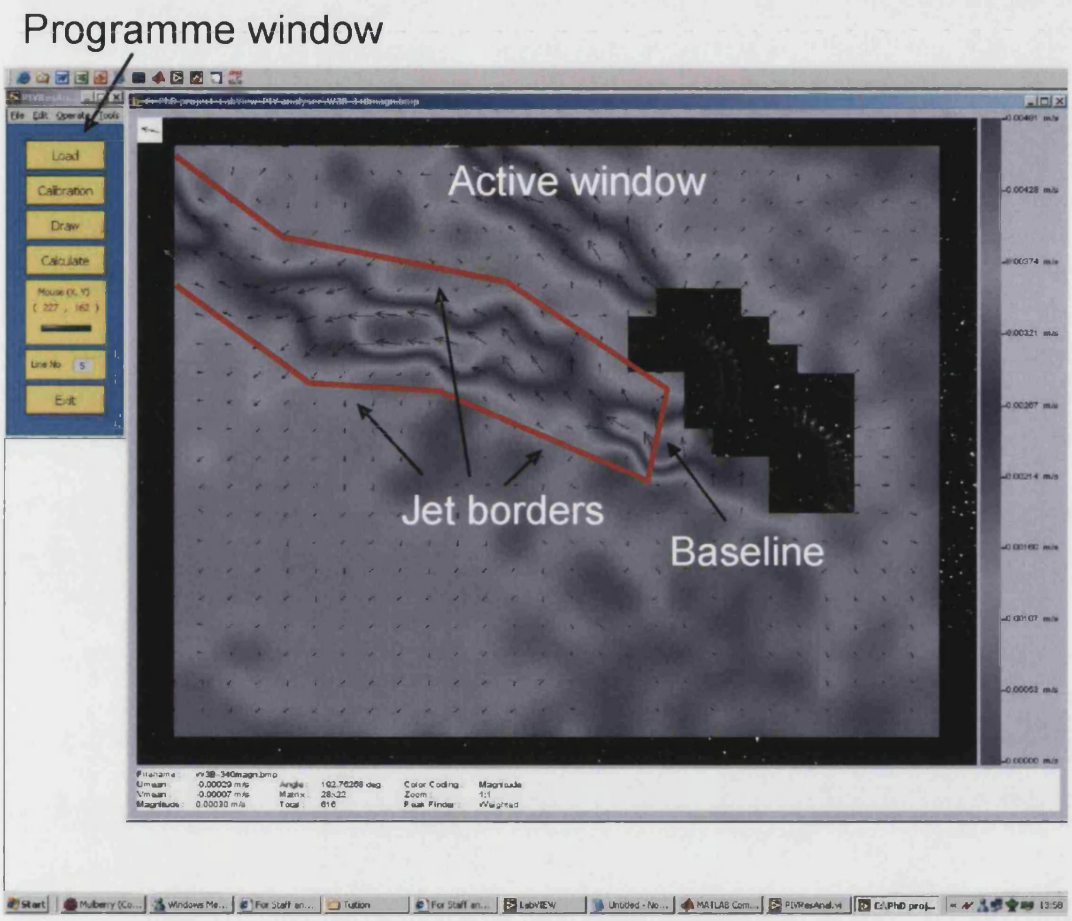

Fig. B.5. A screenshot of the software application PIVResAnal.vi being used to digitise the borders of the jet behind a swimming *Nereis diversicolor*.

B.4 MATLAB programmes for data analysis

The mathematical analysis of the digitised coordinates proved to be easier using small custom-built MATLAB (The MathWorks Inc. 2004) routines than incorporating them into the LABVIEW programmes described above. The output data from the LABVIEW programme in the form of a Microsoft Excel-file was transferred to

the MATLAB routine either by importing the Excel-file data into the current workspace or by loading the Excel-file directly into the MATLAB routine with the xlsread command. MethComp.m uses the latter method to transfer the sequence of 6 calibration marker and 4 reconstruction points from CaliDigitiser.vi (see previous section). The calibration parameters are calculated from given real world coordinates (written directly into the source code) and the found image coordinates of the 6 calibration points (or markers: 1 and 5 for the simple scaling method and markers: 1, 2, 5 and 6 for the 8 parameter 2D-DLT with 4 calibration points) in the main routine (simple scaling method) or in dedicated subroutines (dlt2d.m and dlt2d9.m) using the equations described in appendix A. The linear equations in the 2D-DLT methods were solved by using the Gauss elimination technique (the '/' operator in MATLAB). The calibration parameters are then used to convert the image coordinates of the 4 reconstruction points into real world coordinates using the equations described in appendix A either in the main routine (simple scaling) or in dedicated subroutines (transformdlt8.m and transformdlt9.m). The reconstruction error is found by taking the distance between the actual and found real world coordinates, which together with the coordinates goes into an output Excel file using the command dlmwrite. Generally all the MATLAB routines described in this section write their output data into an Excel file, although usually with the command xlswrite.

The following MATLAB routines are all used to analyse kinematic parameters from the high speed experiments described in chapter 5. They are generally not built as complete programs but designed as functions where the user typically has to provide the array containing the raw data (imported into the current workspace from an Excel file) and information about the recording such as frame rate and which frames and digitised points to include or exclude from the analysis. Crawlamp.m finds the amplitude and wavelength of a crawling worm by first finding the regression line (using the command polyfit to fit a first order polynomial in the least square sense) of the digitised peaks on the body wave. The user can select individual points to be excluded from the analysis such as head and tail and any non consistent peaks. This works by using the nargin command to find the number of excluded points and then to use if loops to match the given exclusion number with the raw data. Data points which are not excluded are written to another data array which is then subsequently used in the analysis. The

digitised points are then projected onto the regression line using the following equations:

$$x = \frac{x_0 + ay_0 - ab}{1 + a^2}$$
$$y = \frac{ax_0 + a^2 y_0 - a^2 b}{1 + a^2} + b$$

Where (x_0,y_0) are the original peak coordinates and a is the slope of the regression line and b the intercept. The same equations are used in all of the below described routines for finding the coordinates of the digitised points projected onto the regression line. In Crawlamp.m the distance between the projected points and the original points gives the amplitude and the distance between every second projected point gives the wavelength. Finally Crawlamp.m displays a geometrical simple worm moving through a sequence of frames by connecting the peak coordinates with a straight line using the link, set and drawnow commands and in the same frame showing the calculated regression line and projected points. This allows the user to verify the calculation of the regression line and manually exclude frames or digitised points where these are visibly wrong. Swimamp.m is used to calculate the amplitude and wavelength of swimming worms and works in a similar fashion to Crawlamp.m except that a global regression line, instead of a local regression line, is found from all digitised points in all frames and used to project the peak coordinates onto.

Crawlspeed.m uses the same imported digitised points as Crawlamp.m to calculate the wave and forward speed of the crawling worm. The user is required to give input on the frame rate (in frames per second), the frame interval to be analysed (all frames, every second frame or every 10^{th} frame etc.) and peak coordinates to be excluded from the analysis (this is similar to what is described for Crawlamp.m above). All points are projected onto the global regression line and the forward speed is calculated as the distance between the current projected head position and the last projected head position and then multiplied by the frame rate and divided by the frame interval. The mod command ensures that only every x'th frame (as given by the frame interval command) is used when finding the projected head position. The wave distance for each peak is the distance between its projected position and the projected position of

the head. By calculating the distance between the current and old wave peak position the wave speed is found for each peak (again by multiplying with the frame rate and dividing by the frame interval). However, since the waves are moving forward, every so often they reach the head and become extinct. In the frame where they become extinct the current wave distance must be paired with the old wave distance of the next peak number (because what was peak 3 in the last analysed frame will be peak 2 in the current frame due to the extinction of a wave at the head etc.). This is done in Crawlspeed.m by calculating the wave speed for both cases (new peak 2 to old peak 2 and new peak 2 to old peak 3 etc) and then use the smallest positive value of the two as the wave speed. Furthermore, the wave speed is compared with a threshold value of 45 mm/s. If the wave speed is higher than this threshold value it is set to zero and later discarded from the analysis. Swimspeed.m finds the wave and forward speed in a swimming worm and works similar to Crawlspeed.m except for some minor differences. The forward speed is calculated from the distance between the current and last projected midpoint. The midpoint is the midpoint between the first projected point and the last projected point in a frame and is used because it minimises the variance. It is possible to use it in swimming worms because here both head and tail are digitised in all frames, unlike in crawling worms. In general due to the higher speed and larger body undulations during swimming the variance in the speed measurements are much higher than during crawling. Therefore, only the second peak in a frame is used to find the wave speed but otherwise the same method as in Crawlspeed.m is used, except that the threshold value is set to 100 mm/s.

Chapter 6 describes the PIV observations of fluid flow behind a worm swimming in water where artificial particles have been added. A commercially available software application (Swift 4.0. Dutch Vision Systems, Breda, The Netherlands) is used to calculate the particle velocities and from that the flow characteristics of the wake. However, the kinematics of the swimming worms are found from the high speed recordings by the MATLAB routine Kinematics.m. This is basically a combination of the Swinamp.m and Swimspeed.m routines described above, but the user cannot exclude any digitised points from the analysis and all frames within a user selected range are used to calculate the kinematics. Furthermore, Kinematics.m calculates three different forward speeds by using the distance between subsequent headpoints,

midpoints and tailpoints. In chapter 6 most of the kinematics of the parapodia are found directly from the digitised data with the help of Excel. However, some of the kinematics and the figure showing the movement of the parapodium over time (Fig 6.2 in chapter 6) come from the MATLAB routine ParaviewPaper.m. The figures are made using the digitised data coordinates (base coordinates and tip coordinates of the parapodium) together with the link, set and drawnow commands. The parapodium length is simply the distance between the base and tip coordinates of the parapodium. The parapodium angle is the angle between the parapodium and the x-axis and it is found in radians by simple trigonometry. To convert radians into angles first the y-coordinates of the tip relative to the base and secondly the x-coordinates of the base relative to the tip are used to determine the quadrant (in the polar coordinate system) in which the parapodium angle is located. The angular velocity of the parapodium is then found as the difference between the current parapodium angle and the old parapodium angle multiplied by the frame rate (given by the user).

JetAnalyser.m analyses the output of the PIV software after the jet limits have been digitised by PIVResAnal.vi as described in the section above. The programme reads data from two Excel files. One is the output file from the PIVResAnal.vi containing the jet limits and the other is the data file from the PIV software containing the coordinates and velocity vectors of each particle in the flow around a swimming worm. The user is also requested to give the interval spacing distance along the midline. The extreme coordinates of the jet limits are used to generate a rectangular interrogation area (Fig B.6). All particle vectors within this area are checked to see if they lie within the jet. This is done in the subfunction Boundarycheck.m by finding the equation of each straight line in the upper and lower jet limits. The correct straight lines in the jet limits are identified by using the x-component of the particle vectors. If the y-component is between the y-values of the upper and lower jet limits for the given x-value, the particle vector is identified as being within the jet. The midline is then found in the main programme by finding the midpoint between all start and endpoints of straight lines in the upper jet limit and their corresponding start and end points of straight lines in the lower jet limit. Straight lines between these midpoints constitute the midline (Fig. B.6). This midline is segmented into intervals with a user defined length. From each interval junction a line is drawn to

the nearest point on the jet limits. The nearest point is identified using the equations given above for projecting a point onto a line. The subset of particle vectors lying inside the interrogation area are then scanned using Boundarycheck.m to identify the particle vectors within each interval along the midline. The found particle vectors are displayed using the quiver command and their mean velocity as well as the number of vectors and the standard deviation of the mean are found and saved in an output Excel-file alongside with the distance along the length of the jet (midline of the jet) and the width of the jet, which is found as the combined distance from the interval junction to the nearest point on both the upper and lower jet limits respectively (Fig. B.6).

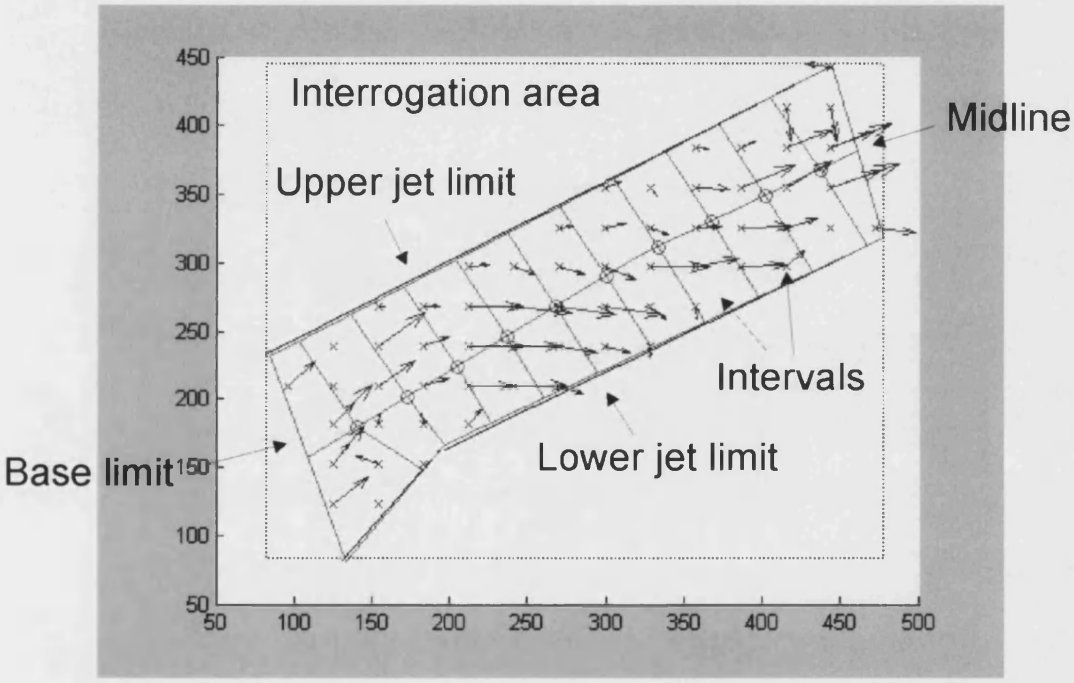

Fig. B.6. A MATLAB figure from the programme JetAnalyser.m that shows the jet limits and the particle velocity vectors within the jet, which are included in the analysis. The area within the dashed line is the scanning area. Text and arrows show points of interest. The interval spacing along the midline is here set to 20 mm.